Measuring the 3D Dynamics of Multiple Colloidal Particles with Digital Holographic Microscopy

Measuring the 3D Dynamics of Multiple Colloidal Particles with Digital Holographic Microscopy

A DISSERTATION PRESENTED
BY
JEROME FUNG
TO
THE DEPARTMENT OF PHYSICS

IN PARTIAL FULFILLMENT OF THE REQUIREMENTS
FOR THE DEGREE OF
DOCTOR OF PHILOSOPHY
IN THE SUBJECT OF
PHYSICS

HARVARD UNIVERSITY
CAMBRIDGE, MASSACHUSETTS

JUNE 2013

Thesis advisor: Vinothan N. Manoharan Jerome Fung

Measuring the 3D Dynamics of Multiple Colloidal Particles with Digital Holographic Microscopy

Abstract

We discuss digital holographic microscopy (DHM), a 3D imaging technique capable of measuring the positions of micron-sized colloidal particles with nanometer precision and sub-millisecond temporal resolution. We use exact electromagnetic scattering solutions to model holograms of multiple colloidal spheres. While the Lorenz-Mie solution for scattering by isolated spheres has previously been used to model digital holograms, we apply for the first time an exact multisphere superposition scattering model that is capable of modeling holograms from spheres that are sufficiently close together to exhibit optical coupling.

We apply the imaging and analysis techniques we develop to several problems. We image static colloidal clusters clusters containing up to 6 particles, which can be modeled as approximately rigid bodies. We also measure 6 degrees of freedom – three-dimensional translation, rotation about two axes, and vibration – in a two-sphere cluster bound by depletion forces. We also track multiple particles moving on the surface of an emulsion droplet. Finally, we perform precision measurements of the anisotropic diffusion of sphere clusters. We measure all the non-zero elements of the diffusion tensor $\mathbf{D}$ to $\sim$1% precision or better for sphere dimers and trimers, and make one of the first single-cluster observations of anisotropic rotational diffusion for a sphere trimer. Our measurements even allow us to resolve the effects of weak symmetry breaking due to slight ($\sim$3%) particle polydispersity in $\mathbf{D}$.

Contents

Listing of figures

List of Tables

Prior Publications

This thesis is primarily based on the following previously published works:

- J. Fung, K. E. Martin, R. W. Perry, D. M. Kaz, R. McGorty, and V. N. Manoharan, "Measuring translational, rotational, and vibrational dynamics in colloids with digital holographic microscopy." *Optics Express* **9**, 8051–8065 (2011).
- J. Fung, R. W. Perry, T. G. Dimiduk, and V. N. Manoharan, "Imaging multiple colloidal particles by fitting electromagnetic scattering solutions to digital holograms." *Journal of Quantitative Spectroscopy and Radiative Transfer* **113**, 2482–2489 (2012).
- J. Fung and V. N. Manoharan, "Holographic measurements of anisotropic three-dimensional diffusion of colloidal clusters," *Physical Review E* **88**, 020302(R) (2013).

Other works to which the author has contributed in graduate school include:

- R. W. Perry, G. Meng, T. G. Dimiduk, J. Fung, and V. N. Manoharan, "Real-space studies of the structure and dynamics of self-assembled colloidal clusters." *Faraday Discussions* **159**, 211–234 (2012).
- A. Perro, G. Meng, J. Fung, and V. N. Manoharan, "Design and synthesis of model transparent aqueous colloids with optimal scattering properties." *Langmuir* **25**, 11295–11298 (2009).
- R. McGorty, J. Fung, D. Kaz, and V. N. Manoharan, "Colloidal self-assembly at an interface." *Materials Today* **13**, 34–42 (2010).

- R. McGorty, J. Fung, D. Kaz, S. Ahn, and V. N. Manoharan, "Measuring dynamics and interactions of colloidal particles with digital holographic microscopy." *Digital Holography and Three-Dimensional Imaging Proceedings*, OSA Technical Digest (CD), paper DTuB1, (2008).

Several other publications relating in part to work discussed in this thesis are in preparation.

Ad majorem Dei gloriam.

Acknowledgments

It is a pleasure to thank the many people who have contributed to both the scientific aspects of the work in this thesis as well as my overall experience in graduate school over the past seven years.

Vinny Manoharan has been an outstanding advisor since the day I began graduate school. I have benefited from his experimental aptitude as well as his approach to doing science in general. I will be ever grateful for the freedom he gave me to try things, make mistakes, and to choose to work on problems I've very much enjoyed. The confidence he placed in me to help advise undergraduate summer researchers was amazing. In that capacity I would like to thank Kamilia Vaneck, K. Eric Martin and Jack Keller.

Although not directly related to digital holographic microscopy, I have also greatly enjoyed working on the theoretical problems concerning scattering by spheres at the interface of two optically distinct media with Prof. Alex Small.

I also wish to thank the other members of my thesis committee, Dave Weitz and Michael Brenner, for their advice and feedback over the past few years. Both Dave and Michael provided encouragement at times of deep frustration. David Nelson also merits thanks for his service on my committee. I also thank Peter Collings both for stimulating my interestin soft matter as an undergraduate as well as for his advice through the years.

I could not have asked for better colleagues than those I have had the pleasure of working with in the Manoharan lab over the past few years. Dave Kaz taught me most of what I know about laboratory optics and building things. I first learned to program in Python and work with colloids and holography from Ryan McGorty. Were it not for Tom Dimiduk, I would

be probably still be writing archaically-styled code. Becca Perry's deep physical insight and probing questions have always been helpful. And I've had a lot of fun working on inertial focusing with Anna Wang, as well as Joseph Martel from Mehmet Toner's group. I learned about particle synthesis and life from Guangnan Meng. Adeline Perro, Manhee Lee, Jin-Gyu Park, Ben Rogers, Jesse Collins, Sofia Magkiriadou, Nick Schade, Maddy Corbett, Emily Gardel, Eleanor Millman, and Dina Aronzon have all been great colleagues too.

I would also like to thank my colleagues in Physics for their inspiration, encouragement, and friendship. It has always been fun to discuss both physics and life with Kate Jensen. My thanks also go to the rest of Team 266 and other honorary members: Josh Dorr, Jason Dowd, Yejin Huh, Matt Barr, Mike Kagan, and Tracy Slatyer. I am also grateful to Sheila Ferguson, Lisa Cacciabaudo, Charlene Newell, and Barbara Drauschke for all their encouragement and administrative support over the past few years. I have also had the privilege of learning from Stan Cotreau in the machine shop and Jim Haldeman in the electronics shop.

In my personal life, I owe much to my parents Teresa and Matthew, and my brother Julian, for their support, love, and prayers. I thank Jillian Waldman, Bethany Ziss, Russell Miller, and Oliver Mayor for their continual friendship. I am also grateful for the fellowship of the Episcopal Chaplaincy at Harvard and to the Rev. Luther Zeigler.

Music has been a huge part of my life in graduate school. Some of my best memories of the past few years are from Ed Jones, the Harvard University Choir, and the Choral Fellows. I have benefited from the chance to study voice with Frank Kelley, and more recently, organ with Chris Lane. On the trad side, Susie Petrov and Jacqueline Schwab have guided my development as a pianist. It has been a pleasure to play in bands with Catherine Miller, Nora Smith, and too many others to name.

Lastly, but certainly not least, my sincere thanks and love go to Jennifer Dodwell for her unfailing devotion and constant support.

1

Introduction

This thesis describes two principal scientific results. First, we have developed methods for performing rapid, precise, three-dimensional (3D) imaging of multiple colloidal particles using a technique called digital holographic microscopy (DHM). Secondly, we have used these techniques to make new measurements of a fundamental physical phenomenon, the anisotropic Brownian motion of clusters of colloidal spheres. These results are described in detail in Chapters 4 and 5, respectively. In this Chapter, we provide a broader scientific context for these results. We begin by discussing colloidal suspensions and colloid physics (Section 1.1). Next, we discuss the crucial role that microscopy has played in colloid physics, along with mature techniques that have been developed for 3D microscopy of colloids, (Section 1.2). We then give a brief, historically-driven overview of the 3D imaging technique at the heart of this thesis, DHM (Section 1.3)

1.1 Colloidal Suspensions, Particles, and Clusters

We will define *colloids* as suspensions of solid particles, $\sim$ 10 nm – 5 μm in size, in fluids. We refer to the particles themselves as *colloidal particles* and the fluid as the *solvent*, even the particles are not, strictly speaking, dissolved. The length scales of the particles are important: we consider here particles that are large enough to behave as classical, non-quantum objects[1], and we also require the particles to be small enough to undergo Brownian motion. The size of colloidal particles, many of which are close to the wavelengths of visible light, mean that individual colloidal particles as well as aggregates can interact strongly with light, something we will subsequently exploit. That said, the particles can be made from inorganic materials such as silica or from polymers such as polystyrene (PS) or polymethyl methacrylate (PMMA). The solvents can also either be aqueous or organic, as in the seminal work of Pusey & van Megen studying PMMA particles in decalin that had nearly hard-sphere interactions [1].

Colloidal particles find practical applications in rheology control as well as optical control. One example may be found in Figure 1.1.1: an scanning electron micrograph of titania particles used to control the optical properties of cosmetics. Further discussion of practical applications of colloids, however, is outside the scope of this thesis.

Rather, our interest in colloids is primarily motivated by their utility as tools to study fundamental physics questions. In many senses, colloidal particles can act as model atoms. Many synthesis routes exist for making macroscopic quantities of monodisperse spherical particles[2] Interactions between colloidal particles, such as electrostatics, van der Waals forces, and depletion interactions are generally short-ranged and mostly well-understood. Consequently, colloids in many ways behave like atoms – with the exception that they are easily visualized and manipulated with light, and can be handled without specialized vacuum or low-temperature facilities.

[1] There is one key exception: a rigorous computation of van der Waals forces does require quantum field theory.

[2] For example, see [2] for a straightforward route for synthesizing cross-linked polystyrene spheres that the author has carried out. Monodisperse colloidal particles are also readily available for commercial purchase, which is how we obtained most of the particles used in this work.

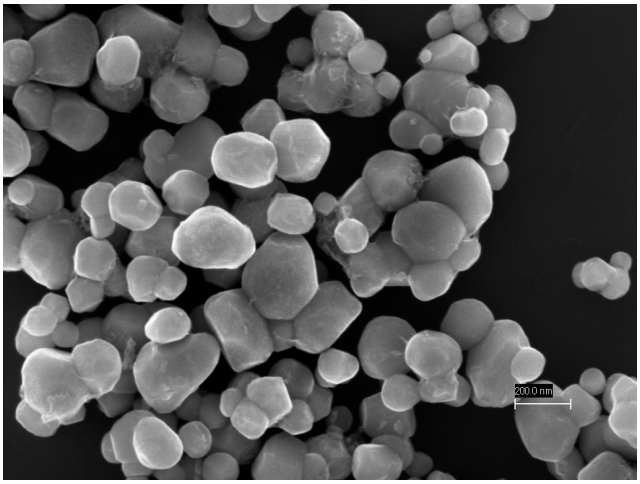

Figure 1.1.1: Scanning electron micrograph of rutile titania (TiO_2) particles; these are not monodisperse spheres. Scale bar, 200 nm. Image courtesy of W. Benjamin Rogers.

We cannot give a full review of the progress that has been made by using colloids as model atomic systems, but we give a few highlights. Phase behavior in bulk hard-sphere systems was one of the first statistical mechanical problems with which computer simulation techniques were pioneered in the 1950's [3]. Thirty years later, Pusey & van Megen's work with hard sphere colloids allowed experimentalists to access phenomena in the laboratory that had previously been the purview of theory and computation [1]. Studies using colloids as model atoms have subsequently become widespread; phenomena such as the glass transition [4] and crystal melting [5] have been studied. In these works, the size of colloidal particles has allowed structure and dynamics to be observed directly in real space with microscopy, as opposed to techniques based on scattering that probe reciprocal space.

Our primary focus in this thesis, however, is on small number of colloidal particles, and in particular, on clusters of colloidal spheres (which we frequently refer to as colloidal clusters.) Some of the first work in this field came from Manoharan *et al.*, who showed that emulsion drops with a given number of particles N bound to their surface always form the same densely packed structure when the contents of the emulsion droplet are leached out [6]. Further numerical and analytical work [7] suggested how this process might be governed by geometrical constraints arising when the droplets are leached. This work was

important for several reasons: it ignited interest in colloidal clusters as a means to study the statistical mechanics of small numbers of particles, and it also suggested a means by which such clusters could be readily produced.

It was, however, the work of Meng *et al.* on the self-assembly of colloidal clusters from particles interacting via depletion interactions [8] that more fully showed how clusters can give insight into statistical mechanics and stimulated my own interest in imaging such clusters in 3D. With the short range of the depletion interaction (close to being a contact force), all rigidly packed clusters with the same number of inter-particle contacts have the same energy. There are two possible rigidly packed clusters that can be formed by six particles: an octahedron and a polytetrahedron[3]. Surprisingly, the octahedron and polytetrahedron do not form with equal probability: rather, the octahedron only forms with about a 4% probability. Meng *et al.* found that the entropy of the clusters must also be taken into account, and that the symmetry of the octahedron results in its having less entropy and a higher free energy as compared to the polytetrahedron. Moreover, Meng observed with conventional microscopy a transition between the two 6-particle free-energy-minimizing states, but the 3D details of the transition were not observable. This observation motivated my own interest in 3D microscopy, and some of the work described in this thesis eventually led to the observation of such a transition using DHM [9].

We have thus suggested some of the physical questions, particularly regarding the statistical mechanics of self-assembly, that can be addressed using colloidal clusters. Colloidal clusters, if rigid, are also non-spherical colloids. There has been much recent interest in such non-spherical clusters, for non-spherical particles might exhibit directional interactions, much as many real atoms do[4]. Colloidal clusters have also generated interest for their optical properties and the potential they offer for creating fluidic metamaterials [11]. We now turn to ways through which such clusters, and colloidal systems in general, can be studied through microscopy.

[3] See Meng [8] or Figure 4.1.2 for an illustration of the polytetrahedron.
[4] See Glotzer & Solomon [10] for an excellent review.

1.2 Microscopy and Colloid Physics

1.2.1 Microscopy: Elucidating Structure, Dynamics, and Interactions

Microscopy is far from the only useful experimental tool in colloid physics, but it is arguably one of the most important. We will not here discuss the relative capabilities and limitations of tools such as static and dynamic light scattering, rheology, and the surface forces apparatus, but will instead discuss how microscopy has enabled studies of real-space structure, dynamics, and interactions in colloidal systems. We do not seek to be comprehensive here, but instead refer the interested reader to the references in Crocker and Grier [12] and to the reviews of Habdas and Weeks [13] and Prasad *et al.* [14].

In bulk colloidal suspensions, microscopy allows the location of every particle in the field of view. It is thus straightforward to observe structure qualitatively. The microscopy of bulk colloidal suspensions can be traced back to Kose and co-workers, who imaged the low-volume fraction crystals formed by 341 nm-diameter charged spheres in a solvent with a very low ionic strength [15]. Due to the difficulty of imaging through many layers of a crystal of densely packed, strongly scattering spheres, other workers focused on imaging structures that were two-dimensional or thin, such as colloids bound to the surface of a flat fluid-air interface [16]. Other early work on structure dealt with the crystallization of nearly-hard spheres confined to narrow gaps. In particular, Pieranski *et al.* showed how the the crystal structure of nearly-hard spheres confined to a wedge changed as the wedge thickness increased: the structure evolved from a triangular monolayer, to two layers with square symmetry, and eventually to two layers with triangular symmetry [17] [5]. Van Winkle and Murray later found different phase behavior in further studies using charged particles [18]. In general, in studies like these, structure can be quantified through the pair correlation function $g(r)$, which can be directly computed from microscopy via a histogram of

[5] The evolution of the crystal symmetry can be explained by a packing argument. When the wedge thickness is comparable to $2a$, where a is the sphere radius, it is clearly impossible for more than one layer of particles to form. But the height of the second plane in a close-packed system exhibiting square symmetry (such as the (100) plane of a maximally dense bcc lattice) is $\sqrt{2}a \approx 1.41a$, while for a triangular lattice (e.g. the spacing between (111) planes in an fcc lattice) the height is $(2\sqrt{6}/3)a \approx 1.63a$. Consequently, as the wedge thickness increases to allow the formation of a second layer, a square symmetry is initially favored.

interparticle separations. This stands in contrast to scattering techniques which typically measure the structure factor $S(q)$, the Fourier transform of $g(r)$.

Time-resolved microscopy, particularly video microscopy, is also capable of tracking how the structure of a colloidal suspension evolves in time, particularly during phase transitions. Examples of the physical situations that have been explored this way include the melting of colloidal crystals [19], the formation of colloidal crystals [20], the movement of crystal defects [21], and how defects can serve as nucleation sites for melting [5]. These are but a few examples of works that examine particle trajectories, or correlation functions from those trajectories, obtained through microscopy. Crocker and Grier [12] were particularly instrumental in establishing particle tracking techniques and software.

Another aspect of dynamics that has been successfully probed with microscopy, and which is particularly relevant to this thesis, is diffusion. We will defer a more detailed discussion of Brownian motion to Chapter 5, but qualitatively, it consists of the continuous random motion of small particles dispersed in a fluid as they are buffeted by molecular motions. The quantitative study of Brownian motion using microscopy can be traced to Jean Perrin, who in 1909 experimentally confirmed Einstein's theory of Brownian motion [22]. Perrin quantified the displacements of monodisperse, submicron emulsion droplets of natural rubber latex; his work helped to definitively establish the existence of atoms [6]. The Stokes-Einstein relation that Perrin's work helped establish related mean-squared displacements of spheres in n dimensions over a lag time τ to a diffusion constant D:

$$\langle \Delta \mathbf{r}^2(\tau) \rangle = 2nD\tau \tag{1.1}$$

where

$$D = \frac{k_B T}{6\pi\eta a}. \tag{1.2}$$

Here k_B is Boltzmann's constant, T the absolute temperature, η the solvent viscosity, and a the sphere radius. This relation allows the unknown viscosity of a fluid to be determined

[6] The author commends Jean Perrin's original work to any reader with a reading knowledge of French, despite its length. An English translation, entitled "Brownian Movement and Molecular Reality," was made by Frederick Soddy and published by Taylor and Francis in 1910. Perrin's descriptions of his experimental details, including matters such as his preparation of a monodisperse emulsion through a serial centrifugation process, are fascinating.

by measuring trajectories of particles of known size undergoing Brownian diffusion, or alternately (as is usually the case in dynamic light scattering [23]) for spheres diffusing in a fluid of known viscosity to be sized.

In recent years research in this vein has been revitalized in two ways. First, in 1995, Mason and Weitz developed microrheology and the use of a generalized Stokes-Einstein relation not solely to measure the viscosity η of a Newtonian fluid, but rather the frequency-dependent complex modulus $G^*(\omega)$ of a viscoelastic material [24]. Here, $G^*(\omega) = G'(\omega) + iG''(\omega)$, where the storage modulus $G'(\omega)$ describes the elastic component of the material's stress and the loss modulus $G''(\omega)$ describes the viscous component. While the earliest work in microrheology was based on light scattering rather than microscopy [24], it was not long before microscopic tracking of individual particles was used to calculate mean-square displacements and thence G^* via a laser deflection scheme [25]. Later, workers such as Apgar *et al.* [26] and Valentine *et al.* [27] realized that particle-tracking microrheology via video microscopy allowed the motion of many particles to be observed simultaneously, allowing for better statistics, particularly in inhomogeneous environments. Microrheology continues to be a useful tool in biophysics, in part because it allows *in situ* measurements of the mechanical properties of living cells [28]. Secondly, the more complex Brownian dynamics of non-spherical particles has begun to have been explored; the work of Han and co-workers in Arjun Yodh's group on the 2D Brownian diffusion of ellipsoidal polystyrene particles has been of particular importance [29]. We will explore this topic further in Chapter 5.

Another important use of microscopy in colloid physics lies in measuring colloidal interactions. All such techniques are based on observing in some manner the statistics of the relative motion of interacting colloids. For a pair of particles that experience an interaction potential $U(r)$, the Boltzmann distribution states that the probability $p(r)$ of finding the particles separated by r is

$$p(r) \propto \exp\left[-\frac{U(r)}{k_B T}\right]. \tag{1.3}$$

For a system with many particles, a similar relation holds for the pair correlation function

$g(r)$ [30] [7]:

$$g(r) = \exp\left[-\frac{U(r)}{k_B T}\right]. \tag{1.4}$$

The various techniques, which we review here, differ in how they probe $p(r)$ or $g(r)$.

One approach is to observe motions and fluctuations that are entirely driven by natural thermal motion. One example of such a technique is the work of Kepler and Fraden [31], who studied the attractions between like-charged colloidal particles confined between two plates. Kepler and Fraden measured $g(r)$ for an dilute ensemble of particles via video microscopy. They sought to measure a pair potential $U_p(r)$, but except in the limit of an infinitely dilute suspension, the $U(r)$ extracted from Equation 1.4 will be subject to many-body contributions. Thus, Kepler and Fraden had to combine their experiments with iterative Monte Carlo simulations to extract $U_p(r)$. A more recent example of an approach based on natural fluctuations is the measurement by Nikolaides *et al.* of the still-mysterious like-charge attractions experienced by charged particles on a droplet [32]. But, it might be argued, Kepler and Fraden's techniques do not result in a direct measurement of a pair potential. Moreover, Nikolaides's measurement hinged on the particles on the droplet forming a symmetric structure and on the particles being pinned to the quasi-2D droplet surface. In a bulk suspension, particles would likely move out of the focal plane of the microscope, at which point measuring particle separations would be difficult.

A related technique that enables strictly 2-body measurements and overcomes the problem of particles moving out of the focal plane uses line optical tweezers. Optical trapping was introduced by Ashkin [33], who trapped colloidal particles in the focus of a laser beam. If such a focused beam is rastered in a horizontal line, a particle in the trap can be confined to the line but left essentially free to move along the line. If two particles are trapped in this way, their separation distance will be governed by Equation 1.3, and the particle separation can be monitored via microscopy. This approach was taken by Crocker *et al.* [34], who used a scanning line trap to measure an oscillatory depletion interaction between two large spheres in a bath of smaller spheres at high volume fraction. Similar techniques were subsequently used to explore other interactions, such as the interaction potential between

[7] Here, as is generally the case in colloid physics, $U(r)$ is not strictly the interaction energy between two particles in vacuum, but is an effective interaction that coarse-grains over the solvent.

particles coated with complementary DNA sequences [35]. The scanning line trap technique does require the measurement and subtraction of the potential induced by the scanning trap, and it does not account for optical forces which may be induced between the trapped particles. Finally, in all of these techniques based on natural thermal motion, the interactions that were measured were primarily attractive. Techniques like these are ill-suited for measuring strong interactions, or strongly repulsive interactions, for the simple reason that particles are highly unlikely to be found at distances where $U(r)$ is more than a few $k_B T$ higher than the minimum.

A complementary technique uses blinking optical traps to manually place particles in positions (even at separations where the particles experience a strong repulsion) and then let them go. The particle trajectories are subsequently governed by a combination of the interaction forces and random thermal forces. This was first introduced by Crocker and Grier for measuring the interaction forces between charged colloids [36]. Subsequently this technique was also used to study long-ranged attractions between charged particles induced by confinement [37]. Related analysis techniques were introduced by Sainis *et al.* [38], who used blinking holographic optical traps to measure many-body electrostatic interactions between particles in a nonpolar, oily solvent [39]. The use of optical traps to manipulate particles, and not merely to confine them as in line optical tweezer techniques, allows repulsive interactions with strengths of tens of $k_B T$ to be measured. In all cases here, microscopy plays the key role of enabling the position of two or more particles to be tracked with precisions of tens of nm [34].

1.2.2 3D Microscopies

We have discussed how microscopy is useful to colloid physics. Thus far, we have focused on conventional microscopy, albeit perhaps with video recording.

Much physics, however, happens in not 2 but 3 spatial dimensions. While there are many systems, such as particles at fluid-fluid interfaces or on very large emulsion droplets, where the particles are at least locally two-dimensional, this is not true for most bulk suspensions. Confining particles to 2D, such as with glass walls, can introduce complications relating to charge or hydrodynamics [37]. Moreover, much interesting self-assembly happens in 3D.

A particular promise of colloidal self-assembly is the possibility of building inherently 3D structures, and microscopic tools that can observe this in real time and with high spatial resolution would be of value. Obtaining quantitative 3D information, similar to that which can be obtained from 2D particle detection and tracking techniques [12], is challenging. In particular, depth estimation is difficult as no micrograph image is formed only by light coming from the focal plane. As an example, we might for instance want quantitative 3D information about the emulsion-based self-assembly of clusters pioneered by Manoharan [6].

We do mention that there are some circumstances under which 3D information can be gained from conventional 2D microscopy. Several workers [40, 41] have reported schemes in which, essentially, the amount of defocus or blur in micrographs of spheres are used to quantify their axial distance from the microscope focal plane. Also, Colin *et al.* recently reported a means for quantifying the orientation of large aspect ratio nanowires by measuring their projections onto the microscope focal plane [42]. These techniques, however, are not particularly general. In particular, it is difficult to observe motions beyond a $\sim$10 μm range [41], and Colin's techniques would be difficult to apply to objects with aspect ratios near unity.

We thus briefly discuss two specialized microscopies that are capable of giving quantitative 3D information: total internal reflection microscopy (TIRM) and confocal microscopy. We focus on these techniques because they have been used widely and effectively in colloidal systems; we do not discuss, for instance, the multiphoton microscopies that have proven especially useful for live-cell biological imaging.

Total internal reflection microscopy is capable of detecting the position of spheres several μm in diameter or larger with nm precision in the axial direction. TIRM was introduced by Prieve and colleagues [43], and its operating principle is illustrated in Figure 1.2.1(a). When a plane wave reflects from an optical interface, such as that between glass and water, and the angle of incidence θ_i exceeds a critcal angle, the wave is totally internally reflected. The critical angle θ_c is given by $\sin\theta_c = n_2/n_1$, where n_1 is the index of the medium from which the wave is incident. However, an evanescent wave (which transports no energy on average) is present in medium 2. The evanescent wave propagates parallel to the interface and decays exponentially away from the interface. This evanescent wave can

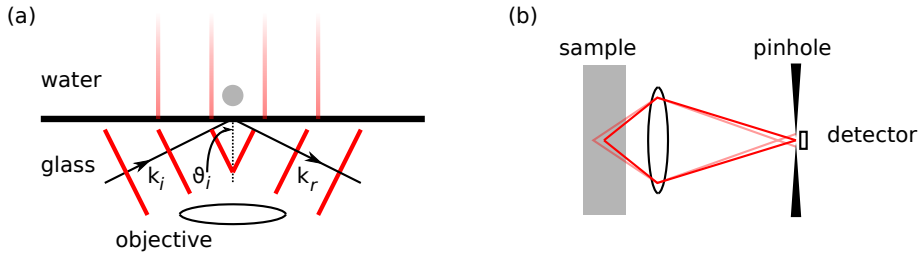

Figure 1.2.1: Schematic illustrations of (a) total internal reflection microscopy and (b) confocal microscopy. (a): When the angle of incidence θ_i of an incident wave exceeds the critical angle $\theta_c = \sin^{-1}(n_{\text{water}}/n_{\text{glass}})$, where n_{water} and n_{glass} denote the refractive indices of water and glass, the incident wave is totally internally reflected. An evanescent wave propagates from left to right in the water and decays exponentially in the vertical direction. The evanescent wave can scatter from a particle in a manner that is highly sensitive to the height of the particle. (b): Working principle of confocal detection. A pinhole prior to the detector enables light to be detected from only a small spot in the sample (solid red lines). Light from nearby planes (lighter red lines), which would contribute to out-of-focus intensity in a conventional microscope, gets blocked by the pinhole. For clarity, we do not show the optics needed in a real confocal microscope to excite fluorescence.

scatter light. A theory of the scattering of an evanescent wave from a sphere was worked out by Chew *et al.* [44]. Critically, the amount of light scattered by a sphere due to the evanescent field also varies exponentially with the height of the sphere from the interface. This allows nanometer-scale changes in the height of a particle to be detected [43, 45, 46].

TIRM has been used to measure colloidal interactions, including the depletion interaction between a sphere and a flat plate [47], as well as the hydrodynamically hindered diffusion of a particle near a wall [46]. However, TIRM's greatest strength, the exponential decaying evanescent field which enables precision axial tracking, is also its greatest weakness: typical decay lengths are around 100 nm [46]. Particles much further from the interface will not appreciably scatter the evanescent wave. The weak scattering cross section from evanescent waves also requires the use of particles at the upper end of the colloidal length scale, at least several μm in diameter.

Confocal fluorescence microscopy is probably the most widely used 3D microscopy in colloid physics today. Confocal microscopes combine point-source fluorescence excita-

tion with point-like detection to build up 3D image volumes. In a confocal microscope, images can be recorded wherein all the detected light comes from a narrow $\sim$ 100 nm optical section [48]. When multiple such images, each corresponding to a different axial distance, are recorded, this z-stack can be reconstructed to create a full 3D volumetric image. We illustrate the principle behind confocal detection in Figure 1.2.1. In a confocal microscope, a pinhole effectively allows light to be collected from a single point in the sample[8]. The pinhole blocks out-of-focus light.

Several features of confocal microscopy are relevant to colloid physics. First of all, effective 3D confocal microscopy places significant limitations on the samples used. The colloidal particles themselves need to be index-matched to the solvent; otherwise, scattering will make it impossible to image deep into a sample. The most common system consists of polymethyl methacrylate (PMMA) spheres in a mixture of decalin and cyclohexyl bromide [48], although other systems involving silica spheres are possible. Moreover, all of these systems need to incorporate a fluorescent dye, most commonly inside the particles. Most importantly, the approximately point-like detection of confocal microscopy requires scanning both within a lateral plane and in the z direction. It can therefore take on the order of seconds for a confocal microscope to fully image a 3D volume several microns on a side. This necessarily restricts confocal microscopes to studying systems that exhibit relatively slow dynamics. Much excellent work has been done using confocal microscopy to study colloidal glasses and gels; see Prasad *et al.* for a review [14]. But as we will discuss in Chapter 5, the slow speed of confocal microscopes can be a serious disadvantage in some situations.

1.3 Digital Holographic Microscopy

1.3.1 Encoding 3D Information

Digital holographic microscopy (DHM), the focus of this dissertation, can overcome some of the limitations of other 3D microscopy techniques. We argue that DHM complements

[8] This discussion ignores the effects of the point spread function and the finite size of the pinhole in a real confocal microscope.

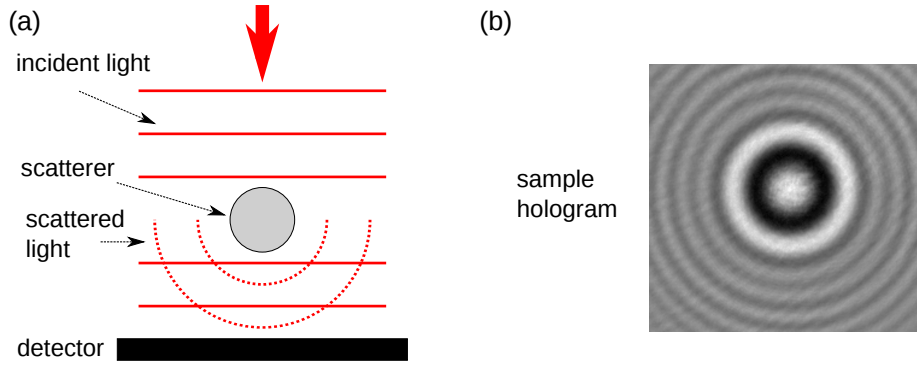

Figure 1.3.1: (a) Schematic overview of in-line DHM. A coherent plane wave from a laser illuminates scatterers in a sample. A camera records the interference pattern, or hologram, formed between scattered light and unscattered incident light. (b) Typical hologram of a 1 μm diameter polystyrene sphere in water. Center of circular fringes encodes particle x and y position (perpendicular to the optical axis). Fringe spacing encodes particle position along z (along optical axis).

techniques such as confocal microscopy. As we will subsequently discuss, the rapid temporal resolution of DHM makes it particularly useful for observing rapid colloidal dynamics or rare events. Appendix D describes the use of DHM to perform 3D location and single-shot particle velocimetry for polystyrene spheres flowing at high speed ($\sim$ 1 m/s) in a microfluidic channel; such measurements would be impossible using confocal microscopy. At the same time, we will also discuss how DHM is challenging to perform in dense colloidal suspensions, such as those near the glass transition, but in which confocal microscopy works well.

Figure 1.3.1(a) illustrates the working principle of in-line DHM, the technique we use. In DHM, instead of illuminating a sample of colloidal suspension with an incoherent white light source (or, in the case of fluorescence microscopy, with approximately monochromatic but incoherent light), we use a coherent laser for illumination. As we will describe in further detail in Chapter 3, we collimate the laser beam so that the illumination can be approximated as a plane wave. Some of this incident light scatters from particles in the sample, but in a dilute suspension most of the incident light is not scattered. Subsequently, we record the interference pattern, or hologram, formed between the scattered light and un-

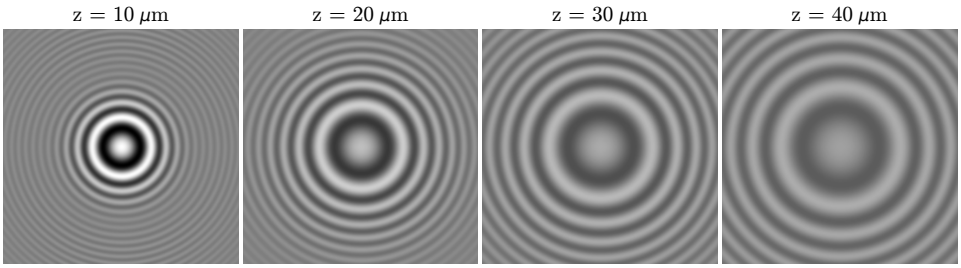

Figure 1.3.2: Simulated holograms of a 1 μm-diameter polystyrene sphere in water. z is the distance along the optical axis between the particle and the hologram plane. As z increases, the spacing between the hologram fringes increases. Holograms are simulated using the Lorenz-Mie formalism described in Chapter 2.

scattered incident light. A typical sample hologram formed by a colloidal sphere is shown in Figure 1.3.1(b). One of the key advantages of DHM, namely rapid acquisition rates, stems from holograms being 2D images that are straightforward to record with conventional CMOS cameras. While the work described in this thesis uses research-grade cameras with frame grabbers or high-speed cameras, it is even possible to perform DHM using commercial digital cameras [49].

DHM is useful as a 3D imaging technique because 2D holograms encode 3D information. The sample hologram in Figure 1.3.1(b) illustrates this. The concentric circular fringes have a center whose position corresponds to the particle position in the lateral (x and y) directions, perpendicular to the optical axis. The spacing of the fringes encodes the position of the particle in z, along the optical axis. This is further illustrated by the series of simulated holograms in Figure 1.3.2. As the distance z between the particle and the hologram recording plane increases, two effects are readily noticeable. First, the spacing of the fringes increases. This may be understood by thinking of the scattered waves from the particles as being approximately spherical. In the limit of infinitely large z, a spherical wave will look planar, and there will be no phase variations leading to inteference fringes as one traverses the hologram plane. Secondly, the contrast in the hologram fringes decreases as z increases. This is entirely due to the approximate $1/r$ dependence of the scattered electric field, as we will discuss in Chapter 2.

In addition to particle positions, holograms also encode information about the scatter-

ers themselves. As is apparent in Figure 1.3.2, the amplitude of the hologram fringes is not constant, but rather decreases towards the edges (or equivalently, as the scattering angle increases). This is because the amplitude of the hologram fringes is modulated by the angular dependence of the scattered light from the particle: the same quantity that is probed in static light scattering experiments. The angular dependence of the scattering from a particle will depend, in general, on its size and refractive index. We illustrate this effect in Figure 1.3.3, where we show simulated holograms of a weak scatterer, a 200 nm diameter polystyrene sphere, and of a stronger scatterer, a 2 μm diameter polystyrene sphere. The plots of the intensity across the horizontal dashed lines clearly indicate that the fringes of the two holograms have very different envelopes, even though they have approximately the same fringe spacing away from the center. The envelope of the fringes is approximately set by the amplitude of the scattered electric field, as shown by the dotted lines. Note that this breaks down near the center of the hologram of the strongly scattering sphere in Figure 1.3.3(b), for reasons we will soon discuss.

1.3.2 Historical Development of Digital Holographic Microscopy

Holography can be traced back to the 1948 work of Dennis Gabor, who at the time was working on electron microscopy and was seeking ways to avoid the problems caused by primitive electron lenses that suffered from spherical aberration [50]. Specifically, Gabor's proposal avoided lenses entirely and was based on a diverging incident wave. Figure 1.3.4 illustrates Gabor's proposal, which today we would refer to as *point source in-line holographic microscopy*. Gabor recognized that his proposal would apply to light as well, and indeed demonstrated his idea by using a mercury arc lamp and a pinhole to create an approximately monochromatic, coherent source of spherical waves [50, 51]. Gabor recorded holograms of 2D test images and recovered his original images from the holograms by illuminating the holograms in reverse, which is known as reconstruction. We discuss reconstruction in more detail in Section 1.3.3.

Despite Gabor's seminal work, holographic microscopy did not become practical until

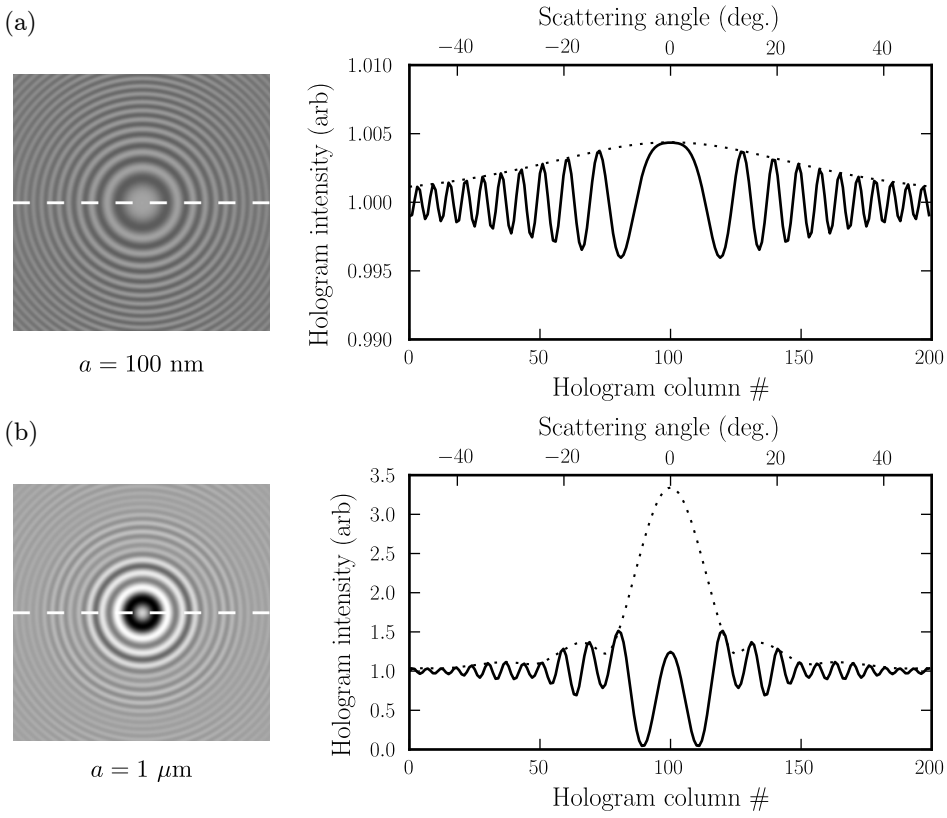

Figure 1.3.3: Amplitude of scattered field sets envelope of hologram fringes. Simulated holograms shown of 100 nm radius (a) and 1 μm radius (b) polystyrene spheres in water. Solid lines in plots show hologram intensity along horizontal dashed lines. Dotted lines show amplitude of in-plane components of scattered electric field computed in simulations. The dotted lines have been shifted vertically for clarity.

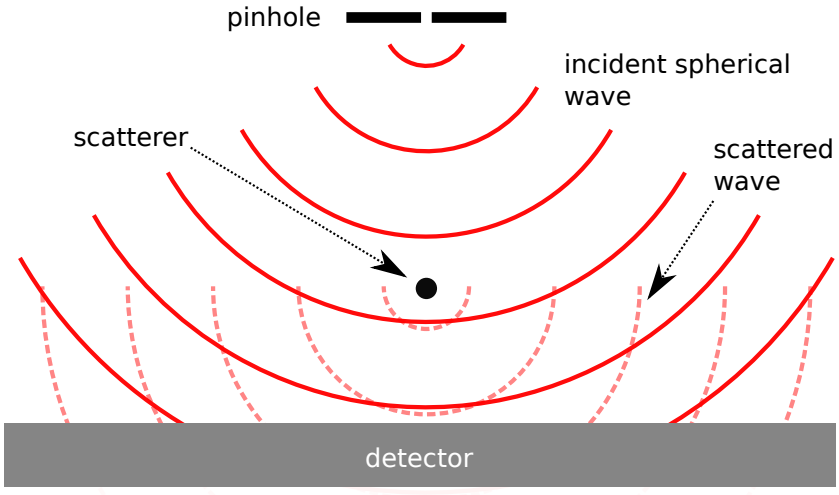

Figure 1.3.4: Schematic illustration of point source in-line holographic microscopy as proposed by Gabor. A spherical incident wave emanates from a pinhole and illuminates a scatterer. Because the scatterer is downstream from the pinhole, the phase difference between the scattered and incident waves will vary over the detector, which will consequently record a fringe pattern.

the development of digital holographic microscopy in the 1990's [9]. Even after lasers became readily available sources of intense, coherent light, recording holograms generally required finely grained photographic films, which were difficult to handle and time-consuming to process prior to optical reconstruction. The development of CCD cameras, along with improvements in computing, eventually made it possible to record holograms digitally and to simulate the optical reconstruction process numerically [52].

One of the earliest works demonstrating both digital recording and numerical hologram reconstruction was that of Schnars and Juptner [53]. This was not microscopy: Schnars and Juptner were imaging an ordinary gaming die. The size of the die, large enough to block a substantial amount of incident light, required the use of an off-axis rather than in-line configuration. Schnars and Juptner recognized at this stage one of the limitations of CCD's as opposed to the specialized photographic films previously used for holography: the large ($\sim$10 μm) pixel size, almost 2 orders of magnitude larger than the resolution of

[9] We refer the reader interested in the intervening historical development, as well as to the development of related applications of holography, to Kreis's book [52] and the references therein.

holographic films. The resulting loss of high-spatial frequency information necessarily degraded the imaging resolution. Still, the convenience of digital recording and numerical reconstruction, when compared with the tedium of wet-processing photographic films, was substantial.

Schnars and Juptner were not the only workers to recognize the limitations posed by the pixel sizes of CCDs. One solution to this problem was to use lenses to magnify holograms. This approach was taken by a variety of workers, including Cuche and coworkers [54], as well as Zhang and Yamaguchi [55]. The approach of combining magnifying lenses and an off-axis holographic configuration led to some beautiful results, particularly in the area of biological microscopy [56]. However, off-axis holographic setups have the disadvantage of a much more challenging setup and alignment, and quantitatively precise reconstruction can also be more difficult.

An alternative approach to overcome the problem of large CCD pixel sizes was introduced by Kreuzer and colleagues. Kreuzer opted to use an in-line configuration with illumination by a point source, much as in Gabor's original proposals and in Figure 1.3.4 [57, 58]. In particular, the since the reference wave from the point source diverges as it propagates, it is possible to magnify the hologram fringe pattern without any lenses whatsoever, simply by placing the detector further away. This approach allowed Xu *et al.* to image both colloidal [58] as well as biological samples [57]. The comparatively straightforward setup of this approach, with no lenses that might introduce optical aberrations, was clearly advantageous over off-axis configurations. But Kreuzer's lensless, point-source configuration is arguably not ideal. In particular, once the detector is moved far away from the point source and the scatterers (to enhance the magnifying effect of free-space propagation), the price paid by having detectors that might only be $\sim$ 2 cm on a side is poor coverage of scattering angles. As we have seen in Figure 1.3.3, coverage of scattering angles encodes information about the size and contrast of scatterers.

The optical configuration we use in this thesis, which has been adopted by other workers (in particular David Grier's group [59]), combined the magnifying optics first used by Cuche *et al.* [54] with the simplicity of Kreuzer's in-line setup [57]. This configuration, introduced by Sheng, Malkiel, and Katz [60], was similar to the schematic in Figure 1.3.1(a), with the insertion of a microscope objective lens between the scatterer and the detector.

This lens, as in prior work, served to magnify the hologram, or equivalently, to effectively minify the detector pixels. This setup allowed the effective hologram plane to remain relatively close to the scatterers (within tens of μm), allowing for good scattering angle coverage with high numerical aperture immersion objectives, while making the hologram fringes large enough that finite pixel size effects were basically negligible.

1.3.3 Holographic Formation and Reconstruction

We now examine in greater detail the formation of a hologram and how reconstruction works. Reconstruction techniques generally model light as a scalar wave. To understand hologram formation, we will adopt the following physical picture. We will assume that a scatterer is illuminated by an incident wave E_{inc}. This incident wave scatters from the particle to create a scattered wave, E_{scat}; both of these waves illumine a detector, which records an interference pattern. To model this mathematically, throughout this section we will assume and suppress a harmonic time dependence, $e^{-i\omega t}$.

In general, detectors (such as the pixels of a camera, or the human eye) are sensitive not to electric fields directly, but to intensity I. In particular, because the detector in an in-line configuration records both the scattered wave as well as the unscattered incident wave, the intensity recorded for a hologram will be

$$\begin{aligned} I &= |E_{\text{inc}} + E_{\text{scat}}|^2 \\ &= |E_{\text{inc}}|^2 + E_{\text{inc}}E_{\text{scat}}^* + E_{\text{inc}}^* E_{\text{scat}} + |E_{\text{scat}}|^2 . \end{aligned} \tag{1.5}$$

This relation holds true (within the limitations of scalar wave optics) regardless of any assumptions made by a reconstruction technique. The first term is a DC term: for plane wave illumination, $|E_{\text{scat}}|^2$ gives a constant background intensity across the detector.

The essential physical nature of reconstruction is illustrated in Figure 1.3.5. The fringes of a recorded hologram essentially act as a zone plate and can focus light when illuminated. In particular, by shining light backwards through the hologram, it is possible to reconstruct the field scattered by the particle, as we will show.

We now make this qualitative picture more rigorous, and it is here that the reconstruc-

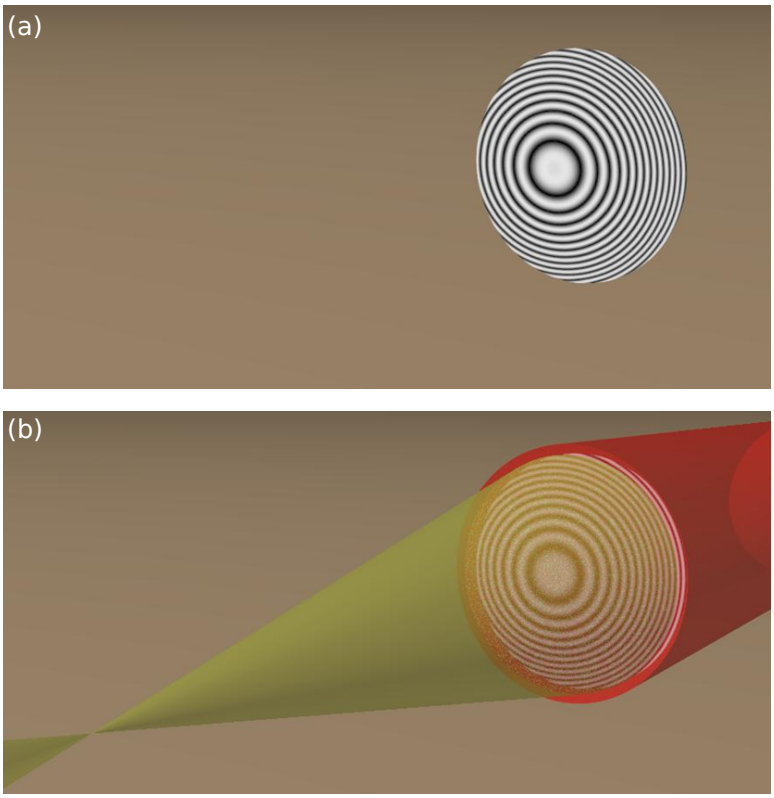

Figure 1.3.5: Schematic illustration of hologram reconstruction. A film hologram, whose fringes act like a zone plate, is illuminated (a). The fringes cause the illuminating light to be focused to the location of the source of the spherical waves that originally formed the hologram (b). Under suitable approximations, this is the location of the scatterer.

tion approach begins to make approximations. First of all, one assumes that scattering is weak: $|E_{\text{scat}}| \ll |E_{\text{inc}}|$. Consequently, the last term in Equation 1.5 may be neglected relative to the remaining terms. Illuminating the hologram backwards is akin to multiplying Equation 1.5 by E^*_{inc} (if we had an incident plane wave, e^{ikz}, a backwards-propagating wave would have the form e^{-ikz}). Thereafter, we obtain

$$E^*_{\text{inc}} I = E^*_{\text{inc}} |E_{\text{inc}}|^2 + E^*_{\text{scat}} + E^{*2}_{\text{inc}} E_{\text{scat}} \tag{1.6}$$

at the hologram plane. The second term here is E^*_{scat}, a backwards-propagating version of the scattered wave. In particular, if E_{scat} is a spherical wave with amplitude A outgoing from the origin,

$$E_{\text{scat}} = A \frac{e^{ikr}}{-ikr} \tag{1.7}$$

where r is the distance between the particle and a point on the hologram plane, then

$$E^*_{\text{scat}} = A \frac{e^{-ikr}}{ikr}. \tag{1.8}$$

This is a spherical wave converging at the origin, where the particle was. It is in this sense that reconstruction recovers the wave scattered by the particle.

It is clear, however, that E^*_{scat} is not the only component when a hologram is illuminated in reverse, in Equation 1.6. The first term, arising from the DC background, will once again be constant [10]. But the third term, proportional to E_{scat}, will give rise to the twin image: a wave that converges on the opposite side of the hologram plane as the real image from E^*_{scat}. This twin image problem was recognized early on by Gabor [51], and eliminating it was a motivation for developing off-axis techniques. In-line reconstruction approaches generally ignore the twin image; it is assumed that the field due to the twin image near the focal point of the real image is small.

Once we have E^*_{scat} at the hologram plane (from Equation 1.6, neglecting DC and twin image contributions), it is then necessary to propagate this field from the hologram plane. The field $E^*_{\text{scat}}(x', y', z')$ at an arbitrary point (x', y', z') is related to the field $E^*_{\text{scat,hp}}$ at the

[10] If necessary, it is also possible to measure and subtract off the DC background term prior to reconstruction.

hologram plane via the Fresnel-Kirchoff diffraction formula [52]:

$$E^*_{\text{scat}}(x', y', z') = \frac{i}{\lambda} \int\int E^*_{\text{scat,hp}}(\xi, \eta) \frac{e^{ik\rho}}{\rho} \, d\xi \, d\eta. \tag{1.9}$$

Here λ is the wavelength of the illuminating light, ξ and η are coordinates in the hologram plane, the integrals run over the entire hologram plane, and

$$\rho = \sqrt{(\xi - x')^2 + (\eta - y')^2 + z'^2}. \tag{1.10}$$

We have here neglected the obliquity factor z'/ρ. Since the integrand in Equation 1.9 depends only on the differences $\xi - x'$ and $\eta - y'$, we may write $E^*_{\text{scat}}(x', y', z')$ as a convolution:

$$E^*_{\text{scat}}(x', y', z') = E^*_{\text{scat,hp}} \star h \tag{1.11}$$

where h_z is the impulse response function of free space:

$$h(\xi - x', \eta - y') = \frac{i}{\lambda} \frac{e^{ik\rho}}{\rho}. \tag{1.12}$$

Recalling the convolution theorem, thanks to the fast Fourier transform it is computationally faster to compute $E^*_{\text{scat}}(x', y', z')$ using the transfer function $H = \mathcal{F}\{h\}$, where $\mathcal{F}$ denotes the Fourier transform:

$$E^*_{\text{scat}}(x', y', z') = \mathcal{F}^{-1}\{\mathcal{F}\{E^*_{\text{scat,hp}}\} \cdot H\}. \tag{1.13}$$

The actual computational implementation is somewhat less straightforward than this; in particular, experimentally recorded holograms are not continuous functions. Since reconstruction is not the focus of this thesis, we refer the interested reader to Kreis [61] for details.

1.3.4 Fitting Techniques

Despite the relative simplicity and above all generality of analyses of digital holograms based on reconstruction, it eventually became clear to other workers in the field that recon-

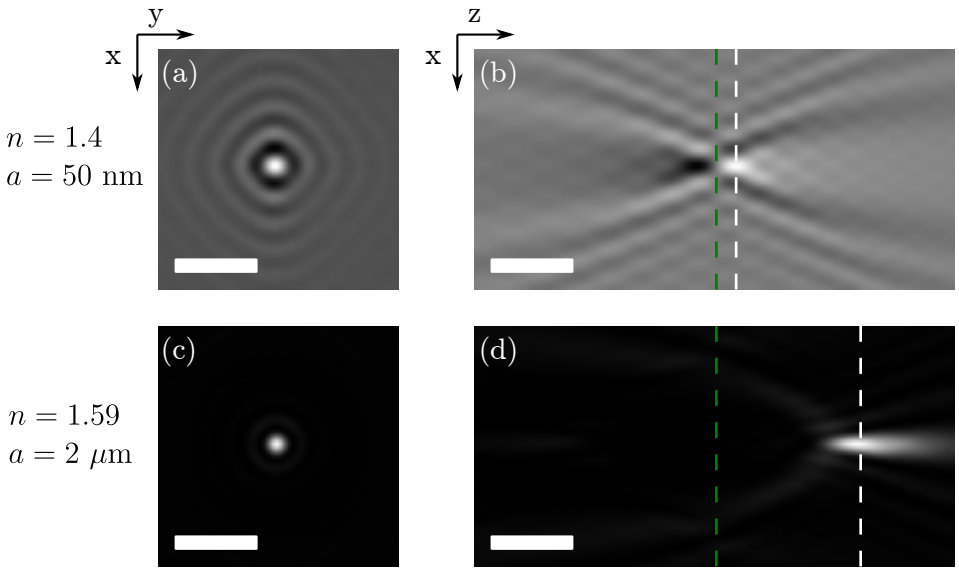

Figure 1.3.6: Reconstructions of simulated holograms. (a) and (b) are for a weakly scattering sphere suspended in water, with refractive index $n = 1.4$ and radius $a = 50$ nm. (c) and (d) are for a strongly scattering polystyrene sphere in water, $n = 1.59$ and $a = 2$ μm. Left column: slices in the $x - y$ plane. Right column: slices in the $x - z$ plane. $x - y$ slices are computed at the white dashed lines, and $x - z$ slices are computed at the vertical midplane of the $x - y$ slices. Green dashed lines denotes actual z position of scatterer. Scale bars, 2 μm.

struction techniques had their limitations. It had long been known, as early as Xu's work in lensless holography [58], that reconstructions of spherical particles tended to appear elongated by an order of magnitude or more in the axial direction. We illustrate this effect in Figure 1.3.6, where we display reconstructions of simulated ideal holograms. The elongation is particularly noticeable for the 4 μm-diameter polystyrene sphere in Figure 1.3.6(c) and (d); it is markedly less severe for the weak scatterer in Figure 1.3.6(a) and (b). While it would be straightforward to detect the lateral $(x - y)$ positions of the particles with sub-voxel precision, the precision for detecting the axial position of the particle in Figure 1.3.6(d) might be an order of magnitude worse – hundreds of nm or more.

The physical origin of this effect was first studied carefully by Pu and Meng [62]. Building on work about conventional microscopy by Ovryn and Izen [63], Pu and Meng used

an exact scattering solution, the Lorenz-Mie solution for the scattering of a plane wave by isolated spheres, to model the formation of holograms. By reconstructing these modeled holograms, as we did in Figure 1.3.6, Pu and Meng demonstrated that the elongation arose from the waves scattered by large (particle radius a being comparable to or larger than the incident wavelength λ), strongly scattering particles being far from spherical. Pu and Meng also discovered another effect, which we also demonstrate in Figure 1.3.6: the intensity maxima are displaced along the optical axis from the true position of the scatterers. Figure 1.3.6(d) shows that this displacement can be as large as a particle diameter. Subsequent workers have shown that models can be created to account for this displacement [64], and that the maxima in the reconstructed volume correspond to the focal caustics of the particles [65].

Pu and Meng's studies demonstrated both how the challenges of reconstruction techniques largely stemmed from neglecting the details of how particles scattered light, and how an exact scattering solution could be used to model hologram formation. A seminal step was then taken in 2007 when Sang-Hyuk Lee and colleagues in David Grier's group at New York University used a model based on the Lorenz-Mie scattering solution not simply to model hologram formation, but also to extract physical information from experimentally recorded holograms through a fitting procedure [59]. Using the fitting procedure, Lee *et al.* were not only able to measure the 3D position of micron-sized spheres with $\sim$10 nm or better precision in all directions, but they were also able to measure the size and refractive index of the particles.

We must briefly digress into the Lorenz-Mie scattering solution in order to explain the model used by Lee *et al.*; we will postpone a more detailed discussion to Chapter 2. The Lorenz-Mie scattering solution is a vector field solution to Maxwell's equations for scattering of a plane wave by a sphere. We will assume the incident wave to be a plane wave propagating in the positive z direction and to have polarization vector $\boldsymbol{\varepsilon}$:

$$\mathbf{E}_{\text{inc}} = E_{\text{inc}} e^{ikz}\, \boldsymbol{\varepsilon}. \tag{1.14}$$

A key feature is that the Lorenz-Mie scattered field, $\mathbf{E}_{\text{scat}}$, depends linearly on the amplitude

of the incident field $\mathbf{E}_{\text{inc}}$:

$$\mathbf{E}_{\text{scat}} = E_{\text{inc}}\mathbf{f}(\mathbf{r}). \tag{1.15}$$

Here, $\mathbf{f}(\mathbf{r})$ is the vector scattering amplitude of the sphere. It depends not only on the separation vector $\mathbf{r}$ between the sphere and a detector point, but also on the polarization and wavelength of the incident light, the sphere radius a, and the relative index $m \equiv n_{\text{p}}/n_{\text{med}}$, where n_{p} is the particle refractive index and n_{med} is the refractive index of the surrounding medium. With this in mind, we may re-express Equation 1.5 for the measured hologram intensity I in vector form:

$$\begin{aligned} I &= \left|\mathbf{E}_{\text{inc}} + \mathbf{E}_{\text{scat}}\right|^2 \\ &= \left|\mathbf{E}_{\text{inc}}\right|^2 + \mathbf{E}_{\text{inc}} \cdot \mathbf{E}^*_{\text{scat}} + \mathbf{E}^*_{\text{inc}} \cdot \mathbf{E}_{\text{scat}} + \left|\mathbf{E}_{\text{scat}}\right|^2 \\ &= \left|\mathbf{E}_{\text{inc}}\right|^2 + 2\Re\{\mathbf{E}^*_{\text{inc}} \cdot \mathbf{E}_{\text{scat}}\} + \left|\mathbf{E}_{\text{scat}}\right|^2. \end{aligned} \tag{1.16}$$

Lee *et al.* normalized their measured holograms by dividing by a background image of an empty field of view, which measured $\left|\mathbf{E}_{\text{inc}}\right|^2$:

$$\frac{I}{\left|\mathbf{E}_{\text{inc}}\right|^2} = 1 + \frac{2\Re\{\mathbf{E}^*_{\text{inc}} \cdot \mathbf{E}_{\text{scat}}\}}{\left|\mathbf{E}_{\text{inc}}\right|^2} + \frac{\left|\mathbf{E}_{\text{scat}}\right|^2}{\left|\mathbf{E}_{\text{inc}}\right|^2} \tag{1.17}$$

$$= 1 + 2\Re\{\mathbf{f} \cdot \boldsymbol{\varepsilon}\, e^{-ikz}\} + \left|\mathbf{f}\right|^2 \tag{1.18}$$

The models fitted by Lee *et al.* (as well as by us throughout this thesis) to normalized holograms follow this general form, with one exception: a scaling factor a_s for every power of $\mathbf{E}_{\text{scat}}$:

$$I_{\text{norm}} \equiv \frac{I}{\left|\mathbf{E}_{\text{inc}}\right|^2} = 1 + 2a_s\Re\{\mathbf{f} \cdot \boldsymbol{\varepsilon}\, e^{-ikz}\} + a_s^2\left|\mathbf{f}\right|^2. \tag{1.19}$$

The nature of a_s is still a matter of active debate and research; we will not discuss it further at this time.

Analyzing holograms by fitting scattering solutions to them had several clear advantages over reconstruction techniques. First, the $\sim$10 nm tracking precisions attained [59] in the axial direction surpassed what could easily be attained by analyzing reconstructed volumes. The problem of intensity maxima in the reconstructed volumes being offset (Figure 1.3.6

and [64, 65]) was also totally eliminated. Fits of scattering models also allowed reliable information about the size and optical contrast of the scatterers to be obtained directly from holograms. The fitting techniques developed by the Grier group also had a certain advantage of convenience as compared to reconstruction techniques. Whereas reconstruction methods required computations to back-propagate light to many focal planes, and particle-finding analysis on the resulting reconstructed volume was needed to obtain particle positions, fitting allowed particle positions to be precisely determined from holograms in a single processing step. For these reasons, it seemed that fitting techniques might play an important role in studies of colloids using DHM. Indeed, the Grier group quickly applied DHM with fits to the Lorenz-Mie solution to studies of the size distribution of fat globules in milk [66], quantifying the binding of neutravidin to biotinylated spheres [67], and monitoring the optical fractionation of spheres based on their size and refractive index [68].

One limiting aspect of Lee *et al.*'s seminal work was readily apparent: since the Lorenz-Mie solution strictly applies only to single spheres in an infinite, perfectly homogeneous medium, it was not clear how (or whether) fitting techniques could be applied to holograms formed by either by nonspherical particles, or by multiple particles in close proximity. Given the examples described in Section 1.1 of the rich physics exhibited by nonspherical colloids and dense suspensions, the stage was ripe for efforts to extend this fitting paradigm to new types of scattering models. These efforts, and the scientific results therefrom, will be the subject of the remainder of this thesis.

1.4 Overview

The remainder of this thesis is structured as follows. In Chapter 2, we describe the models based on exact and approximate multiple sphere scattering solutions with which we model holograms. We describe the details of our implementation of DHM and fitting in Chapter 3. We describe some of the results we have obtained from imaging sphere clusters containing up to six spheres as well as particle-laden emulsion droplets in Chapter 4, and discuss the anisotropic Brownian diffusion of sphere dimers and trimers in Chapter 5. Finally, we summarize our results and discuss the outlook of DHM in Chapter 6.

2

Modeling Holograms from Colloidal Spheres and Clusters With Scattering Solutions

Recall that the fundamental equation with which we model holograms is

$$I_{\text{norm}} = 1 + 2a_s \Re\{\mathbf{f} \cdot \boldsymbol{\varepsilon}\, e^{-ikz}\} + a_s^2 \left|\mathbf{f}\right|^2 . \tag{2.1}$$

Recall that $\mathbf{f}$ is a dimensionless scattered electric field: $\mathbf{E}_{scat} = E_0 \mathbf{f}$, where E_0 is the amplitude of the incident electric field. It follows that understanding the formation of holograms from any object, and being able to model holograms, requires a detailed understanding of how those objects scatter light. We therefore turn our attention in this chapter to scattering theory as applied to the colloidal objects considered in this thesis: spheres and sphere clusters. We begin by discussing the Lorenz-Mie solution for scattering by a sphere (also

known as Mie theory[1]) both because of its experimental importance and because it will allow us to introduce ideas that will be needed for the more complex case of sphere clusters. We will then consider techniques for calculating scattering by multiple spheres, and finally briefly consider scattering from other colloidal objects.

2.1 Scattering from Isolated Spheres

2.1.1 Lorenz-Mie Solution: Scattered Fields

We begin by qualitatively outlining the process of obtaining the Lorenz-Mie solution for the scattering of a plane wave by a sphere. While we tend to treat the Lorenz-Mie solution as the paradigmatic model for hologram formation by colloidal spheres, we should recognize that there are some inherent assumptions. First, we assume that the particles are spherical: we neglect any surface roughness (polystyrene spheres, in particular, are not atomically smooth) or asphericity. We also assume that the particle are optically homogeneous. Finally, we assume that the incident beam is sufficiently well-collimated that it may be regarded as a plane wave, even though it is in actuality a Gaussian beam [2]. This is not to undermine the importance of the Lorenz-Mie solution, but to emphasize that some physical assumptions underlie its use.

We will not work out the detailed derivation of the Lorenz-Mie solution, but we will give an overview and highlight a few aspects that are important for our research. The general plan is as follows:

1. Determine the eigenfunctions of the Helmholtz equation $\nabla^2\mathbf{E} + k^2\mathbf{E} = 0$ for a

[1] The term "Mie theory" is a personal pet peeve of the author. As Kerker [69] argues, Ludvig Lorenz certainly had priority over Gustav Mie in publishing the solution for scattering of a plane wave by a sphere. Moreover, in the author's opinion, the Lorenz-Mie solution is a purely mathematical *solution*, with no inherent physical content, within the framework of Maxwell's electrodynamics. In contrast, there is considerable physical content in the theory of special relativity, or Maxwell's theory of electromagnetism, or in a quantum field theory like quantum electrodynamics.

[2] A formalism known as generalized Lorenz-Mie theory (see [70] for a review) can handle Gaussian beams, essentially by regarding them as a suitable superposition of plane waves. We do not consider the matter further here.

spherical geometry[3]. These will be vector spherical harmonics (VSHs), which we will describe.

2. Expand the incident plane wave in VSH.

3. Write the internal and scattered fields as an expansion in VSH.

4. Apply boundary conditions: the components of the total electric field **E** and the total magnetic field **H** tangent to the sphere must be continuous. The boundary conditions determine the scattering expansion coefficients.

5. Formulate computationally useful (in particular, numerically stable) algorithms for calculating the scattering expansion coefficients.

Our treatment and notation here will generally follow that of Bohren & Huffman [71], a standard reference on the subject, whose notation finds wide acceptance.

Step 1 of this program is to find the VSH. The natural coordinate system to use is spherical coordinates with origin at the center of the scattering sphere. Manipulating vector fields is cumbersome, so the trick is to define vector fields **M** and **N** in relation to a scalar field ψ:

$$\mathbf{M} = \nabla \times (\psi \mathbf{r}) \tag{2.2}$$

and

$$\mathbf{N} = \frac{\nabla \times \mathbf{M}}{k}. \tag{2.3}$$

It can be shown that **M** and **N** will satisfy the vector Helmholtz equation if ψ satisfies the scalar Helmholtz equation. Subsequently, we separate variables[4] to determine ψ. The end product, the VSH in Bohren & Huffman's notation, is:

$$\mathbf{M}_{emn}^{(j)} = -\frac{m}{\sin\theta}\sin(m\varphi)P_n^m(\cos\theta)z_n^{(j)}(\rho)\hat{\boldsymbol{\theta}} - \cos(m\varphi)\frac{dP_n^m(\cos\theta)}{d\theta}z_n^{(j)}(\rho)\hat{\boldsymbol{\phi}}, \tag{2.4}$$

[3] We remind the reader that the Helmholtz equation arises from assuming a harmonic time dependence $e^{-i\omega t}$ for the fields.

[4] The problem of determining ψ is highly analogous to the infinite square well in spherical coordinates in quantum theory.

$$\mathbf{M}^{(j)}_{omn} = \frac{m}{\sin\theta}\cos(m\varphi)P^m_n(\cos\theta)z^{(j)}_n(\rho)\hat{\boldsymbol{\theta}} - \sin(m\varphi)\frac{dP^m_n(\cos\theta)}{d\theta}z^{(j)}_n(\rho)\hat{\boldsymbol{\phi}}, \quad (2.5)$$

$$\mathbf{N}^{(j)}_{emn} = \frac{z^{(j)}_n(\rho)}{\rho}\cos(m\varphi)n(n+1)P^m_n(\cos\theta)\hat{\mathbf{r}} + \cos(m\varphi)\frac{dP^m_n(\cos\theta)}{d\theta}\frac{1}{\rho}\frac{d}{d\rho}[\rho z^{(j)}_n(\rho)]\hat{\boldsymbol{\theta}} - m\sin(m\varphi)\frac{P^m_n(\cos\theta)}{\sin\theta}\frac{1}{\rho}\frac{d}{d\rho}[\rho z^{(j)}_n(\rho)]\hat{\boldsymbol{\phi}}, \quad (2.6)$$

$$\mathbf{N}^{(j)}_{omn} = \frac{z^{(j)}_n(\rho)}{\rho}\sin(m\varphi)n(n+1)P^m_n(\cos\theta)\hat{\mathbf{r}} + \sin(m\varphi)\frac{dP^m_n(\cos\theta)}{d\theta}\frac{1}{\rho}\frac{d}{d\rho}[\rho z^{(j)}_n(\rho)]\hat{\boldsymbol{\theta}} + m\cos(m\varphi)\frac{P^m_n(\cos\theta)}{\sin\theta}\frac{1}{\rho}\frac{d}{d\rho}[\rho z^{(j)}_n(\rho)]\hat{\boldsymbol{\phi}}. \quad (2.7)$$

This notation may seem intimidatingly cumbersome. The $P^m_n(\cos\theta)$ are the associated Legendre functions defined in the usual way [5]. The indices e and o denote either an even azimuthal angle dependence for ψ ($\sim \cos(m\varphi)$ or an odd dependence ($\sim \sin(m\varphi)$). $\rho = kr$ is a dimensionless radial variable. $z^{(j)}_n(\rho)$ denote solutions to the radial equation obtained by separating the Helmholtz equation for ψ. From Sturm-Liouville theory, there are two families of solutions: the spherical Bessel functions $j_n(\rho)$ and the spherical Neumann functions $y_n(\rho)$. Alternately one may use linear combinations of the spherical Bessel and Neumann functions, the spherical Hankel functions:

$$h^{(1)}_n(\rho) = j_n(\rho) + iy_n(\rho) \quad (2.8)$$

[5] There is a good argument for indexing the VSH with azimuthal quantum number ℓ instead of n. Alex Small points out that this makes explicit the connections to the quantum theory of angular momentum for photons. The author is inclined to agree, but here with some reluctance retains n because of its widespread use in scattering literature.

$$h_n^{(2)}(\rho) = j_n(\rho) - iy_n(\rho) \tag{2.9}$$

The most useful of these are $j_n(\rho)$ and $h_n^{(1)}(\rho)$. Unlike $y_n(\rho)$, $j_n(\rho)$ is finite at $\rho = 0$. Moreover, the $h_n^{(1)}(\rho)$ asymptotically behave like outgoing spherical waves for large ρ:

$$h_n^{(1)}(\rho) \sim (-i)^n \frac{e^{i\rho}}{i\rho} \tag{2.10}$$

and so these are physically meaningful for scattering. We use $j = 1$ to denote VSH with $z_n^{(j)}(\rho) = j_n(\rho)$ and $j = 3$ to denote VSH with $z_n^{(j)}(\rho) = h_n^{(1)}(\rho)$. Note that the $\mathbf{M}$ have no radial components while the $\mathbf{N}$ do. It can be proven that these form a mutually orthogonal eigenbasis; see [71] for some of the details.

The next step in the Mie solution is to expand the incident plane wave in VSH. To best make use of spherical symmetry, we assume that the incident wave propagates in the z direction. Without loss of generality, we also assume that the wave is x polarized. Bohren and Huffman then show that the expansion of $\mathbf{E}_{inc} = E_0 e^{ikz}\hat{\mathbf{x}}$ in VSH is

$$\mathbf{E}_{inc} = \sum_{n=1}^{\infty} E_n(\mathbf{M}_{o1n}^{(1)} - i\mathbf{N}_{e1n}^{(1)}) \tag{2.11}$$

where

$$E_n \equiv E_0 i^n \frac{2n+1}{n(n+1)}. \tag{2.12}$$

There are several important physical implications along the way. First, from the geometry of spherical coordinates,

$$\hat{\mathbf{x}} = \sin\theta\cos\varphi\hat{\mathbf{r}} + \cos\theta\cos\varphi\hat{\boldsymbol{\theta}} - \sin\varphi\hat{\boldsymbol{\phi}}, \tag{2.13}$$

which combined with the orthogonality of sines and cosines kills off two of the four possibilities in Equations 2.4-2.7 and requires $m = 1$. The limitation to $m = 1$ has significant implications for the design and performance of Mie codes as Equation 2.11 and all other field expansions contain a single sum over n as opposed to double sums over both n and m. Finally, we use only a radial dependence on $j_n(\rho)$ because a plane wave at the origin must

clearly be finite.

Next, we denote the field inside the particle as $\mathbf{E}_{int}$, and the scattered field as $\mathbf{E}_{scat}$. The field outside the particle is thus [6] $\mathbf{E}_{inc} + \mathbf{E}_{scat}$. We write both $\mathbf{E}_{int}$ and $\mathbf{E}_{scat}$ as expansions in the VSH. For $\mathbf{E}_{int}$, the form of the plane wave expansion (Equation 2.11) along with the requirement for finiteness at the origin requires

$$\mathbf{E}_{int} = \sum_{n=1}^{\infty} E_n \left(c_n \mathbf{M}_{o1n}^{(1)} - i d_n \mathbf{N}_{e1n}^{(1)} \right) . \tag{2.14}$$

Meanwhile, since we know that scattering results in outward-going waves, we require that the scattered wave $\mathbf{E}_{scat}$ have radial dependence on $h_n^{(1)}(\rho)$:

$$\mathbf{E}_{scat} = \sum_{n=1}^{\infty} E_n \left(i a_n \mathbf{N}_{e1n}^{(1)} - b_n \mathbf{M}_{o1n}^{(3)} \right) . \tag{2.15}$$

The a_n, b_n, c_n, and d_n are unknown coefficients. For each order n there are 4 unknowns, but also 4 boundary conditions: equality of θ and φ components of $\mathbf{E}$ and $\mathbf{H}$ across the spherical interface. In particular, a_n and b_n are termed scattering coefficients. These coefficients depend only on two dimensionless parameters: the relative index $m \equiv n_{particle}/n_{medium}$ and the size parameter $x \equiv ka$ where a is the sphere radius, $k = 2\pi n_{med}/\lambda_o$, and λ_o is the vacuum wavelength.

Application of the boundary conditions give expressions for a_n and b_n. The expressions for these use the Riccati-Bessel functions, which we will rely on extensively later:

$$\psi_n = \rho j_n(\rho) \tag{2.16}$$

$$\xi_n = \rho h_n^{(1)}(\rho) \tag{2.17}$$

[6] This is a standard assumption in scattering theory. It is certainly valid in the far field for an incident plane wave of infinite extent. Whether this truly applies for DHM is currently the subject of research related to the nature of a_{sc}.

With these in hand, we get

$$a_n = \frac{m\psi_n(mx)\psi_n'(x) - \psi_n(x)\psi_n'(mx)}{m\psi_n(mx)\xi_n'(x) - \xi_n(x)\psi_n'(x)} \tag{2.18}$$

$$b_n = \frac{\psi_n(mx)\psi_n'(x) - m\psi_n(x)\psi_n'(mx)}{\psi_n(mx)\xi_n'(x) - m\xi_n(x)\psi_n'(x)} \tag{2.19}$$

where the primes denote differentiation with respect to the argument.

Thus the Lorenz-Mie problem is essentially solved; the special functions appearing in the expressions above for a_n and b_n are all well-known. However, it must be noted that the forms above for a_n and b_n are ill-suited to computation. In particular, $j_n(z)$ tends to diverge for large complex arguments (as might arise for large, strongly absorbing particles). The problems are avoided by rewriting the expressions in terms of logarithmic derivatives:

$$D_n^{(1)}(z) = \frac{\psi_n'(z)}{\psi_n(z)}, \; D_n^{(3)}(z) = \frac{\xi_n'(z)}{\xi_n(z)}. \tag{2.20}$$

Care must also be taken in the computation of the logarithmic derivatives and other special functions to avoid numerical instability. We refer the reader to the discussions in Bohren & Huffman for further details. We mention that in our implementation of the Lorenz-Mie solution in HoloPy, we use the recommended forms based on $D_n^{(1)}$. Any computed solution must also truncate the infinite series expansion at some point; we use the widely accepted criteria of Wiscombe to determine the number of terms to keep, N_{max} [72]:

$$N_{max} = x + 4.05x^{1/3} + 2. \tag{2.21}$$

2.1.2 Standard Approximations and DHM

We have just described the relatively easy part of computing the Lorenz-Mie solution: obtaining the scattering coefficients. This need only be done once for any given particle; the more time-consuming part comes from calculating $\mathbf{E}_{scat}$ at many points to model a hologram. To discuss this, we must first introduce some scattering geometry and the concept of the *scattering plane*.

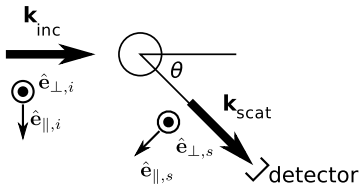

Figure 2.1.1: Geometry of scattering plane showing incident and scattered wavevectors $\mathbf{k}_{inc}$ and $\mathbf{k}_{scat}$. We consider components of the incident and scattered electric fields parallel to and perpendicular to the scattering plane.

We will assume the laboratory system to consist of a fixed set of axes, as usual with z being the direction of propagation of the incident wave. As illustrated in Figure 2.1.1, it is useful to consider scattering not with respect to the laboratory coordinates but with respect to a plane defined by the wavevectors of the incident and scattered electric fields.

Most scattering experiments are performed in the far field, where $kr \gg 1$. Since for visible light, $k \approx 10^7\ \mathrm{m}^{-1}$, for a detector located at a macroscopic distance (such as in a goniometer-based light scattering instrument), the far-field approximation will be a good one. In this approximation, one may write the incident and scattered fields in terms of a complex 4×4 amplitude scattering matrix:

$$\begin{pmatrix} E_{inc,\parallel} \\ E_{inc,\perp} \end{pmatrix} = \frac{e^{ikr}}{-ikr} \begin{pmatrix} S_2 & S_3 \\ S_4 & S_1 \end{pmatrix} \begin{pmatrix} E_{scat,\parallel} \\ E_{scat,\perp} \end{pmatrix}. \tag{2.22}$$

In the far-field limit, the waves are assumed to be purely transverse, the radial components of $\mathbf{N}$ fall off as $1/\rho^2$ and are neglected. The radial dependence is to be asymptotically that of a spherical wave, and the amplitude scattering matrix $\mathbf{S}$ depends only on angles and the particle properties. For the Lorenz-Mie problem, symmetry requires the off-diagonal terms S_3 and S_4 to be 0 [7]. It may be shown by considering the forms of the VSH that

$$S_1 = \sum_{n=1}^{\infty} \frac{2n+1}{n(n+1)} (a_n \pi_n + b_n \tau_n) \tag{2.23}$$

[7] See van de Hulst [73] as well as the chapter by Hovenier and van der Mee in [74] for a much more extensive discussion on symmetries and their consequences for $\mathbf{S}$.

$$S_2 = \sum_{n=1}^{\infty} \frac{2n+1}{n(n+1)}(a_n\tau_n + b_n\pi_n) \tag{2.24}$$

where

$$\pi_n(\theta) = \frac{P_n^1(\cos\theta)}{\sin\theta} \tag{2.25}$$

and

$$\tau_n(\theta) = \frac{dP_n^1(\cos\theta)}{d\theta}. \tag{2.26}$$

We note that the scattered waves are *not* spherical waves because S_2 and S_1 depend on θ.

This recipe, unfortunately, does not quite work out for the case of DHM. We often record holograms at a z distance of as low as $\sim$ 10 μm. For 660 nm light in water, this amounts to $kz \sim 100$, which is large but not quite in the far-field limit. In particular, if we examine the next-to-leading order asymptotic expressions for for $h_n^{(1)}(\rho)$, we find [75]:

$$h_n^{(1)}(\rho) \approx (-i)^n \frac{e^{i\rho}}{i\rho}\left(1 + \frac{in(n+1)}{2\rho} + \mathcal{O}(\rho^{-2})\right) \tag{2.27}$$

Given that for micron-sized spheres, the expansions may go up to order $n = 15$ or more, it is clear that the next-to-leading order term is comparable to the leading term. We have found it necessary, therefore, to incorporate the full radial dependence on $h_n^{(1)}(kr)$, making $\mathbf{S}$ dependent on both kr and θ. We obtain the following modified expressions for S_1 and S_2 by looking at the VSH expansion for $\mathbf{E}_{scat}$ (Equations 2.15, 2.6, and 2.5):

$$S_1(\rho,\theta) = (-i\rho e^{-i\rho}) \sum_{n=1}^{\infty} i^n \frac{2n+1}{n(n+1)}\left(ia_n\pi_n(\theta)\frac{[\rho h_n^{(1)}(\rho)]'}{\rho} - b_n\tau_n(\theta)h_n^{(1)}(\rho)\right) \tag{2.28}$$

$$S_2(\rho,\theta) = (-i\rho e^{-i\rho}) \sum_{n=1}^{\infty} i^n \frac{2n+1}{n(n+1)}\left(ia_n\tau_n(\theta)\frac{[\rho h_n^{(1)}(\rho)]'}{\rho} - b_n\pi_n(\theta)h_n^{(1)}(\rho)\right). \tag{2.29}$$

These expressions "undo" the radial dependence assumed by Equation 2.22 so that they may be substituted in for the conventional expressions. They reduce to the conventional forms (Equations 2.23 and 2.24) if the asymptotic expressions for $h_n^{(1)}(\rho)$ are substituted.

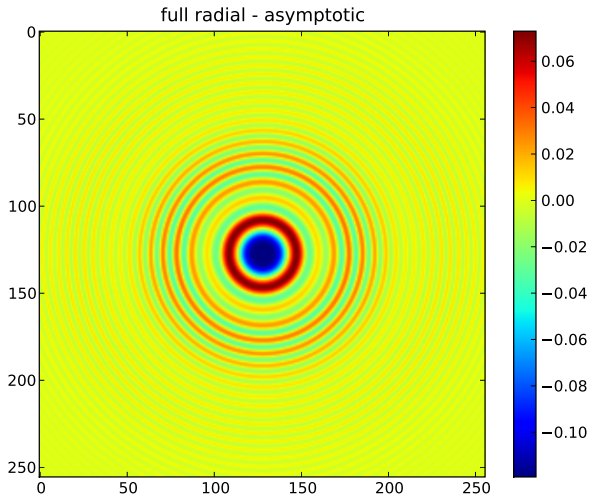

Figure 2.1.2: Difference between holograms simulated using full $h_n^{(1)}(kr)$ radial dependence and asymptotic e^{ikr}/ikr radial dependence. Hologram computed for a particle with $m = 1.2 + 10^{-3}i$, $x = 10$, at $z = 15$ μm.

Using the full radial dependence can significantly affect calculated holograms as well as fits to data. Figure 2.1.2 shows the difference between a hologram computed with the full radial dependence and with asymptotic radial dependence. Both holograms have a DC level of 1, so the differences between them are up to 10%, particularly near the forward direction. Comparing best-fit parameters obtained by fitting models to experimental holograms shows that there can be differences of tens of nm in the best-fit z position. All the holograms we model in this thesis therefore include the full radial dependence.

Recently we have also incorporated the radial components of $\mathbf{E}_{scat}$ into our Lorenz-Mie calculations. Near normal incidence, the radial components point nearly in the z direction, and thus cannot be responsible for depositing energy into a detector (since the Poynting vector $\mathbf{E} \times \mathbf{H}$ is perpendicular to $\mathbf{E}$). This may not be true, however, at very large scattering angles, or for detectors that are not oriented perpendicular to $\mathbf{k}_{inc}$. Noting that only the terms in $\mathbf{E}_{scat}$ proportional to a_n will have any radial component, and recalling that the initial assumption of x polarization in the plane wave expansion (Equation 2.11) means

that $E_{inc,\parallel} = E_\circ \cos\varphi$, we have

$$E_{scat,r} = E_{inc,\parallel} a_n i^{n+1}(2n+1)\sin\theta\pi_n(\theta)\frac{h_n^{(1)}(\rho)}{\rho}. \tag{2.30}$$

While the inclusion of the radial component of $\mathbf{E}_{scat}$ is currently included in HoloPy, we find that it does not make much difference in hologram modeling, resulting in differences in best-fit z of several nm at most, which are comparable or smaller than the typical particle tracking uncertainty.

2.1.3 Radiometric Quantities

We pause to attend to certain radiometric quantities that are of some importance for our work – these are quantities that involve integration of scattered power in some way. We imagine surrounding our spherical particle with a large imaginary surface (such that we are in the far field) and integrate the Poynting vector due to the external fields (incident and scattered) over this surface. The rate at which energy is lost inside the surface is

$$W_a = -\int \mathbf{S}\cdot d\mathbf{a}. \tag{2.31}$$

If we divide this by the incident irradiance I_i, which for a z-propagating incident field is the z component of its Poynting vector, we get something with units of area. This is the absorption cross section, C_{abs}. In a similar way, considering the scattered power, we can define the scattering cross section:

$$C_{scat} = \frac{1}{I_i}\int \mathbf{S}_{scat}\cdot d\mathbf{a} \tag{2.32}$$

where $\mathbf{S}_{scat}$ is calculated with the scattered field. The extinction cross section C_{ext} is given by the sum of the scattering and absorption cross sections: $C_{ext} = C_{scat} + C_{abs}$; C_{ext} is related to the total energy removed from the incident beam, by absorption and scattering. One also frequently encounters these cross sections non-dimensionalized as efficiencies Q, where the non-dimensionalization comes from dividing by some geometric cross sectional area of the particle. For a sphere this is naturally πa^2, but for more complex particles (such

as sphere clusters) conventions can vary.

We can also characterize how homogeneously a sphere scatters light. Recall that the electric field radiated from a point dipole scatterer is (for polarization perpendicular to the scattering plane) independent of θ. A large particle, by contrast, tends to scatter most strongly in the forward direction. We can quantify this with the asymmetry parameter $\langle \cos\theta \rangle$. If we define a dimensionless vector scattering amplitude $\mathbf{X}$ such that $\mathbf{E}_{scat} = (e^{ikr}/(-ikr))E_o\mathbf{X}$, then it can be shown that a suitable integral over 4π of solid angle gives the scattering cross section:

$$C_{scat} = \int \frac{|\mathbf{X}|^2}{k^2}\, d\Omega. \tag{2.33}$$

Consequently $|X|^2/k^2 C_{scat}$ is normalized with respect to integration over solid angle, and the asymmetry parameter is defined such that

$$\langle \cos\theta \rangle \equiv \int \frac{|\mathbf{X}|^2}{k^2 C_{scat}} \cos\theta \, d\Omega. \tag{2.34}$$

For a dipole scatterer, $\langle \cos\theta \rangle = 0$, whereas for a very large sphere scattering mainly in the forward direction, $\langle \cos\theta \rangle$ approaches 1.

Light carries not only energy but momentum p. Light can therefore exert forces on objects, such as in optical tweezers [33]. One such effect that will matter in our experiments is radiation pressure, which can be qualitatively thought of as incident photons pushing a scatterer in the direction of propagation. Our discussion here of the radiation pressure cross section follows van de Hulst [73]. From our previous discussion, the rate at which energy is removed from the incident beam is $I_i C_{ext}$. The momentum of any such photons that are absorbed will clearly be transfered to the particle. But photons that scatter from a particle with scattering angle θ still carry forward momentum proportional to $\cos\theta$. Averaging over all of solid angle, $I_i C_{scat}\langle \cos\theta \rangle$ will be proportional to the power emitted in the forward direction by the scattered photons. Therefore, the momentum lost by the incident light is will be proportional to $C_{ext} - C_{scat}\langle \cos\theta \rangle$. Consequently, we define the radiation pressure cross section C_{rp} as

$$C_{rp} = C_{ext} - C_{scat}\langle \cos\theta \rangle. \tag{2.35}$$

$I_i C_{rp}$ has units of power. Since the energy and momentum of light are related by $1/c$, the change in momentum per unit time, or radiation pressure force F_{rp}, is given by

$$F_{rp} = \frac{I_i C_{rp}}{c}. \tag{2.36}$$

Another important result related to radiometry is the optical theorem, which relates C_{ext} to the far-field scattering amplitude in the forward direction. We mention it here because we will need it in our discussion of Mie superposition. For the case of Lorenz-Mie scattering,

$$C_{ext} = \frac{4\pi}{k^2}\mathrm{Re}[S(0)] \tag{2.37}$$

where S is either nonzero element of the amplitude scattering matrix $\mathbf{S}$, which are identical at $\theta = 0$.

Expressions for C_{ext}, C_{scat}, and the asymmetry parameter $\langle \cos\theta \rangle$ for the Lorenz-Mie problem are given in standard references like Bohren & Huffman [71]. They all involve summations over the scattering coefficients a_n and b_n; we do not discuss them further except to say that they are implemented in the standard ways in HoloPy.

2.1.4 Layered Particles

A closely related problem to that of scattering by a homogenous sphere is that of scattering by layered particles. These codes in general work by expanding the scattered field in each layer of the particles. Bohren & Huffman give a code for two layers, BHCOAT [71]. Algorithms that can accomodate multiple layers are considerably more general, however, as any refractive index profile for a sphere that depends only on the radius $n(r)$ can be approximated with many uniform layers. One of the first such algorithms was due to Bhandari [76]; further developments were made by Mackowski *et al.* [77], whose code was reportedly stable for particles containing up to 100 layers. Another key work, which used the idea of using Taylor expansions to compute ratios of Riccati-Bessel functions in adjacent layers, was that of Kai and Massoli [78]. We here briefly describe the algorithm we have adopted, due to Yang [79]. Yang showed that his algorithm could be stably applied to larger particles with more layers than the Kai and Massoli algorithm [79].

Yang's code is based on expanding the electric fields inside the layers in the same vector spherical harmonics that apply in the Mie solution. A different set of coefficients apply inside each layer, which we index by l. For the innermost layer, containing $r = 0$, the wave functions must be regular at the origin, so the radial dependence of field $\mathbf{E}_1$ is on spherical Bessel functions j_n:

$$\mathbf{E}_1 = \sum_{n=1}^{\infty} E_n \left(c_n^{(1)} \mathbf{M}_{o1n}^1 - i d_n^{(1)} \mathbf{N}_{e1n}^{(1)} \right) \tag{2.38}$$

where E_n is defined as in the Mie problem. For layers beyond the first, recall that there two solutions to the radial equation. Normally, we have physical grounds for eliminating one: either regularity at the origin, or in the case of the scattered field, that the waves be outgoing spherical waves with $h_n^{(1)}(kr)$ radial dependence. For $l > 1$, we must include both solutions of the radial equation. Thus, the internal field $\mathbf{E}_l$ is given by

$$\mathbf{E}_l = \sum_{n=1}^{\infty} E_n \left(c_n^{(l)} \mathbf{M}_{o1n}^1 - i d_n^{(l)} \mathbf{N}_{e1n}^{(1)} + i a_n^{(l)} \mathbf{N}_{e1n}^{(3)} - b_n^{(l)} \mathbf{M}_{o1n}^3 \right). \tag{2.39}$$

Note that the basis is, strictly speaking, not linearly independent, since $h_n^{(1)}(kr) = j_n(kr) + i y_n(kr)$; the coefficients are nonetheless unique. Expansions of the incident and scattered fields proceed as in the Mie problem, and boundary conditions provide four equations to be solved for the unknown coefficients $a_n^{(l)}$, $b_n^{(l)}$, $c_n^{(l)}$, and $d_n^{(l)}$ for each n and l. In Yang's algorithm, a recursive procedure is used to determine ratios of the coefficients at layer $l+1$ from those at layer l. We refer the reader to the original paper for the rather notationally and algebraically involved details. In the end, the relevant coefficients are written in terms of logarithmic derivatives of ψ_n and ξ_n, for which there are stable recursion relations [77], and the ratio

$$Q_n(z_1, z_2) = \frac{\psi_n(z_1)}{\xi_n(z_1)} \frac{\xi_n(z_1)}{\psi_n(z_1)} \tag{2.40}$$

which can be stably calculated by upwards recursion.

Note that Yang's algorithm results in external scattering coefficients a_n and b_n that are exactly identical in form to those of the Lorenz-Mie problem. Consequently, all results depending only on the scattering coefficients for the Lorenz-Mie problem (such as formulae

for radiometric quantities) can be applied without modification.

We have developed code based on Yang's algorithm and incorporated it into HoloPy. The code allows the calculation of differential scattering cross sections as well as holograms and radiometric quantities. We have used this code, in conjunction with turbidimetry measurements, to characterize core-shell particles consisting of a polystyrene core surrounded by a shell of poly(*N*-isopropylacrylamide-*co*-acrylic acid) hydrogel (PNIPAM) [80]. When these particles are dispersed in water, the shells are highly swollen and nearly index-matched. By comparing C_{scat} for the core-shell particles and the cores alone, we determined that the refractive index mismatch between the shells and the solvent was at most of order 10^{-3}.

These particles, which have a much smaller C_{scat} than homogenous polystyrene spheres of the same radius, may be particularly useful for studies of the self-assembly of colloidal clusters. It is hoped that the greater separation of their scattering cores will ease the task of determining initial particle positions through reconstruction. We note here that the layered sphere code may be important for analyzing holograms of such particles because differences in scattering due to a nearly-matched shell will be most apparent in the forward direction, where DHM is particularly sensitive. Figure 2.1.3 shows differential scattering cross sections (polarization perpendicular to the scattering plane) for a 170 nm diameter polystyrene core alone and surrounded by uniform layers. For near-perfect index matching, differences between the scattering intensity for the core only (blue line) and the core-shell particle (green) are most apparent for $\theta < 20°$. For a larger index mismatch (red), the scattering of the shell dominates that of the core.

It has recently come to our attention that we are not the only workers aside from Yang to have written code based on his algorithm and made it publicly available. Peña and Pal have released a code in C, scattnlay, that uses this method [81]. Our implementation in HoloPy has some advantages in terms of usability, but scattnlay may be useful if maximum speed is a priority. We are moreover heartened to find someone else agreeing with us about the superiority of Yang's algorithm.

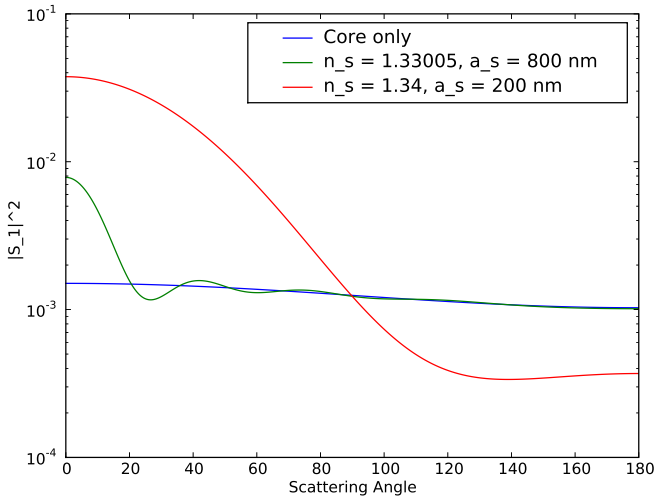

Figure 2.1.3: Angular dependence of scattering for incident polarization perpendicular to scattering plane for a 170 nm diameter polystyrene shell surrounded by uniform shells. For a n index mismatch of 10^{-2}, the shell scattering dominates the core, while for near-perfect matching, differences are most apparent near the forward direction.

2.2 Scattering From Multiple Spheres: Mie Superposition

The simplest approach to calculating the fields scattered by multiple spheres is a technique we will call Mie superposition. This merely involves superposing the fields calculated from the Lorenz-Mie solution for each of the spheres, taking into account the phase differences arising from the displacement of the spheres along the optical axis. Mie superposition assumes that only a plane wave illuminates each sphere. It completely neglects electromagnetic coupling, including multiple scattering, between the spheres. $\mathbf{E}_{scat}$ calculated from Mie superposition is the lowest-order approximation to the exact multisphere superposition approach we will discuss next.

To quantify the validity of Mie superposition for calculating $\mathbf{E}_{scat}$, we propose a dimensionless figure of merit. Mie superposition assumes that the exciting field at any sphere, $\mathbf{E}_{ex}$, is approximately equal to the incident plane wave $\mathbf{E}_{inc}$. $\mathbf{E}_{ex}$ for any given sphere i will be equal to the sum of the incident plane wave and the scattered waves from every other

sphere at i:

$$\mathbf{E}_{ex,i} = \mathbf{E}_{inc} + \sum_{j \neq i}^{N} \mathbf{E}_{scat,j}. \tag{2.41}$$

For Mie superposition to be valid, $|\mathbf{E}_{scat,j}|$ must be much smaller than $|\mathbf{E}_{inc}|$. This requires the particles to be far enough apart that their near fields do not couple. Then, $|\mathbf{E}_{scat,j}|$ scales approximately as $|\mathbf{E}_{inc}|S/kR$, where R is a typical interparticle distance and S denotes the magnitude of the amplitude scattering matrix of sphere j in the Lorenz-Mie solution. Recall from the optical theorem (Equation 2.37) that the forward scattering amplitude is given by $\mathrm{Re}[S(0)] = k^2 C_{ext}/4\pi = x^2 C_{ext}/4$, where x is the size parameter. Thus, we propose the criterion that if

$$Q_{ext} x^2 / kR \ll 1, \tag{2.42}$$

$|\mathbf{E}_{scat,j}| \ll |\mathbf{E}_{inc}|$ and Mie superposition should be valid.

2.3 Scattering From Multiple Spheres: Multisphere Superposition

Clearly, the Mie superposition approach will not be valid in many cases, particularly when particles are close together. We now describe an alternate approach that lets us compute $\mathbf{E}_{scat}$ exactly in such cases; this multisphere superposition (also known as T-matrix) approach underlies most of the results in this thesis.

We begin once again by describing the basis functions used. Since we are once again dealing with spheres, the natural bases are once again vector spherical harmonics. However, workers who have implemented these techniques (in particular Mackowski [74, 82]) use a different convention for VSH than the one we described for Lorenz-Mie scattering. Our conventions will follow those in the users' guide for SCSMFO, as our work relies on that code. Mackowski's VSH are of the form $\mathbf{N}^{\nu}_{mnp}(\mathbf{r})$. Specifically,

$$\mathbf{N}^{(\nu)}_{mn2}(\mathbf{r}) = \sqrt{\frac{2n+1}{n(n+1)} \frac{(n-m)!}{(n+m)!}} \nabla \times \left(\mathbf{r} \psi^{(\nu)}_{mn}(\mathbf{r}) \right) \tag{2.43}$$

$$\mathbf{N}^{(\nu)}_{mn1}(\mathbf{r}) = \nabla \times \mathbf{N}^{(\nu)}_{mn2}(\mathbf{r}) \tag{2.44}$$

where

$$\psi_{mn}^{(\nu)}(\mathbf{r}) = z_n(r) P_n^m(\cos\theta) e^{im\varphi} \tag{2.45}$$

with radial dependence given by $z_n = j_n$ for $\nu = 1$ and $z_n = h_n^{(1)}$ for $\nu = 3$. The $\mathbf{N}_{mn2}$ are roughly equivalent to Bohren & Huffman's $\mathbf{M}$, and Mackowski's VSH with $p = 1$ are roughly equivalent to the B&H $\mathbf{N}$. Note that the φ dependence is now in complex exponentials (with m allowed to run from $-n$ to n) instead of in sines and cosines. The angular dependence of $\psi_{mn}^{(\nu)}$ is almost identical to the spherical harmonics $Y_l^m(\theta, \varphi)$ familiar from quantum mechanics, differing only by a factor of $1/\sqrt{4\pi}$ and the Condon-Shortley phase factor.

A key step in the multisphere superposition method involves relating the scattered fields of one sphere, in a basis of VSH centered at that sphere, to a basis of VSH centered on another sphere. This is accomplished via translation theorems that express VSH centered about origin ℓ' in terms of a sum of VSH centered about origin ℓ, which is possible because any set of VSH form a complete basis:

$$\mathbf{N}_{mnp}^{(\nu')}(\mathbf{r}_{\ell'}) = \sum_{l=1}^{\infty} \sum_{k=-l}^{l} \sum_{q=1}^{2} A_{klqmnp}^{\ell\ell'} \mathbf{N}_{klq}^{(\nu)}(\mathbf{r}_{\ell}). \tag{2.46}$$

The coefficients $A_{klqmnp}^{\ell\ell'}$ depend on $\mathbf{r}_{\ell'} - \mathbf{r}_{\ell'}$, as does the type of radial dependence ν to be summed over. The coefficients are tedious to write out, and their derivation is a mathematical *tour de force*. So we merely give the references here [83, 84].

Armed with the VSH and the translation theorems, we may proceed. We assume as before that $\mathbf{E}_{inc}$ may be expanded in VSH:

$$\mathbf{E}_{inc} = \sum_{n=1}^{\infty} \sum_{m=-n}^{n} \sum_{p=1}^{2} p_{mnp} \mathbf{N}_{mnp}^{(1)}. \tag{2.47}$$

We gain some necessary insight from revisiting the Lorenz-Mie problem. In that problem,

we expressed $\mathbf{E}_{scat}$ as a sum over VSH:

$$\begin{aligned}\mathbf{E}_{scat} &= \sum_{n=1}^{\infty}\sum_{m=-n}^{n}\sum_{p=1}^{2} a_{mnp}\mathbf{N}^{(3)}_{mnp} \\ &= \sum_{n=1}^{\infty}\sum_{m=-n}^{n}\sum_{p=1}^{2} \bar{a}_{np}p_{mnp}\mathbf{N}^{(3)}_{mnp}.\end{aligned} \tag{2.48}$$

Here the $\bar{a}_{np}$ are the traditional Lorenz-Mie coefficients (Equations 2.18 and 2.19). We do not rehash the proofs here[8], but the key physical insight is that Lorenz-Mie scattering can be viewed as a process where some *exciting wave* hits a sphere, generating some scattering response. The plane wave p_{mnp} coefficients describe the excitation, and the Lorenz-Mie coefficients $\bar{a}_{np}$ give the response to incident VSH of order n and type p. If we now imagine a different exciting field (the physical nature of which we have not yet specified):

$$\mathbf{E}_{ex} = \sum_{n=1}^{\infty}\sum_{m=-n}^{n}\sum_{p=1}^{2} f_{mnp}\mathbf{N}^{(1)}_{mnp}, \tag{2.49}$$

from the linearity of Maxwell's equations it follows that the coefficients for the scattering response will be given by $f_{mnp}\bar{a}_{np}$, with the boundary conditions on the sphere *implicitly* taken care of automatically.

This is precisely the idea that underlies multisphere superposition. The fundamental assumption is that the total scattered field from N_S spheres, $\mathbf{E}_{scat}$, can be written as a sum of scattered fields from each sphere ℓ:

$$\mathbf{E}_{scat} = \sum_{\ell=1}^{N_S} \mathbf{E}_{scat,\ell} \tag{2.50}$$

[8]There are some subtle differences here extending beyond a different convention for VSH; in particular, the p_{mnp} plane wave coefficients can be formulated for a plane wave propagating in any direction and with arbitrary polarization. The conventions used in our discussion of the Lorenz-Mie solution simplify matters greatly.

where $\mathbf{E}_{scat,\ell}$ can be written as a sum of VSH centered about sphere ℓ:

$$\mathbf{E}_{scat,\ell} = \sum_{n=1}^{\infty} \sum_{m=-n}^{n} \sum_{p=1}^{2} a_{mnp}^{\ell} \mathbf{N}_{mnp}^{(3)}(\mathbf{r}_{\ell}). \tag{2.51}$$

We will consider the exciting field $\mathbf{E}_{ex,\ell}$ at sphere ℓ to be the sum of the incident field and the scattered fields from every other sphere at ℓ:

$$\mathbf{E}_{ex,\ell} = \sum_{n,m,p} p_{mnp}^{\ell} \mathbf{N}_{mnp}^{(1)}(\mathbf{r}_{\ell}) + \sum_{\substack{\ell'=1 \\ \ell' \neq \ell}}^{N_S} \sum_{n,m,p} a_{mnp}^{\ell'} \mathbf{N}_{mnp}^{(3)}(\mathbf{r}'_{\ell}). \tag{2.52}$$

The first term is just the incident field at sphere ℓ (there may be phase differences between different spheres), and the second term contains a sum over $N_S - 1$ expansions over *different* VSH. This is a mess, but one that can be rectified using the translation theorems. It turns out that translating type $\nu = 3$ VSH beyond the center-to-center distance between origins turns them into type $\nu = 1$:

$$\mathbf{E}_{ex,\ell} = \sum_{n,m,p} \left(p_{mnp}^{\ell} + \sum_{\substack{\ell'=1 \\ \ell' \neq \ell}}^{N_S} \sum_{k,l,q} A_{mnpklq}^{\ell\ell'} a_{klq}^{\ell'} \right) \mathbf{N}_{mnp}^{(1)}. \tag{2.53}$$

We remark that this breaks down if any of the spheres overlap; thus multisphere superposition cannot apply in this case (though the spheres need not touch.) Our exciting coefficients f_{mnp} are in the big parentheses. It follows that the scattering response coefficients for sphere ℓ will be $f_{mnp}\bar{a}_{np}^{\ell}$, where the superscript ℓ denotes the Mie coefficients for sphere ℓ:

$$a_{mnp}^{\ell} = \left(p_{mnp}^{\ell} + \sum_{\substack{\ell'=1 \\ \ell' \neq \ell}}^{N_S} \sum_{k,l,q} A_{mnpklq}^{\ell\ell'} a_{klq}^{\ell'} \right) \bar{a}_{np}^{\ell} \tag{2.54}$$

where we already dealt with detailed boundary conditions in solving the Lorenz-Mie prob-

lem and are now reaping the fruits of linearity. Algebraic rearrangement then leads to

$$a^{\ell}_{mnp} - \bar{a}^{\ell}_{np} \sum_{\substack{\ell'=1 \\ \ell' \neq \ell}}^{N_S} \sum_{k,l,q} A^{\ell\ell'}_{mnpklq} a^{\ell'}_{klq} = \bar{a}^{\ell}_{np} p^{\ell}_{mnp}. \tag{2.55}$$

On the left hand side, the scattering coefficients a^{ℓ}_{mnp} are all unknown. But on the right hand side, the plane wave and Mie coefficients are known. Therefore, provided that all expansions are truncated to some upper limit, this expression is a linear system that can be solved for the unknown coefficients.

There are several ways to solve this system. The one that is most physically meaningful is the Born approximation, also known as order-of-scattering. We assume that the scattering coefficients are given, to lowest order, by the Mie scattering coefficients, with some correction:

$$a^{\ell}_{mnp} \approx \bar{a}^{\ell}_{np} p^{\ell}_{mnp} + {}^{1}a^{\ell}_{mnp} + \dots \tag{2.56}$$

where we explicitly show the first-order correction. If we substitute this into Equation 2.54, we can show that the first-order correction comes from the right side approximated to zeroth order:

$${}^{1}a^{\ell}_{mnp} = \bar{a}^{\ell}_{np} \sum_{k,l,q} A^{\ell\ell'}_{mnpklq} \bar{a}^{\ell'}_{lq} p^{\ell'}_{klq}. \tag{2.57}$$

This can be continued to higher orders. Note that the zeroth order is precisely Mie superposition.

Once the scattering coefficients for each sphere are determined, it is possible to apply the translation theorems once more to calculate two final set of expansion coefficients $a_{mnp,\parallel}$ and $a_{mnp,\perp}$ corresponding to incident polarization parallel to or perpendicular to the scattering plane[9]. Some further manipulation (and observation of the VSH) allows us to write

[9]This is especially confusing in the users' guide to SCSMFO, scsmfo.ps. SCSMFO returns coefficients of the type $a_{mnp,v}$ (Equation 19 in the users' guide) which get turned into the parallel and perpendicular coefficients via Equations 20 and 21. But the angles in those two equations should be $\varphi + \gamma$ rather than γ. Here γ is an Euler angle for rotating the cluster and φ is the lab frame spherical coordinate to the detector point relative to the cluster center of mass, with incident propagation in the z direction. The added complexity in SCSMFO comes from letting it handle multiple orientations of the cluster with as little computational redundancy as possible.

down expressions for the amplitude scattering matrix **S** in terms of these coefficients and angular functions, much as in the Lorenz-Mie solution. This time, due to the lack of spherical symmetry, there are off-diagonal elements in **S** as well. This translation of coefficients makes the code more efficient for dense clusters of spheres, but may be disadvantageous for widely separated clusters, since the further away a VSH is translated, the more terms are needed to represent it to the same level of precision.

We must once again incorporate the exact radial dependence on $h_n^{(1)}(kr)$. Working this out requires us to work out the explicit vector components of $\mathbf{N}_{mnp}^{(3)}$ (something not in Mackowski's papers). Neglecting the non-radiative radial field components for the moment, one can show after considerable but straightforward algebra and vector calculus that

$$\mathbf{N}_{mnp}^{(3)} = e^{im\varphi}\left(i\tau_{mnp}(\theta)\,\hat{\boldsymbol{\theta}} - \tau_{mn3-p}(\theta)\,\hat{\boldsymbol{\phi}}\right) R_{np} \tag{2.58}$$

where

$$R_{n1}(\rho) = -\frac{i}{\rho}\frac{d}{d\rho}\left(\rho h_n^{(1)}(\rho)\right), \tag{2.59}$$

$$R_{n2}(\rho) = h_n^{(1)}(\rho), \tag{2.60}$$

$$\tau_{mn1}(\theta) = \frac{1}{\sqrt{E_{mn}}}\frac{dP_n^m(\cos\theta)}{d\theta}, \tag{2.61}$$

and

$$\tau_{mn2}(\theta) = \frac{1}{\sqrt{E_{mn}}}\frac{mP_n^m(\cos\theta)}{\sin\theta} \tag{2.62}$$

with

$$E_{mn} \equiv \frac{n(n+1)}{2n+1}\frac{(n+m)!}{(n-m)!}. \tag{2.63}$$

We quote the modified results[10] for the elements of **S**:

$$S_1 = i\rho e^{-i\rho}\sum_{n=1}^{\infty}\sum_{m=-n}^{n}\sum_{p=1}^{2} R_{np}(\rho)\,a_{mnp,\perp}\,\tau_{mn(3-p)}(\theta)\,e^{im\varphi} \tag{2.64}$$

[10]These differ slightly from the versions in Ref. [85] by including the factors to "undo" the assumed asymptotic radial dependence in Equation 2.22.

$$S_2 = \rho e^{-i\rho} \sum_{n=1}^{\infty} \sum_{m=-n}^{n} \sum_{p=1}^{2} R_{np}(\rho) a_{nmp,\parallel} \tau_{nmp}(\theta) e^{im\varphi} \tag{2.65}$$

$$S_3 = \rho e^{-i\rho} \sum_{n=1}^{\infty} \sum_{m=-n}^{n} \sum_{p=1}^{2} R_{np}(\rho) a_{mnp,\perp} \tau_{mnp}(\theta) e^{im\varphi} \tag{2.66}$$

$$S_4 = i\rho e^{-i\rho} \sum_{n=1}^{\infty} \sum_{m=-n}^{n} \sum_{p=1}^{2} R_{np}(\rho) a_{nmp,\parallel} \tau_{mn(3-p)}(\theta) e^{im\varphi}. \tag{2.67}$$

For completeness' sake, we also address the radial dependence of the VSH. Only $\mathbf{N}^{(3)}_{mn1}$ has a radial component. The derivation of this involves calculating the curl of Equation 2.58. There is once again much tedious algebra; the only tricky bit is that one needs to use the associated Legendre differential equation to eliminate second derivatives with respect to $\cos\theta$. When the dust clears, we are left with

$$\left(\mathbf{N}^{(3)}_{mn1}\right)_r = \frac{n(n+1)}{m} e^{im\varphi} \sin\theta \tau_{mn2}(\theta) \frac{h^{(1)}_n(\rho)}{\rho}. \tag{2.68}$$

From this, we can conclude that the radial scattered field is

$$\left(\mathbf{E}_{scat}\right)_r = \sum_{v=\parallel,\perp} \sum_{n=1}^{\infty} \sum_{m=-n}^{n} a_{mn1,v} \frac{n(n+1)}{m} e^{im\varphi} \sin\theta \tau_{mn2}(\theta) \frac{h^{(1)}_n(\rho)}{\rho} E_{inc,v}. \tag{2.69}$$

We briefly remark on radiometric quantities for multisphere superposition as implemented in HoloPy. This is somewhat trickier than in Lorenz-Mie scattering since all these quantities depend the relative orientation between the sphere cluster and the incident polarization state. The polarization-dependent forward scattering amplitude is easy to calculate, so we obtain C_{ext} via the optical theorem. We obtain C_{scat} by summing up the a_{mnp} coefficients, much as we do in the Mie solution, except that there is a polarization dependence. There is no closed-form solution for C_{abs}, so we just compute $C_{ext} - C_{scat}$. Finally, there being no closed form for $\langle\cos\theta\rangle$ for polarized illumination, we have no alternative but to use numerical quadrature. The original Mackowski code implements a closed-form calculation for unpolarized incident illumination, but we have not implemented this in

HoloPy.

2.4 Other Approaches

We have gone through a considerable amount of labor in this chapter, but in a sense our portfolio of scattering techniques is still quite limited. We can calculate anything we want for isotropic, isolated spheres, or spheres that have a radially varying refractive index. Using multisphere superposition, we can also calculate holograms from multiple spheres or from sphere clusters. Though this has not been done, it would be straightforward to extend the multisphere superposition code to layered spheres – we would just change the response coefficients $\bar{a}_{np}$ from the Lorenz-Mie coefficients to the output of Yang's algorithm. But we are still stuck with spherical objects.

Exact scattering solutions are possible for symmetric scatterers not composed of spheres using what are called T-matrix methods, or extended boundary condition methods. See [74, 86] for good reviews. These codes in general require numerically computing integrals of expressions involving VSH inside a particle. They are therefore most readily applied to axisymmetric particles such as ellipsoids and circular cylinders; a publicly available code is [87]. Numerical issues make such codes impractical, however, for either very large particles (size parameters $>\sim 50$) or particles with extreme aspect ratios (such as very long, thin cylinders).

A completely different approach is to avoid trying to compute a scattered field expansion over some set of basis functions. One of the most useful such approaches is the discrete dipole approximation (DDA). The DDA models completely arbitrary scatterers (which need not have any regular geometric shape, and whose composition can vary arbitrarily) as an array of point dipoles. These dipoles respond to an incident field as well as to the fields produced by all the other dipoles. By solving self-consistently for all the dipole polarizations, the scattered field can be computed. We refer the reader to the seminal review by Draine and Flatau [88] and to a more recent review by Yurkin and Hoekstra [89]. A DDA code, ADDA (Amsterdam Discrete Dipole Approximation) has been incorporated into HoloPy [90]. While the DDA is extremely general, it requires tremendous computational resources. Fitting models based on the DDA to holograms of particles much larger

than 1 μm is at present impractical, but since DDA calculations are parallelizable, it may be possible to improve on this in the future.

3

Performing Digital Holographic Microscopy

In this chapter we describe some of the experimental methods by which we record and analyze digital holograms. We pay particular attention to features that enable the experiments to be described in subsequent chapters.

3.1 Inverted Holographic Microscope

We perform all the DHM experiments in this thesis on a holographic microscope built on the body of a Nikon TE-2000 inverted microscope (Figure 3.1.1). We describe here the main features of this microscope.

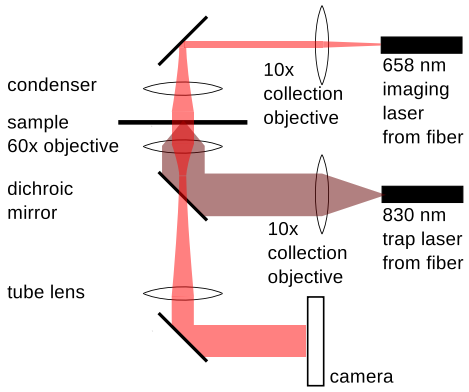

Figure 3.1.1: Diagram of digital holographic microscope.

3.1.1 Imaging Optics

We must provide a collimated, clean incident beam for holographic imaging. In our apparatus, light from a 658 nm laser diode (Opnext HL6535MG with Stanford Research Systems LDC 501 current and temperature controller) is coupled to the microscope through a single-mode fiber. The fiber circularizes the elliptical diode beam and spatially filters it. Light is then collected by a 10x, 0.25 NA Newport objective, and collimated by a 0.59 NA long working distance condenser (Nikon). For imaging, we use either a 60x, 1.20 NA Plan Apo water immersion objective (Nikon) for experiments in aqueous samples, or a 100x, 1.40 NA Plan Apo VC oil immersion objective (Nikon) for experiments with emulsions. We choose the objective and immersion liquid to minimize spherical abberations due to the index mismatch between the glass coverslip and the medium in the sample. Images are captured by a Photon Focus MVD-1024E-160 camera.

Our microscope is also capable of conventional bright-field imaging, as the mirror which steers the imaging beam into the condensor is on a flip mount and can swing out of the way.

3.1.2 Optical Trapping

Our holographic microscope also contains an optical tweezer. Light from a fiber-coupled 830 nm laser diode (Sanyo DL-8142-201, with Thorlabs TCM1000T temperature controller and LD1255 current controller) is collected by another 10x, 0.25 NA Newport ob-

jective. The light then passes through the back aperture of the 60x Nikon objective used for imaging and is focused in the sample. We use the trap only to isolate particles and form clusters in our samples; it remains off during the measurements.

3.1.3 Minimizing Radiation Pressure Forces: Laser Pulsing

The incident illumination system has received custom adaptations for studying the diffusion of colloidal clusters. In Chapter 2 we discussed radiation pressure forces and the radiation pressure cross section C_{rp}. As it turns out, radiation pressure from the imaging laser can create measurable perturbations that affect DHM measurements.

The first experimental evidence for radiation pressure being a concern came from qualitative observations of particle diffusion. Polystyrene spheres appeared to sediment while being observed with DHM – particles, and especially larger clusters, tended to consistently sink towards the imaging plane in a manner inconsistent with a Brownian process. Inadequate density matching seemed like the most obvious culprit, but the effect persisted despite the addition of increased amounts of D_2O. We observed the sedimentation in a sample containing 64% v/v D_2O. Subsequently, upon centrifuging a macroscopic volume of the sample at $(1.4 \times 10^4)g$ rcf, we found that the particles had creamed to the top of the sample.

We show through an order-of-magnitude estimate that radiation pressure forces may be comparable to gravitational forces on polystyrene spheres in water. Recall from Chapter 2 that the radiation pressure force on a sphere of radius a is given by

$$F_{rp} = \frac{n_{med} I_i C_{rp}}{c} \tag{3.1}$$

where C_{rp} is the radiation pressure cross section, and we have accounted for the increase in momentum of a photon propagating with an increased wavevector k in a medium of index n_{med}. Imaging studies suggest that the $1/e$ radius of our imaging beam may be as small as 100 μm; with 60 mW of power, using this as an estimate on the beam size gives an intensity of roughly 2×10^6 W/m. For a 1.3 micron polystyrene sphere in water illuminated by 660 nm light, we find $\langle \cos\theta \rangle \sim 0.926$ and $Q_{scat} \sim 3.39$, giving a radiation pressure efficiency $Q_{rp} \sim 0.25$. Consequently, the force on such a particle is on the order of 3×10^{-15} N.

In contrast, the same particle suspended in water (with a density mismatch of 50 kg/m^3) would experience a net force due to gravity and buoyancy of 5.6×10^{-16} N. Clearly, the radiation pressure forces can be problematic.

An intense laser is helpful for acquiring enough photons such that exposure times can be kept short, which minimizes motion blur. Typical frame times for diffusion measurements might be 40 ms, with an actual exposure time of 15 μs. It was obvious that decreasing the duty cycle of the imaging laser would straightforwardly provide a thousandfold decrease in the time-averaged radiation pressure force.

We decrease the duty cycle by using a laser diode current controller (LDC501, Stanford Research Systems) that accepts a modulation input with up to 1 MHz bandwidth. The PhotonFocus camera has a "camera strobe" feature that can output a square wave pulse, with polarity and width controlled by software, when the shutter is activated. We use this strobe signal as the master timing signal. The effective output circuit is shown in Figuer 3.1.2. The camera contains an opto-coupler driving the base of a transistor switch. The user needs to supply a pull-up resistor to a voltage rail. This was accomplished via a custom cable built by D. Kaz, who used the same 12.5 V rail that powers the camera with a 3.3 kΩ pull-up resistor; the strobe output signal comes across a BNC-terminated coaxial cable. We built a box containing the 1.5 kΩ resistor shown in the diagram, which acts as a voltage divider, reducing the strobe signal to a $\sim$ 4 V TTL-level signal[1].

The strobe signal then triggers a single square wave pulse from a Tektronix AFG 3022B arbitrary waveform generator (AWG) operating in "burst" mode. By adjusting the period of this square wave, we control the amount of time in each exposure during which the laser is on. The peak-to-peak amplitude of the AWG pulse is typically 6 V. This pulse then drives the modulation input of the LDC 501, where the laser current increases by 25 mA per volt supplied. By operating the laser at a current of 20 mA (below lasing threshhold), this signal causes the current to rise to 170 mA (full power). One critical detail is that the modulation input of the LDC 501 has a low input impedance near 2 kΩ – a discussion with an engineer

[1]Kaz's cable wiring reverses the polarity of the signal (such that the signal is active high when set in software to be active low.) One could argue that this is dubious electronics practice, especially given that there is a real likelihood of ground loops, but in practice we have not observed any problems, and the TTL trigger input of our AFG 3022B function generator appears to be differential.

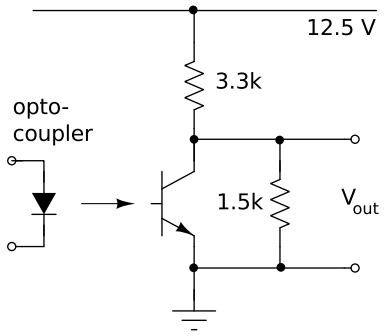

Figure 3.1.2: Schematic diagram of camera strobe circuit.

at SRS revealed that this was to keep the RC time constant associated with the input low. We performed measurements of the imput impedance at DC by supplying known voltages from an Agilent E3630A DC power supply and measuring the output across a voltage divider formed by a known 2k resistor and the unknown input impedance. The calibration curve is shown in Figure 3.1.3; its slope shows that the unknown impedance is 1.9 kΩ. It is critical to correctly set this load impedance in the AWG controls.

Figure 3.1.4 shows the results of this system in an oscilloscope capture with three traces: the camera strobe signal (yellow, set for a width much longer than the exposure time, so that its falling edge is not seen); a 15 μs-wide pulse from the AWG (blue), and the output laser power as measured by a photodiode (purple). Some roll-on and roll-of is noticeable in the photodiode signal, but in practice this is not problematic. Since using this pulsing system, we have not observed perturbations due to radiation pressure [2].

3.1.4 Validation of Pulsing System

Subsequent to the design of the pulsing system, and its widespread use in experiments (including the work discussed in Chapter 5), we performed further experiments to validate

[2]One might remark that a disadvantage of this system is that the laser duty cycle is slaved to the frame rate. This could cause unwanted thermal fluctuations if the frame rate needs to be changed during a measurement. We have not found this to be a problem, most likely due to the very short duty cycle when operating at typical frame rates of 25–100 fps.

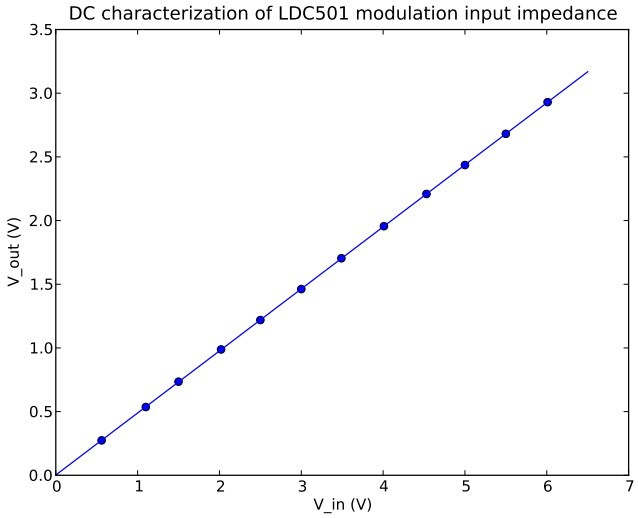

Figure 3.1.3: Output of a voltage divider formed by a known 2k resistor and the unknown input impedance. The slope of the best-fit line is 0.4871, from which we obtain an input impedance of 1.9k.

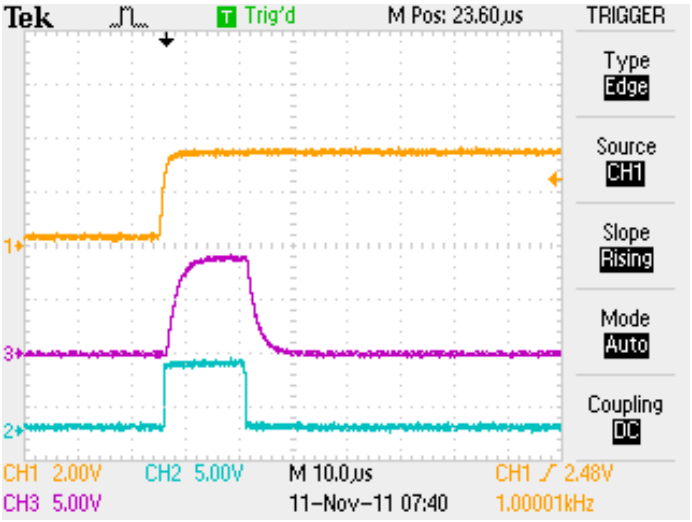

Figure 3.1.4: Timing of laser pulses captured by a Tektronix TDS 2024B storage oscilloscope. Channel 1 (yellow) shows the TTL-level strobe signal; its width is 100 μs. Channel 2 (blue) shows the 6V signal sent to the LDC 501 modulation input. Channel 3 (magenta) shows the output laser power, in arbitrary units, detected by a Thorlabs PDA 36A amplified silicon photodetector, where the laser has been attenuated with an ND 3 filter.

the following: that the pulsing system changes the Brownian dynamics in a measurable way, and that the anomalous drifts we observed were in fact due to radiation pressure forces. While the measurements we discuss in Chapter 5 indirectly validate the system, we wanted to check these points directly.

To verify these points, we observed the Brownian dynamics of an aqueous suspension of colloidal spheres with and without pulsing the imaging laser. We studied 2 μm-diameter sulfate polystyrene spheres (Invitrogen). We chose to study spheres because their radiation pressure cross section is independent of the particle orientation, which is not the case for clusters of spheres, and chose the particle size such that the drift we posited was due to radiation pressure was observable, but such that the particles remained Brownian. We suspended the particles in a 10 mM NaCl solution containing 47.5% D_2O v/v, and verified the density matching through centrifugation for 20 minutes at $1.4 \times 10^4 g$ rcf.

While performing the experiments, the presence of the drift when the imaging laser was continuously on and its absence when the laser was pulsed was manifestly evident. Figure 3.1.5 illustrates a typical z trajectory with continuous illumination and indicates that fitting a line allows us to measure an average drift velocity. We further quantified the drift by computing $\langle \Delta z(\tau) \rangle$ for a 75 s trajectory on two different particles, during one of which the laser was continuously on (Figure 3.1.6). For continuous (cw) illumination, for all τ, $\langle \Delta z \rangle$ is negative and differs from 0 by several standard deviations. Moreover, $\langle \Delta z \rangle$ scales linearly with τ, as expected for Brownian motion in a uniform force field. The data in 3.1.5 also facilitate a more precise measurement of the average drift velocity $\langle v_z \rangle$: we measure $\langle \Delta v_z \rangle = -0.267 \pm 0.019$ μm s^{-1}. In contrast, we do not observe a downward drift with pulsed illumination. The data suggest a small upwards drift, but $\langle \Delta z \rangle$ lies close to a standard deviation from 0 for all τ. Clearly, the dynamics change significantly when the imaging laser is pulsed.

The average drift velocity $\langle v_z \rangle$ is the most directly accessible manifestation of the force we attribute to radiation pressure. We now show that the drift velocity we measure is in reasonable agreement with expectations. By balancing the radiation pressure force F_{rp} against

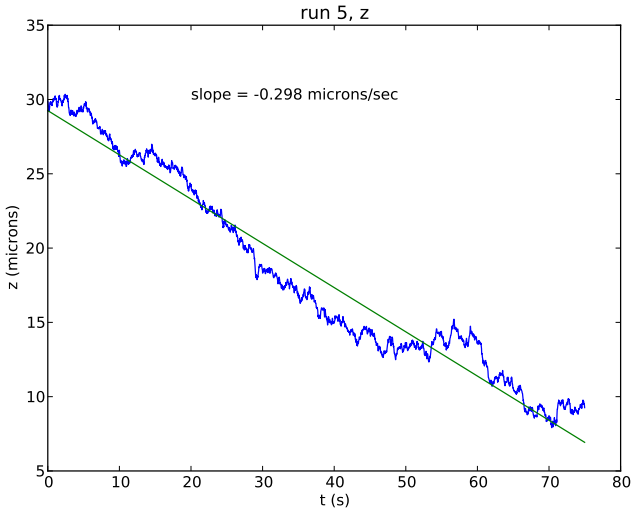

Figure 3.1.5: z position of a 2 μm-diameter polystyrene sphere under continuous wave illumination. The particle exhibits a downwards drift (in the direction of imaging laser propagation) from which we extract an average drift velocity.

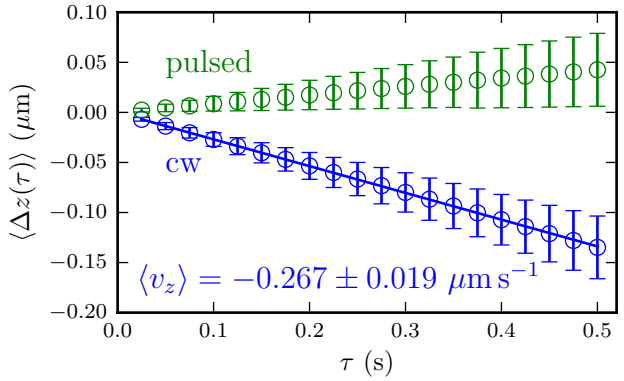

Figure 3.1.6: Average z displacement $\langle \Delta z(\tau) \rangle$ for two 2 μm-diameter spheres, one illuminated with continuous wave (cw) illumination and the other with pulsed illumination. Solid line for cw data is a linear fit that allows the average drift velocity $\langle v_z \rangle$ to be determined.

Stokes drag, we conclude that the magnitude of the average drift velocity is given by

$$|\langle v_z \rangle| = \frac{F_{rp}}{6\pi\eta a}. \tag{3.2}$$

Here as usual a is the sphere radius and η the fluid viscosity. As discussed in Chapter 2, $F_{rp} = \frac{n_{med} I_i C_{rp}}{c}$, where I_i is the incident intensity assuming a uniform plane wave and C_{rp} is the sphere's radiation pressure cross section [3].

The incident intensity I_i requires experimental determination. We know the power P_i incident on the sample through measuring the power of the imaging laser ($\sim$50 mW), but the intensity will depend on the beam size. Our imaging laser beam is by design a TEM 00 Gaussian beam, with an intensity profile $I(r)$ at the waist taking the form

$$I(r) = I_0 \exp\left(-\frac{r^2}{2\sigma^2}\right) \tag{3.3}$$

where σ describes the beam radius [4]. Integrating $I(r)$ over area to determine the total power in the beam gives $P = 2\pi I_0 \sigma^2$. We will assume that the particles being imaged are roughly in the center of the beam and take I_0 as the intensity incident on them. Consequently, we conclude that the expected drift velocity is

$$|\langle v_z \rangle| = \frac{n_{med} P_i C_{rp}}{12\pi^2 \sigma^2 \eta a c}, \tag{3.4}$$

where σ is to be determined by an experimental measurement.

Figure 3.1.7 shows an experimental determination of the beam profile: we image the beam using the same objective as in the holographic experiments, but with 1x rather than 1.5x magnification, and fit a 2D Gaussian. We determine $\sigma = 85$ μm. Given that our 2 μm-diameter spheres have $C_{rp} = 8.847 \times 10^{-13}$ m^2, and assuming an approximate solvent viscosity of 1 cP, we find from Eq. 3.4 that we expect $|\langle v_z \rangle| = 0.23$ μm s^{-1}. This is within

[3] There is a tricky question of whether the factor fo n_{med} should be included or not, concerning the definition of momentum for light in a medium. See the review article by Milonni and Boyd [91] for further details.

[4] Note that our σ differs from the traditional waist diameter w_0 in the theory of Gaussian beams by a factor of 2: $w_0 = 2\sigma$.

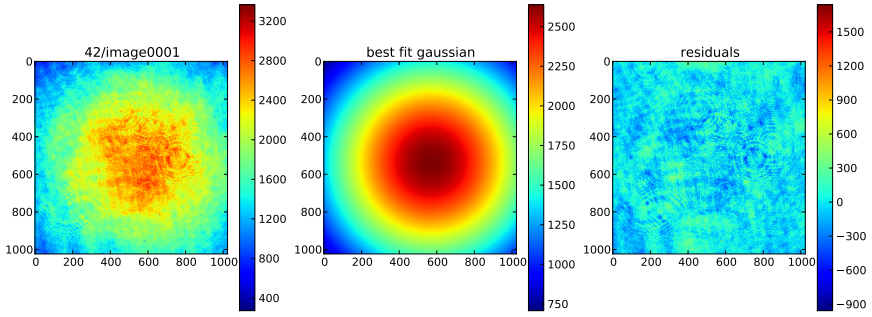

Figure 3.1.7: Experimental determination of beam radius σ: experimental image of beam, best-fit Gaussian, and residuals. We determine $\sigma = 85$ μm.

about 10% of the experimentally determined value; we are therefore confident that the drift is indeed due to radiation pressure.

3.1.5 Data Acquisition

We acquire data from the Photon Focus camera using a frame grabber (EPIX PIXCI E4) connected to a compute using a CameraLink bus. The frame grabber is controlled by a custom application programmed in Visual Studio. It is impossible for data to be written to hard disk rapidly enough; images are therefore stored in RAM and subsquently writen to hard disk. We can acquire up to about 12,000 512×512 images before filling the memory buffer.

As the user interface of the custom control program leaves much to be desired, an overhaul is currently under way.

3.2 Sample Preparation

We image our samples in glass cells made from a standard microscope slide and a #1 cover slip. Because the high NA objectives we use for DHM have a short working distance, we use #1 cover slips to enable us to image as deep as possible. We typically use 76-μm strips of Mylar A (DuPont Teijin) as spacers between the glass surfaces. The strips allow us to

make relatively thick sample chambers (so that particles or clusters can undergo Brownian motion with minimal perturbations due to boundaries) while keeping the refracting glass surfaces as parallel as possible. We clean the glass surfaces either with a pyrolysis oven or a plasma cleaner to make the surfaces hydrophilic. We carefully rinse them with Millipore water and dry them with compressed ultra-high purity nitrogen to minimize dust, which can be a huge problem due to the large depth of field of DHM. We typically also heat the Mylar strips slightly their glass transition temperature T_g at 100 °C in an oven, under compression with weights, to flatten them and any cut edges as much as possible.

We usually prepare a "sandwich" with the slide on the bottom, the Mylar spacers, and then the coverslip, and pin this together along the top and bottom edges with binder clips. Then, we apply Norland 60 UV-curing epoxy to the corners where the slide, Mylar strips, and coverslip meet. We cure this briefly under a UV lamp to pin the corners and subsequently seal the top edges (parallel to the Mylar strips) with Norland epoxy; the sides remain open. It is subsequently easy to fill these cells with aqueous solutions via capillary action; they typically hold $\sim$ 20 μL of fluid. After we fill the sample holders, we seal the side edges with Devcon 5-minute epoxy. Figure 3.2.1 shows a typical sample holder, the only difference being that the chamber has been filled with a solution of red food coloring (Allura Red AC).

As we will discuss in the next chapter, we study some systems where a depletion force due to PNIPAM hydrogel particles binds clusters together. In these experiments, we prevent depletion interactions between the PS particles and the glass surfaces by coating both the slides and cover slips used with PNIPAM. This is done by first silanizing the glass surfaces by immersion in a 1% w/w solution of 3-methylacryloxypropyl-trimethoxysilane (98%, Sigma) in anhydrous ethanol for 24 hours at room temperature. Next, the surfaces are rinsed with ethanol, dried with compressed nitrogen, and heated in an oven at 110° C for one hour. Finally, the slides and coverslips are immersed in an aqueous suspension of 100-nm-diameter PNIPAM particles for at least 24 hours at room temperature. After this procedure, the PNIPAM particles do not desorb from the surfaces.

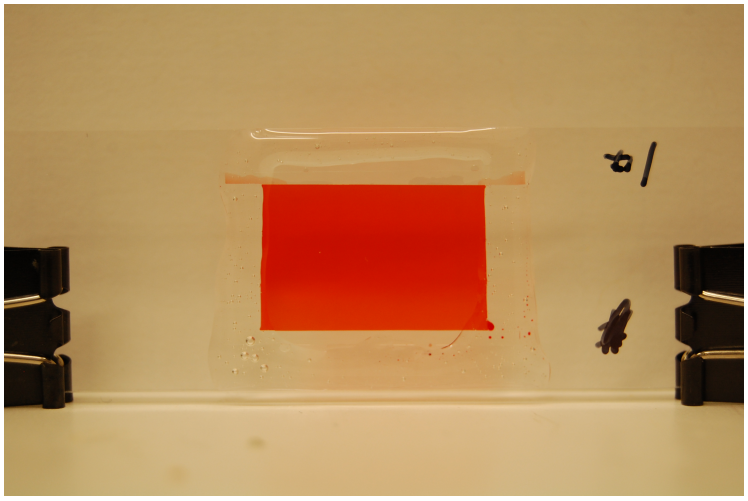

Figure 3.2.1: Photograph of a typical sample holder. The chamber has been filled with red food coloring for visualization. The Mylar strips run horizontally, and the sample holder is filled either from the right or the left.

3.3 Fitting Models to Holograms with HoloPy

3.3.1 General Design of Code

Our hologram analysis code is publicly available as the package HoloPy in Launchpad: `https://launchpad.net/holopy`. HoloPy contains certain core modules for image input/output, basic image processing, and visualization. HoloPy relies on Python and NumPy/SciPy; there are also extensions in Fortran 77 and 90 that are needed to perform scattering computations.

The scientific bulk of HoloPy consists of three main portions: code for optical propagation, scattering computations, and fitting. The propagation code (which performs reconstructions as a special case) uses the convolution approach to the Fresnel-Kirchoff integral. The scattering module performs Lorenz-Mie (including layered sphere and Mie superposition calculations), multisphere superposition, and DDA calculations. The fitting module provides a default Python-based Levenberg-Marquardt fitter, `nmpfit`, based on Craig Markwardt's IDL code [92]. It is also possible to use other fitters with HoloPy.

3.3.2 Parameterizing Multi-Particle Configurations

There are several ways to parameterize hologram models that contain multiple particles. The obvious way is to fit for the $3N$ coordinates of N particles. This is necessary when the particles are far apart and move freely, as they do in the emulsion system. Fitting with all $3N$ coordinates is necessary in clusters where the particle position fluctuations are large enough that they cannot be described as perturbations from some reference (such as when clusters rearrange [9]), but can require numerical tricks like allowing the particles to pass through each other. Thus, when the particles have manifest constraints, we find it more effective to reduce the number of degrees of freedom in the fit by explicitly incorporating the constraints.

In particular, we can treat colloidal clusters as (essentially) rigid bodies. Instead of fitting for $3N$ coordinates, we can fit for three center-of-mass coordinates and at most 3 Euler angles. In some cases we can also incorporate internal degrees of freedom for small perturbations away from a rigid reference structure. For every cluster we consider, we define a *reference orientation*; the exact orientation of the reference orientation is irrelevant and is chosen for convenience.

Our Euler angle convention requires some discussion. We define Euler angles in an active, *zyz* picture. A cluster forming a given hologram is in some configuration in the laboratory frame, and the Euler angles define an active rotation of the cluster from its reference orientation to its actual orientation. Specifically, we rotate the cluster first by an angle α about the laboratory z axis, second by β about the laboratory y axis, and lastly by γ about the laboratory z axis. The rotation matrix $\mathbf{R}$ that describes this is

$$\begin{aligned}\mathbf{R} &= \mathbf{R}_\gamma \mathbf{R}_\beta \mathbf{R}_\alpha \\ &= \begin{pmatrix} \cos\gamma & -\sin\gamma & 0 \\ \sin\gamma & \cos\gamma & 0 \\ 0 & 0 & 1 \end{pmatrix} \begin{pmatrix} \cos\beta & 0 & \sin\beta \\ 0 & 1 & 0 \\ -\sin\beta & 0 & \cos\beta \end{pmatrix} \begin{pmatrix} \cos\alpha & -\sin\alpha & 0 \\ \sin\alpha & \cos\alpha & 0 \\ 0 & 0 & 1 \end{pmatrix}. \end{aligned} \tag{3.5}$$

Multiplying this out, we obtain

$$\mathbf{R} = \begin{pmatrix} \cos\alpha\cos\beta\cos\gamma - \sin\alpha\sin\gamma & -\sin\alpha\cos\beta\cos\gamma - \cos\alpha\sin\gamma & \sin\beta\cos\gamma \\ \cos\alpha\cos\beta\sin\gamma + \sin\alpha\cos\gamma & -\sin\alpha\cos\beta\sin\gamma + \cos\alpha\cos\gamma & \sin\beta\sin\gamma \\ -\cos\alpha\sin\beta & \sin\alpha\sin\beta & \cos\beta \end{pmatrix}. \tag{3.6}$$

We define this rotation matrix as acting from the left on a column vector (which in practice, describes the coordinates of a particle relative to the cluster COM). The angles are defined such that a positive rotation is *clockwise* if viewed from the origin looking along the positive direction of the associated axis[5].

Note that usual definitions for the Euler angles constrain β to the interval $[0, \pi]$, which if α and γ are constrained to $[0, 2\pi]$ allows for a one-to-one mapping between 3 Euler angles and rotation matrices. For fiting purposes, we let the angles take any value, with Equation 3.6 defining the rotation. Also, note that α and γ are modulo 2π, while β is *not* modulo π.

For colloidal dimers (or any other axisymmetric object), only two Euler angles are meaningful. We enforce $\alpha = 0$ and allow β and γ to vary continuously. We define the reference configuration to have the rotational symmetry axis be the x axis, allow both particle sizes to vary, and also allow for a nonzero gap distance between the particles.

For trimers, we allow all three particle sizes to vary, as well as a gap distance between all three particles. The reference configuration is as shown in Figure 3.3.1, with all particles in the xy plane. The three spheres have radii a_1, a_2, and a_3, and g_{12} denotes the gap distance between particles 1 and 2. We define $r_{12} = a_1 + a_2 + g_{12}$ and define r_{13} and r_{23} similarly. r_{12} points at a 60° angle from the y axis, as shown. Initially, particle 1 has coordinates $(0, 0)$, particle 2 has coordinates $(r_{12}\sqrt{3}/2, r_{12}/2)$, and particle 3 has coordinates $(r_{13}\sin(2\pi/3 - \delta), -r_{13}\cos(2\pi/3 - \delta))$ where

$$\cos\delta = \frac{r_{12}^2 + r_{13}^2 - r_{23}^2}{2r_{12}r_{13}}. \tag{3.7}$$

[5]This convention is new to HoloPy 2.0. Previous incarnations of the code were more heavily tied to the Euler angle conventions of scsmfo1b.for, which uses a *passive* rotation picture. Previous interpretations of the rotations as an active transformation thus had rotation angles signed in the opposite sense. While the new convention breaks backwards compatability, it makes much more sense.

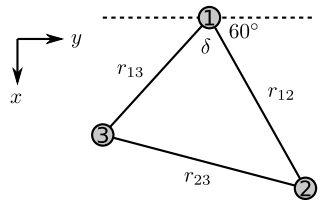

Figure 3.3.1: Reference configuration for rigid trimer.

We then numerically shift the coordinates so that the center of mass lies at $(0, 0)$. We can apply a similar parameterization to a trimer whose particles are in a linear chain, where instead of specifying g_{23} we specify the subtended angle δ.

Euler angles are not the only way to parameterize $\mathrm{SO}(3)$, the group of rigid body rotations. Quaternions are another possibility, which have the advantage of avoiding the phenomenon of *gimbal lock*: when $\beta = 0$ or 2π, only the sum $\alpha + \gamma$ matters, not the two angles independently. Fitting with quaternions (which have 4 parameters) requires a minimizer capable of handling implicit constraints between fit parameters, but if implemented may be more effective.

3.3.3 Running Fits

Levenberg-Marquardt fitters, like `nmpfit` as principally used in this work, require an initial guess for the fit parameters. There are two ways we obtain them. First, we can manually adjust fit parameters such as positions and orientation angles, perhaps guided by reconstructions. Second, we can use a "bootstrap" method for a time series of holograms, where the best-fit parameters of one frame are used as the initial guess for the next.

Recently, we have found that fitting a randomly chosen fraction of the pixels in a hologram – as low as 1% for single spheres – is surprisingly effective. In a sense this is not surprising since we are typically trying to determine ~ 10 fit parameters from a 200×200 hologram; the fitting problem is grossly overdetermined. Typically, what we do is to use the manual guessing method to determine initial guesses for one frame, and then use bootstrapping to do a rough fit to 10% of the pixels. Subsequently the rough fit results can be used as an initial guess for a fit to all the pixels. This stage is embarassingly parallelizable.

While HoloPy runs on local desktop computers for development and testing, manual guessing, and small batch jobs, the majority of heavy-duty hologram analysis is done on the Odyssey computational cluster, where we use up to hundreds of 2.3-GHz, 64-bit processors simultaneously.

3.3.4 Quantifying the Goodness of Fit

After fitting a scattering model to a hologram, we quantitatively confirm the fit of the model by examining two statistical measures of the goodness-of-fit. The first measure, chi-squared per pixel χ_p^2, is the quantity the fitting algorithm attempts to minimize:

$$\chi_p^2 = \frac{1}{N}\sum_{i=1}^{N}(I_{holo} - I_{fit})^2. \tag{3.8}$$

The sums run over all N pixels of the recorded normalized hologram I_{holo} and the best-fit model hologram I_{fit}. For any given hologram, comparing χ_p^2 to an expected noise level allows us to assess whether deviations between the recorded hologram and best-fit model are due to instrumental noise or to a systematic error in the model's description of the underlying data. Assuming noise in the least significant bit of an 8-bit camera, we would expect χ_p^2 values greater than $(1/255)^2 = 1.54 \times 10^{-5}$ to have originated from systematic errors.

The second statistical measure we use was the coefficient of determination R^2. We defined R^2 as

$$R^2 = 1 - \frac{\sum_{i=1}^{N}(I_{holo} - I_{fit})^2}{\sum_{i=1}^{N}(I_{holo} - \bar{I}_{holo})^2} = 1 - \frac{\sum_{i=1}^{N}(I_{holo} - I_{fit})^2}{\sum_{i=1}^{N}(I_{holo} - 1)^2} \tag{3.9}$$

where $\bar{I}_{holo}$ is the mean value of the recorded hologram, which is 1 by our normalization [93]. R^2 measures the fraction of the variation of the recorded hologram from its mean value that is captured by the best-fit model, independent of the amount of variation in the hologram. Whereas χ_p^2 varies significantly across physical systems that differ in scattering cross section and hence hologram fringe amplitude, R^2 does not. Therefore, we use R^2 to assess the validity of the scattering models with which we fit holograms. In particular, as

we discuss in the next chapter, R^2 helps to assess the validity of using the Mie superposition approximation.

4

Imaging Multiple Colloidal Particles

This chapter discusses our imaging of multiple colloidal particles with DHM in two contexts: colloidal clusters and particles on emulsion droplets. We discuss how we produce and image clusters of different morphologies, and discuss the internal dynamics of clusters that have internal degrees of freedom. The anisotropic Brownian dynamics of clusters, a major topic in itself, will be deferred to Chapter 5. We will then discuss what we can learn about DHM as well as interparticle interactions from looking at emulsion droplets.

4.1 Colloidal Clusters

4.1.1 Introduction

We have already discussed the importance of colloidal clusters for self-assembly in Chapter 1. Aside from these, however, clusters are also among the simplest examples of non-

spherical colloidal particles, which may be more common than monodisperse spheres in real suspensions. As such, they provide an important test case for the utility of DHM to go beyond isolated spheres. We will particularly emphasize in this Chapter the importance of multisphere superposition.

4.1.2 Making Clusters

We have three main ways to make colloidal clusters: using depletion forces in combination with optical tweezers, using van der Waals forces and optical tweezers, and through arrested aggregation (also known as salting-out quenching.) The latter two techniques produce clusters that are essentially rigidly bonded together; with the first technique, it is possible to make clusters that have internal degrees of freedom or even undergo morphological changes.

Depletion forces arise entropically due to excluded volume effects in suspensions of bidisperse spheres or spheres and polymers. The effect is schematically illustrated in Figure 4.1.1. The size of the smaller particles sets the thickness of an excluded volume layer around the large particles into which the centers of the smaller particles are sterically forbidden from entering. When two large spheres come close to each other, their excluded volumes overlap, resulting in a larger free volume for the small spheres. This then lowers the free energy of the system and gives rise to an effective attraction between the spheres. A model for the depletion interaction was first formulated by Asakura and Oosawa (AO) [94, 95]. The AO model is formulated for the potential at center-to-center separation r between two large hard spheres of radius a_L, dispersed in a gas of small hard spheres of radius a_S at volume fraction φ:

$$U_{AO}(r) = \frac{k_B T \varphi}{(2a_s)^3} (2a_S + 2a_L - r)^2 \left(2a_S + 2a_L + \frac{r}{2}\right) \tag{4.1}$$

for $2a_L < r < 2(a_L + a_S)$. For larger r, $U_{AO}(r) = 0$. We give the AO model here to illustrate the overall scaling of the effect, but we note that it fails to model what happens when the small spheres are not dilute [34, 96] or when the particles do not interact as hard spheres.

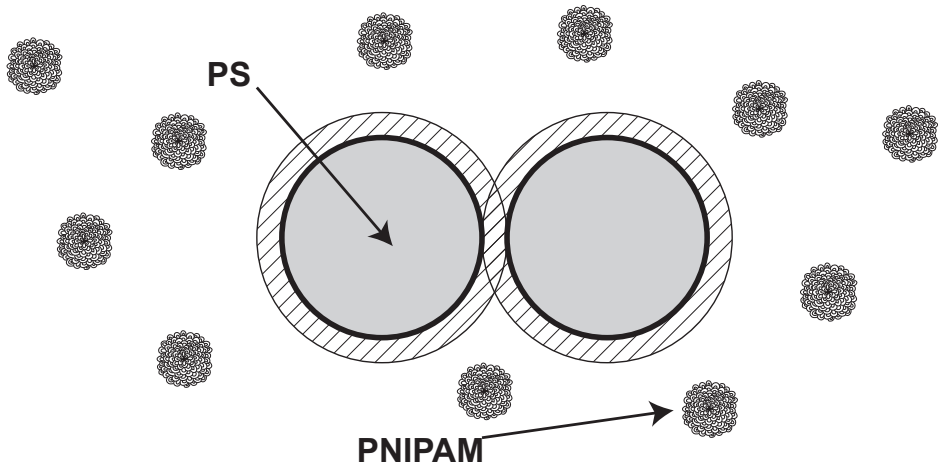

Figure 4.1.1: Cartoon of experimental system and of the depletion interaction. Shaded area around each polystyrene sphere shows the excluded volume around each sphere, set by the radius of the depletant particles (here, made of PNIPAM hydrogel). The centers of the depletant particles cannot enter the shaded areas.

We perform experiments with two different systems of depletants. One system is based on poly-N-isopropylacrylamide (PNIPAM) hydrogel particles, which are highly swollen at room temperature and are effectively index-matched in an aqueous solution. The system contains 0.99-μm-diameter, surfactant-free, sulfate-stabilized polystyrene (PS) spheres (Invitrogen) and 80-nm-diameter PNIPAM hydrogel particles, synthesized according to [97]. The volume fraction of PS in the sample is 2×10^{-5}, and the approximate weight fraction of PNIPAM is 0.05. We use equal proportions of H_2O and D_2O to density-match the polystyrene spheres, and we add 15 mM NaCl to screen electrostatic interactions and 0.1% w/w Pluronic P123 triblock copolymer surfactant to stabilize the particles. Because the PNIPAM is index-matched, we treat everything in the system other than the PS particles as an optically homogeneous solvent with refractive index $n = 1.3349$, as measured with an Abbé refractometer. As we will discuss, the depth of the potential well in this system is several k_BT at room temperature.

The other system consists of a dilute suspension of monodisperse, 1.3-μm-diameter surfactant-free, sulfate-stabilized polystyrene spheres (Invitrogen) at a volume fraction of 8×10^{-6} in an aqueous solution containing 5 mM NaCl and 246 mM sodium dodecyl sul-

fate (SDS). Because the SDS concentration is far above the critical micelle concentration [98], the SDS forms micelles, which act as depletants. The micelles should be spheres with a diameter of about 4 nm.

We also make clusters from 1.3-μm-diameter surfactant-free, sulfate polystyrene spheres (Invitrogen). These particles are suspended at a volume fraction of about 8×10^{-4} in a 0.1 M NaCl solution. This reduces the stability conferred by the charged sulfate groups on the particles, which allows the particles to bind irreversibly to each other due to a van der Waals force when brought close together.

In all of these cases, we use the optical trap in the inverted Nikon microscope described in Chapter 3 to assemble the particles. We grab individual particles with the trap, and then pull all the spheres into the trap focus. This is relatively easier to do with the two depletion systems, but is much more finicky with the van der Waals system. In particular, anecdotal experience suggests that the charge on the particles can vary based on preparation conditions such as washing, and that charges (or the lack thereof) on glass sample holders can affect whether particles can be easily bound together in free-energy minimizing configurations in the bulk. The other inherent disadvantage of the optical trap method for making clusters is that it is not scalable.

Consequently, we use a different method, based on arrested aggregation, to make dimers and trimers of sulfate polystyrene spheres [99]. We make dimers from 1.3-μm diameter spheres and trimers from 1-μm diameter spheres. We transfer these particles into a 250 mM NaCl solution to screen the charge of the stabilizing sulfate groups and start the aggregation, then we decrease the ionic strength by quenching with deionized water (Millipore) after 1 minute to arrest the aggregation. We then suspend the resulting mixture of single particles, dimers, and larger clusters in a density-matched solvent consisting of 50% v/v D_2O and 50% v/v H_2O with a salt concentration of 1 mM. The arrested aggregation method produces a range of cluster sizes and geometries, ranging from single particles to aggregates of many spheres. This is not a problem for our diffusion experiments with DHM since they study single clusters, whose geometry we can verify *in situ* with bright field microscopy and check *post hoc* by fitting hologram models.

Figure 4.1.2 shows bright-field micrographs of some of the clusters produced using optical tweezers and depletion with SDS micelles. We are able to produce geometries including

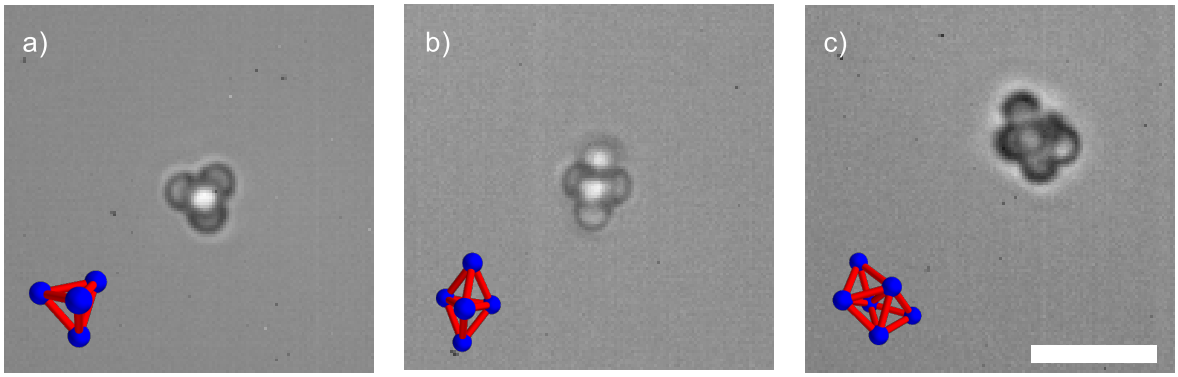

Figure 4.1.2: Bright field micrographs of clusters made from 1.3-μm diameter polystyrene spheres, recorded with a 60$\times$ 1.20 NA water immersion objective. Clusters bound by depletion forces induced by SDS micelles. Ball-and-stick models, indicating cluster geometry and orientation, are a guide to the eye. Scale bar 5 μm. n_s denotes the number of spheres in each cluster. a) Tetrahedron ($n_s = 4$). b) Trigonal bipyramid ($n_s = 5$). c) Polytetrahedron ($n_s = 6$).

tetrahedra with $n_s = 4$ spheres, trigonal bipyramids with $n_s = 5$, and polytetrahedra with $n_s = 6$. Figure 4.1.3 shows a mixture of single spheres, dimers, trimers, and larger clusters from the arrested aggregation method dried on a glass coverslip.

4.1.3 Cluster Holograms and Analysis

We first show that we can record and model holograms of clusters whose shape is essentially constant. We study a dimer of 1 micron spheres bound by a depletion interaction induced by PNIPAM hydrogel particles in Figure 4.1.4. The dimer model allows one refractive index for both particles, both particle radii, the center-of-mass position, 2 Euler angles, the interparticle separation, and α_{sc} to vary. We find excellent agreement between the experimental hologram and the best-fit model, with a per-pixel χ^2 of 3.596×10^{-4}. Similarly, Figure 4.1.5 shows the comparison between the experimental hologram and the best-fit model for a trimer of 1 micron spheres produced by using the optical trap to rigidly bind particles together. The trimer hologram model varies one refractive index, one sphere

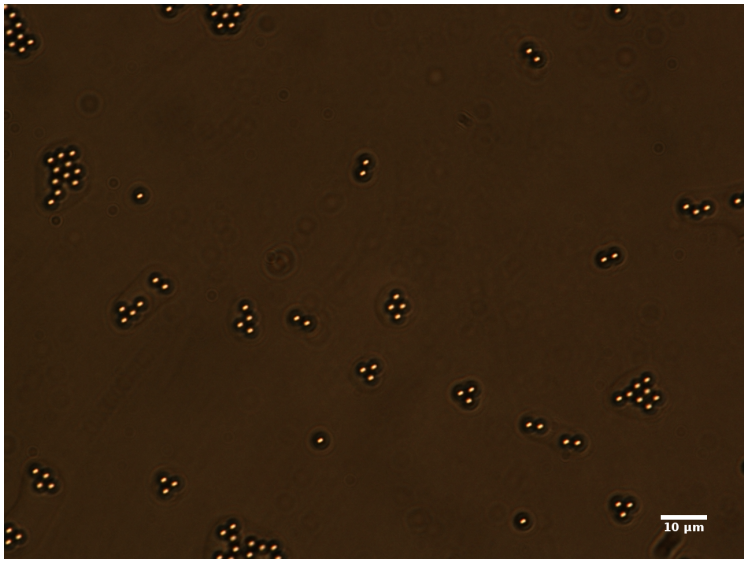

Figure 4.1.3: Clusters made from 1.3 μm-diameter polystyrene spheres and arrested aggregation technique [99]. The technique produces a range of cluster sizes. Scale bar, 10 μm.

radius, the three center-of-mass coordinates, three Euler angles, and a_{sc}. For this hologram and best-fit model, the normalized χ^2 is 6.556×10^{-4}. Note, however, that the values of χ^2 per pixel are larger than what we would expect due to noise: for noise in the least significant bit of an 8-bit camera, we would expect χ^2 values on the order of $(1/255)^2 = 1.54 \times 10^{-5}$.

Figure 4.1.6 compares recorded and best-fit model holograms, calculated with multi-sphere superposition, for tetrahedral, trigonal bipyramidal, and polytetrahedral clusters. These clusters are bound by depletion forces induced by SDS micelles. Qualitatively, we observe excellent agreement between the recorded and best-fit holograms. In particular, the best-fit models reproduce the highly non-axisymmetric fringes in the recorded holograms, which depend strongly on the cluster orientations. The quality of the agreement is confirmed by the R^2 values of the fits, which are close to 1 (Table 4.1.1). Also, the fitted particle radii are close to the manufacturer's reported value of 650 nm. However, the values of χ_p^2 we observe are an order of magnitude larger than what we would expect due to camera noise, and indicate that further improvements to fits will depend on modeling

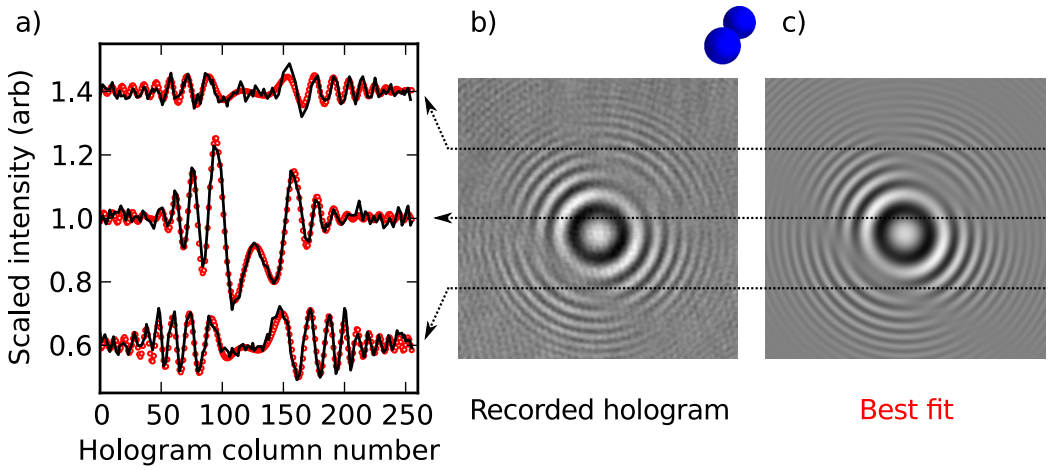

Figure 4.1.4: Hologram of a dimer composed of 1 micron spheres, held together by a depletion interaction induced by PNIPAM hydrogel particles. (a) Comparison of the recorded hologram (solid black lines) to the best fit, as calculated from the multisphere superposition scattering model (red symbols), along the three dashed lines indicated. (b) Recorded hologram. (c) Best fit model. The blue diagram above the holograms shows a rendering of the particle positions from the fit. The upper sphere is rotated 34.9° into the page. The rendering is oriented so that the incident light direction is into the page.

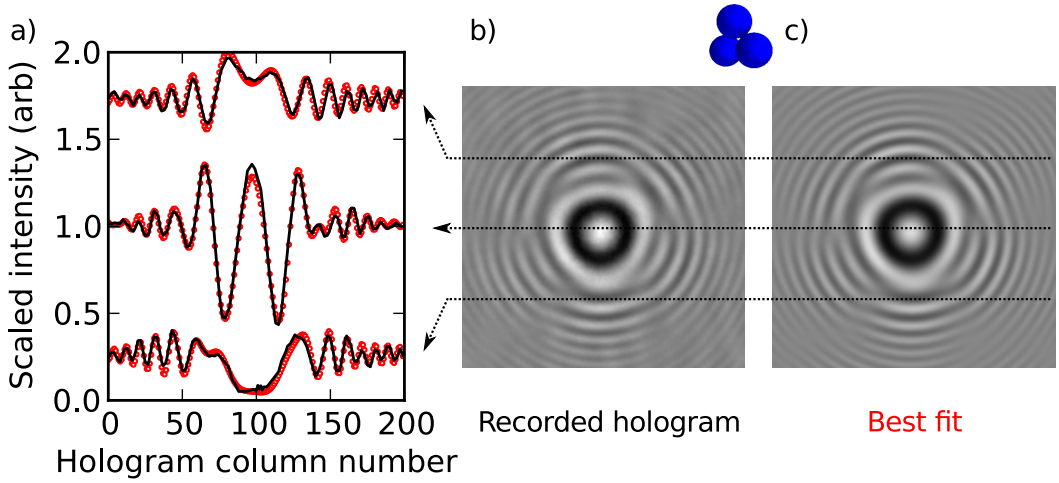

Figure 4.1.5: Hologram of a trimer of 1.3 micron spheres produced by binding charged spheres in an optical trap. (a) Comparison between the recorded hologram (solid black line) and the best fit, as calculated from the multisphere superposition scattering model (red symbols), along the three dashed lines indicated. (b) Recorded hologram. (c) Best fit. The blue diagram above the holograms shows a rendering of the particle positions from the fit. The leftmost sphere is rotated 38.3° into the page. The rendering is oriented so that the incident light direction is into the page.

additional physical phenomena or improving the convergence of the fitter.

We emphasize that with these clusters, the use of multisphere superposition is critical. Figure 4.1.7 shows that there are qualitative differences between simulated holograms where $\mathbf{E}_{scat}$ is computed with multisphere superposition and with Mie superposition. According to our criterion in Equation 2.42, we have in this case (for individual spheres with $x = 10$ and $m = 1.2 + 10^{-4}i$)

$$\frac{Q_{ext}x^2}{kR} \approx \frac{(3.683)(10^2)}{20} = 18.4, \tag{4.2}$$

so it is not surprising that the Mie superposition approximation is inadequate.

As we might expect from these estimates, Mie superposition totally fails to fit holograms from the multi-particle clusters discussed in Figure 4.1.6. There, the constituent spheres have a relative index $m \approx 1.2$ and size parameter $x \approx 8.3$. A fit to the polytetrahedron hologram of Figure 4.1.6c using a Mie superposition model yields $\chi_p^2 = 5.39 \times 10^{-3}$ and $R^2 = 0.463$ (Figure 4.1.8). These values are much poorer than the values associated with the multisphere superposition model. Moreover, qualitative differences between the best-fit Mie superposition model and the experimental hologram are readily apparent.

Using these fitting techniques, we can also characterize clusters that have internal degrees of freedom. We give two illustrations of this: first, with the depletion-bound dimer in Figure 4.1.4, and second with a trimer where there is a large gap between two of the particles.

In the first case, recall that our model allows the determination of the center-to-center distance between the particles. We can invert the Boltzmann distribution of center-to-center separations to determine the pair potential $U(r)$, shown in Figure 4.1.9. The measured potential is qualitatively consistent with what we expect for this system. At short range, we expect a van der Waals attraction and an electrostatic repulsion. The sum of these two competing interactions should lead to a potential well, which is what we observe.

We do not make a quantitative comparison between our measured potential and a model

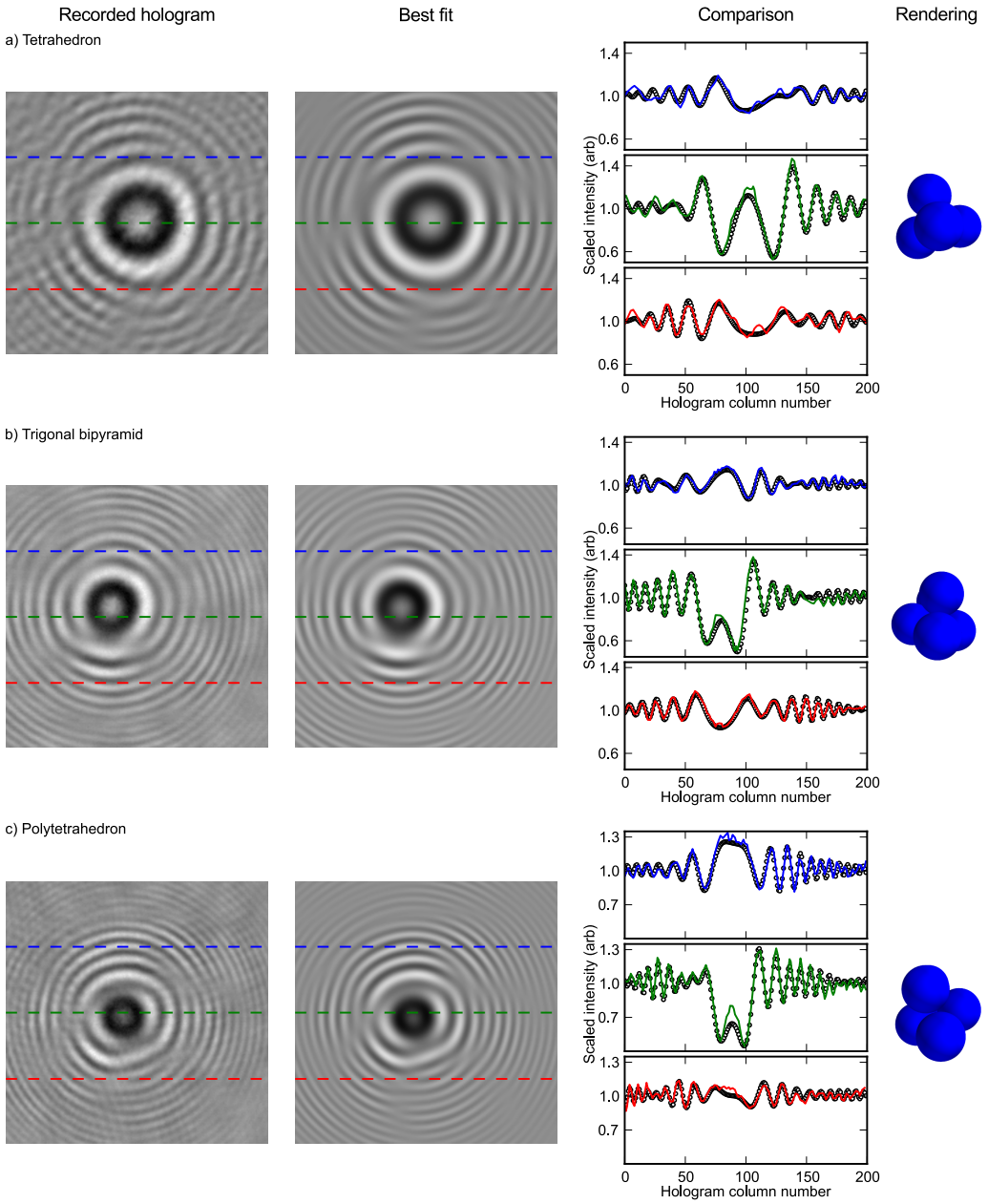

Figure 4.1.6: Recorded and best-fit model holograms of rigid clusters. The third column compares the recorded holograms (solid lines) to the best-fit models (open symbols) along the color-coded dashed horizontal lines shown in the holograms. The renderings in the rightmost column show the cluster orientations determined from the fits. In the renderings, the incident light propagates into the page. a) Tetrahedron ($n_s = 4$). b) Trigonal bipyramid ($n_s = 5$). c) Polytetrahedron ($n_s = 6$).

Table 4.1.1: Fitted radii and goodness-of-fit statistics χ_p^2 and R^2 for rigid clusters holograms in Figure 4.1.6.

Cluster	Radius (nm)	χ_p^2	R^2
Tetrahedron	670 ± 30	1.18×10^{-3}	0.923
Trigonal bipyramid	640 ± 30	9.48×10^{-4}	0.910
Polytetrahedron	650 ± 20	1.24×10^{-3}	0.877

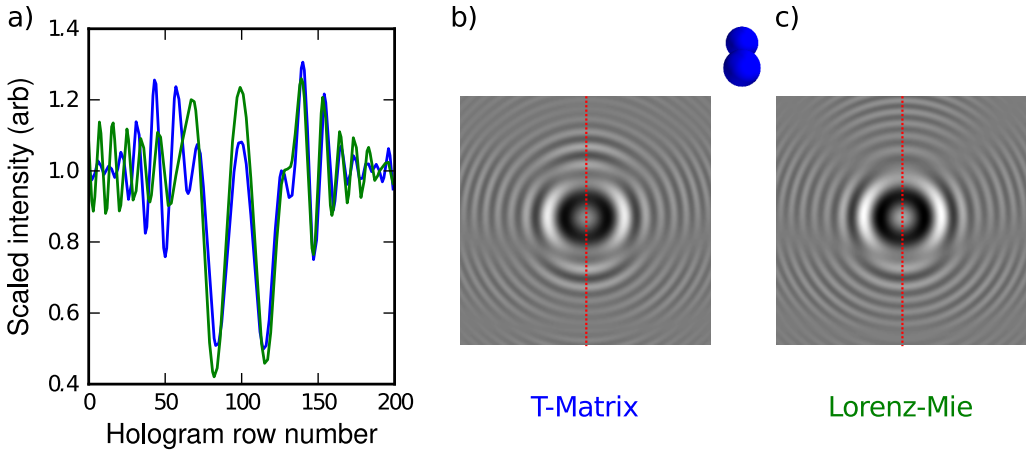

Figure 4.1.7: Comparison between simulated hologram calculated using multisphere superposition method and simulated hologram computed from Mie superposition, for a dimer composed of 1.57 μm polystyrene spheres in water with 658 nm incident illumination. As shown in the blue rendering, the upper particle is rotated 45° into the page. The rendering is oriented so that the incident light direction is into the page. (a) Hologram intensity along red dashed lines in (b) and (c). The hologram calculated from a multisphere superposition solution (blue) differs qualitatively from the hologram calculated by superposing the Lorenz-Mie solution for two spheres (green) due to near-field coupling. (b) Simulated hologram computed from T-matrix code. (c) Simulated hologram calculated by Lorenz-Mie superposition.

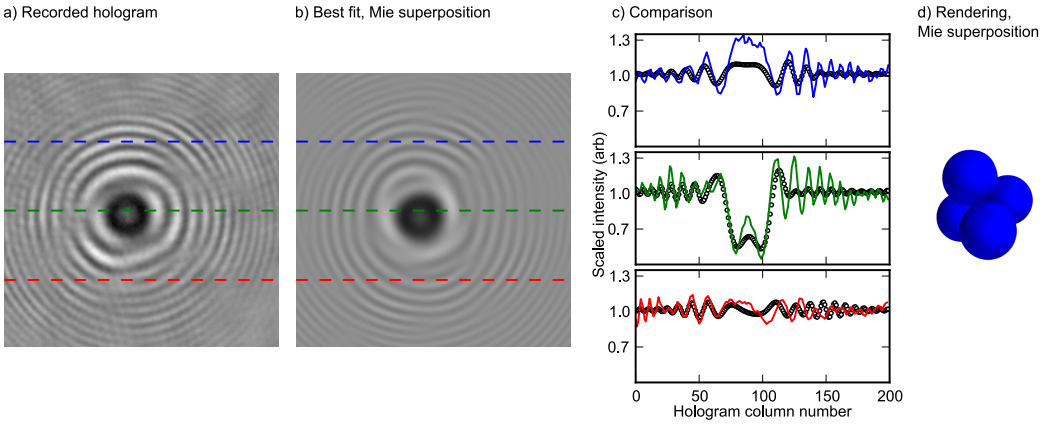

Figure 4.1.8: Fit of polytetrahedron hologram in Figure 4.1.6c performed using Mie superposition. a) Recorded hologram (shown again for ease of comparison). b) Best-fit model determined from Mie superposition. c) Comparison between recorded hologram (solid lines) and Mie superposition model (open symbols) along the dashed lines in the holograms. d) Rendering showing cluster orientation determined by Mie superposition fit. The incident light propagates into the page.

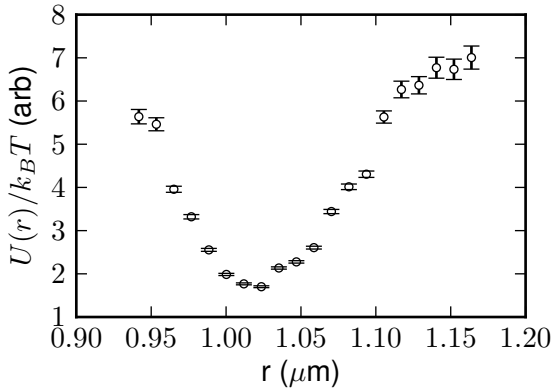

Figure 4.1.9: Measured pair potential for a colloidal dimer. Only differences in $U(r)$ are relevant; the actual values are arbitrary. The measured potential is qualitatively consistent with an attractive depletion force and an electrostatic repulsion. The bin width of the histogram of particle center-to-center separations, from which we determine the distribution of separations and the potential, is 11.7 nm.

potential, such as the Asakura-Oosawa potential [94], [95], because our system does not conform well to existing depletion models: our depletants are not hard spheres, nor is their concentration low. Moreover, we never observed the dimer break apart. Thus only differences in U are meaningful, as we are unable to observe the particles at large separations where they are non-interacting. Also, the results depend strongly on the fitted radii: the particle radii are encoded in low spatial frequency variations in the magnitude of the hologram fringes, which can lead to a large uncertainty, on the order of 10-100 nm. This is why there are a few frames in which the measured separation distance is smaller than 0.95 μm. Using the DHM with multisphere superposition scattering models to accurately determine pair potentials will require optimizing the fitting technique and improving the fidelity of the low spatial frequencies in the holograms.

Nonetheless, the results are promising and qualitatively consistent with our expectations: the range of the measured potential is on the order of the depletant size, and the depth of the well is several k_BT, consistent with our observations that the dimers do not break apart for at least several minutes.

Finally, we examine a cluster of 1.3 μm spheres, bound by depletion from SDS micelles, that is not a free-energy minimum. Namely, we examine a cluster where three particles are bound in a linear chain, but where the two end particles are not close enough to interact. We show an experimental hologram and a best-fit model hologram in Figure 4.1.10. Here, the three particles subtend an angle of 111.1°. These results indicate how clusters whose geometries are changing can be studied in detail using DHM and scattering solutions, as Perry and co-workers have subsequently done [9].

4.2 Particles on Emulsion Droplets

4.2.1 Introduction

Particles on liquid-liquid interfaces, and particularly on droplets, are of interest for several reasons. Particles and droplets can be used to build useful materials such as colloidosomes [100], whose potential applications include drug delivery. Emulsions can also be stabilized by colloidal particles; these are known as Pickering emulsions [101]. In such emulsions,

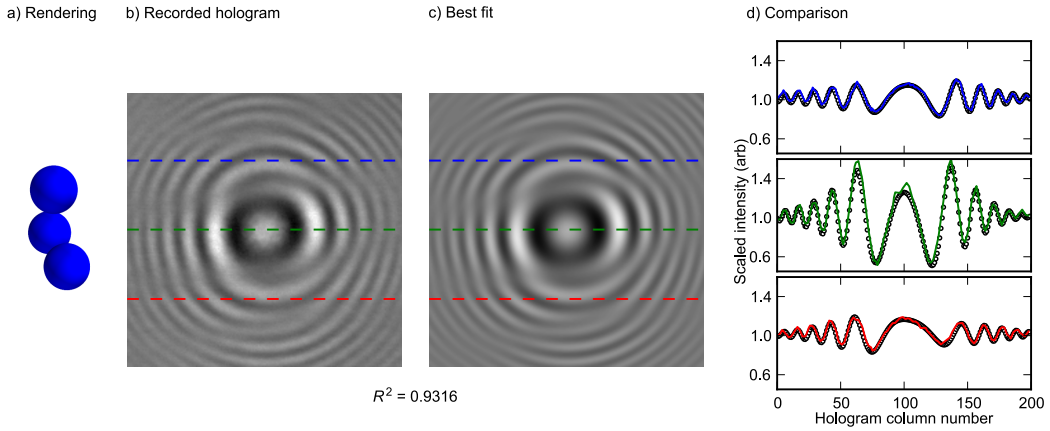

Figure 4.1.10: Bent trimer hologram. (a) Rendering of particle positions and orientations determined from best-fit model. (b) Recorded hologram. (c) Best-fit model. (d) Comparison of experimental hologram (solid lines) with best-fit model (open symbols) along the horizontal dashed lines.

particles bound to the droplet interface can prevent the droplets from coalescing. How one might either stabilize emulsions with particles, or destabilize particle-laden emulsions (as in oil recovery) is of great industrial importance.

More importantly, much of the fundamental physics governing the interactions between particles at liquid-liquid interfaces remains poorly understood. There is a classic equilibrium picture due to Young that describes the binding of an isolated particle to an interface. This is illustrated in Figure 4.2.1(a) for a sphere at an oil-water interface. Young's equation balances the horizontal forces due to three competing surface tensions: oil-water (γ_{ow}), particle-oil (γ_{po}), and particle-water (γ_{pw}). Balancing the forces along the three-phase contact line gives rise to Young's equation for the contact angle θ_c:

$$\cos\theta_c = \frac{\gamma_{pw} - \gamma_{po}}{\gamma_{ow}}. \tag{4.3}$$

There is another way to derive this, via an energetic argument, by minimizing the free energy of the particle-interface system as a function of the contact angle [102]. In so doing, one may derive the free-energy difference between the sphere of radius a being wholly in

one phase initially (say, the oil) and then sitting at the interface:

$$\Delta F = -\pi a^2 \gamma_{ow} (1 - \cos\theta_c)^2. \tag{4.4}$$

A qualitative way to think about this that the particle removes area from an energetically costly oil-water interface (with a typical surface tension of $\gamma_{ow} \sim 40$ mN/m. Pulling a particle with $a = 1\ \mu$m off such an interface will cost on the order of $10^{10} k_B T$ at room temperature[1]. But this picture fails to capture what happens when multiple particles lie on an interface. Figure 4.2.1(b)-(g) illustrate some of the possible effects. These include attractions due to capillary deformations due to gravity [104], electric fields [32], and surface roughness [105]; electrostatic repulsions due to asymmetric counterion clouds [16] or patches of trapped water [106]. Most theoretical and experimental works have considered flat interfaces, but curvature (as on a spherical droplet) may change the physical picture, inducing for instance new capillary effects [107, 108]. While all of these possibilities have been suggested, some remain controversial and a detailed physical understanding is still lacking.

Thus, experimental studies of particles on emulsion droplets may lead to a better understanding of interparticle interactions at liquid-liquid interfaces. In particular, the systems we will consider here typically have small numbers (< 10) of micron-sized particles on droplets several μm in diameter. These differ from systems with many particles that are essentially jammed on the droplet surface, where topology rather than interparticle interactions govern the formation of spherical crystals with defects [109]. These droplets are also small enough that they cannot be considered locally flat; curvature matters. Our particle-laden droplets will also serve as a test bed for DHM, and in particular its ability to study systems of many particles that have no interparticle constraints (unlike rigid clusters), as well as the Mie superposition approximation.

[1] Kaz *et al.* recently showed that this equilibrium picture is insufficient, and that colloidal particles logarithmically relax to their equilibrium contact angles on a very clean interface [103]. The relaxation of individual particles that penetrate liquid-liquid interfaces continues to be under active investigation by A. Wang.

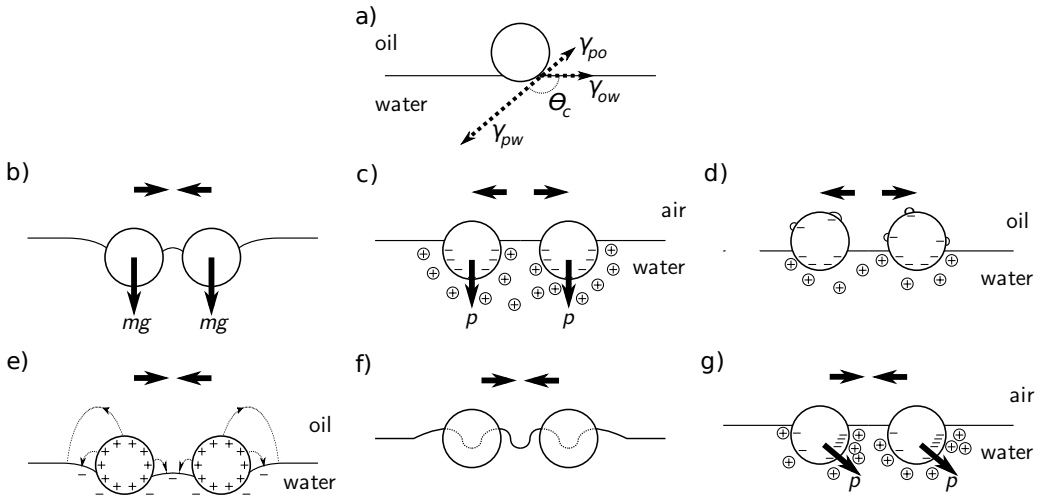

Figure 4.2.1: Illustrations of interactions between colloidal particles at liquid-liquid interfaces. (a) Geometry for Young's equation. (b) Gravitational forces on large particles cause them to deform the interface, resulting in an attraction (the "Cheerios effect.") (c) At an air-water interface, charged groups on the portions of particles in the water can dissociate. The resulting dipoles lead to repulsion. (d) At an oil-water interface, patches of water can lead to repulsions through the oil. (e) Electric fields from charged particles can deform the interface. (f) Contact line undulations due to particle surface roughness or a patchy charge distribution (exaggerated for clarity) can result in capillary multipole interactions. (g) Particles with patchy charge form dipoles with a component parallel to the interface.

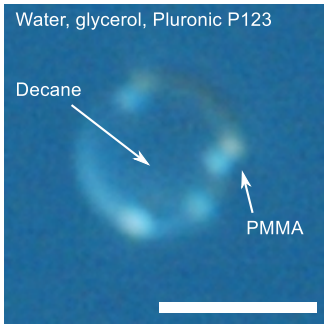

Figure 4.2.2: Bright field micrograph of decane droplet with 4 PMMA spheres on its surface, recorded under 100× magnification and differential interference contrast (DIC). Here, a slight index mismatch between the decane and the continuous phase makes the droplet visible under DIC. Scale bar 5 μm.

4.2.2 Sample Preparation

We prepare emulsion droplets laden with colloidal spheres by dispersing a suspension of microspheres in oil into an aqueous continuous phase. We suspend 0.8 μm diameter polymethyl methacrylate (PMMA) spheres coated with poly(12-hydroxystearic acid) stabilizer [110, 111] in decane at a mass fraction of 2.1×10^{-3}. The aqueous continuous phase contains 0.2% w/w Pluronic P123 triblock copolymer surfactant and 56% w/w glycerol. The glycerol matches the refractive index of the continuous phase to that of decane, so that only the PMMA spheres scatter light. We prepare the emulsions by mixing 0.5 mL of the PMMA-containing decane with 20 mL of the continuous phase in a 40 mL scintillation vial and shearing the mixture for 3 minutes at 9500 rpm with an Ika T9 Basic homogenizer equipped with a S25N-8G dispersing tool. After emulsification, we dilute the emulsion to 17% v/v with additional continuous phase. A micrograph of a typical emulsion droplet, laden with 4 particles but with the continuous phase slightly mismatched to allow the droplet to be seen, is shown in Figure 4.2.2.

While the emulsion droplets are index-matched[2], we cannot simultaneously match the

[2]We check the index-matching with an Abbé refractometer. The match is close, typically to 5×10^{-4} on the refractometer. Still, this does not account for either the variation of the refractive indices of either the decane or the continuous phase with temperature, or with wavelength.

density of the dispersed and continuous phases. Consequently, the less-dense oil droplets tend to cream to the top glass surface of the sample holders. This is problematic for two reasons. First, nearby glass surfaces may affect the interparticle interactions. Secondly, scattered light may back-reflect off the glass surface. Consequently, we use negative dielectrophoresis (NDEP) to keep the particle-laden droplets away from the top of our sample cells. The following expression is usually quoted for the dielectrophoretic force on a spherical particle of radius a with dielectric permittivity ε_p in a medium of permittivity ε_m [112]:

$$F_{DEP} = 2\pi\varepsilon_m a^3 \left(\frac{\varepsilon_p - \varepsilon_m}{\varepsilon_p + 2\varepsilon_m}\right)(\nabla E^2). \tag{4.5}$$

The term in parentheses is the Clausius-Mossotti factor for the particle's effective polarizability. For oil ($\varepsilon_r \sim 1$) in water ($\varepsilon_r \sim 80$) this factor is negative, and due to the large dielectric constant of water this factor CM $\sim$ 0.5. Hence we speak of *negative* dielectrophoresis: oil droplets in water will be repelled from an electric field gradient. We do not discuss the derivation of this here, but note that this is only approximately valid for our droplets since the derivation assumes that the droplets are much smaller than the length scale of variations in the electric field E. Note that the a^3 dependence of the force helps to ensure that the forces on a micron-diameter colloidal particle will be at more than 100 times smaller than the forces on a 5 micron droplet.

It is clear that to maximize the NDEP effect, a large *gradient* of E^2 is needed. This can be done with an interdigitated geometry, schematically illustrated in Figure 4.2.3, in which adjacent conducting strips have voltages applied to them that are 180° out of phase. We apply an AC field instead of a DC field to prevent electro-osmosis. A model due to Morgan *et al.*, assuming a 1D periodic pattern of very long conducting strips, allows us to model the electric fields of our devices [113]. Following Morgan's model[3], the maximum downward (y) component of ∇E^2 occurs centrally between conducting strips of width d to which a potential V_o is applied. The gradient is given by

$$\nabla(E^2)_y = -\frac{16V_o^2}{\pi d^3}\frac{\cosh\hat{y}}{\sqrt{2}\cosh(2\hat{y})}\arctan\left(\frac{1}{\sqrt{2}\sinh\hat{y}}\right) \tag{4.6}$$

[3]The following may be derived using Equations 19 and 20 in Morgan's paper [113].

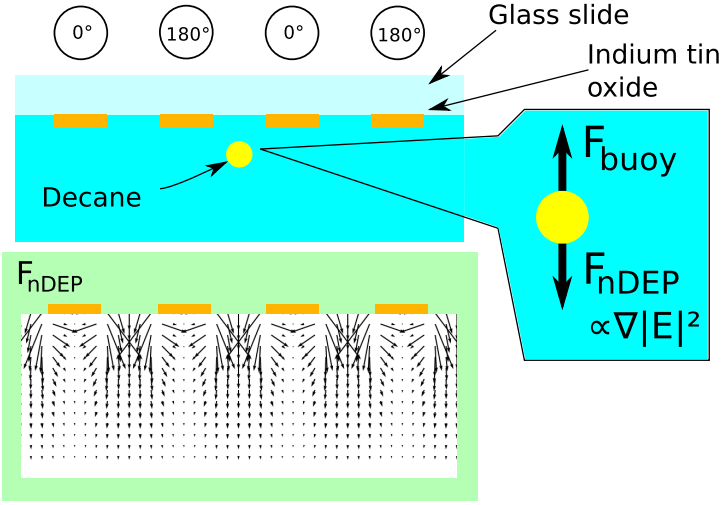

Figure 4.2.3: Schematic illustration of NDEP devices produced by etching ITO-coated glass slides. Voltages applied to adjacent interdigitated conducting strips are 180° out of phase. The resulting NDEP force, calculated using [113], is illustrated in the vector plot.

where $\hat{y} = \pi y/2d$.

We use photolithography and wet etching to prepare interdigitated electrode arrays with a 40 μm spacing between adjacent electrodes on microscope slides coated with a 30 nm layer of ITO (Delta Technologies, CB-90IN coating). We spin-coat the ITO surface of the slides with Shipley S1813 positive photoresist at 5000 rpm and soft bake the slides on a 115°C hot plate for 1 minute. We first define the electrode pattern by exposing the photoresist to UV light through a photomask (150 mJ/cm² exposure at 405 nm), then develop the photoresist by immersion in Microposit MF CD-26 developer for 1 minute at room temperature. Following an overnight hard bake in a 90°C oven, we etch away the excess ITO with an aqueous solution containing 40% v/v HCl and 10% v/v HNO_3 for 12 minutes at room temperature. The NDEP devices are typically operated by applying a 10 V peak-to-peak, 300 kHz square wave with an arbitrary waveform generator (Agilent AFG 3022B). Diffraction from the edges of the ITO electrodes was negligible.

Figure 4.2.4 shows a typical NDEP device; the 40 μm electrode patterning is not visible.

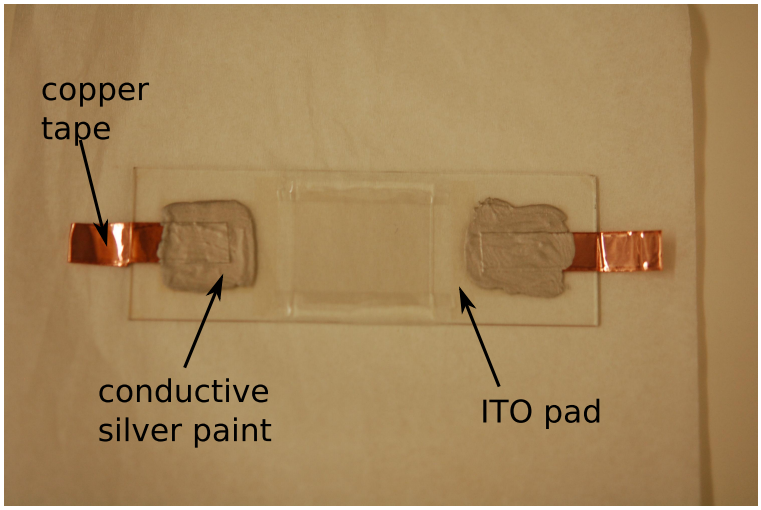

Figure 4.2.4: Photograph of sample holder with NDEP devices fabricated on a 75 mm wide slide.

The edges of the ITO pads (from which the electrodes run horizontally) are visible. We use copper tape and conductive silver paint to ensure a good electrical contact between the waveform generator and the devices. Figure 4.2.5 shows a device in action; with a 15 V peak-to-peak square wave, $\sim$ 10 μm-diameter droplets can be repelled about 30 μm from the top of the sample cell.

4.2.3 Results: Imaging Particle-Laden Droplets

Here we show that our fitting techniques may also be applied to multisphere systems without a fixed geometry. Figure 4.2.6 shows a hologram of six particles bound to the surface of a decane droplet and a best fit model calculated using Mie superposition. Again, the qualitative agreement between the fringes of the recorded hologram and the best-fit model is good. Quantitatively, we found $\chi_p^2 = 7.29 \times 10^{-5}$ and $R^2 = 0.811$. χ_p^2 was much lower than the values we obtained for the clusters, primarily because the peak amplitude of the hologram in Figure 4.2.6 was significantly smaller than the peak amplitudes of the cluster

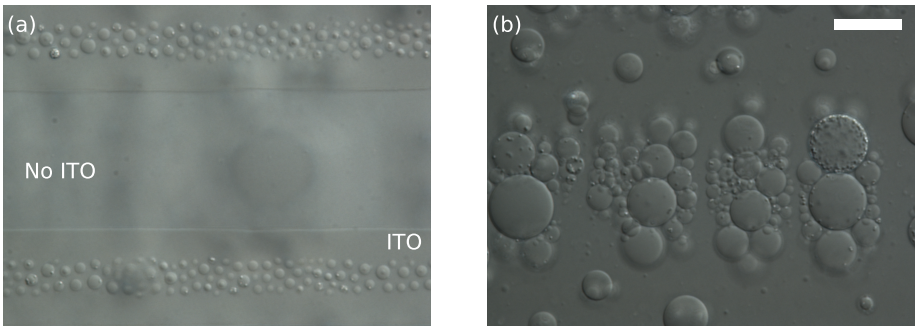

Figure 4.2.5: ITO devices with decane emulsion droplets. Continuous phase is partially index mismatched for visibility; the AC field is on. (a) Field of view focused at the top of the sample cell. Droplets visible where there is ITO (and consequently, where $\mathbf{E}$ is approximately uniform; no droplets are in focus in the region between the electrodes. (b) Same field of view, focused 30 μm below (a). Droplets, some with PMMA particles, are visible in the region between the ITO electrodes. Micrographs recorded at 40x magnification with DIC. Scale bar, 20 μm.

holograms in Figure 4.1.6. The value of R^2 indicates that the fit was slightly worse than the fits for the clusters. However, because we knew the particles were bound to the surface of a spherical droplet, we independently tested the accuracy of the fitted particle positions. While we could not directly image the decane droplet, which was index-matched to the continuous phase, we fit the surface of a sphere to the particle coordinates, as shown in Figure 4.2.6d. The average difference between the radial distance of each particle from the droplet center and the fitted droplet radius was 60 $\pm$ 60 nm. Differences of this scale are comparable to previously reported precisions for DHM [59, 85], and may be partially accounted for by variations in the interfacial contact angle between different particles [103].

To determine whether the slightly worse value of R^2 obtained in this fit is due to the Mie superposition approximation, we examine the validity of this approximation in further detail.

To confirm that Mie superposition is a suitable means for analyzing holograms like that in Figure 4.2.6, in which multiple weakly scattering spheres are situated several diameters apart, we fit a model based on multisphere superposition to the same hologram. The multisphere superposition fit yielded $\chi_p^2 = 8.08 \times 10^{-5}$ and $R^2 = 0.790$, comparable to the

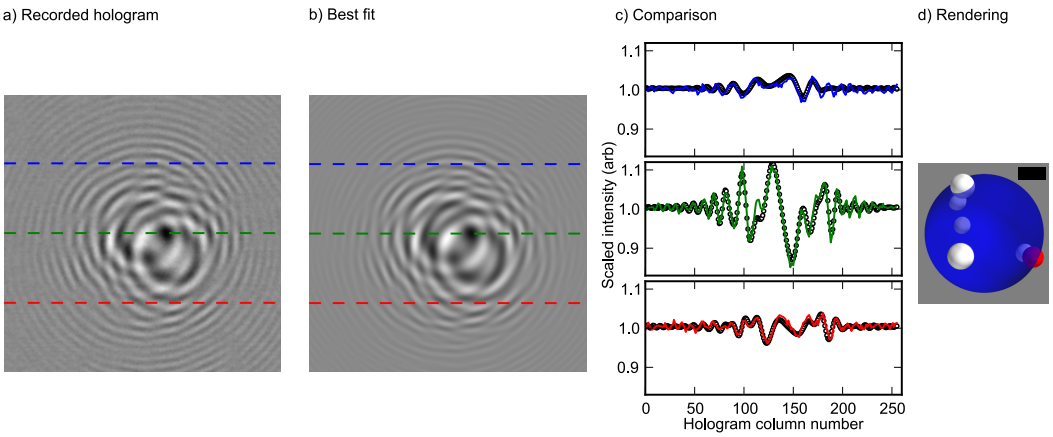

Figure 4.2.6: Holograms of six PMMA spheres on a decane droplet. a) Recorded hologram. b) Best-fit model. c) Comparison between recorded hologram (solid lines) and best-fit model computed using Mie superposition (open symbols) along the dashed horizontal lines in the holograms. d) Rendering showing the sphere positions determined by fitting the holograms. The incident light propagates into the page, and the scale bar is 1 μm. The larger blue sphere is a guide to the eye; its position and diameter, 4.35 μm, were determined by fitting a sphere to the coordinates of the six particles. The small red sphere indicates the particle showing the largest discrepancy in position along the optical axis between fits to Mie superposition and multisphere superposition.

Mie superposition fits. Differences between fitted particle coordinates in the two in-plane directions, perpendicular to the optical axis, were at most 22 nm. The largest difference between fitted coordinates along the optical axis was 154 nm. The sphere showing the largest displacement along the optical axis is highlighted in red in Figure 4.2.6d. The size of these differences, as well as the lack of improvement in the goodness-of-fit using the multisphere superposition code, indicate that Mie superposition is an appropriate approximation. We conclude that the smaller R^2 values for this system stem from physical effects—such as weak scattering by the decane droplet—that neither multisphere superposition nor Mie superposition account for.

Further insight into the applicability of Mie superposition comes from examining the particle showing the largest coordinate difference along the optical axis. As shown in Figure 4.2.6d, the largest difference occured when two particles nearly occluded one another. In such a configuration, the assumption that the field incident on each sphere is simply the illuminating plane wave is clearly invalid, as the colloidal spheres scatter most strongly in the forward direction. The field incident on the occluded sphere should therefore include a significant component of the scattered field from the first sphere. Whereas the multisphere superposition solution accounts for this multiple scattering effect, Mie superposition does not.

We can check our dimensionless figure of merit, Equation 2.42. Taking the fitted drop diameter of 4.35 μm as a typical interparticle spacing for PMMA spheres like those in the droplet experiments, we find $Q_{ext}x^2/kR = 0.11$, in agreement with our previous conclusion that the Mie superposition approximation is accurate for this sample. However, if we consider the sphere shown in red in Figure 4.2.6d, using the nearest-neighbor distance of 1.19 μm for R yields $Q_{ext}x^2/kR = 0.35$. This larger value indicates that Mie superposition is a poorer approximation for this particle, as borne out by the 150 nm difference in the fitted position from Mie superposition and multisphere superposition. In contrast, for the polystyrene spheres used in the cluster experiments, which are separated from each other by approximately a particle diameter, $Q_{ext}x^2/kR = 13$. We therefore conclude that $Q_{ext}x^2/kR$ should be approximately 0.1 or smaller for Mie superposition results to be trusted to a precision of 100 nm or better.

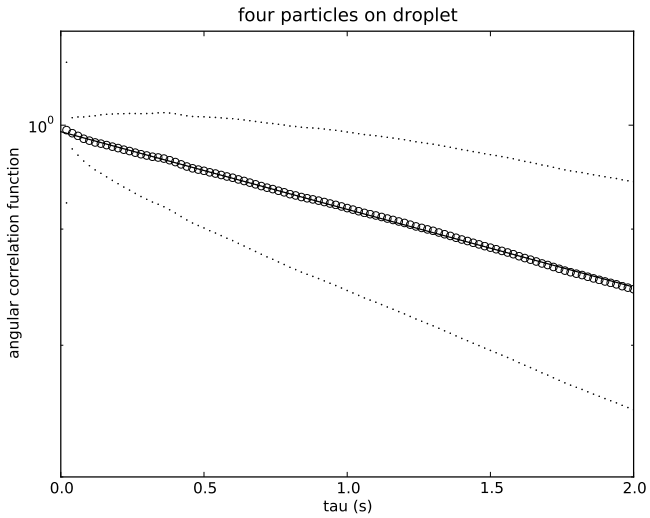

Figure 4.2.7: Autocorrelation of $\mathbf{u}$ for four particles on a decane droplet. Solid line: best fit to exponential decay.

4.2.4 Dynamics on a Droplet

Finally, we discuss some preliminary data suggesting that these PMMA spheres are non-interacting. We study four particles moving on a 4.33 μm-diameter droplet. In particular, we examine the autocorrelation of the normalized distance $\mathbf{u}$ from a best-fit droplet center (determined from fitting the particle positions) to the particle center. Figure 4.2.7 shows the results obtained from 2000 holograms. We fit these data to an exponential decay with decay constant $2D_r = (7.8 \pm 1.1) \times 10^{-2}\ \mathrm{s}^{-1}$. As we will describe in much more detail in the next chapter, the exponential decay is indicative of rotational diffusion – what we would observe if the particles were completely noninteracting.

While these measurements do not reveal anything about particle interactions at liquid-liquid interfaces, these measurements do demonstrate that DHM with scattering solutions is a potential means by which such interactions can be measured.

5

Anisotropic 3D Diffusion of Colloidal Clusters

5.1 Introduction

In this section we discuss measurements of diffusion tensors for anisotropic colloidal particles: clusters composed of approximately identical spheres. This work has been motivated by several primary considerations. First, diffusion may be highly relevant to colloidal self-assembly. Recent theoretical work by Holmes-Cerfon and co-workers has indicated that the kinetics self-assembly in colloidal systems with short-ranged interactions may be primarily governed by diffusion rather than by energy barriers [114]. Second, diffusion constants can be theoretically difficult to predict. As we discuss in more detail in this chapter, such predictions require solving the Stokes creeping flow equations, which is only possible for spheres or highly symmetric particles such as ellipsoids [115] or sphere dimers [116] in

unbounded fluids. In contrast, during self-assembly, anisotropic colloidal particles diffuse near other particles and boundaries. Analytical techniques are of minimal help here, and so experimental measurements would be of value. Finally, diffusion and Brownian motion are fundamental physical processes; our work here includes some of the first measurements of heretofore unmeasured aspects of Brownian motion. Our work here focuses on single clusters rather than ensembles. While bulk techniques such as depolarized dynamic light scattering [117] can be used to measure diffusion in colloidal systems, it is difficult to resolve the multiple diffusional timescales exhibited by anisotropic particles using such techniques.

The author's interest in anisotropic colloidal diffusion was ignited by the seminal work of Han and co-workers in Arjun Yodh's group at the University of Pennsylvania. Han *et al.* studied the anisotropic diffusion of micron-sized polystyrene ellipsoids diffusing in a quasi-2D geometry using video microscopy [29]. Subsequent work by this group showed how the confining 2D walls played a large role in the measured anisotropic diffusion, and in particular enhanced the anisotropy beyond what could be observed in 3D [118]. Anthony *et al.* also studied the 2D diffusion of anisotropic 2D sphere clusters all of whose particles lay in a plane [119].

Measuring 3D anisotropic colloidal diffusion is more challenging due to the need for a 3D quantitative microscopy technique, as described in Chapter 1. Several measurements using confocal microscopy have been reported in the literature. Mukhija and Solomon measured the diffusion of ellipsoids in 3D [120]. Hunter *et al.* studied the motion of tetrahedral sphere clusters [121]. While tetrahedral clusters diffuse isotropically, like spheres, it is possible to track their rotational motions, and Hunter's work was primarily motivated by the possiblity of using such particles to study the dynamics of glassy colloidal suspensions primarily consisting of spheres. While techniques based on confocal microscopy are quite general, it is usually only possible to study slow diffusional processes due to the necessary acquisition times. Mukhija and Solomon embedded polymethyl methacrylate ellipsoids in a solvent containing cyclohexyl bromide, decalin, and polydimethylsiloxane with a viscosity of 2 Pa s, more than three orders of magnitude larger than that of water. Hunter's work used clusters made from spheres 2.45 μm in diameter [121]. These particles were more than double the size of the particles used in these experiments; by dimensional anal-

ysis, the rotational diffusion of such particles would be more than 8 times slower due to size effects alone. We mention this not to be critical of these workers, but because the timescales affect the precision to which elements of the diffusion tensor can be measured, a key advantage of our techniques.

Digital holographic microscopy has been used to study anisotropic diffusion as well. Cheong and co-workers in David Grier's group measured the rotational diffusion of long copper oxide nanorods using DHM and reconstruction techniques [122]. These techniques, however, would be difficult to apply to systems that did not have large aspect ratios. Fung *et al.* reported measurements of the diffusion of a colloidal sphere dimer bound by a weak depletion interaction in the first report of using DHM in conjunction with scattering solutions for anisotropic particles [85]. However, the focus in that work was on measuring translational, rotational, and vibrational degrees of freedom for a single cluster, and not on making high-precision measurements of colloidal diffusion for rigid clusters, which is the focus of this chapter.

Recently we discovered that similar measurements have been made by Daniela Kraft and co-workers at NYU [123]. Our measurements and findings, which are in agreement with theirs, complement theirs. Kraft *et al.* have considered a wider range of clusters than we have using confocal microscopy, and in fact have measured translation-rotation coupling in clusters made out of spheres of different sizes [123]. As we shall discuss, our measurements have some advantages, in particular high precision.

5.2 Theory of Anisotropic Brownian Motion

We describe the derivation of certain essential results in the theory of anisotropic Brownian motion. Our discussion of Fick's Law and $\mathbf{D}$ will mostly follow Brenner [124]. We will next discuss the friction tensor following Brenner [124], Happel and Brenner [125], and Harvey and García de la Torre [126]. Finally, we will discuss the generalized Stokes-Einstein relation following Harvey [127]; see Brenner [124, 128] for another approach.

5.2.1 Generalized Fick's Law and the Diffusion Tensor **D**

We begin by considering a colloidal particle that is an arbitrary rigid body, neglecting (for example) any vibrational or soft modes that may exist in systems such as sphere clusters.

To fully describe the position and orientation of such a particle, we need six coordinates. These coordinates will consist of three spatial coordinates and three orientation angles. We will thus describe the particle via its position q^i in this six-dimensional space, where q^1, q^2, and q^3 will be position coordinates and q^4, q^5, and q^6 will be spatial coordinates[1]. While we could choose our generalized coordinates q^i in an arbitrary way, we will make our lives simple by choosing a particular representation: coordinates fixed to the particle. We will choose an origin O inside the particle and three orthogonal Cartesian axes fixed to this origin; call these axis vectors $\mathbf{u}_1$, $\mathbf{u}_2$, and $\mathbf{u}_3$. While these axes move in space as the particle undergoes Brownian motion, we can describe any finite displacement of the particle between instants t_1 and t_2 in terms of the components along $\mathbf{u}_i$ at t_1. Similarly, we can describe an infinitesimal Brownian rotation of the particle in terms of three rotations about the $\mathbf{u}_i$. Note that such rotations must be infinitesimal, as finite rotations do not commute (see, for instance, the discussions in Goldstein [129].) We will use these *body coordinates* as our generalized coordinates q^i.

We next consider an ensemble of N identical particles undergoing Brownian diffusion. We define a generalized particle current density J^i such that the flux integral

$$\int J^i \, d^6A \tag{5.1}$$

gives the number of particles crossing a generalized area of the six-dimensional space per unit time. We can also define a particle density $\sigma(q^i, t)$, such that

$$\int \sigma(q^i, t) \, d^6q^i \tag{5.2}$$

gives the number of particles in the volume d^6q^i. Obviously this must be N if the limits are extended to all of the 6-dimensional configuration space. With these concepts in hand,

[1] Throughout this Section we will restrict our conventional boldface vector notation $\mathbf{v}$ to quantities that are 3-dimensional vectors or pseudovectors.

we can now define the diffusion tensor $\mathbf{D}$, or in index notation D^{ij}, as a set of proportionality constants in a generalized Fick's law relating the current density J^i to the generalized gradient of σ:

$$J^i = -D^{ij}\frac{\partial \sigma}{\partial q^i} \tag{5.3}$$

where we have adopted the summation convention on repeated indices. We also postulate a continuity equation for the particle density σ:

$$\frac{\partial \sigma}{\partial t} + \frac{\partial J^i}{\partial q^i} = 0. \tag{5.4}$$

Here the second term is a generalization of the divergence. Combining Equations 5.3 and 5.4 leads us to the diffusion equation:

$$\frac{\partial \sigma}{\partial t} = D^{ij}\frac{\partial^2 \sigma}{\partial q^i \partial q^j}. \tag{5.5}$$

Either Equations 5.3 or 5.5 may be viewed as the definition of D^{ij}. It can be shown that D^{ij} is both symmetric and positive-definite; we refer the reader to Brenner [124] for the proofs.

This means of defining D^{ij}, while rigorous, does not lead to a straightforward physical intepretation or a way to experimentally measure D^{ij}. We now proceed to prove the following correlation relation for displacements in the generalized coordinates over a short time interval τ:

$$\langle \Delta q^i(\tau) \Delta q^j(\tau) \rangle = 2D^{ij}\tau. \tag{5.6}$$

As previously discussed, this will only apply over intervals τ short enough such that any angular diffusion of the particles is infinitesimally small. We will proceed following Brenner with an approach in the spirit of the Fokker-Planck equation [130].

We will consider a particle initially with coordinates q^i and consider the probability that due to Brownian motion over an interval τ, its coordinates will change by Δq^i. We will define a transition probability density $W(\Delta q^i; \tau)$ such that the probability that the coordinates q^i change by an amount between Δq^i and $\Delta q^i + d\Delta q^i$ is given by $W(\Delta q^i; \tau) d\Delta q^i$. By

conservation of probability density, we can evaluate the change in σ in terms of W:

$$\begin{aligned}\sigma(q^i; t+\tau) &= \int \sigma(q^i + \Delta q^i; t) W(-\Delta q^i, \tau)\, d\Delta q^i \\ &= \int \sigma(q^i + \Delta q^i; t) W(\Delta q^i, \tau)\, d\Delta q^i \end{aligned} \tag{5.7}$$

where the integrals run over 6 dimensions and the second line follows from Brownian steps in either direction being equally likely. We now Taylor expand both sides of this expression:

$$\begin{aligned}\sigma(q^i; t) + \frac{\partial \sigma}{\partial t}\tau + \ldots = \\ \int \left(\sigma(q^i; t) + \frac{\partial \sigma}{\partial q^i}\Delta q^i + \frac{1}{2}\frac{\partial^2 \sigma}{\partial q^i \partial q^j}\Delta q^i \Delta q^j + \ldots \right) W(\Delta q^i; \tau)\, d\Delta q^i.\end{aligned} \tag{5.8}$$

Because W is normalized, the first term on the RHS of Equation 5.8 is just $\sigma(q^i; t)$. In addition, as a probability density W allows the computation of ensemble averages:

$$\langle \Delta q^i \rangle = \int \Delta q^i W(\Delta q^i; \tau)\, d\Delta q^i. \tag{5.9}$$

Proceeding in like manner, we arrive at

$$\sigma + \frac{\partial \sigma}{\partial t}\tau = \sigma + \frac{\partial \sigma}{\partial q^i}\Delta q^i + \frac{1}{2}\frac{\partial^2 \sigma}{\partial q^i \partial q^j}\langle \Delta q^i \Delta q^j \rangle. \tag{5.10}$$

However, $\langle \Delta q^i \rangle = 0$. Therefore, after division by τ, we are left with

$$\frac{\partial \sigma}{\partial t} = \frac{1}{2}\frac{\langle \Delta q^i \Delta q^j \rangle}{\tau}\frac{\partial^2 \sigma}{\partial q^i \partial q^j}. \tag{5.11}$$

Comparison with the diffusion equation, Equation 5.5 immediately yields the desired result:

$$\langle \Delta q^i(\tau) \Delta q^j(\tau) \rangle = 2D^{ij}\tau. \tag{5.12}$$

Note that this derivation, based on Taylor expansions, and this result are only valid in the limit of short time intervals τ and small generalized displacements Δq^i. This result both

allows us to interpret **D** in terms of correlated displacements and allows us a means to measure **D**, as we will later discuss.

5.2.2 The Friction Tensor **R**

We now turn to the problem of the hydrodynamic drag forces and torques exerted on small particles moving slowly in fluids. For the benefit of the reader, we recall the full Navier-Stokes equation for a fluid of mass density ρ with an Eulerian velocity field $\mathbf{u}(\mathbf{r}, t)$, pressure field p, and viscosity η:

$$\rho\left(\frac{\partial \mathbf{u}}{\partial t} + \mathbf{u}\cdot\nabla\mathbf{u}\right) = -\nabla p + \eta\nabla^2\mathbf{u}. \tag{5.13}$$

The nonlinear terms in the Navier-Stokes equation make it impossible to solve exactly. A common scheme for solving it approximately is to consider the relative size of the inertial terms, on the LHS, with the viscous term proportional to η via the Reynolds number:

$$Re = \frac{\rho u L}{\eta} \tag{5.14}$$

where L is a typical length scale in the flow problem. For flow due to moving colloidal particles, Re is small, and that means the inertial terms can be neglected. We get the Stokes equation:

$$\nabla^2\mathbf{u} = \frac{1}{\eta}\nabla p. \tag{5.15}$$

Combined with the continuity equation for an incompressible fluid, $\nabla\cdot\mathbf{u} = 0$, these equations with suitable boundary conditions describe the fluid problem. Note that these equations are linear in the fluid velocity **u**.

What we need to calculate is the fluid forces and torques on a particle that is moving with linear velocity **v** and angular velocity $\boldsymbol{\omega}$. The reader is reminded of the Stokes drag force F and torque T on a sphere of radius a (see Happel and Brenner for details [125]):

$$F = -6\pi\eta a\, v;\ T = -8\pi\eta a^3\omega. \tag{5.16}$$

We will not prove it here, but the linearity of the Stokes equations essentially guarantees that the drag force and torque will be linear in $\mathbf{v}$ and $\boldsymbol{\omega}$ even for an arbitrary particle; once again, see Happel and Brenner [125] for the proof. The end result is that the following relations hold:

$$\mathbf{F} = -\mathbf{K} \cdot \mathbf{v} - \mathbf{C}^{tr} \cdot \boldsymbol{\omega} \tag{5.17}$$

$$\mathbf{T} = -\mathbf{C} \cdot \mathbf{v} - \boldsymbol{\Omega} \cdot \boldsymbol{\omega}. \tag{5.18}$$

Here, $\mathbf{K}$ is the translational resistance tensor, $\boldsymbol{\Omega}$ the rotational resistance tensor, and $\mathbf{C}$ the coupling tensor. These are all 3×3 tensors; they depend linearly on the fluid viscosity η and the particle geometries. All elements of the tensor will depend on the choice of coordinate basis, and $\boldsymbol{\Omega}$ and $\mathbf{C}$ are origin-dependent [125]. We can write these two equations in terms of one big matrix:

$$\begin{pmatrix} \mathbf{F} \\ \mathbf{T} \end{pmatrix} = - \begin{pmatrix} \mathbf{K} & \mathbf{C}^{tr} \\ \mathbf{C} & \boldsymbol{\Omega} \end{pmatrix} \begin{pmatrix} \mathbf{v} \\ \boldsymbol{\omega}. \end{pmatrix} \tag{5.19}$$

We will refer to

$$\begin{pmatrix} \mathbf{K} & \mathbf{C}^{tr} \\ \mathbf{C} & \boldsymbol{\Omega} \end{pmatrix} \tag{5.20}$$

as the resistance tensor $\mathbf{R}$. Some other authors call this the friction tensor instead.

5.2.3 The Generalized Stokes-Einstein Relation

We now derive a generalization of the Stokes-Einstein relation that will connect the diffusion tensor $\mathbf{D}$ and the resistance tensor $\mathbf{R}$.

In the derivation of the conventional Stokes-Einstein relation for a sphere, some dynamical information is needed. In particular, it is necessary to account for both the frictional Stokes forces due to fluid viscosity that damp out the motion of a diffusing particle, as well as the random fluctuating forces a particle experiences due to molecular kicks from the fluid. One way of doing this is by writing Newton's second law with a fluctuating force; this is called the Langevin equation [130]. This approach is somewhat cumbersome to apply for the case of arbitrary particles we need to consider here. We will follow an approach

due to Harvey [127] that is rooted in Lagrangian dynamics. We will model the random thermal kicks by assuming that at intervals Δt, the diffusing particle gets a random initial generalized velocity: $u^i(0) = \dot{q}^i(0)$. The Lagrangian will allow us to compute how this initial kick decays based on **R**. Then, we will calculate the average kinetic energy of the particle and relate that result to **D**. Finally, we will use the equipartition theorem to bring in $k_B T$ and tie everything together.

We begin with a brief foray into an aspect of Lagrangian dynamics that was unfamiliar to the author. We here follow Goldstein's treatment [129]. The reader is probably familiar with the concept of the Lagrangian L of a system:

$$L = K - U \tag{5.21}$$

where K is the kinetic energy and U is the potential energy. One expresses L in terms of generalized coordinates q^i and their time derivatives, and equations of motion follow from Lagrange's equation:

$$\frac{d}{dt}\left(\frac{\partial L}{\partial \dot{q}^i}\right) - \frac{\partial L}{\partial q^i} = 0. \tag{5.22}$$

In the usual applications of the Lagrangian approach to dynamics (central force motion, free particles in quantum mechanics, or the sorts of diabolical inventions one finds in mechanics textbooks involving things like blocks with attached springy pendula sliding down inclined planes), the systems involved are frictionless or otherwise have no dissipative forces. Mechanical energy is conserved. It turns out, however, that if there are dissipative forces that are linear in the generalized velocities, it is possible to adopt the Lagrangian approach. One defines a Rayleigh dissipation function [129]

$$\mathcal{F} = \frac{1}{2} R_{ij} u^i u^j \tag{5.23}$$

where u_i is the 6-dimensional generalized velocity and R_{ij} is the resistance tensor. Then, Lagrange's equations become

$$\frac{d}{dt}\left(\frac{\partial L}{\partial \dot{q}^i}\right) - \frac{\partial L}{\partial q^i} = -\frac{\partial \mathcal{F}}{\partial \dot{q}^i}. \tag{5.24}$$

We will begin using this approach by computing the Lagrangian of an arbitrary particle in a fluid. We will neglect gravitation (or assume that the particle is density-matched) and also assume that there are no external forces (like an electric field) that give rise to a potential energy. So L consists only of the kinetic term, K. This term can be written

$$K = \frac{1}{2} M_{ij} u^i u^j \tag{5.25}$$

where M_{ij} is a 6×6 symmetric matrix with dimensions of mass whose elements depend on the particle geometry [129]. We will not prove its existence or give a recipe for its calculation here. Substitution into the relevant form of Lagrange's equations (Equation 5.24) yields

$$\frac{1}{2} M_{ij} \dot{u}^j = -\frac{1}{2} R_{ij} u^j \tag{5.26}$$

where the dot denotes a time derivative. This gives a system of six first-order equations of motion for u^i, which have an exponential solution:

$$u^i(t) = \exp\left(-M_{ij}^{-1} R_{jk} t\right) u^k(0). \tag{5.27}$$

If we wish to know the generalized displacement Δq^i that occurs during the time step Δt, we can integrate our solution for $u^i(t)$. Here we make an additional assumption: we assume the damping forces are large enough that the particle essentially comes to rest prior to the end of the time step. (We will make a *post hoc* check of this assumption at the end of the derivation.) If so, then we can extend the limit of integration to ∞:

$$\Delta q^i = \int_0^{\Delta t} u^i(t)\, dt \tag{5.28}$$

$$\approx \int_0^{\infty} \exp\left(-M_{ij}^{-1} R_{jk} t\right) u^k(0) \tag{5.29}$$

$$= R_{ij}^{-1} M_{jk} u^k(0). \tag{5.30}$$

Now we compute the average kinetic energy during one time step Δt. Using Equations

5.25 and 5.27,

$$\overline{K} = \frac{1}{\Delta t}\int_0^{\Delta t} K(t)\,dt = \frac{1}{2\Delta t}\int_0^{\Delta t} \exp(-M_{ij}^{-1}R_{jk}t)u^k(0)M_{i\ell}\exp(-M_{\ell m}^{-1}R_{mn}t)u^n(0). \tag{5.31}$$

The matrix elements in this expression can be rearranged because M_{ij} and R_{ij} are symmetric tensors[2]. After much algebra and rearranging of indices,

$$\overline{K} = \frac{1}{2\Delta t}\int_0^{\Delta t} u^k(0)M_{kl}\exp\left(-2M_{\ell m}^{-1}R_{mn}t\right)u^n(0). \tag{5.32}$$

We will once again extend the upper limit of integration to infinity, from which we obtain[3]

$$\overline{K} = \frac{1}{4\Delta t}u^k(0)M_{k\ell}R_{\ell m}^{-1}M_{mn}u^n(0). \tag{5.33}$$

Using Equation 5.30,

$$4\overline{K}\Delta t = u^k(0)M_{k\ell}\Delta q^\ell \tag{5.34}$$

$$= \Delta q^k R_{k\ell}\Delta q^\ell \tag{5.35}$$

where we have inserted the identity tensor. This object should be thought of as the matrix product of a six-element row vector q^k, the matrix $R_{k\ell}$, and the column vector q^ℓ. But exploiting the symmetry of the resistance tensor, we can rearrange this in terms of the tensor $(\Delta q\Delta q)_{kl}$, the outer product of Δq^k and Δq^ℓ:

$$4\overline{K}\Delta t = R_{\ell k}(\Delta q\Delta q)_{kl}. \tag{5.36}$$

We now perform an average over many time steps Δt in the trajectory. This allows us to invoke equipartition: each of the 6 quadratic terms in the kinetic energy, corresponding to a degree of freedom, has a value of $\frac{1}{2}k_BT$. Ensemble-averaging $(\Delta q\Delta q)_{kl}$ also enables us to write this displacement-correlation tensor in terms of the diffusion tensor $\mathbf{D}$ for a temporal

[2]Working this out is rather tedious; the key is to Taylor-expand the matrix exponential and to work with each piece in the expansion.

[3]Again, this may be proved by a Taylor expansion of the matrix exponential.

displacement Δt (Equation 5.6):

$$4 \cdot 3k_B T \Delta t = 2R_{\ell k} D_{k\ell} \Delta t. \tag{5.37}$$

The right hand side is a trace; we have

$$6k_B T = \mathrm{Tr}\left(\mathbf{RD}\right). \tag{5.38}$$

To move forward we must make several other assumptions. First, as symmetric tensors, both $\mathbf{R}$ and $\mathbf{D}$ are diagonalizable by the spectral theorem of linear algebra[4]. On physical grounds, we assert that the basis that diagonalizes $\mathbf{R}$ will also diagonalize $\mathbf{D}$; thus in this basis, $\mathbf{RD}$ is diagonal. Asserting that by equipartition, thermal energy is equally shared among all elements of this eigenbasis and also noting that these are 6-dimensional tensors allows us to assert that $\mathbf{RD} = k_B T \mathbf{I}$. Hence, the generalized Stokes-Einstein relation

$$\mathbf{D} = k_B T \mathbf{R}^{-1} \tag{5.39}$$

follows.

This admittedly rather sketchy derivation hinges on the ability to choose a time step Δt satisfying two conditions:

1. Δt must be large enough that the particle generalized velocity from an initial thermal kick is completely damped out. In multiple places we extended time integrals to infinity, which would be incorrect if this did not hold.

2. Δt must be short enough that displacements are small enough so that it is valid to relate correlations in the generalized displacements to $\mathbf{D}$.

We can do an order-of-magnitude check of these conditions for a diffusing colloidal sphere. For a sphere of radius a and mass m undergoing one-dimensional translation in

[4]This discussion does not imply that translation-rotation coupling or the coupling tensor $\mathbf{C}$ always vanish. See the discussion of the screw-propeller in Chapter 5 of Happel & Brenner. We may choose principal axes that diagonalize $\mathbf{K}$, $\mathbf{\Omega}$, and $\mathbf{C}$ individually, but then $\mathbf{R}$ will not be diagonal. The eigenbasis for $\mathbf{R}$ will be a set of generalized displacements combining translation and rotation.

a fluid of viscosity η, the equation of motion following an initial velocity $v(0)$ is

$$v(t) = v(0) \exp\left(-\frac{6\pi\eta a}{m} t\right). \tag{5.40}$$

We can thus define a damping timescale $\tau_{\text{damp}} \equiv m/6\pi\eta a$. We want τ_{damp} to be much smaller than the time τ_{trans} for a particle to translate a small fraction of its radius, say $0.01a$. Since Stokes-Einstein gives $\langle \Delta x^2 \rangle = 10^{-4} a^2 = 2D\tau_{\text{trans}}$, we have

$$\tau_{\text{trans}} = 10^{-4} a^2 \frac{6\pi\eta a}{2k_B T}. \tag{5.41}$$

Balancing these timescales, we find

$$\frac{\tau_{\text{trans}}}{\tau_{\text{damp}}} = 10^{-4} \frac{27}{2} \pi \frac{a\eta^2}{k_B T \rho} \tag{5.42}$$

where ρ is the particle mass density. Inserting typical values for a polystyrene sphere with radius $a = 1\ \mu$m gives $\tau_{\text{trans}}/\tau_{\text{damp}} \approx 100$, so our conditions are satisfied.

5.3 Symmetries and Their Consequences

We now turn to a discussion of the effects of symmetry on the tensors $\mathbf{D}$ and $\mathbf{R}$. In light of the generalized Stokes-Einstein relation, we will restrict ourselves to a discussion of $\mathbf{R}$, since the properties of $\mathbf{D}$ will follow from it. Our discussion in general follows that in Happel and Brenner [125]. We will outline the approach and then describe its application to spheres, dimers, and trimers.

Happel and Brenner's symmetry arguments consider what happens when the basis (principal axes in Cartesian space) that is used to describe $\mathbf{K}$, $\mathbf{\Omega}$, and $\mathbf{C}$ changes. If the particle has a symmetry such that it looks geometrically identical under a change of basis, then the change of basis must leave $\mathbf{K}$, $\mathbf{\Omega}$, and $\mathbf{C}$ unchanged. Let $\mathbf{A}$ denote the change-of-basis matrix whose columns are the new basis vectors expressed in the old basis. Then, a general matrix $\mathbf{M}$ may be expressed in the new basis as $\mathbf{M}' = \mathbf{AMA}^{-1}$. The translation tensor $\mathbf{K}$ and the rotation tensor $\mathbf{\Omega}$ transform in exactly this way; the coupling tensor is a pseudotensor

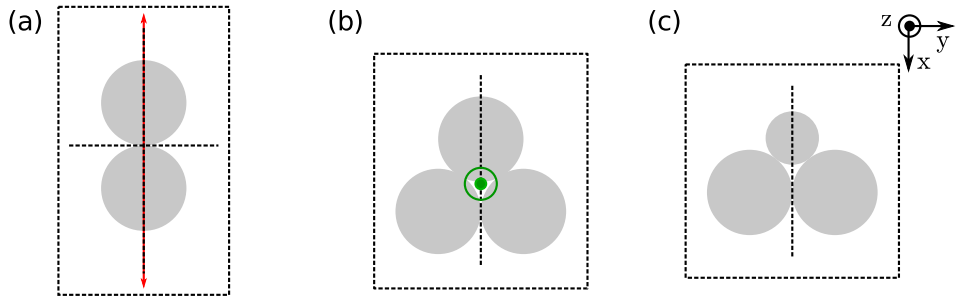

Figure 5.3.1: Symmetries of colloidal clusters. (a): A dimer of identical spheres contains three perpendicular planes of reflection symmetry (dashed lines, and the plane of the figure), as well as an axis of continuous rotational symmetry (red line). (b) A trimer of identical spheres has two planes of reflection symmetry and a threefold rotational symmetry axis (green). (c) A trimer with one sphere of a different size has only two planes of reflection symmetry. Inset shows orientation of axes.

and so it transforms with a factor of the determinant:

$$\mathbf{C}' = \det(\mathbf{A})\mathbf{A}\mathbf{C}\mathbf{A}^{-1}. \tag{5.43}$$

One of the simplest basis transformations is inversion about the z axis, for which the change-of-basis matrix is

$$\mathbf{A} = \begin{pmatrix} 1 & 0 & 0 \\ 0 & 1 & 0 \\ 0 & 0 & -1 \end{pmatrix} \tag{5.44}$$

This matrix allows us to see how the submatrices of $\mathbf{R}$ are constrained for a particle with reflection symmetry across the xy plane.

The simplest colloidal particle, a sphere, can be treated this way, although this machinery is not strictly necessary. It suffices to note that a sphere looks identical along any set of orthogonal axes centered at the sphere center. It can then be shown that $\mathbf{C} = 0$, and that $\mathbf{K} = K\mathbf{I}$ and $\boldsymbol{\Omega} = \Omega\mathbf{I}$, where $\mathbf{I}$ is the 3×3 identity.

We next consider a dimer of two identical spheres. A dimer of two identical spheres has three perpendicular planes of symmetry, as illustrated in Figure 5.3.1(a). It also has an axis of continuous rotational symmetry. As a consequence, the sub-matrices of $\mathbf{R}$ have the

following form [125]:

$$\mathbf{K} = \begin{pmatrix} K_{\parallel} & 0 & 0 \\ 0 & K_{\perp} & 0 \\ 0 & 0 & K_{\perp} \end{pmatrix} ; \ \mathbf{\Omega} = \begin{pmatrix} \Omega_{\parallel} & 0 & 0 \\ 0 & \Omega_{\perp} & 0 \\ 0 & 0 & \Omega_{\perp} \end{pmatrix} \tag{5.45}$$

and $\mathbf{C} = 0$ (if computed about the center of reaction.)

Trimers of three identical spheres have two orthogonal symmetry planes as well as a threefold symmetry axis (Figure 5.3.1(b)). Happel & Brenner treat the case of two orthogonal symmetry planes; these symmetries force $\mathbf{K}$ and $\mathbf{\Omega}$ to be diagonal

$$\mathbf{K} = \begin{pmatrix} K_1 & 0 & 0 \\ 0 & K_2 & 0 \\ 0 & 0 & K_3 \end{pmatrix} ; \ \mathbf{\Omega} = \begin{pmatrix} \Omega_1 & 0 & 0 \\ 0 & \Omega_2 & 0 \\ 0 & 0 & \Omega_3 \end{pmatrix} \tag{5.46}$$

and most of $\mathbf{C}$ to be zero

$$\mathbf{C} = \begin{pmatrix} 0 & 0 & 0 \\ 0 & 0 & C_{23} \\ 0 & C_{32} & 0 \end{pmatrix} . \tag{5.47}$$

Happel & Brenner do not treat the case of a discrete symmetry axis, and so we work it out here both for completeness and to illustrate the general approach. We will first work out the change-of-basis matrix for an arbitrary rotation by an angle θ about the z axis; we will require $\mathbf{K}$, $\mathbf{\Omega}$, and $\mathbf{C}$ to be invariant under rotations of $\theta = \frac{2\pi}{3}$ and $\frac{4\pi}{3}$. The matrix $\mathbf{A}$ is given by

$$\mathbf{A} = \begin{pmatrix} \cos\theta & \sin\theta & 0 \\ -\sin\theta & \cos\theta & 0 \\ 0 & 0 & 1 \end{pmatrix} \tag{5.48}$$

and its inverse by

$$\mathbf{A}^{-1} = \begin{pmatrix} \cos\theta & -\sin\theta & 0 \\ \sin\theta & \cos\theta & 0 \\ 0 & 0 & 1 \end{pmatrix} . \tag{5.49}$$

We now compute $\mathbf{K}' = \mathbf{AKA}^{-1}$ with $\mathbf{K}$ from Equation 5.46:

$$\mathbf{K}' = \begin{pmatrix} K_1 \cos^2\theta + K_2 \sin^2\theta & -K_1 \sin\theta\cos\theta + K_2 \sin\theta\cos\theta & 0 \\ -K_1 \sin\theta\cos\theta + K_2 \sin\theta\cos\theta & K_1 \sin^2\theta + K_2 \cos^2\theta & 0 \\ 0 & 0 & K_3 \end{pmatrix}. \tag{5.50}$$

For this to be identical to Equation 5.46, we must have

$$(-K_1 + K_2)\sin\theta\cos\theta = 0. \tag{5.51}$$

Since $\sin\theta\cos\theta$ is nonzero for $\theta = \frac{2\pi}{3}$ and $\frac{4\pi}{3}$, it follows that $K_1 = K_2$. The same argument gives $\Omega_1 = \Omega_2$. Turning our attention to $\mathbf{C}'$, we find from Equation 5.47,

$$\mathbf{C}' = \begin{pmatrix} 0 & 0 & C_{23}\sin\theta \\ 0 & 0 & C_{23}\cos\theta \\ C_{32}\sin\theta & C_{32}\cos\theta & 0 \end{pmatrix}. \tag{5.52}$$

It follows that C_{23} and C_{32} are both 0, and hence $\mathbf{C}$ vanishes entirely.

As we will subsequently discuss, we will also examine the possibility of weak symmetry breaking due to particle polydispersity for the case of a trimer. The simplest way to model polydispersity is to have two spheres of the same size and one of a different size, as shown in Figure 5.3.1(c). In this case we have only the two planes of reflection symmetry, and Equations 5.46 and 5.47 apply. Note that the tensor components corresponding to motion along the x and y axes are now different, which gives us a way to search for this symmetry breaking. Having all three particles of different sizes would result in there being a single plane of reflection symmetry, and there would be off-diagonal elements in $\mathbf{K}$ and $\mathbf{\Omega}$. These would be quite challenging to measure, however, as would the coupling terms that would also become nonzero. Finally, we note that the axisymmetry of a dimer makes detecting particle size differences from measurements of $\mathbf{D}$ or $\mathbf{R}$ impossible.

5.4 Theoretical Predictions of **D** and **R**

Computing the resistance tensor is in general a difficult task. Analytical solutions are generally possible only in cases where a suitable curvilinear coordinate system exists in which the Stokes equation (Equation 5.15) can be solved by separation of variables. The canonical example here is the sphere (see Happel and Brenner [125] or any standard text on fluid dynamics for details.) Perrin computed the frictional forces on an ellipsoid [115], and Nir and Acrivos found a solution for two touching spheres, which need not be the same size [116]. We rely heavily on the Nir and Acrivos solution to assess our dimer data, and so we quote the results here. Nir and Acrivos found for the drag torque for a rotation perpendicular to the dimer long axis,

$$T = -29.92\pi\eta a^3. \tag{5.53}$$

For translational drag along the axis,

$$F_{\parallel} = -7.740\pi\eta a \tag{5.54}$$

and perpendicular to the axis

$$F_{\perp} = -8.691\pi\eta a. \tag{5.55}$$

The constants have been numerically computed via quadrature of complicated integrals of Bessel functions [116]. Aside from these geometries, however, numerical methods are generally necessary. Finite-element methods are in principle capable of great generality [131–133], but they can be time-consuming and inherently approximate.

Rather than explicitly solving the Stokes equations for some arbitrary geometry, it might occur to the reader that it might be possible to build up an arbitrary particle from subunits made of particles for which the Stokes equations can be solved. This intuition would be correct, particularly for the sphere clusters we are interested in. We use a version of this idea known as shell modeling, in which particles composed of spherical or ellipsoidal subunits are represented by shells composed of small spherical beads. An example of a shell representation is given in Figure 5.4.1. Of course, the Stokes forces on each of the beads will not solely be given by the Stokes drag $6\pi\eta a$, but rather will also include hydrodynamic

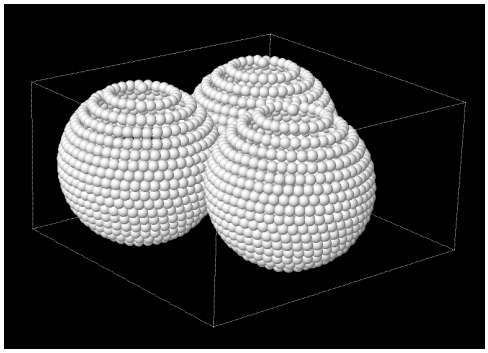

Figure 5.4.1: Shell model generated by HYDROSUB [134] for the computation of the resistance tensor of a trimer of three identical spheres each with a diameter of 1.3 μm. The model consists of 2000 beads; note the inherent roughness of the bead representation, particularly near the poles of the colloidal spheres. Rendering produced by FirstGlance in Jmol (http://firstglance.jmol.org).

interactions, whereby the flow field around any given subunit, will be affected by the flow fields caused by all other subunits.

Shell models are necessary because the approximations required to treat the hydrodynamic interactions between spherical subunits assume that the subunit radius is much smaller than the inter-subunit separations. Consider just the case of two spheres separated by a distance $\mathbf{R}$. The force on sphere 1, $\mathbf{F}_1$, in the Stokes approximation will depend on both the velocity of sphere 1, $\mathbf{v}_1$, as well as the velocity of sphere 2 $\mathbf{v}_2$:

$$\mathbf{F}_1 = -6\pi\eta a\mathbf{v}_1 - \mathbf{T}^{-1}\mathbf{v}_2. \tag{5.56}$$

Here $\mathbf{T}$ is a 3×3 hydrodynamic interaction tensor. The simplest approximation for $\mathbf{T}$, which considers the particles to be points, is the Oseen tensor [135]:

$$\mathbf{T} = \frac{1}{8\pi\eta|\mathbf{R}|}\left(\mathbf{I} + \frac{\mathbf{RR}}{|\mathbf{R}|^2}\right) \tag{5.57}$$

where the second term contains an outer product in the numerator. There are corrections to the Oseen tensor due to Rotne and Prager of order $a^2/|\mathbf{R}|^3$ [135–137], but the point remains that the subunit size needs to be small compared to the separation. Hence shell

modeling is necessary, and representing each sphere in a cluster as a single bead is inappropriate.

We perform the shell modeling hydrodynamic simulations using in this thesis using the code HYDROSUB [134]. The accuracy of these simulations is approximately 1% from prior studies comparing the shell models to systems such as spheres and ellipsoids where there are analytical solutions for $\mathbf{R}$ [137, 138].

5.5 Measuring $\mathbf{D}$

We now turn our attention to measuring the elements of the diffusion tensor $\mathbf{D}$. Much as we partitioned $\mathbf{R}$ into blocks describing translational, rotational, and coupling forces, due to the generalized Stokes-Einstein relation $\mathbf{D}$ can be partitioned in a similar way:

$$\mathbf{D} = \begin{pmatrix} \mathbf{D}^{tt} & \mathbf{D}^{\dagger tr} \\ \mathbf{D}^{tr} & \mathbf{D}^{rr} \end{pmatrix}. \tag{5.58}$$

$\mathbf{D}^{tt}$ describes translational diffusion, $\mathbf{D}^{rr}$ rotational diffusion, and $\mathbf{D}^{tr}$ translation-rotation coupling [5].

Conceptually, the $\mathbf{D}^{tt}$ translation block is the easiest to measure; we can simply apply the displacement correlation tensor (Equation 5.6). In particular, to measure a diagonal element D_i of $\mathbf{D}^{tt}$, we can calculate a cluster-frame mean-squared displacement:

$$\langle \Delta x_i^2(\tau) \rangle = 2 D_i \tau. \tag{5.59}$$

Here we use Δx_i to denote a cluster-frame displacement (as opposed to q^i, a generalized displacement that could be either a translation or a rotation.) From DHM, we obtain for each of the two holograms from which we calculate a displacement a set of orientational Euler angles and a center-of-mass position. The lab-frame cluster axis vectors $\mathbf{u}_i$ based on

[5] There are some subtle differences between $\mathbf{D}$ and $\mathbf{R}$ that we have ignored, having to do with origins. One naturally describes $\mathbf{R}$ using an origin at the center of reaction, where the coupling tensor $\mathbf{C}$ is symmetric, since $\mathbf{C}$ and $\boldsymbol{\Omega}$ are origin-dependent. The diffusion tensor $\mathbf{D}$ is naturally described at the center of diffusion, where $\mathbf{D}^{tr}$ is symmetric. These are not necessarily the same point; see [126] for details. Also, as discussed by Harvey, in $\mathbf{D}$ it is the $\mathbf{D}^{rr}$ block that is independent of origin [126].

the orientation in the first frame are calculated. Then we calculate the laboratory-frame displacement $\Delta\mathbf{x}_{\text{lab}}$ and obtain the cluster-frame displacements Δx_i by resolving $\Delta\mathbf{x}_{\text{lab}}$ into components parallel to the cluster axis vectors[6].

Measuring the diagonal elements of the rotational block requires some additional theoretical development, since Equation 5.6 only applies for short lag times and small angular displacements (the notion of a finite vector angular displacement is ill-defined, since finite rotations do not commute [129].) It turns out that we can characterize the diagonal elements of $\mathbf{D}^{rr}$, $D_{r,i}$, by calculating autocorrelations of the cluster axis vectors $\mathbf{u}_i$ as they diffuse in the laboratory frame [139]:

$$\langle \mathbf{u}_i(t) \cdot \mathbf{u}_i(t+\tau) \rangle = \exp\left[\left(D_{r,i} - \sum_j D_{r,j} \right) \tau \right]. \tag{5.60}$$

This was first worked out using operator techniques by Favro [139]; it is also possible but tedious to work this out using tensor techniques [124]. We will indicate where this comes from, as well as show how this reduces to an axis mean-squared displacement (as in Equation 5.6) via a primarily physical argument. We will (neglecting translation-rotation coupling) derive a distribution function for rotational diffusion and then show how Equation 5.60 follows from it; this distribution will also turn out to be critical for assessing our experimental data.

We first consider what happens for isotropic rotational diffusion, such as that for a sphere, and then generalize. This rotational diffusion will be characterized by a single rotational diffusion constant, D_r. Let us consider an imaginary ensemble of identical particles undergoing rotational diffusion, and observe the motion of one body axis $\mathbf{u}_i$. Suppose also that we prepare the ensemble such that at $t = 0$, $\mathbf{u}_i$ lies at the same point on the unit sphere for every particle; choose this to be at $\theta = 0$ in polar coordinates without loss of generality.

[6] One might reasonably ask whether it matters that we choose the orientation from the first frame. We could just as easily choose the orientation from the last frame, or even try to interpolate in the middle. We have found that choosing either the first or the last frame makes no difference.

We seek to compute the probability distribution $f_i(\theta, \varphi;\ \tau)$ such that[7]

$$\int_{\varphi_0}^{\varphi_1} \int_{\theta_0}^{\theta_1} f_i(\theta, \varphi;\ \tau)\ \sin\theta d\theta d\varphi \tag{5.61}$$

gives the probability of finding $\mathbf{u}_i$ between φ_0 and φ_1 and between θ_0 and θ_1 at $t = \tau$. We write down the rotational version of the diffusion equation (which we could obtain from Equation 5.5) [135]:

$$\frac{\partial f_i}{\partial t} = D_r \nabla^2 f_i. \tag{5.62}$$

This must be solved with the initial condition

$$f_i(\theta, \varphi; 0) = \frac{\delta(\theta)}{2\pi \sin\theta}, \tag{5.63}$$

where $\delta(\theta)$ denotes the Dirac delta function. Upon separating variables and noting that the spherical harmonics Y_ℓ^m are eigenfunctions of the Laplacian, we obtain

$$f_i(\theta; \tau) = \sum_{\ell=0}^{\infty} Y_\ell^0(0) Y_\ell^0(\theta) \exp\left(-\ell(\ell+1) D_r \tau\right). \tag{5.64}$$

This is independent of φ due to the symmetric initial condition; the spherical harmonics with $m = 0$ are φ-independent.

We now argue that Equation 5.64 applies for the more general case of a tensorial $\mathbf{D}^{rr}$ with an effective diffusion constant:

$$D_{r,\text{eff}} = \frac{D_{r,j} + D_{r,k}}{2}, \tag{5.65}$$

the mean of the rotational diffusion constants (diagonal elements of $\mathbf{D}^{rr}$) about the two axes other than i. We will now consider preparing an ensemble of identical anisotropic particles such that at $t = 0$, axis $\mathbf{u}_i$ for all the particles points in the same direction. Clearly, the time evolution of f_i must be governed by $D_{r,j}$ and $D_{r,k}$. In our ensemble, prepared such that

[7] This probability density f_i would arise from the general probability density $\sigma(q^i)/N$ defined in Section 5.2.1 by integration over the spatial coordinates and over two of the angular coordinates.

all particles initially have $\mathbf{u}_i$ at $\theta = 0$, the particles will not all have the same orientation: $\mathbf{u}_j$ and $\mathbf{u}_k$ can lie anywhere on the equator of the unit sphere. Consequently, observing only the motion of $\mathbf{u}_i$, we will on average observe f_i evolving according to an effective rotational diffusion constant $D_{r,\text{eff}}$ where $D_{r,\text{eff}} = (D_{r,j} + D_{r,k})/2$.

To compute the expected axis autocorrelations, we note that $\mathbf{u}_i(t) \cdot \mathbf{u}_i(t+\tau) = \cos\theta$, where θ is the angle between the two vectors. Hence,

$$\langle \mathbf{u}_i(t) \cdot \mathbf{u}_i(t+\tau) \rangle = 2\pi \int_0^\pi \cos\theta f_i(\theta;\tau) \sin\theta \, d\theta. \tag{5.66}$$

This integral may be evaluated if we note that $P_1^0(\cos\theta) = \cos\theta$. Thus, only the $\ell = 1$ term in the expansion for f_i has support in the integral. Using the orthogonality relation

$$\int_0^\pi P_\ell(\cos\theta) P_{\ell'}(\cos\theta) \sin\theta \, d\theta = \frac{2}{2\ell+1}\delta_{\ell\ell'}, \tag{5.67}$$

we find

$$\langle \mathbf{u}_i(t) \cdot \mathbf{u}_i(t+\tau) \rangle = \exp(-2D_{r,\text{eff}}\tau). \tag{5.68}$$

Thus, by calculating axis autocorrelations from experimental data, we can extract the $D_{r,i}$. For dimers, we calculate a related quantity, the axis mean squared displacement:

$$\begin{aligned} \langle \Delta\mathbf{u}_i^2(\tau) \rangle &= \langle (\mathbf{u}_i(t+\tau) - \mathbf{u}_i(t))^2 \rangle \\ &= \langle \mathbf{u}_i^2(t+\tau) \rangle + \langle \mathbf{u}_i^2(t) \rangle - 2\langle \mathbf{u}_i(t) \cdot \mathbf{u}_i(t+\tau) \rangle \\ &= 2\left(1 - \exp(-2D_{r,\text{eff}}\tau)\right). \end{aligned} \tag{5.69}$$

Note that for short times where $D_{r,\text{eff}}\tau \ll 1$, this reduces to

$$\langle \Delta\mathbf{u}_i^2(\tau) \rangle = 4D_{r,\text{eff}}\tau \tag{5.70}$$

which can be compared to Equation 5.6. Here we get a factor of 4 instead of 2 since we are effectively combining two orthogonal angular displacements.

Finally, we note that in general our measurements of $\mathbf{D}^{rr}$ are more reliable than our measurements of $\mathbf{D}^{tt}$ the rotational measurements rely only on the orientation angles measured

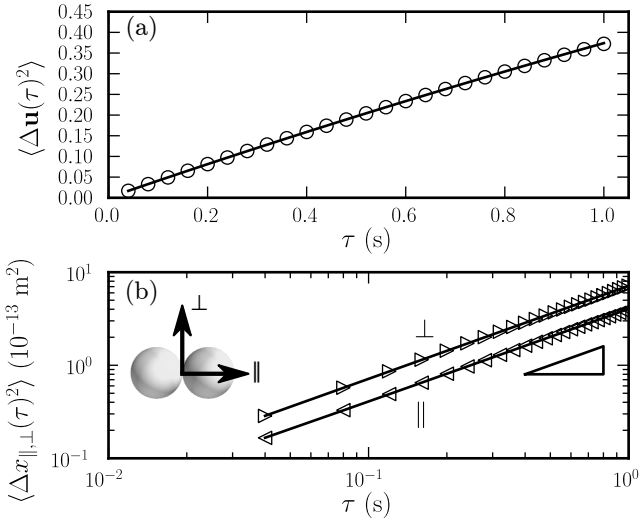

Figure 5.6.1: Rotational and translational correlation functions for a dimer of 1.3-μm polystyrene spheres. (a) Axis MSD $\langle \Delta \mathbf{u}^2(\tau) \rangle$. Open symbols are measurements; solid lines are a best fit to Equation. (b) Cluster-frame MSDs. Open symbols are measurements; solid lines are linear fits. Triangle shows slope of 1 and indicates diffusive behavior. Error bars are comparable in size to the plotting symbols or smaller. Inset: orientation of dimer parallel ($\parallel$) and perpendicular ($\perp$) axes.

via DHM. Measuring translation-rotation coupling, $\mathbf{D}^{tr}$, is a challenge we will briefly address at the end.

5.6 Dimers

We present experimental data from a dimer of 1.3-μm diameter polystyrene spheres. The clusters were produced using the arrested aggregation technique described in Chapter 3; suspensions were loaded into sample cells produced from 76 μm-thick Mylar spacers. We recorded 22,000 holograms at a frame rate of 25 frames per second, with an exposure time of 17.5 μs, and fit a model based on multisphere superposition that depended on a single particle index, the radius of each particle, the dimer center-of-mass position, two Euler angles, and the scaling parameter a_{sc}.

Figure 5.6.1 presents our data. We plot the axis mean-squared displacement of the dimer

Table 5.6.1: Measured diffusion tensor elements for dimer in Fig. 5.6.1, along with analytical calculations from an exact Stokes solution [116] and numerical calculations from HYDROSUB [134]. Calculations use a best-fit particle radius $a_{\text{eff}} = 709$ nm and solvent viscosity $\eta_{\text{eff}} = 1.159$ mPa s.

	Experiment	Exact	HYDROSUB
$D_{r,\perp}$ (s^{-1})	0.1034 ± 0.0006	0.1034	0.104
$D_{\parallel}$ ($\times 10^{-13}$ $m^2 s^{-1}$)	2.015 ± 0.012	2.010	2.02
$D_{\perp}$ ($\times 10^{-13}$ $m^2 s^{-1}$)	1.785 ± 0.007	1.790	1.80
$D_{\parallel}/D_{\perp}$	1.129 ± 0.011	1.123	1.12

axis, **u**, in Figure 5.6.1(a) (Equation 5.69). This depends on the rotational diffusion constants for rotations about the axes perpendicular to **u**, which we call D_r; axisymmetry makes it impossible to observe rotations about the long axis. Cluster-frame mean squared displacements are shown in Figure 5.6.1(b). As can be seen, the behavior is diffusive. In all cases, error bars (the computation of which is discussed in Appendix A) are smaller than or comparable to the plotting symbols.

We determine the elements of **D** reported in Table 5.6.1 by fitting the points in the correlation functions in Figure 5.6.1. For $\langle \Delta \mathbf{u}^2 \rangle$, we use Equation 5.69 with $D_{r,\text{eff}} = D_{r,\perp}$. The fit to a linear function of the cluster-frame translational diffusion perpendicular to the long axis requires some explanation; it has a slope of $4D_{\perp}$ since it combines motion along the two perpendicular axes. The experimental uncertainties in the measured elements of **D** come from a fit using the uncertainity in the correlation function points as weights. We measure all the elements of **D** to a precision of nearly 0.5%.

We can compare these measured diffusion tensors to both the predictions of the Nir & Acrivos solution [116] as well as to HYDROSUB computations. The ratio $D_{\parallel}/D_{\perp}$ is dimensionless, and it depends only on a geometrical factor:

$$D_{\parallel}/D_{\perp} = 1.123. \tag{5.71}$$

We find excellent agreement between our measured ratio and the predicted value. Comparing individual tensor elements is somewhat more challenging since they depend on

the sphere radius a, the solvent viscosity η, and the temperature $k_B T$. Fortunately, for dimers, with the Nir & Acrivos solution, we can find best-fit values. The ratios $D_{r,\perp}/D_{\parallel}$ and $D_{r,\perp}/D_{\perp}$ are both only dependent on a^2 and geometrical factors. From these ratios, we compute a best-fit value of $a_{\text{eff}} = 709$ nm. This is larger than the optical radius $a_{\text{opt}} = 650$ nm obtained from DHM. The larger effective radius is consistent with typical dynamic light scattering measurements of the size of colloidal spheres, which show enhanced hydrodynamic radii due to charge or hairy surface layers on the particles [140, 141].

5.6.1 Solvent Viscosities

Subsequent to determining a_{eff}, we determine the best-fit solvent viscosity. We find $\eta_{\text{eff}} = 1.159$ mPa s for a sample temperature assessed as follows.

In actuality, it is the ratio $k_B T/\eta$ that is relevant. Knowing $k_B T$ and η independently is not simple because the viscosity of our solvent, a density-matching mixture of water and deuterated water, turns out to have a strong temperature dependence. We assessed this by performing viscometry measurements using a Cannon-Manning capillary viscometer and a temperature-controlled bath[8]. These measurements are shown in Figure 5.6.2. It is clear the solvent viscosity can vary by nearly 20% over a 6°C temperature range. We have moreover observed that room temperature in the laboratory can change by several °C over the course of a few hours, most likely due to the cycling of the building heating and air conditioning systems. Moreover, particularly if the laboratory room temperature is changing, the temperature in the sample, sealed in a glass sample cell, may differ from that of the surrounding air.

Consequently, we believe that that the best way to estimate the solvent viscosity is to observe the *in situ* diffusion of single colloidal spheres, which are always present in the sample due to the arrested aggregation technique we use to make the clusters, either immediately before or immediately after imaging the diffusion of a cluster of interest. The Stokes-Einstein relation gives the translational diffusion constant D in terms of the tem-

[8] We immersed the entire viscometer in a large beaker of water, whose temperature was controlled by a Julabo HE-4 water bath. This water bath can only heat and cannot cool. To be able to stably access temperatures below the ambient room temperature, all viscometry measurements were performed in a cold room.

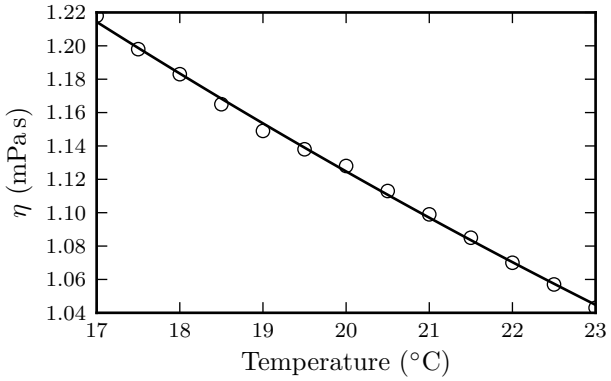

Figure 5.6.2: Temperature dependence of solvent viscosity. Data points, open symbols, were measured with a Cannon-Manning capillary viscometer. The solid line is a best-fit quadratic function that allows for interpolation between the measured points.

perature T, the particle radius a, and the solvent viscosity η:

$$D = \frac{k_B T}{6\pi\eta a}. \tag{5.72}$$

Using Eq. 5.72, once we determine D for a diffusing sphere of radius a, we can infer the ratio $k_B T/\eta$. Because of the strong temperature dependence illustrated in Figure 5.6.2, $k_B T$ and η should not be viewed as independent parameters. Moreover, from dimensional considerations, the elements of $\mathbf{D}$ are always proportional to $k_B T/\eta$. Once we determine $k_B T/\eta$, we use the best-fit line to the data in Figure 5.6.2 to infer η and $k_B T$ separately. While this is not the usual context in which microrheological experiments are performed, we essentially treat the diffusing single spheres as *in situ* thermometers.

We obtain D from an MSD computed from the 3D trajectory of a diffusing particle: $\langle \Delta\mathbf{r}^2(\tau)\rangle = 6D\tau$. In all cases, we obtain the trajectory using DHM and record holograms at 25 frames per second. We obtain a radius, index of refraction, and 3D position from each hologram by fitting a model based on the Lorenz-Mie solution [59].

For the dimer experiment, which used particles with a nominal radius of 650 nm, we measure $D = 2.533 \pm 0.017 \times 10^{-13}\ \mathrm{m^2 s^{-1}}$ for a diffusing particle with an optical radius of 639 nm. If we assume that the particle has the same enhanced hydrodynamic radius of 709 nm as we inferred from the dimer data, independent of any considerations of $k_B T$ or η, we

can subsequently use the data in Figure 5.6.2 to infer a solvent viscosity of 1.187 mPa s. This is within 3% of the best-fit solvent viscosity, 1.159 mPa s, inferred from the dimer diffusion constants and assuming the same temperature. The consistency of these values, along with the excellent agreement between the measured and predicted values of $D_{\parallel}/D_{\perp}$, which is independent of a and $k_B T/\eta$, validates our dimer measurements.

5.6.2 Comparison to HYDROSUB

We have determined best-fit parameters a_{eff} and η_{eff} and shown they are reasonable. As can be seen in Table 5.6.1, these values give rise to predictions that agree well with the measurements. We also compare the predictions of the exact Nir & Acrivos solution to HYDROSUB calculations. Note the small, $\sim$ 1% differences, particularly for $D_{r,\perp}$. We can conclude that our measurement accuracy is at least comparable to, if not better than, that of HYDROSUB.

5.7 Trimers

Because trimers are not axisymmetric, we can observe rotations about all three axes, and we can measure all the diagonal elements of $\mathbf{D}$. We prepared a trimer from 1 μm-diameter polystyrene spheres and observed its diffusion for 20,000 frames at 25 frames per second. We fit a model using one radius for all particles, one refractive index, the center-of-mass position, three Euler angles, and a_{sc}.

The model for the trimer holograms has an additional orientational degree of freedom compared to the model for the dimer holograms. We have noticed that on occasion the fitter converges to best-fit parameters that result in the best-fit model hologram having subtle differences when compared to the experimental hologram; this usually stems from the orientation angles being incorrect. We do not observe this problem for the dimer holograms. To detect holograms with potentially incorrect best-fit parameters, we inspect the R^2 statistic [142] of the fits. We also compute a χ^2 statistic for a binary version of the experimental and best-fit holograms, where all pixels above the mean of 1 are set to a value of 1 and all remaining pixels are set to a value of 0. The binary image is much more sensitive to the shape of the interference fringes.

When we compute correlation functions such as mean-squared displacements from the trimer holograms, we reject the contribution from any holograms where either R^2 or binary χ^2 is worse than 2 standard deviations from a rolling mean. Manual inspection of 200 randomly chosen trimer holograms that were not rejected under these criteria revealed 7 questionable fits. We infer from the Poisson distribution that, to a 99% confidence level, the percentage of remaining bad fits is less than 8%. We also reject the contribution from a given pair of holograms if the probability of obtaining either a center of mass displacement or angular displacement of the observed magnitude is less than 10^{-5}. We compute these probabilities using estimates for the diffusion tensor elements, and choose the threshold of 10^{-5} to avoid biasing the observed distribution and to make the cutoffs weakly sensitive to the estimates for $\mathbf{D}$.

Performing this cutoff procedure requires knowing the probability distributions governing translational and rotational displacements. The probability distribution for translational displacements is Gaussian, but the distribution function for rotational displacements is not, but is rather governed by Equation 5.64 with an effective rotational diffusion constant, $D_{r,\text{eff}}$. Recall that $D_{r,\text{eff}} = (D_{r,j} + D_{r,k})/2$, where $D_{r,j}$ and $D_{r,k}$ are the elements of $\mathbf{D}^{rr}$ describing rotations about the two cluster axes other than i.

After performing the cutoff procedures, we can compute axis autocorrelations and cluster-frame mean-squared displacements. In Fig. 5.7.1, we show the axis autocorrelations $\langle \mathbf{u}_i \cdot \mathbf{u}_i(t+\tau) \rangle$ computed from 20,000 holograms, as well as best fits to exponential decays. The autocorrelation of axis 3 decays more rapidly than the autocorrelations of axes 1 and 2, in agreement with expectations: as shown in Eq. 5.60, $\langle \mathbf{u}_3(t) \cdot \mathbf{u}_3(t+\tau) \rangle$ depends on $D_{r,1}$ and $D_{r,2}$, both of which should be larger than $D_{r,3}$ due to hydrodynamics. The elements of the diffusion tensor that we extract from this data are shown in Table 5.7.1. The difference between $D_{r,3}$ and both $D_{r,1}$ and $D_{r,2}$ is much larger than the experimental uncertainty, showing clear evidence for anisotropic rotational diffusion. The translational diffusion we observe is similarly anisotropic (Fig. 5.7.2 and Table 5.7.1).

Table 5.7.1 also shows comparisons between our measurements and HYDROSUB calculations, for which we once again need an effective particle size and viscosity. For the

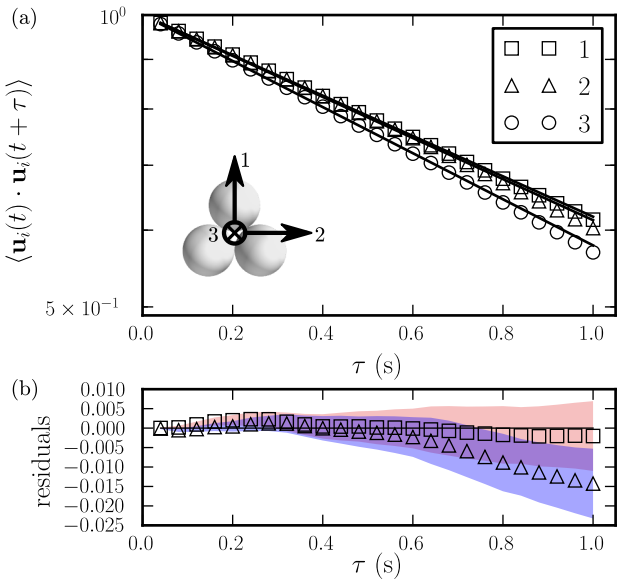

Figure 5.7.1: (a) Cluster axis autocorrelations $\langle \mathbf{u}_i(t) \cdot \mathbf{u}_i(t+\tau) \rangle$ for a trimer of 1-μm diameter spheres, showing anisotropic rotational diffusion. Open symbols are experimental measurements; error bars are comparable to or smaller than symbols. Solid lines are fits to exponential decays. Inset shows cluster axis orientation. (b) Residuals for fits of a single exponential decay to the in-plane axis autocorrelations ($i = 1$ and 2). Solid line indicates best fit exponential. Red (light) and blue (dark) shaded regions denote error bars.

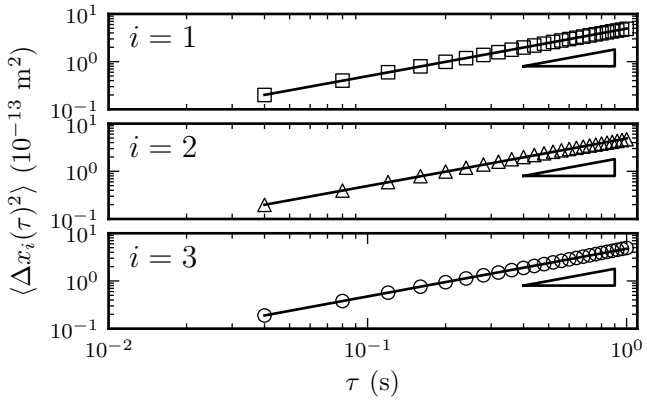

Figure 5.7.2: Body-frame MSDs for the same trimer in Fig. 5.7.1. See inset in Fig. 5.7.1 for axis orientations i. Open symbols are experimental measurements; error bars are comparable to or smaller than symbols. Solid lines are linear fits. Triangles show MSD slope of 1.

Table 5.7.1: Measured diffusion tensor elements for trimer shown in Figs. 5.7.1 and 5.7.2 with comparisons to computations from HYDROSUB [134]. Computations use $a = 500$ nm obtained optically from the best-fit hologram models and $\eta = 1.049$ mPa s from single-particle diffusion data; the difference in η from the dimer measurements is due to a difference in room temperature.

	Experiment	HYDROSUB
$D_{r,1}$ (s^{-1})	0.278 ± 0.002	0.296
$D_{r,2}$ (s^{-1})	0.270 ± 0.002	0.296
$D_{r,3}$ (s^{-1})	0.210 ± 0.002	0.220
$D_{r,1}/D_{r,3}$	1.32 ± 0.02	1.34
$D_{r,1}/D_{r,2}$	1.03 ± 0.02	1.00
$D_{t,1}$ ($\times 10^{-13}$ $m^2 s^{-1}$)	2.466 ± 0.015	2.64
$D_{t,2}$ ($\times 10^{-13}$ $m^2 s^{-1}$)	2.446 ± 0.015	2.64
$D_{t,3}$ ($\times 10^{-13}$ $m^2 s^{-1}$)	2.372 ± 0.015	2.41
$D_{t,1}/D_{t,3}$	1.04 ± 0.01	1.09

trimer experiment, we measured $D = 3.996 \pm 0.055 \times 10^{-13}$ $m^2 s^{-1}$ for a diffusing sphere of nominal radius 500 nm. With no analytical theory as we had for dimers, we cannot rigorously find a best-fit radius for the trimer. We take the optical radius of the particle, 517 nm, as an estimate of the particle size and use the data in Figure 5.6.2 to infer $\eta = 1.049$ mPa s, the value we use in the HYDROSUB calculations.

5.7.1 Verifying Fits

As a final verification that our holographic imaging is correct and that any remaining errors do not substantially affect the dynamics we measure, we compute probability distribution functions for the dynamical quantities we use to measure $\mathbf{D}$ from the data. Figure 5.7.3 shows a representative sample for several lag times τ. We first examine the cosine of the angle traversed by $\mathbf{u}_3$, or $\mathbf{u}_3(t) \cdot \mathbf{u}_3(t+\tau)$, in Figure 5.7.3(a). Aside from a noise floor, we find that the measured distributions agree well with the expected distribution computed from Eq. 5.64 and the measured values of $\mathbf{D}^{rr}$. We observe similarly good agreement for the distribution of particle-frame displacements along axis 3 shown in Figure 5.7.3(b).

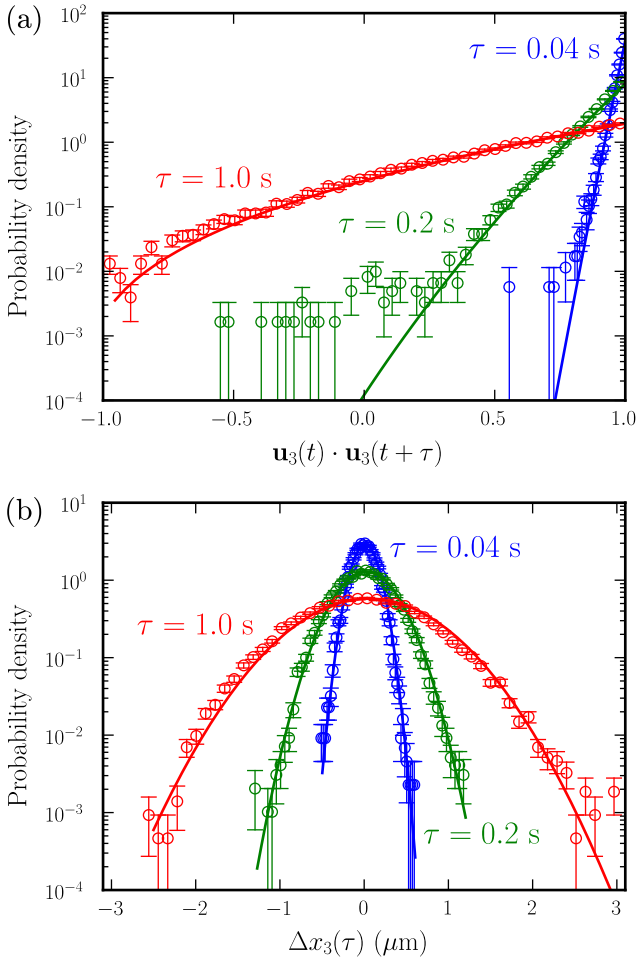

Figure 5.7.3: Distribution functions for trimer angular displacements and cluster-frame displacements. Histogram points computed from experimental data are shown in open symbols; solid lines show theoretical predictions computed from elements of $\mathbf{D}$ reported in Table II of the body of the paper. (a) Rotational dynamics of $\mathbf{u}_3$. Predicted distribution computed from Eq. 5.64. (b) Cluster-frame displacements along axis 3. Theoretical distribution is a Gaussian with a mean of 0 and a variance of $2D_{t,3}\tau$.

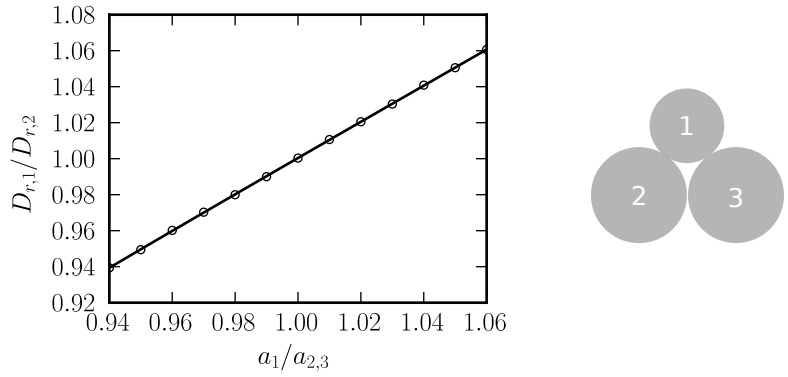

Figure 5.7.4: Simulations of asymmetry between in-plane diagonal elements of $\mathbf{D}^{rr}$ for a trimer where one particle is smaller than the other two. Simulations (open symbols) performed using HYDROSUB. The solid line is a fit to a cubic polynomial, allowing for interpolation. Inset shows labeling of the particles; spheres 2 and 3 have the same radius a.

5.7.2 Weak Symmetry Breaking

Interestingly, although our measurements of the dimensionless ratios $D_{r,1}/D_{r,3}$ and $D_{t,1}/D_{t,3}$ agree well with the HYDROSUB predictions, we observe small but statistically significant differences between the elements of $\mathbf{D}$ corresponding to the two in-plane axes 1 and 2. If the particles in the trimer are identical, the threefold symmetry axis of the trimer ensures that $D_{t,1} = D_{t,2}$ and $D_{r,1} = D_{r,2}$. Thus the differences between these elements of the tensor imply that the particles in our trimer are not in fact identical. We performed HYDROSUB calculations to confirm that weakly breaking threefold symmetry results in differences between the in-plane elements of $\mathbf{D}$. A plot of the results from these calculations is shown in Figure 5.7.4.

Our measured ratio $D_{r,1}/D_{r,2} = 1.03 \pm 0.02$ corresponds to a 3% size difference between the spheres. This is consistent both with the particle manufacturer's certificate of analysis as well as with particle size differences determined from fitting 105 holograms with all radii allowed to vary. This shows that the measurements are precise enough to detect the weak breaking of threefold rotational symmetry due to particle polydispersity.

5.8 Comparison to Confocal Microscopy

The precision with which we measure elements of **D** consequently increases with the number of observed displacements and hence with the length of the trajectories we observe. The rapid acquisition times of holographic microscopy give it an advantage over complementary 3D imaging techniques such as confocal microscopy in that a considerably larger number of 3D images can be acquired in the same amount of experimental time.

The main advantage of holographic microscopy over confocal microscopy, however, lies in the greater sensitivity of experiments using holographic microscopy to weakly anisotropic diffusion. In confocal experiments on diffusion, the acquisition time needed to scan through a 3D volume ($\sim$ 1 s or more) requires the dynamics to be slowed down through the use of larger particles and more viscous solvents. This results in the elements of **D** being much smaller. For example, tetrahedral sphere clusters used in confocal measurements of diffusion [121] have an isotropic rotational diffusion constant of $D_r \sim 5 \times 10^{-3}$ s^{-1}, nearly two orders of magnitude smaller than in our trimer experiment. Consequently, given the same amount of experimental time, confocal experiments access much shorter timescales relative to the rotational diffusion times than holographic experiments. This makes it more challenging to observe statistically significant anisotropy in **D**, as we now show.

Demonstrating anisotropic diffusion requires showing that the ratio of the rotational autocorrelation functions about axes i and j differs from 1 by a statistically significant amount. Eq. 3 of our manuscript gives this ratio in terms of the relevant elements of **D**:

$$\frac{\langle \mathbf{u}_i(t) \cdot \mathbf{u}_i(t+\tau) \rangle}{\langle \mathbf{u}_j(t) \cdot \mathbf{u}_j(t+\tau) \rangle} = \exp\left[-(D_{r,j} - D_{r,i})\tau\right] \tag{5.73}$$

$$\approx 1 - (D_{r,j} - D_{r,i})\tau + \ldots \tag{5.74}$$

where we have assumed in the second step that the anisotropy is small. The ratio differs from 1 in proportion to the *magnitude* of the difference in the rotational diffusion constants, rather than in proportion to the relative difference. Consider a confocal experiment and a holographic experiment on systems with the same relative anisotropy $D_{r,i}/D_{r,j}$, where both experiments measure the same number of independent displacements over the same time

interval τ. Both experiments will compute autocorrelations at τ with the same precision and will require similar amounts of experimental time. But for the confocal experiment, $(D_{r,j} - D_{r,i})\tau$ will be smaller, and may even be comparable to the measurement precision of the autocorrelations. Thus, because holographic microscopy can study more rapidly diffusing clusters, it is easier to observe weakly anisotropic diffusion, as we show in our measurement of the the 3% difference between $D_{r,1}$ and $D_{r,2}$ for the trimer.

5.9 Summary

We have studied the anisotropic diffusion of colloidal sphere dimers and trimers. Our measurements reveal how the diffusion tensor **D** evolves as symmetries get broken. Along with Kraft and co-workers at NYU, we have made one of the first measurements of anisotropic rotational diffusion. We have demonstrated that the technique we use, digital holographic microscopy, is capable of measuring elements of **D** to precisions of 1% or better, enough so that it is possible to detect weak symmetry breaking due to particle polydispersity. The high precision of these measurements is enabled by the short acquisition times of DHM, which in contrast to confocal measurements allow us to observe rapidly diffusing systems on time scales ranging from a fraction of a rotational diffusion time $1/D_{r,i}$ to hundreds.

Our measurements based on DHM also suggest how diffusion constants in environments relevant to self-assembly, such as near other particles or boundaries, can be measured with high precision.

6

Conclusions and Outlook

In this thesis we have measured dynamics of multiple colloidal spheres in 3D. We here describe some possible extensions of this work and some general concluding thoughts.

6.1 Future Work

We discussed nonspherical colloids at the beginning of this thesis. An obvious extension of the work would be to study the dynamics of other types of nonspherical particles, beside sphere clusters. In particular, an ongoing project involving stabilizing emulsions seeks to study the behavior of ellipsoidal particles on interfaces. Modeling holograms of these particles would be straightforward using EBCM codes such as that of Mishchenko *et al.* [87].

While the computational challenges are daunting, it is conceivable to use other types of scattering models, namely the DDA, to study particles that are not axisymmetric or uni-

form. We are currently engaged in studies of the dynamics of Janus spheres, partly coated with metal on one side, using DDA models and DHM.

There are possible extensions of the diffusion experiments. Recently Kraft and colleagues have measured translational-rotational coupling in asymmetric clusters made of spheres of different sizes and compositions [123]. We note that it is in principle possible to observe translation-rotation coupling in *chiral* clusters of identical spheres; the smallest such cluster has 7 spheres. Also, recent theoretical work by Moths and Witten has suggested how sedimenting anisotropic sphere clusters might achieve complete orientational alignment [143]. In cases like these, the fast time resolution and inherent precision of DHM with fits of scattering solutions might make it a useful experimental tool.

We are also interested in continuing studies of the self-assembly of colloidal spheres, particularly the nucleation and growth of clusters containing up to $\sim$20 particles. Fitting scattering models of clusters containing this many particles to experimental holograms will be a challenge, but one that should be achievable. We have successfully simulated holograms of 20-particle clusters undergoing a structural transition in which one particle rolls, and can successfully fit models to the holograms and detect this motion. Getting initial guesses will be the primary challenge here, but here using core-shell particles can help. In particular, we can coat $\sim$100 nm polystyrene cores with either PNIPAM or silica shells to build micron-sized composite particles and index-match the shells with an aqueous solvent. For particles that effectively scatter much more weakly, as these would, reconstruction should be much more useful than it is for particles made of strongly-scattering, homogeneous polystyrene spheres.

6.2 Limits on DHM

A natural question to ask as we consider possible future work that can be done with DHM is whether we will reach the limits of using DHM along with scattering solutions to study colloidal particles and clusters, particularly in terms of the number of particles (or, effectively, the number of degrees of freedom in the fit of a scattering solution.) There are two limiting factors: practical limits arising from computational challenges, and fundamental physical limits.

While the computational challenges of routinely fitting holograms of clusters of more than $\sim$10 spheres are real, they are surmountable largely because most of the required computations are embarassingly parallelizable. Any technique involving fitting a scattering solution to an experimental hologram requires one to compute the scattering solution for many values of the fit parameters (such as computing the Jacobian matrix in a least-squares algorithm.) Both the computation of single scattering solutions and the many computations needed for fitting can be parallelized. For scattering solutions that involve the expansion of the scattered field over some set of basis functions (such as the Mie solution or the multisphere superposition method), the computational tedium has generally come from having to calculate the basis functions and sum the series at many points on a hologram, rather than from computing the series expansion coefficients [1]. But the computations at each point are independent. Similarly, computations of the scattering solution for different parameter values are independent. While extensive parallelization efforts have not been undertaken, and have not yet been necessary, they would be in principle straightforward.

Moreover, significant speed-ups in fitting scattering solutions have recently come about by fitting to a random subset of the pixels in a hologram rather than to all of the pixels. For cases such as single colloidal spheres, we can get away with fitting as few as 1-2% of the pixels in a 256 $\times$ 256 hologram, thus obtaining a nearly 50-fold speed-up. A manuscript about this technique is currently in preparation.

The more pressing question, however, is whether there is a fundamental physical limit. Is there some maximal number of particles (or density of particles within a given volume) beyond which it will be impossible to either obtain initial guesses or fit scattering models? Clearly some limit exists – illuminating a macroscopic volume of a dense colloidal suspension would result in a speckle pattern from which it would not be possible to extract microscopic information. Recall the fundamental mathematical description of a hologram:

$$I = |\mathbf{E}_{\text{inc}}|^2 + 2\Re\{\mathbf{E}_{\text{inc}}^* \cdot \mathbf{E}_{\text{scat}}\} + |\mathbf{E}_{\text{scat}}|^2 . \tag{6.1}$$

Speckle fundamentally arises from the third term here: the speckle pattern arises from the

[1] Even in cases where this could potentially be problematic, such as for a multisphere superposition calculation for $\sim$ 100 particles, the computation of the expansion coefficients can be parallelized [144].

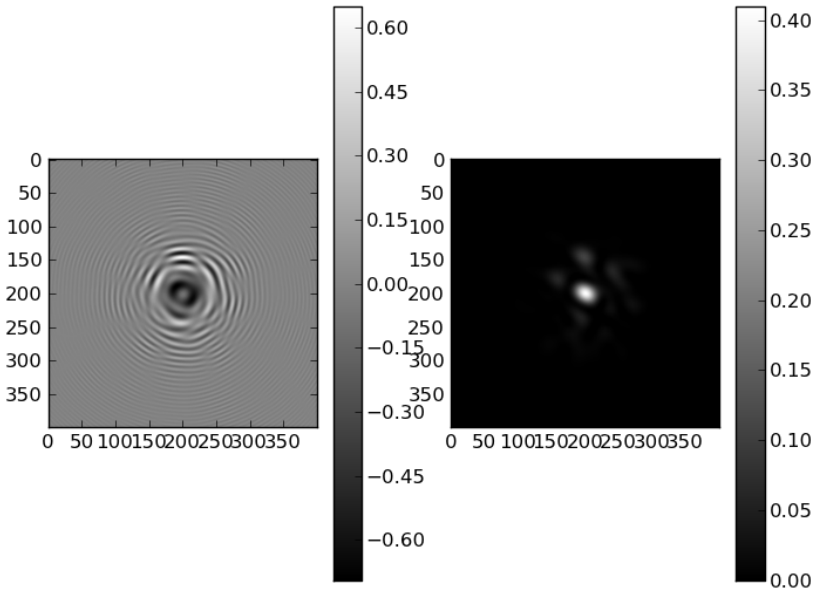

Figure 6.2.1: Left: contribution from hologram term linear in $\mathbf{E}_{\text{scat}}$ to a hologram of 8 spheres in a cube with a 3 μm side length. Right: contribution of the term quadratic in $\mathbf{E}_{\text{scat}}$.

interference of the fields scattered from different particles with each other rather than interference with the incident beam. Moreover, reconstruction, which can be crucial for helping to find initial guesses, relies on ignoring the third term. It would thus seem plausible that where the third term dominates the second term, which encodes the phase of the scattered wave, usefully analyzing digital holograms is likely to be difficult.

We verified this assertion through simulating holograms of 1 μm-diameter polystyrene spheres randomly dispersed in a cubical box. We were then able to separately compute the normalized contributions of the second and third terms in 6.1. Some results are presented below.

We first consider the case in Figure 6.2.1 where 8 particles are dispersed in a 3 μm box.

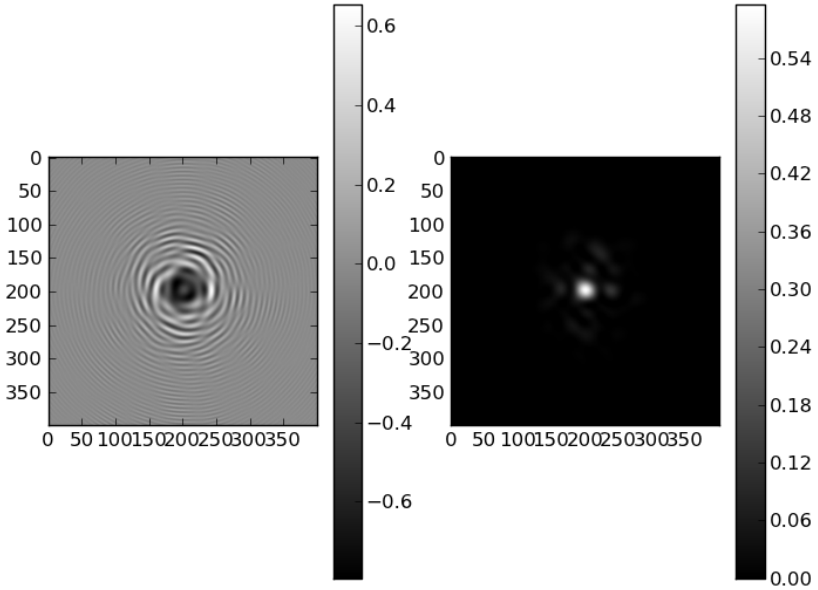

Figure 6.2.2: Same as Figure 6.2.1, but for 12 spheres in a cube with a 3 μm side length.

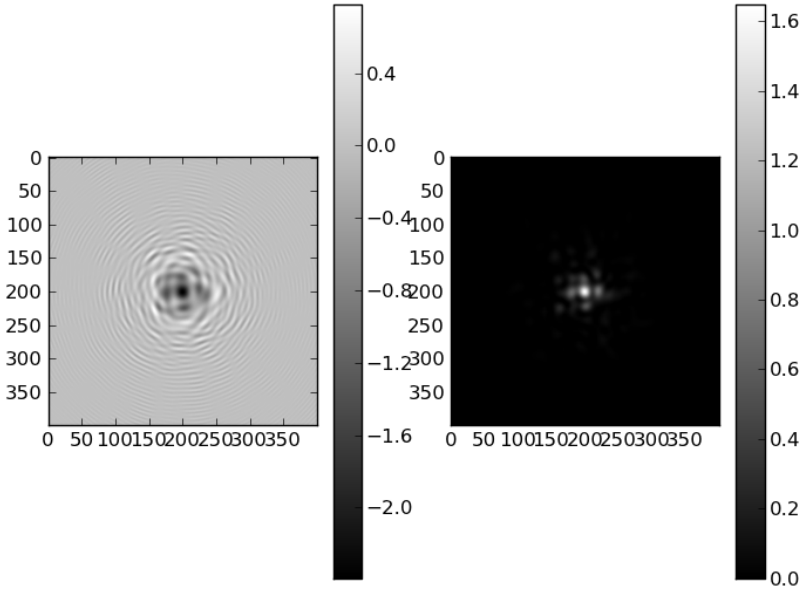

Figure 6.2.3: Same as Figure 6.2.1, but for 32 spheres in a cube with a 5 μm side length.

The second-order contribution is only large near the forward direction, and the second order term also has lower spatial frequencies than the linear hologram term. Configurations like these are easy to analyze with reconstruction, and fitting is straightforward.

The case of 12 particles in the same box, Figure 6.2.2, is somewhat more challenging. It was impossible to detect all the particles by reconstruction, although a fit in which the particle coordinates were perturbed from their known values was successful. Here we find larger contributions from the second-order term over a larger portion of the hologram.

But when 32 particles are dispersed in a 5 μm box (Figure 6.2.3), the second-order term swamps the linear term over much of the hologram. Reconstruction utterly fails in this case, where near the forward direction the hologram begins to look reminiscent of speckle. Fits of a scattering model have not been attempted, but might be challenging. It is not yet clear whether this case is truly impossible to deal with, and a more detailed investigation is needed. Nonetheless, these examples do suggest that DHM is likely to be successful so long as the contribution linear in $\mathbf{E}_{\text{scat}}$ dominates.

6.3 Final Remarks

This thesis has largely concerned the development of DHM for imaging multiple particles. When I began my graduate research, high-precision particle detection from digital holograms was in its infancy. It has been a privilege to help to develop DHM as a tool for studying the dynamics of multiple particles to the point where it has been possible for the first time to make precision measurements of anisotropic 3D diffusion. While both technical challenges and some fundamental questions about ultimate limits remain, I close this work with the knowledge and hope that the range of physical questions that DHM will help to address will only continue to grow.

A

Error Analysis and Dynamical Correlation Functions

A.1 Introduction

As we have described in Chapter 5, we have made measurements of elements of the diffusion tensor **D** to a precision of 1% or better. Such a claim, upon which hinges our conclusions that we have measured anisotropic rotational diffusion and weak symmetry breaking due to particle polydispersity, requires careful justification. In this Appendix we address the issue of uncertainties in dynamical correlation functions.

To measure an element of **D**, we generally need to compute a correlation function. This might be a cluster-frame mean-squared displacement:

$$\langle \Delta x_i^2(\tau) \rangle = 2D_{t,i}\tau \tag{A.1}$$

or an axis autocorrelation:

$$\langle \mathbf{u}_i(t) \cdot \mathbf{u}_i(t+\tau) \rangle = \exp\left[\left(D_{r,i} - \sum_j D_{r,j}\right)\tau\right]. \tag{A.2}$$

It is obvious that the uncertainties we report in $D_{t,i}$ or $D_{r,i}$ will depend on the uncertainties in the correlation functions. This is true whether we report tensor elements from a single correlation function computed at a single time interval τ (in which case the relative uncertainties will be equal) or if we compute for many intervals and perform a weighted regression, as we do throughout Chapter 5. In particular, the covariance matrix from a nonlinear least squares regression can provide error estimates on fit parameters, such as the elements of $\mathbf{D}$, so long as the points being fit (here, correlation functions) are weighted with appropriate 1σ errors. Correctly computing the error bars on these correlation functions is therefore critical.

An underlying physical distribution underlies all Brownian processes. This is easiest to understand for 1-dimensional translational Brownian diffusion characterized by a diffusion constant D. While we have not explicitly derived this in Chapter 5, it is straightforward to show that the probability density function for taking a Brownian step Δx is Gaussian [130]:

$$\begin{aligned} P(\Delta x) &= \frac{1}{\sqrt{2\pi\langle \Delta x^2(\tau)\rangle}} \exp\left[-\frac{(\Delta x)^2}{2\langle Deltax^2(\tau)\rangle}\right] \\ &= \frac{1}{4\pi D\tau} \exp\left[-\frac{(\Delta x)^2}{4D\tau}\right]. \end{aligned} \tag{A.3}$$

The physical quantity we want to know, $D_{t,i}$, is related to the *variance* σ^2 of the parent Gaussian distribution. To estimate the unknown variance, we experimentally observe some number N of displacements and calculate $\langle \Delta x_i^2 \rangle$. If we choose N sufficiently large, we can get a good estimate of σ^2. This Appendix will primarily focus on making "sufficiently large" and "good estimate" more quantitatively precise.

Suppose that I as an experimenter observe N independent displacements, from which I calculate $\langle \Delta x_i^2 \rangle$. If I choose a different set of N independent displacements, I will get a different value for $\langle \Delta x_i^2 \rangle$. It turns out that for an underlying Gaussian parent distribution,

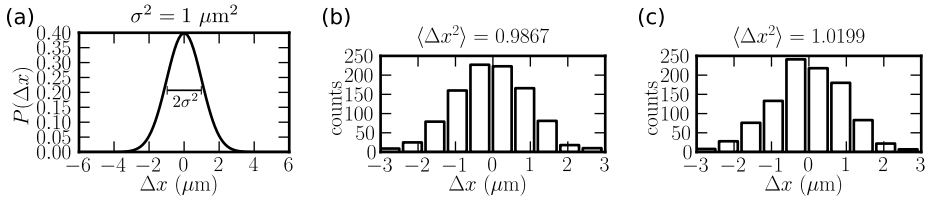

Figure A.1.1: (a) Parent Gaussian distribution for 1-dimensional translational diffusion where $2D\tau = 1\ \mu\text{m}^2$ (Equation A.3. (b) Histogram of 1000 imaginary displacements. Displacements obtained by choosing 1000 random numbers with a mean of 0 and variance of 1. Note that the sample variance differs from 1. (c) Same as (b), but for a different set of 1000 displacements.

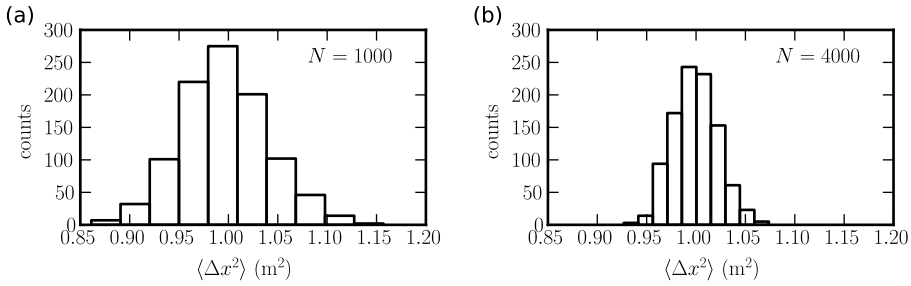

Figure A.1.2: Distributions of MSDs obtained from $N_{exp} = 1000$ simulated experiments in which N displacements are sampled. Simulations performed by choosing normally distributed random numbers with a mean of 0 and variance of 1 μm^2. (a) $N = 1000$. (b) $N = 4000$. The distribution in (b) is about half as wide as in (a), illustrating the approximate $1/\sqrt{N}$ scaling of the standard error of the variance.

if I carry out this process of measuring N independent displacements N_{exp} times, the distribution of MSD's I observe will in fact be approximately normally distributed [1]. The error bar σ on the MSD I need to calculate, therefore, is going to be related to the variance of this distribution of variances.

Figures A.1.1 and A.1.2 may help to clarify these issues. The parent distribution Gaussian distribution governing the Brownian displacements at a fixed time interval is shown in Figure A.1.1(a). Any experiment sampling N displacements governed by this Gaussian

[1] Technically, the distribution is a chi-square distribution with $N - 1$ degrees of freedom, but for large N the distribution is approximately Gaussian by the central limit theorem [145, 146].

distribution will result in a set of displacements. Each set of displacements will be different and will have a slightly different sample mean and variance, as can be seen in Figures A.1.1(b) and (c). Note that the experimentally observed variance differs from the true variance. If we do the sampling experiment N_{exp} times, we can build up a distribution of variances, as in Figure A.1.2, where we show histograms of the MSD's we observe for performing $N_{exp} = 1000$ experiments where we observe N displacements. Clearly, the distribution becomes sharper as N increases.

In a computer simulation based on sampling random numbers, like this one, performing hypothetical experiments many times is almost trivial, and one could analyze the distributions in Figure A.1.2 to estimate their width, which would be related to the desired MSD uncertainty. Performing a comparable number of real experiments with DHM and diffusing clusters is impractical. We thus need a means of estimating the uncertainty in a MSD or other dynamical correlation function from a single experiment.

For the case of translational Brownian motion, this is possible because of the standard error of the variance. The sample variance follows a χ^2 distribution, from which the relative standard error of the variance, $\sigma_{\text{var}}/\text{var}$, can be computed [145]:

$$\frac{\sigma_{\text{var}}}{\text{var}} = \sqrt{\frac{2}{N_{ind} - 1}} \tag{A.4}$$

where N_{ind} is the number of independent displacements[2]. Equation A.4 gives the experimental 1-sigma relative uncertainty in an MSD. The $1/\sqrt{N}$ dependence is apparent in Figure A.1.2.

We have said nothing, however, about how N_{ind} is to be determined. In a real experiment, we observe a trajectory and obtain a list of particle positions of length N_{traj} at evenly spaced time intervals: $x_1, x_2, \ldots, x_{N_{traj}}$. For displacements of 1 time step, we have $x_2 - x_1$, $x_3 - x_2, \ldots$, for $N_{traj} - 1$ independent displacements. But trouble arises for displacements of larger time steps. For the case of two time steps, for instance, we could compute $x_3 - x_1$, $x_4 - x_2$, and so on. The problem is that these two displacements overlap and are not inde-

[2]We must distinguish between the true but unknown variance σ^2 and the sample variance S^2 (the experimental MSD.) It is $(N_{ind} - 1)S^2/\sigma^2$ that follows a chi-squared distribution $\chi^2_{N_{ind}-1}$ with a variance of $2(N_{ind}-1)$ [145]. The result in Equation A.4 follows from the square root of this, noting that for a constant a and a random variable X, $\text{var}(aX) = a^2\text{var}(X)$.

pendent.

There are three viable ways to proceed:

1. Choose N non-overlapping displacements, and then use the standard error of the variance (Equation A.4) with $N_{ind} = N$.

2. Calculate all possible displacements, including overlapping ones, but estimate N_{ind} in some other way. Thereafter, use Equation A.4.

3. Use a block decorrelation technique to estimate the error on an average of correlated data.

We reject the first possibility because we inherently throw out a great deal of information, particularly involving displacements at larger intervals, when we restrict ourselves to non-overlapping intervals. Consider a trajectory 101 time steps long. We can compute 90 possible displacements with an interval of 10 time steps, but only 10 non-overlapping displacements.

The second approach is a frequently used one in colloid physics, and will hereafter be called CGW after its proponents John Crocker, David Grier, and Eric Weeks. The approach, to the author's knowledge, has not been described in detail in peer-reviewed literature, but is described in the documentation of IDL particle tracking codes by these authors: `http://www.physics.emory.edu/~weeks/idl/msd.html`. For a trajectory of length N timesteps, it is possible to calculate $N-n$ displacements between positions n timesteps apart. The number of non-overlapping displacements would be $(N-n)/n$. The number of *independent* steps in the CGW is then given by

$$N_{ind,CGW} = 2\frac{N-n}{n} \tag{A.5}$$

or twice the number of strictly independent displacements. While this *ad hoc* factor of 2 seems reasonable, the author is not aware of a rigorous justification for it. The CGW approach also requires that the underlying distribution be Gaussian. This is a reasonable assumption for translational Brownian motion. But it is only approximately valid for axis mean-squared displacements in rotational Brownian motion, and even without detailed

computations it would seem obvious that the axis autocorrelation $\langle \mathbf{u}_i(t) \cdot \mathbf{u}_i(t+\tau) \rangle$ cannot be governed by a Gaussian distribution, since the dot product cannot exceed 1.

We thus favor the third approach, based on a block decorrelation technique first described by Flyvbjerg and Petersen [147]. We will hereafter refer to this method as the FP method. We will describe FP block decorrelation algorithm, and then present simulations comparing FP to CGW for simulated Brownian dynamics.

The author first became aware of the FP method through Savin and Doyle's work on the statistical issues involved in multiple particle tracking in homogeneous materials [148]. Aside from Savin and Doyle's work, the FP technique appears to have received little attention from experimentalists, and certainly not for assessing standard errors on single-particle diffusion. We note that Flyvbjerg and Petersen, in their 1989 paper on the technique [147] which has been widely cited in the simulation community, themselves deny credit for having invented the technique. Our naming the technique after them may be viewed as an example of what John David Jackson calls the zeroth theorem of the history of science [149][3]

A.2 Flyvbjerg-Petersen Block Decorrelation

Rather than being based on statistical results for normal distributions, the Flyvbjerg-Petersen block decorrelation technique assesses the variance of the mean of a correlated data set without assumptions as to its underlying distribution. This has the advantage of being more readily applied to situations like rotational diffusion. A key difference is that while in CGW we think of a mean-squared displacement as a variance, in the FP we think of it as a mean.

The FP algorithm supposes that we have some series x_i of N correlated data points. We wish to compute the variance on the mean, $\mathrm{var}(\bar{x}_i)$. For completely uncorrelated data, it possible to estimate this by computing the variance of the data:

$$\mathrm{var}(\bar{x}_i) = \frac{\mathrm{var}(x_i)}{N} \tag{A.6}$$

[3] Jackson, the man of *Classical Electrodynamics* fame (or infamy?) did not himself come up with this term, attributing it to Ernst Fischer.

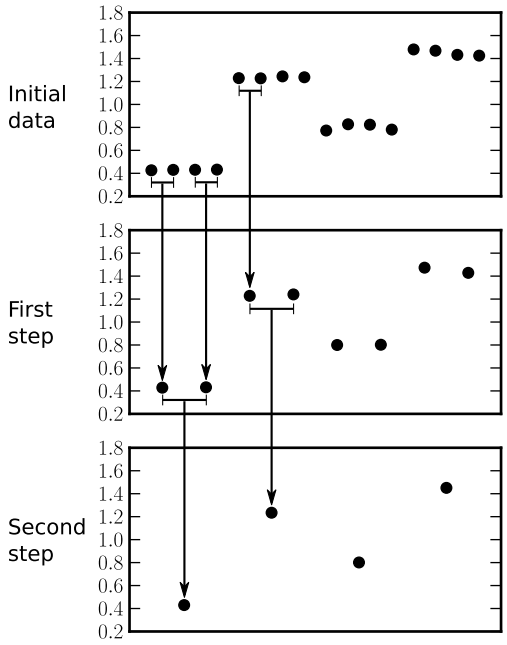

Figure A.2.1: Schematic illustration of FP block decorrelation algorithm. Raw data set is subjected to two decorrelating block transformations, governed by Equation A.7.

but this will be an underestimate for correlated data [147]. The idea is to transform the correlated data set x_i into a smaller but uncorrelated set. The transformation averages together pairs of neighboring data points. To be precise, the transformed set x'_i, having half as many points N' as x_i, is given by

$$x'_i = \frac{x_{2i-1} + x_{2i}}{2}. \tag{A.7}$$

The block transformation is shown schematically for an artificial data set in Figure A.2.1. Flyvbjerg & Petersen show that this transformation preserves both the mean and the variance: that $\bar{x'}_i = \bar{x}_i$ and $\mathrm{var}(x'_i) = \mathrm{var}(x_i)$ [147]. After each block transformation, $\mathrm{var}(x'_i)/(N'-1)$ is computed. It will increase in succeeding block transformation steps When the transformation has been carried out enough times, the data set should be decorrelated, and $\mathrm{var}(x'_i)/(N'-1)$ should approach a fixed point, which is then taken as the estimate of the variance on $\bar{x}_i$. We refer the reader to the original paper for the proofs.

The block transformations themselves are straightforward to implement in Numpy, but it becomes necessary to detect when a sufficient number of block transformations has occurred. Flyvbjerg and Petersen point out that at the fixed point, the x_i' are independent. Provided that N' is large enough, the central limit theorem guarantees that the distribution of x_i' is Gaussian to good approximation. Then, Equation A.4 gives a means to estimate the variance of the variance. If the estimates of the variance, $\mathrm{var}(x_i')/(N'-1)$, agree within the 1-sigma uncertainty given by Equation A.4, then we can say that the fixed point has been reached.

Our FP algorithm thus works as follows:

1. Begin with correlated data (i.e., a set of squared displacements) x_i
2. Block-decorrelate the data. At each block decorrelation step, calculate $\mathrm{var}(x_i')/(N'-1)$ as well as the uncertainty in this estimate based on A.4. Proceed until N' reaches some minimum (the technique is insensitive to the cutoff).
3. To find the leftmost fixed-point region (smallest number of decorrelation steps), check if the variance estimate after j transformations lies within the 1-sigma error bars of the variance estimate after $j+1$ transformations. The leftmost point to be considered fixed is the first point satisfying this criterion.
4. Repeat Step 3 from the right to find the rightmost edge of the fixed point region.
5. Compute a weighted average of all the $\mathrm{var}(x_i')/(N'-1)$ in the fixed-point region, where the weights are given by the 1-sigma error bars.

This process is illustrated in Figure A.2.2, which shows the estimates on the variance of the mean as a function of the number of FP decorrelation steps for a simulated random walk. The data are shown for a simulated 1D random walk where $D\tau = 5 \times 10^{13}$ m^2 and mean-squared displacements are computed for positions separated by 25 time steps. The estimated variance on the mean rises over the first few FP steps as the data set becomes decorrelated, before reaching a fixed point. After many FP steps, however, N' becomes small enough that the estimates are unreliable.

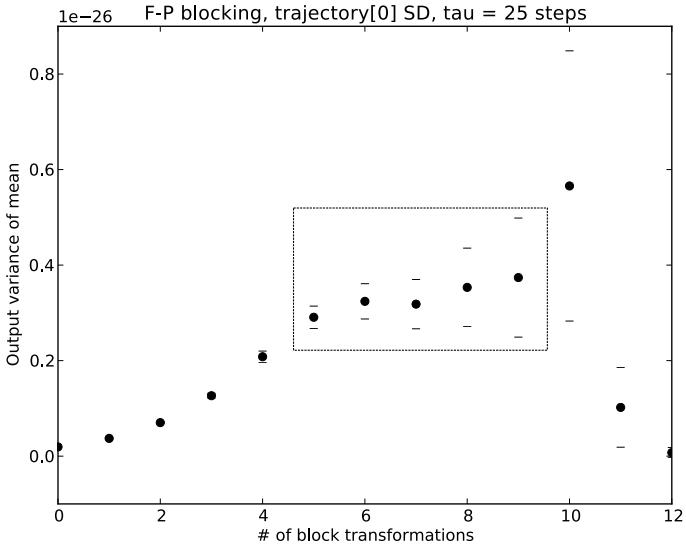

Figure A.2.2: Estimate of variance of mean as a function of the number of FP block transformations. Data shown from a simulated random walk. Dashed box indicates the fixed-point values that are averaged to determine the variance on the sample mean.

A.3 Validation of FP by Brownian Dynamics Simulations

Having described the FP algorithm, we show that it is superior to the CGW method through simulations of both translational and rotational Brownian motion. We can simulate a trajectory similar to that obtained from a real experiment and from the trajectory calculate error bars on dynamical correlation functions just as we would for real data, using both the CGW and FP methods. But because simulating data is fast, we can generate many trajectories satisfying the same statistical properties and measure the variance on the dynamical correlation functions within this ensemble. We show that in all cases, the FP error bars are closer to the standard deviations obtained from the ensemble of trajectories than the CGW error bars.

Simulating a translational Brownian walk, where positions are observed at instants separated by a time interval Δt, is straightforward. To simulate a trajectory of length N_{traj}, which we choose to be 10^4, we choose N_{traj} normally distributed random numbers with a mean of 0 and a variance of $2D\Delta t$. We choose $D = 10^{-12}$ m^{2}s^{-1}. These random numbers physically correspond to steps. The simulated trajectory is then obtained by cumulatively summing the steps. We analyze one such trajectory using CGW and FP, but also generate an ensemble of 1000 trajectories in the same way, from which we generate what we will term *sample standard errors*.

Figure A.3.1 compares the relative sample standard errors to the predictions of CGW and FP. The sample standard errors increase with τ since the number of independent displacements decreases. It is apparent that while the CGW standard errors follow the same trend as the sample standard errors, CGW gives a consistent under-estimate. In contrast, with the exception of the longest τ, the FP standard errors track the sample standard errors almost perfectly. The kinks that appear at several points for FP arise from integer jumps in the number of points being used to compute the weighted average in Step 5.

We simulate homogeneous rotational diffusion governed by a rotation constant $D_r = 0.1$ s^{-1} and with the same Δt using an algorithm by Beard and Schlick [150]. The simplest way to simulate rotational diffusion would be to choose normally distributed angles for rotation about principal axes, but this can introduce a bias because finite rotations do not

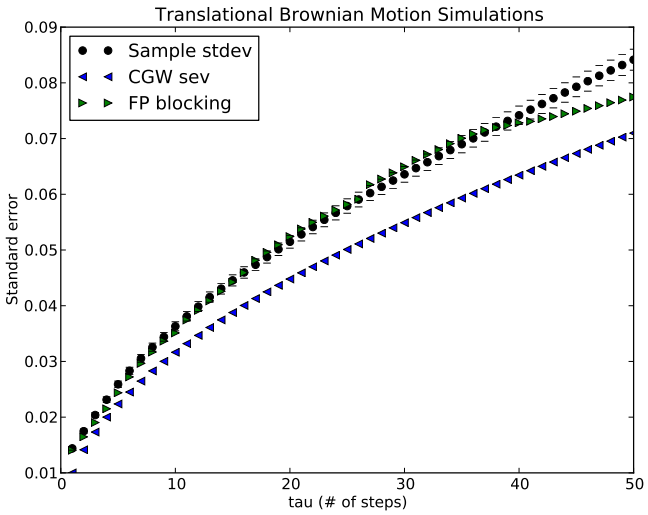

Figure A.3.1: Comparison between relative sample standard errors on MSDs computed for different intervals τ. Sample standard errors (black circles) are computed from the standard deviation of MSDs calculated for an ensemble of 1000 trajectories; error bars from the standard error of the variance. Blue triangles show standard errors computed from the CGW method, while green triangles show the FP standard errors.

commute [150][4]. Beard and Schlick avoid this problem by integrating the equations of motion for a rigid body and deriving a matrix [5] based on 3 normally distributed angles with a variance of $2D_r\Delta t$. We use the Beard-Schlick algorithm to compute 1000 trajectories of the body x axis in the same manner as we did for translations.

Figure A.3.2 compares relative sample standard errors to the standard errors obtained from the CGW and FP methods for a body axis mean squared displacement, $\langle \mathbf{u}^2(\tau) \rangle$. This time, CGW consistently overestimates the sample standard errors, although it at least correctly follows the trend of the sample standard errors. FP tracks the sample standard errors much more closely. The results are more dramatic for the axis autocorrelations $\langle \mathbf{u}(t) \cdot \mathbf{u}(t+\tau) \rangle$ in A.3.3. Here, CGW grossly overestimates the standard error; it even fails to qualitatively capture the τ dependence of the sample standard error. Whereas for the body axis MSD, the underlying distribution is at least approximately Gaussian, the distribution underlying the axis autocorrelations (Equation 5.60) is not.

On the basis of these simulations, as well as the *ad hoc* nature of the crucial factor of 2 underlying the estimation of N_{ind} in the CGW method, we strongly encourage other experimentalists to adopt the FP method for placing error bars on MSDs and other dynamical correlation functions.

[4] The alternative to this is to choose a simulation timestep Δt_{sim} which is much smaller than the experimentally observed trajectory timestep Δt. This is the approach taken by Fernandes *et al.* in the code BROWNRIG, which we use to simulate anisotropic Brownian dynamics including translation-rotational coupling [151].

[5] Anyone interested in using the Beard-Schlick algorithm should note that there is a typographical error in the key equation of their paper. In particular, the entry U_{22} of the operator $\mathbf{U}$ in Beard and Schlick's Equation 5 should read, in their notation,

$$U_{22} = \left(\frac{(\Omega_a^2 + \Omega_c^2)\cos\Omega + \Omega_b^2}{\Omega^2} \right) \tag{A.8}$$

The author thanks Prof. Tamar Schlick for helpful discussions on this point.

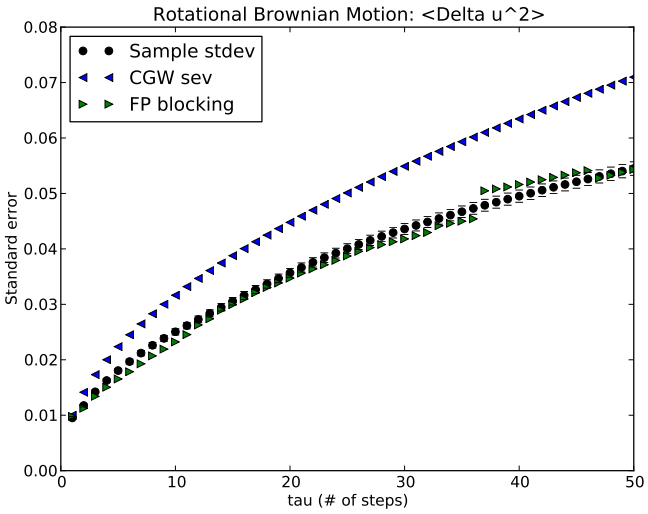

Figure A.3.2: Comparison of relative sample standard errors to results from CGW and FP methods for rotational diffusion with $\Delta t = 0.02$ s. Standard errors are computed for the axis MSD, $\langle \mathbf{u}^2 \rangle$. Black circles denote sample standard errors, blue triangles CGW, and green triangles FP.

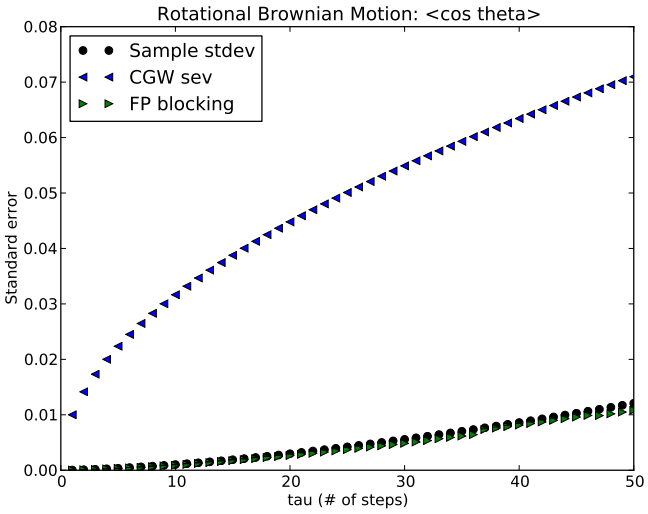

Figure A.3.3: Comparison of relative sample standard errors to CGW and FP standard errors, for same data as in Figure A.3.2. Standard errors are computed for axis autocorrelations, $\langle \mathbf{u}(t) \cdot \mathbf{u}(t+\tau) \rangle$.

B

Additional Scattering Problems

Here we discuss several additional scattering problems that are not directly pertinent to modeling holograms of colloidal particles, but which nonetheless are of some utility and interest.

B.1 Computing Lorenz-Mie Internal Fields

For the purposes of computing holograms, or for that matter any scattering quantity, the internal field $\mathbf{E}_{int}$ is of little relevance. There is no experimental way to probe $\mathbf{E}_{int}$ directly. Nonetheless, one may sometimes wish to be able to visualize the internal fields of a scatterer for pedagogical or other purposes. In addition, certain techniques based on topological derivatives for solving the inverse problem in scattering require computations of $\mathbf{E}_{int}$ [152]. It turns out that stably computing the internal field is not trivial. Since this problem has not received much direct attention in the scattering literature, we briefly discuss it here.

Recall that the internal fields may written as an expansion in the vector spherical harmonics defined in Chapter 2:

$$\mathbf{E}_{int} = \sum_{n=1}^{\infty} i^n \frac{E_o(2n+1)}{n(n+1)} \left(c_n \mathbf{M}_{o1n}^{(1)} - i d_n \mathbf{N}_{e1n}^{(1)} \right). \tag{B.1}$$

Recall that E_o is the amplitude of the incident wave, and that the superscript on the vector spherical harmonics denotes a radial dependence on spherical Bessel functions, $j_n(n_p k_o r)$. It might seem that the problem is trivial, as Bohren & Huffman give the expansion coefficients c_n and d_n in terms of j_n and $h_n^{(1)}$. Alternately, one could imagine computing c_n and d_n once the external scattering coefficients a_n and b_n are known through the linear relations that enforce the boundary conditions on the sphere surface:

$$j_n(mx)c_l + h_n^{(1)}(x)b_n = j_n(x) \tag{B.2}$$

$$m j_n(mx)d_n + h_n^{(1)}(x)a_n = j_n(x). \tag{B.3}$$

The relative index m and size parameter x are defined here in the usual way. Neither of these approaches should be used, however, because they require computing the spherical Bessel function $j_n(mx)$ inside the particle, which may be absorbing. As we have mentioned, computing j_n for complex argument is fraught with peril.

As a first step towards a more computionally friendly formulation, we rewrite c_n and d_n in terms of Riccati-Bessel functions:

$$c_n = \frac{m\psi_n(x)\xi_n'(x) - m\xi_n(x)\psi_n'(x)}{\psi_n(mx)\xi_n'(x) - m\xi_n(x)\psi_n'(mx)} \tag{B.4}$$

$$d_n = \frac{m\psi_n(x)\xi_n'(x) - m\xi_n(x)\psi_n'(x)}{m\psi_n(mx)\xi_n'(x) - \xi_n(x)\psi_n'(mx)}. \tag{B.5}$$

This only helps somewhat, as $\psi_n(z)$ inherits the same pathologies as $j_n(z)$ for a large imaginary argument. Much as the computations of the external Mie coefficients are aided by using logarithmic derivatives, we can rewrite Equations B.4 and B.5 in terms of logarithmic

derivatives:

$$D_n^{(1)}(z) = \frac{\psi_n'(z)}{\psi_n(z)};\ D_n^{(3)}(z) = \frac{\xi_n'(z)}{\xi_n(z)}. \tag{B.6}$$

A bit of algebraic manipulation yields

$$c_n = m\frac{\psi_n(x)}{\psi_n(mx)}\left(\frac{D_n^{(3)}(x) - D_n^{1}(x)}{D_n^{(3)}(x) - mD_n^{(1)}(mx)}\right) \tag{B.7}$$

$$d_n = m\frac{\psi_n(x)}{\psi_n(mx)}\left(\frac{D_n^{(3)}(x) - D_n^{(1)}(x)}{mD_n^{(3)}(x) - D_n^{(1)}(mx)}\right). \tag{B.8}$$

This form is useful because all the pieces appearing therein can be computed stably. The logarithmic derivative $D_n^{(1)}$ is familiar from computations of the external coefficients and can be calculated by downward recurrence. Mackowski *et al.* give stable upwards recursion relations for computing $D_n^{(3)}(z)$, together with the product $\psi_n(z)\xi_n(z)$, once $D_n^{(1)}(z)$ is known [77]:

$$\psi_n(z)\xi_n(z) = \psi_{n-1}(z)\xi_{n-1}(z)\left[\frac{n}{z} - D_{n-1}^{(1)}(z)\right]\left[\frac{n}{z} - D_{n-1}^{(3)}(z)\right] \tag{B.9}$$

$$D_n^{(3)}(z) = D_n^{(1)}(z) + \frac{i}{\psi_n(z)\xi_n(z)}. \tag{B.10}$$

These relations are initialized with $D_0^{(3)}(z) = i$ and $\psi_0(z)\xi_0(z) = -ie^{iz}\sin z$ [77]. The other necessary ingredient is a ratio of Riccati-Bessel functions; the use of such ratios to stabilize scattering computations was initially pointed out by Toon and Ackerman [153]. Sitarski [154] as well as Mackowski *et al.* give a stable upward recursion for the ratio of ψ_n for two different complex arguments z_1 and z_2 from logarithmic derivatives:

$$\frac{\psi_n(z_1)}{\psi_n(z_2)} \equiv R_n^{(1)}(z_1, z_2) = R_{n-1}^{(1)}(z_1, z_2)\frac{D_n^{(1)}(z_2) + n/z_2}{D_n^{(1)}(z_1) + n/z_1}. \tag{B.11}$$

This method of calculating the Mie internal coefficients, in Equations B.7 and B.8, has been implemented in HoloPy. While the elements that go into computing c_n and d_n this

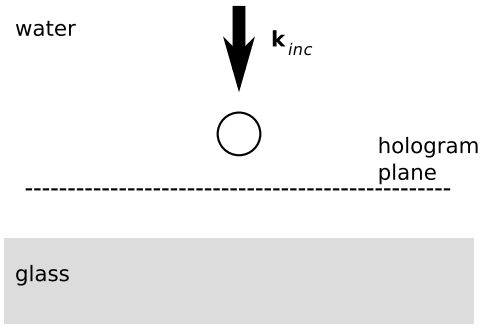

Figure B.2.1: Schematic illustration of scattering with reflections. A plane wave, propagating in the normal direction with respect to a water-glass interface, illumines a sphere. The detection plane is assumed to be in the water.

way are not novel, to the author's knowledge, Equations B.7 and B.8 have not previously appeared in the literature. Their use is recommended whenever Mie internal fields, particularly for strongly absorbing particles.

B.2 Lorenz-Mie Scattering Near an Interface: Reflections

We now turn our attention to the approximate modeling of the effect of reflecting surfaces on holograms. While our usual hologram modeling ignores such effects, there is a physical basis for considering them. Typically, our experiments are conducted on aqueous samples inside sample chambers made from glass. Thus, there will always be reflections at the glass-water interface. In particular, we will consider the schematic geometry in Figure B.2.1, where both the scatterer and the hologram plane are assumed to be in the aqueous medium.

Modeling these effects in a rigorous way turns out to be difficult. The following things can happen:

1. The incident plane wave illuminates the sphere (normal case of Lorenz-Mie scattering)

2. The incident plane wave reflects from the interface. This reflected incident wave also illuminates the sphere.

3. The wave scattered by the sphere will also reflect from the interface. This wave, also, will illuminate the sphere.

The author is unaware of a theoretical treatment which rigorously treats all of these effects. One of the most detailed is due to Gorden Videen [155, 156]. Videen's treatment assumes that all the scattered light reflects from the interface as though it struck the interface at normal incidence (in other words, it neglects the angular dependence of the Fresnel reflection coefficients). Even this approximate treatment results in a system of linear equations to be numerically solved [155], much as is the case with the multisphere superposition approach. We did not deem a full implementation of Videen's solution to be worthwhile, given that it still is inherently approximate. Instead, inspired by aspects of Videen's solution, we model the situation in the following way:

1. Assume that both an incident wave $\mathbf{E}_{inc}$ and the reflection of this wave from the interface, $\mathbf{E}_{refl}$, illuminate the sphere. As we will show, this will change the scattering coefficients a_n and b_n.

2. Assume that at the hologram plane, the incident field we detect is $\mathbf{E}_{inc} + \mathbf{E}_{refl}$. The scattered field we detect will be the sum of direct waves scattered from the sphere as well as reflected waves. We will account for the angle dependence of the Fresnel coefficients here.

In other words, we will neglect reflections of the scattered wave impinging on the sphere (what Videen terms interaction terms), but will rigorously account for all other effects.

We first consider the reflection of the incident wave and its effect on the scattering coefficients. Suppose a plane wave $E_0 e^{ikz}\hat{\mathbf{x}}$ (where we assume x polarization without loss of generality) strikes the interface at normal incidence (at normal incidence, there is no difference between TE and TM polarization.) Suppose the phase is 0 at the center of the particle, and that the distance between the particle center and the interface is d. The amplitude of $\mathbf{E}_{refl}$ will be smaller by a factor of the Fresnel coefficient $r(0)$:

$$r(0) = \frac{1 - n_2/n_1}{1 + n_2/n_1} \tag{B.12}$$

where n_1 is the index of the first medium (water) and n_2 is the index of the second medium (glass). Note that the reflected wave gets a π phase shift if $n_2 > n_1$, as is the case for water and glass. There is an additional phase shift due to the round-trip propagation to and from the interface. Therefore,

$$\mathbf{E}_{refl} = E_0 \left(\frac{1 - n_2/n_1}{1 + n_2/n_1} \right) e^{2ikd} e^{-ikz}. \tag{B.13}$$

Recall the expansion of a plane wave $E_0 e^{ikz\hat{\mathbf{x}}}$ in vector spherical harmonics:

$$\mathbf{E}_{inc} = E_0 \sum_{n=1}^{\infty} i^n \frac{2n+1}{n(n+1)} \left(\mathbf{M}_{o1n}^{(1)} - i\mathbf{N}_{e1n}^{(1)} \right). \tag{B.14}$$

It is clear that up to the multiplicative factors for the Fresnel coefficient and the phase shift, we will get the expansion of $\mathbf{E}_{refl}$ by taking the complex conjugate of this:

$$\mathbf{E}_{refl} = E_0 \left(\frac{1 - n_2/n_1}{1 + n_2/n_1} \right) e^{2ikd} \sum_{n=1}^{\infty} (-i)^n \frac{2n+1}{n(n+1)} \left(\mathbf{M}_{o1n}^{(1)} + i\mathbf{N}_{e1n}^{(1)} \right) \tag{B.15}$$

noting that the VSH of the first kind, depending on j_n, are pure real. We also recall the expansion of the scattered field in the Lorenz-Mie solution

$$\mathbf{E}_{scat} = \sum_{n=1}^{\infty} E_n \left(i a_n \mathbf{N}_{e1n}^{(3)} - b_n \mathbf{M}_{o1n}^{(3)} \right) \tag{B.16}$$

where $E_n = i^n E_0 (2n+1) / \left(n(n+1) \right)$. Now, we could repeat the arguments that lead to the a_n and b_n in the Mie solution. We note, however, that Maxwell's equations are linear, and that the $\mathbf{M}$ and $\mathbf{N}$ vector spherical harmonics are orthogonal. We may thus arrive at a new solution for a_n by seeing how the input proportional to $\mathbf{N}_{e1n}^{(1)}$ changes between this problem and the Lorenz-Mie solution. Similarly, we get a new solution for b_n by examining the input proportional to $\mathbf{M}_{o1n}^{(3)}$. Defining

$$R_n \equiv \left(\frac{1 - n_2/n_1}{1 + n_2/n_1} \right) (-1)^n e^{2ikd}, \tag{B.17}$$

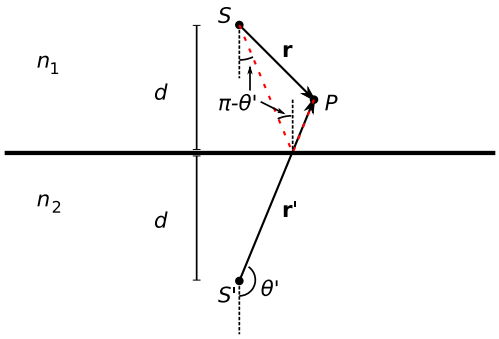

Figure B.2.2: Geometric construction for reflection of light scattered by sphere at S to field point P. The scattered light travels the red dashed path, reflecting from the interface. The distance traveled is equal to the distance that light would travel from an imaginary image sphere at S', mirrored across the interface. The light that reflects from the interface is scattered at an angle of $\pi - \theta'$. The angle of incidence of the scattered wave onto the interface is also $\pi - \theta'$.

we can write the scattering coefficients for illumination in this case (primed) in terms of the Lorenz-Mie scattering coefficients (unprimed):

$$\begin{aligned} a'_n &= (1 - R_n)a_n \\ b'_n &= (1 + R_n)b_n. \end{aligned} \tag{B.18}$$

The minus sign in the expression for a'_n comes from the change in sign of the terms proportional to $\mathbf{N}^{(1)}_{e1n}$ in Equation B.15.

Calculation of the direct scattered field can now proceed in the usual way, so long as we use the scattering coefficients in Equation B.18. We now come to the computation of the reflected scattered field $\mathbf{E}_{sr}$. Here, we use a geometric trick from Videen's solution [155], and illustrated in Figure B.2.2. In particular, if we have a field point (where we want to calculate $\mathbf{E}_{scat}$ and its reflection) at $\mathbf{r}$ from the particle center, we can imagine the reflection of the scattered field as coming from an image particle mirrored across the interface. We can then draw the vector $\mathbf{r}'$ from the image particle to the field point. The reflected scattered field will be the scattered field of the same particle computed at spherical coordinates $(r', \pi - \theta', \varphi')$, up to Fresnel coefficients.

We will follow Jackson's conventions for the Fresnel coefficients [157]. For transverse electric polarization (polarization perpendicular to the plane of incidence, which is here identical to the scatttering plane), we have

$$r_{TE}(\theta_i) = \frac{\cos\theta_i - \sqrt{(n_2/n_1)^2 - n_1^2 \sin^2\theta_i}}{\cos\theta_i + \sqrt{(n_2/n_1)^2 - n_1^2 \sin^2\theta_i}}. \tag{B.19}$$

The Fresnel coefficient for transverse magnetic polarization (parallel to the plane of incidence) is given by

$$r_{TM}(\theta_i) = \frac{(n_2/n_1)^2 \cos\theta_i - \sqrt{(n_2/n_1)^2 - \sin^2\theta_i}}{(n_2/n_1)^2 \cos\theta_i + \sqrt{(n_2/n_1)^2 - \sin^2\theta_i}}. \tag{B.20}$$

Furthermore, it is apparent that the $\hat{\boldsymbol{\phi}}$ component of $\mathbf{E}_{scat}$ (perpendicular to the plane of Figure B.2.2) is in fact TE polarized, and that the $\hat{\boldsymbol{\theta}}$ component of $\mathbf{E}_{scat}$ is TM polarized. The relevant angle of incidence is $\pi - \theta'$. So, recalling that our usual amplitude scattering matrix formalism gives us these two components of $\mathbf{E}_{scat}$, we may then conclude that

$$\begin{aligned} E_{sr,\theta} &= E_{scat,\theta}(r', \pi - \theta', \varphi') r_{TM}(\pi - \theta') \\ E_{sr,\varphi} &= E_{scat,\varphi}(r', \pi - \theta', \varphi') r_{TE}(\pi - \theta'). \end{aligned} \tag{B.21}$$

Our code to model holograms with reflection can thus proceed as follows:

1. For a given sphere, compute scattering coefficients a_n and b_n according to Equation B.18.

2. For each hologram point, compute the spherical coordinates (r, θ, φ) from the sphere as well as the spherical coordinates (r', θ', φ') from the image sphere.

3. Compute $\mathbf{E}_{scat}$ in the usual way.

4. Compute $\mathbf{E}_{sr}$ following Equation B.21.

5. Obtain a hologram by interfering the total incident field $\mathbf{E}_{inc} + \mathbf{E}_{refl}$ and the total

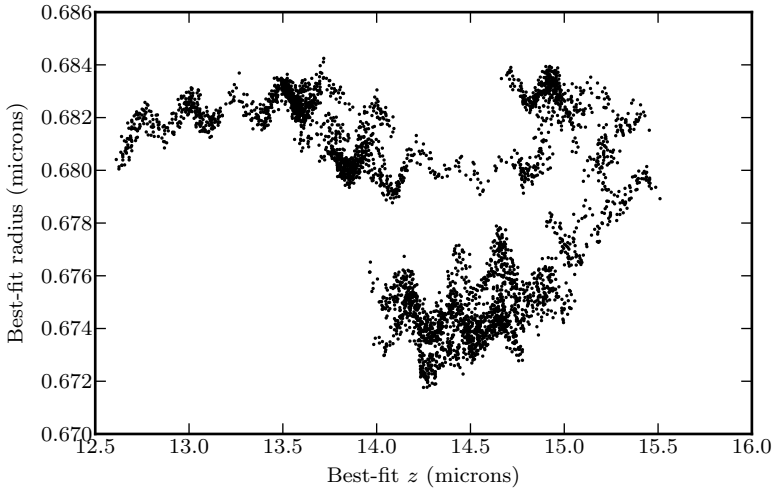

Figure B.2.3: Scatter plot of best-fit radius and best-fit z for a 1.3 μm polystyrene sphere. Data courtesy of R. W. Perry.

scattered field[1] $\mathbf{E}_{scat} + \mathbf{E}_{sr}$.

We have used this code to examine whether reflections might be responsible for some unusual physical effects we have observed. Figure B.2.3 shows the best-fit radius versus the best-fit z position for holograms of a 1.3 μm-diameter polystyrene sphere, where the usual Lorenz-Mie model was fit to the data. An oscillation in the fitted radius as z varies is clearly apparent; the oscillation have a period of about 250 nm in z, which is approximately half the wavelength of light in the aqueous medium.

This effect can be reproduced in simulations. We simulated a 1.26 μm diameter polystyrene sphere sedimenting in water, with the hologram plane located 5 μm above a reflecting glass interface. We calculated holograms using the code described above, but fit ordinary Lorenz-Mie scattering models to these holograms. The results, in Figure B.2.4 have the same feature as the experimental data: a clear oscillation with a wavelength of $0.5\lambda_{med}$. We attribute this effect to interference of the scattered field with its reflection.

[1] We convert all scattered fields to Cartesian coordinates prior to performing the sum.

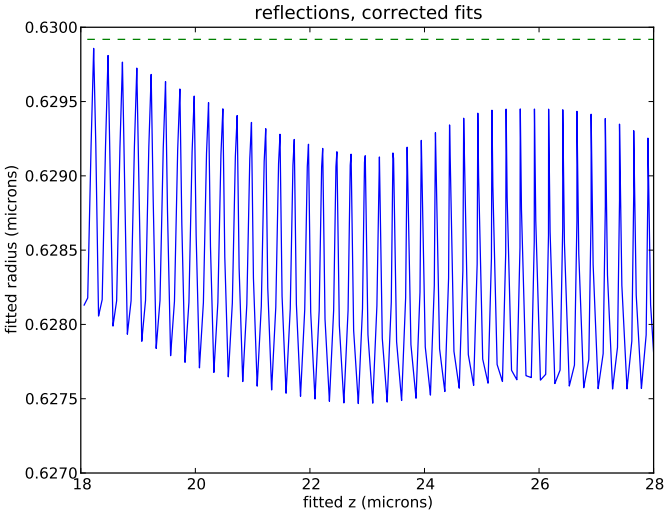

Figure B.2.4: Best-fit radii vs. z for simulations of a sedimenting polystyrene sphere. Holograms calculated accounting for reflections were analyzed with Lorenz-Mie models. The input particle radius is shown by the green dashed line.

C

Towards Understanding the Scattering by Particles at Non-Index Matched Liquid-Liquid Interfaces

Here we describe some theoretical work conducted in collaboration with Alex Small (Cal. Poly., Pomona) on scattering by particles at mismatched liquid-liquid interfaces.

C.1 Motivation

Experiments by Kaz and McGorty [103] examined the approach of micron-sized colloidal spheres to planar oil-water interfaces. In those experiments, glycerol was added to the aqueous phase to index-match to decane. We were always intrigued by the possibility of doing these experiments with a non-index matched interface. In particular, this seemed to offer

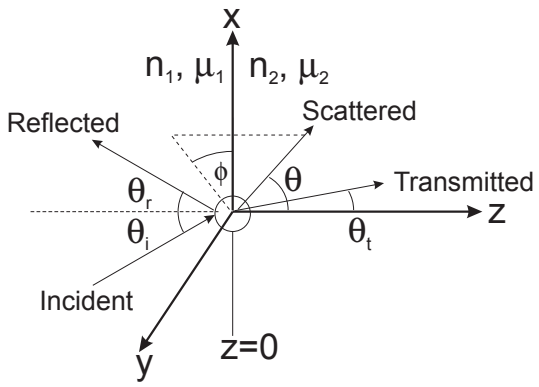

Figure C.1.1: Diagram of interfacial scattering geometry.

the possibility of performing *in situ* contact angle measurements. Solving the interfacial scattering problem has turned out to be challenging, and a complete practical solution is not yet at hand. Here we highlight some aspects that we have addressed.

Figure C.1.1 shows the basic setup of the problem. A sphere of index n_3 is embedded with its equator at the interface between a media of indices n_1 and n_2. We will generally assume that the incident wavevector is normal to the interface ($\theta_i = 0$).

C.2 Naive Solution: Differential Approach

The simplest approach, which we first attempted, is to expand the fields in both external media in VSH appropriate for that media. One can then generate coefficients that are matched at boundary conditions: at the interface of the sphere with each medium, and at the liquid-liquid interface.

This is unfortunately problematic for a very simple reason: it turns out to be impossible to satisfy boundary conditions at the liquid-liquid interface ($\theta = \pi/2$) without requiring the fields to vanish there. Recall that the radial dependence of the scattered fields must be in terms of spherical Hankel functions: $h_n^{(1)}(nk_0 r)$. These have different spatial frequencies in the two media, and it is impossible to match them everywhere.

We thus take an alternate approach, based on an absorbing boundary condition formulated by Grote & Keller [158]. We show that this allows us to rederive the Lorenz-Mie

solution; it may be useful in getting a solution to the interfacial problem

C.3 Absorbing Boundary Condition and the Lorenz-Mie Solution

C.3.1 Setup

We are more or less following Grote & Keller's 1995 SIAM paper, "Exact Nonreflecting Boundary Conditions for the Time Dependent Wave Equation." We will make several distinctions from them, however. Using Debye potentials, we can reduce the Mie problem of solving for the vectorial **E** and **H** fields from a plane wave incident on a sphere in an infinite, isotropic, homogeneous medium to that of solving the scalar wave equation:

$$\frac{n_{med}^2}{c^2}\frac{\partial^2}{\partial t^2}U(\mathbf{r},t) - \nabla^2 U(\mathbf{r},t) = F(\mathbf{r}, U, \nabla U). \tag{C.1}$$

Here F is a source term which we assume to vanish outside the surface at which we applying the absorbing boundary condition. Note that G & K set $c/n = 1$. Unlike G & K, we will also explicitly assume harmonic time dependence at long times, so our Debye potential $u(\mathbf{r})$ relates to U as

$$U(\mathbf{r}, t \to \infty) = e^{-i\omega t}u(\mathbf{r}). \tag{C.2}$$

In the usual manner we Fourier-expand u in terms of spherical harmonics $Y_l^m(\theta, \varphi)$. But since orthogonality applies in the Mie problem, and the expansion of a plane wave involves just spherical harmonics with magnetic quantum number $m = 1$, we choose to work with the associated Legendre polynomials $P_l^1(\cos\theta)$, following Bohren & Huffman. Because of normalization differences, in lieu of G & K's equation 2.4 we have

$$u(\mathbf{r}) = \sum_{l=1}^{\infty} \frac{2l+1}{2l(l+1)} u_l(r) P_l^1(\cos\theta)\cos\varphi. \tag{C.3}$$

To summarize what G & K do, they show that an integral transform of u, $G_l[u]$, satisfies the one-dimensional wave equation. Using the fact that there are no fields at $t = 0$, they argue that $G_l[u]$ is outgoing and depends only on $r - ct/n$, and subsequently arrive at a boundary condition on u in Section 4. Subsequently, G & K derive a lemma (7.1) relating

ru to radial derivatives of $G_l[u]$, and use that to arrive at the following boundary condition at $r = R$, where R is the radius of the spherical surface over which we're applying the ABC:

$$\left(\partial_r + \frac{n}{c}\partial_t\right)[ru_l] = -\frac{(-1)^l}{r}\sum_{j=1}^{l}\frac{j\gamma_{lj}}{r^j}\left(\frac{n}{c}\partial_t\right)^{l-j} G_l[u_l]. \tag{C.4}$$

Here γ_{lj} is defined as

$$\gamma_{lj} = \begin{cases} \frac{(l+j)!}{(l-j)!j!2^j} & j \leq l \\ 0 & j > l. \end{cases} \tag{C.5}$$

We also need to solve an ODE for $w_l(t) \equiv G_l[u_l](a,t)$:

$$\left(\frac{n}{c}\partial_t\right)^l w_l(t) = (-1)^l R u_l(R,t) - \sum_{j=1}^{l}\frac{\gamma_{lj}}{R^j}\left(\frac{n}{c}\partial_t\right)^{l-j} w_l(t). \tag{C.6}$$

Here we can use our assumption of harmonic time dependence to good advantage: since $\frac{n}{c}\partial_t = -ink_0$, solving the ODE is trivial:

$$w_l(t) = \frac{R\left(\frac{1}{ink_0}\right)^l u_l}{1 + \sum_{j=1}^{l}\frac{\gamma_{lj}}{(-ink_0R)^j}}. \tag{C.7}$$

Therefore, our absorbing boundary condition (C.4) becomes

$$(\partial_r - ink_0)[ru_l(r)] = -\sum_{j=1}^{l}\frac{j\gamma_{lj}}{(-ink_0R)^j}\frac{1}{1 + \sum_{j=1}^{l}\frac{\gamma_{lj}}{(-ink_0R)^j}}u_l(r). \tag{C.8}$$

Our goal is to apply this ABC just outside a sphere of radius R. Defining the scattering size parameter $x \equiv nk_0R$, we introduce the following notation to simplify writing:

$$F_l \equiv \sum_{j=1}^{l}\frac{j\gamma_{lj}}{(-ix)^j}\frac{1}{1 + \sum_{j=1}^{l}\frac{\gamma_{lj}}{(-ix)^j}}. \tag{C.9}$$

We emphasize that the physical interpretation of the absorbing boundary condition, C.8,

is that the scattered fields are purely outgoing.

C.3.2 Determination of the Internal Field Coefficients

We here do not try to solve the full problem for the internal field for in the interfacial case we are ultimately interested in; that work is still in progress. We do, however, show that this is a viable path forward by explicitly rederiving the Lorenz-Mie solution using the ABC.

At this point we need to note a few notational differences that caused the author some confusion. If you compare the formulae for the scattering coefficients a_l and b_l on p. 123 of van de Hulst with p. 101 of Bohren & Huffman, they are identical. But, if you make the same comparison for the internal coefficients c_l and d_l, one finds that

$$c_{l,B\&H} = m d_{l,vdH} \tag{C.10}$$

$$d_{l,B\&H} = m c_{l,vdH} \tag{C.11}$$

where $m \equiv n_{part}/n_{med}$ is the relative refractive index. We will for now assume that all magnetic permeabilities are equal.

Let us begin therefore with solving for d_l, following van de Hulst's conventions aside from his time dependence, which is $e^{i\omega t}$ rather than $e^{-i\omega t}$. As usual we can expand the Debye potential v corresponding to an incident plane wave of unit amplitude as follows:

$$v_{inc} = \sin\varphi \sum_{l=1}^{\infty} i^l \left(\frac{2l+1}{l(l+1)} \right) j_l(nk_\circ r) P_l^1(\cos\theta). \tag{C.12}$$

Outside the particle, the scattered field can be written in a similar way, but with radial dependence via the spherical Hankel function of the first kind since these are (as $r \to \infty$) outgoing spherical waves:

$$v_{scat} = -\sin\varphi \sum_{l=1}^{\infty} i^l \left(\frac{2l+1}{l(l+1)} \right) h_l^{(1)}(nk_\circ r) P_l^1(\cos\theta) b_l. \tag{C.13}$$

We can expand the Debye potential for the field inside the sphere in an analogous manner.

Note that there's an extra factor of m:

$$v_{int} = \sin\varphi \sum_{l=1}^{\infty} i^l \left(\frac{2l+1}{l(l+1)} \right) m j_l(mnk_0 r) P_l^1(\cos\theta) d_l. \tag{C.14}$$

As van de Hulst argues, we must match the Debye potential v inside and outside the particle:

$$v_{int} = v_{inc} + v_{scat} \tag{C.15}$$

$$m j_l(mx) d_l = j_l(x) - h_l^{(1)}(x) b_l \tag{C.16}$$

for each l. Here $x \equiv nk_0 R$ is the size parameter. Now, here is our novel approach: instead of invoking the continuity of radial derivatives of v, we apply the absorbing boundary condition to v_{scat}. From matching v, we know that

$$v_{scat,l} = m j_l(mx) d_l - j_l(x). \tag{C.17}$$

Therefore, the ABC gives

$$(\partial_r - ink_0)[R v_{scat,l}] = -F_l v_{scat,l} \tag{C.18}$$

$$(1 - ix + F_l) v_{scat,l} + R\partial_r v_{scat,l} = 0. \tag{C.19}$$

Substitute (C.17) into the above:

$$(1 - ix + F_l)\left(m j_l(mx) d_l - j_l(x) \right) + m^2 x j_l'(mx) d_l - x j_l'(x) = 0 \tag{C.20}$$

$$(1 - ix + F_l) m j_l(mx) d_l + m^2 x j_l'(mx) d_l = (1 - ix + F_l) j_l(x) + x j_l'(x). \tag{C.21}$$

Therefore,

$$d_l = \frac{(1 - ix + F_l) j_l(x) + x j_l'(x)}{(1 - ix + F_l) m j_l(mx) + m^2 x j_l'(mx)}. \tag{C.22}$$

We now outline the derivation of the c_l coefficients, which proceeds in a largely similar way. We require the following boundary conditions on the total Debye potential u:

- mu must be continuous across any interface. Recall that $m = 1$ outside the sphere in the Mie problem.
- $\frac{1}{m}\frac{\partial(ru)}{\partial r}$ must be continuous.

See p. 123 of van de Hulst for these boundary conditions. In particular, it is not correct to merely say that $\frac{1}{m}\partial_r u$ must be continuous. These boundary conditions on mu and $\frac{1}{m}\partial_r(ru)$ come from requiring continuity of the tangential field components E_θ, E_φ, H_θ, and H_φ on the surface of the sphere.

From the continuity of mu, we obtain

$$u_{l,scat} = m^2 j_l(mx)c_l - j_l(x). \tag{C.23}$$

Using the continuity condition on $\frac{1}{m}\partial_r(ru)$,

$$\begin{aligned}
\partial_r(ru_{l,scat}) &= \frac{1}{m}\partial_r(ru_{l,int}) - \partial_r(ru_{l,inc}) && \text{(C.24)}\\
&= \frac{1}{m}u_{l,int} + \frac{1}{m}r\partial_r u_{l,int} - u_{l,inc} - r\partial_r u_{l,inc} && \text{(C.25)}\\
&= j_l(mx)c_l + \frac{1}{m}rmnk_0 j_l'(mx)c_l - j_l(x) - xj_l'(x) && \text{(C.26)}\\
&= \left(j_l(mx) + mxj_l'(mx)\right)c_l - j_l(x) - xj_l'(x). && \text{(C.27)}
\end{aligned}$$

We must now substitute into the ABC:

$$\partial_r(ru_{l,scat}) - ixu_{l,scat} + F_l u_{l,scat} = 0 \tag{C.28}$$

$$\left(j_l(mx) + mxj_l'(mx)\right)c_l - j_l(x) - xj_l'(x) - (ix - F_l)\left(m^2 j_l(mx)c_l - j_l(x)\right) = 0. \tag{C.29}$$

Rearranging to solve for c_l, we find

$$c_l = \frac{-(ix - F_l)j_l(x) + j_l(x) + xj_l'(x)}{j_l(mx) + mxj_l'(mx) - (ix - F_l)m^2 j_l(mx)}. \tag{C.30}$$

We must now show that the our expressions for d_l and c_l, (C.22) and (C.30), are equivalent to those derived in the conventional technique. It initially bothered the author that

these expressions do not contain any $h_l^{(1)}$, but we will see that this is not a problem.

For convenience, we will show that Bohren & Huffman's equations 4.52 on p. 100 are identical to our equations (C.22) and (C.30) subject to the correspondences noted at the beginning of Sec. C.3.2. Bohren & Huffman's formulas contain expressions of the form $[xh_l^{(1)}(x)]'$. We will make use of a theorem proven in another document:

$$[zh_l^{(1)}(z)]' = (iz - F_l)h_l^{(1)}(z). \tag{C.31}$$

Let us begin with Bohren & Huffman's expresion for c_l:

$$c_{l,B\&H} = \frac{j_l(x)[xh_l^{(1)}(x)]' - h_l^{(1)}(x)[xj_l(x)]'}{j_l(mx)[xh_l^{(1)}(x)]' - h_l^{(1)}(x)[mxj_l(mx)]'}. \tag{C.32}$$

Using the theorem (C.31),

$$c_{l,B\&H} = \frac{j_l(x)[(ix - F_l)h_l^{(1)}(x)] - h_l^{(1)}(x)[xj_l(x)]'}{j_l(mx)[(ix - F_l)h_l^{(1)}(x)] - h_l^{(1)}(x)[mxj_l(mx)]'} \tag{C.33}$$

$$= \frac{h_l^{(1)}(x)\left[(-1 + ix - F_l)j_l(x) - xj_l'(x)\right]}{h_l^{(1)}(x)\left[(-1 + ix - F_l)j_l(mx) - mxj_l'(mx)\right]} \tag{C.34}$$

$$= \frac{(1 - ix + F_l)j_l(x) + xj_l'(x)}{(1 - ix + F_l)j_l(mx) + mxj_l'(mx)}. \tag{C.35}$$

It is immediately apparent that the preceding expression is equal to m times our expression for d_l in Equation C.22), as we wanted to show.

We can similarly show that our expression for c_l (Equation C.30) is equivalent to the Bohren & Huffman expression for d_l. Using the spherical Hankel theorem, Equation C.31,

we obtain

$$c_l = \frac{-\frac{[xh_l^{(1)}(x)]'}{h_l^{(1)}(x)} j_l(x) + (j_l(x) + xj_l'(x))}{(j_l(mx) + mxj_l'(mx)) - \frac{[xh_l^{(1)}(x)]'}{h_l^{(1)}(x)} m^2 j_l(mx)} \tag{C.36}$$

$$= \frac{-[xh_l^{(1)}(x)]' j_l(x) + h_l^{(1)}(x)[xj_l(x)]'}{h_l^{(1)}(x)[mxj_l(mx)]' - m^2[xh_l^{(1)}(x)]' j_l(mx)}, \tag{C.37}$$

which indeed agrees with Bohren & Huffman's expression for d_l, up to a factor of m. This completes the proof that the ABC can reproduce the Lorenz-Mie solution, and suggests that it should be useful for attacking the more difficult interfacial scattering problem.

C.4 Generalized Optical Theorem

Another related problem we have considered is the derivation of a generalization of the Optical Theorem for the case of a particle breaching a liquid-liquid interface. The Optical Theorem relates the the extinction cross section σ_e of a scatterer to the scattering amplitude in the forward direction, and is useful for checking the results of scattering calculations. We give an outline of the derivation of the basic case here. Our work has been motivated in part by similar results obtained by Torrungrueng and co-workers [159].

C.4.1 Geometry

We recapitulate our geometrical setup here. In our coordinate system (Fig. C.4.1), the plane $z = 0$ corresponds to the interface between two media of indices n_1 ($z < 0$) and n_2 ($z > 0$), and corresponding magnetic permeabilities μ_1 and μ_2. We assume that a scattering particle straddles the interface. While Fig. C.4.1 is drawn such that the particle has its approximate center at the origin, we do not assume this.

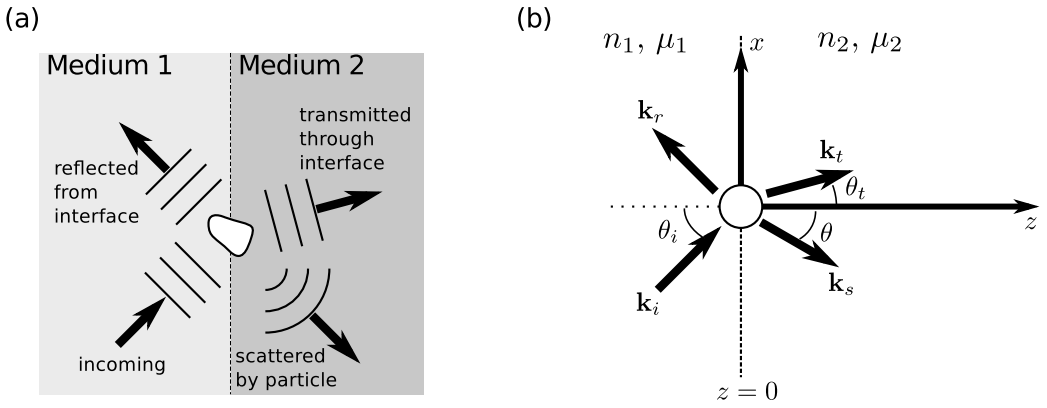

Figure C.4.1: (a) Schematic and (b) coordinate system for the particle and interface, as well as the directions of the incident, reflected, transmitted, and scattered fields.

C.4.2 Incident, reflected, and transmitted fields

We assume the system to be illuminated by a plane wave coming from the first medium (n_1, μ_1), propagating in the $+z$ direction. Its wave vector in the first medium is $\mathbf{k}_i = n_1 k_\circ (\cos\theta_i \hat{\mathbf{z}} + \sin\theta_i \hat{\mathbf{x}})$; that is, it travels in the (x, z) plane. We assume that the incident electric field has vector amplitude $\hat{\mathbf{E}}_{1,i}$. The magnitude of $\hat{\mathbf{E}}_{1,i}$ is unity (for convenience), and the direction indicates the polarization. We will only consider the case of no total internal reflection. Thus, when the wave hits the interface, it is partially reflected and partially transmitted. The amplitudes of the reflected $(\hat{\mathbf{E}}_{1,r})$ and transmitted $(\hat{\mathbf{E}}_{2,t})$ electric fields are determined by the Fresnel coefficients for the TE and TM components, and the directions by the Law of Reflection and Snell's Law. The associated magnetic fields are determined from Faraday's Law:

$$\nabla \times \mathbf{E} = -\frac{1}{c}\frac{\partial \mu \mathbf{H}}{\partial t} \rightarrow i\mathbf{k} \times \mathbf{E} = ik_\circ \mu \mathbf{H}$$
$$\mathbf{H} = \frac{\mathbf{k}}{\mu k_\circ} \times \mathbf{E} \tag{C.38}$$

The incident power is determined from the magnitude of the time-averaged Poynting vector $\langle \mathbf{S} \rangle = \frac{c}{2}\mathrm{Re}\,(\mathbf{E} \times \mathbf{H}^*)$. For notational convenience, we leave out the time-averaging brackets in what follows, and we let $c = 1$. Because $|\mathbf{B}| = n|\mathbf{E}| = \mu|\mathbf{H}|$, and the incident

field has unit amplitude, the incident power per unit area is:

$$I_{\text{inc}} = \frac{n_1}{2\mu_1} \tag{C.39}$$

This relation is needed at the end of the derivation, when we divide the scattered power by incident intensity to determine the cross-section.

To be consistent with derivations of the Optical Theorem in homogeneous media, we refer to the incident, reflected, and transmitted fields collectively as $\mathbf{E}_i$ and $\mathbf{H}_i$. While the reflected and transmitted fields are not, of course, "incident," they are independent of the scatterer. For clarity, we will henceforth refer to the incident field in the traditional sense as the *incoming field*.

C.4.3 Scattered fields

In the far field, the scattered fields $\mathbf{E}_s$ and $\mathbf{H}_s$ are:

$$\mathbf{E}_s = \boldsymbol{\xi}(\theta,\varphi)\frac{\exp(ink_o r)}{k_o r} = \left(\xi_\theta(\theta,\varphi)\hat{\boldsymbol{\theta}} + \xi_\varphi(\theta,\varphi)\hat{\boldsymbol{\phi}}\right)\frac{\exp(ink_o r)}{k_o r} \tag{C.40}$$

$$\mathbf{H}_s = \frac{n}{\mu}\hat{\mathbf{r}} \times \mathbf{E}_s \tag{C.41}$$

where $\boldsymbol{\xi}(\theta,\varphi)$ is the vector scattering amplitude for scattering in the (θ,φ) direction, and we have applied Faraday's Law to determine $\mathbf{H}_s$. We suppress the implied $e^{-i\omega t}$ dependence of all fields for convenience. Because the radiated fields are transverse, $\boldsymbol{\xi}$ has only θ and φ components.

C.5 Calculating the scattered power

C.5.1 The form of the key terms

We begin by considering the energy passing through a large imaginary sphere of radius r, centered at the origin and surrounding the particle. We assume $k_o r \gg 1$, so that the scattered fields on the sphere are in the far-field. The rate at which energy is absorbed inside

this sphere is given by the negative of the flux of the Poynting vector through the sphere:

$$W_a = -\frac{1}{2}\mathrm{Re}\left(\int_{4\pi}(\mathbf{E}\times\mathbf{H}^*)\cdot\hat{\mathbf{r}}r^2\,d\Omega\right)$$
$$= -\frac{1}{2}\mathrm{Re}\left(\int_{4\pi}(\mathbf{E}_i\times\mathbf{H}_i^* + \mathbf{E}_s\times\mathbf{H}_s^* + \mathbf{E}_i\times\mathbf{H}_s^* + \mathbf{E}_s\times\mathbf{H}_i^*)\cdot\hat{\mathbf{r}}r^2\,d\Omega\right) \quad \text{(C.42)}$$

where we have left out time-averaging brackets, since the effects of averaging are encompassed in the $\frac{1}{2}$ factor. The first term is the flux due to the incident, reflected (from the interface) and transmitted (through the interface) beams. Since medium 1 and medium 2 are assumed to be non-absorbing, this term integrates to zero. The second term is the negative of the scattered power W_s. The two remaining terms are due to interference between the scattered field and the other fields, which manifests as extinction. Thus:

$$W_a + W_s = W_{ext} = -\frac{1}{2}\mathrm{Re}\left(\int_{4\pi}(\mathbf{E}_i\times\mathbf{H}_s^* + \mathbf{E}_s\times\mathbf{H}_i^*)\cdot\hat{\mathbf{r}}r^2\,d\Omega\right) \quad \text{(C.43)}$$

Since $|\mathbf{k}|/k_\circ = n$, the first term on the right side of Eq. C.43 simplifies to:

$$\hat{\mathbf{r}}\cdot(\mathbf{E}_i\times\mathbf{H}_s^*) = -\mathbf{E}_i\cdot(\hat{\mathbf{r}}\times\mathbf{H}_s^*) =$$
$$-\mathbf{E}_i\cdot\left(\hat{\mathbf{r}}\times\left(\hat{\mathbf{r}}\times\frac{n}{\mu}\mathbf{E}_s^*\right)\right) = \frac{n}{\mu}\mathbf{E}_i\cdot\mathbf{E}_s^* \quad \text{(C.44)}$$

The first step follows from the triple scalar product rule. In the last step, the two cross products of the scattered field with $\hat{\mathbf{r}}$ yield the scattered field (with a minus sign) because $\hat{\mathbf{r}}$ is perpendicular to the field and has unit magnitude.

The second term of Eq. C.43 is similar to the first term, but with the electric and magnetic fields interchanged. We now show that this term has the same magnitude as the first term. In the far-field, the scattered electric and magnetic fields, like the incident fields, are both transverse to the direction of propagation, and are mutually perpendicular to each other. Their magnitudes are also equal, up to a factor of n. Consequently, swapping $\mathbf{E}_i$ for $\mathbf{H}_i$ and $\mathbf{E}_s$ for $\mathbf{H}_s$ does not change the magnitude of the cross product, as one swap gives a factor of n and the other gives a factor of $1/n$, resulting in cancellation under multiplication. (This is only true in the far-field; in the near-field, the electric and magnetic fields can decouple.)

Alternately, if one thinks of the fields as superpositions of plane waves in Fourier space, swapping the electric and magnetic fields amounts to flipping all polarizations, which does not change any relative orientations. Consequently, in the far-field, both vector terms in the integrand Eq. C.43 should have equal magnitude.

However, when electric and magnetic fields are interchanged, there is a sign ambiguity that needs to be considered for determining the sign of the dot product with $\hat{\mathbf{r}}$. In anticipation of the key result of this paper – that the values of the key integrals, Eq. C.43, are proportional to the value of the scattering amplitude in the directions of the "incident" plane waves probing the scatterer – we consider the scattering amplitude in the second term of Eq. C.43 for those directions.

There are two physical possibilities that result in different signs: the "incident" plane wave and the scattered wave can propagate in either the same direction or in opposite directions. For $\mathbf{E}_i$ and $\mathbf{H}_i$ arising from the transmitted and reflected plane waves, in the far-field, the scattered field and the relevant plane wave both propagate in the same direction. Thus, $\mathbf{E}_i \times \mathbf{H}_s^*$ and $\mathbf{E}_s \times \mathbf{H}_i^*$ both yield vectors pointing in the same direction, and as already argued, both of these cross products have the same magnitude (up to complex conjugation) (Fig. C.5.1a). At most, scattering can rotate the scattered field relative to the "incident" field, so that the angle between $\mathbf{E}_s$ and $\mathbf{H}_i$ is the same as the angle between $\mathbf{E}_i$ and $\mathbf{H}_s$. In the direction of the incoming plane wave, however, the scattered field and incoming field transport energy in opposite directions. Consequently, the angle between $\mathbf{E}_s$ and $\mathbf{H}_i$ differs from the angle between $\mathbf{E}_i$ and $\mathbf{H}_s$ by 180 degrees, and swapping the fields introduces a minus sign in the cross product (Fig. C.5.1b).

We therefore have the following relation for the second term in Eq. C.43:

$$\hat{\mathbf{r}} \cdot \mathbf{E}_s \times \mathbf{H}_i^* = \pm \frac{n}{\mu} \mathbf{E}_i^* \cdot \mathbf{E}_s \tag{C.45}$$

that is, plus (for the reflected and transmitted waves) or minus (for the incoming wave) the complex conjugate of the result in Eq. C.44 for the first term. When both terms in Eq. C.43 have the same sign, adding Eq. C.44 to its complex conjugate will give twice its real part. When the second term has a minus sign, we will get $2i$ times the imaginary part of

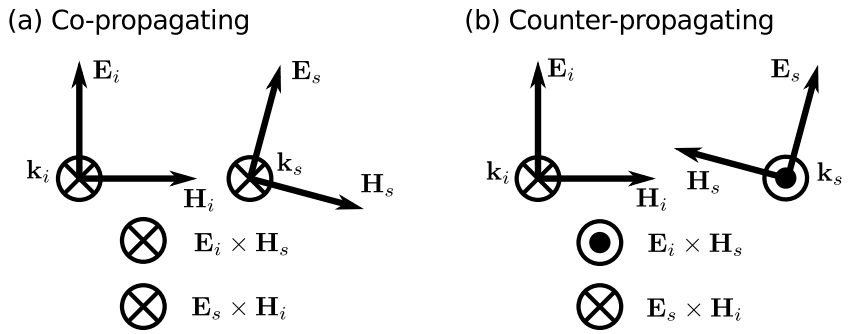

Figure C.5.1: Mutual orientations of $\mathbf{E}_i$ and $\mathbf{H}_s$, and $\mathbf{E}_s$ and $\mathbf{H}_i$, for "incident" and scattered fields that are co-propagating or counter-propagating. All vectors in each part exist at the same physical point, but have been separated for clarity. (a) The "incident" and scattered fields propagate in the same direction, so both $\mathbf{E}_i \times \mathbf{H}_s$ and $\mathbf{E}_s \times \mathbf{H}_i$ point in the same direction. (b) The "incident" and scattered fields propagate in opposite directions; $\mathbf{E}_i \times \mathbf{H}_s$ and $\mathbf{E}_s \times \mathbf{H}_i$ point in opposite directions.

Eq. C.44. Ultimately, after evaluating the integrals in Eq. C.43, we will take the real part to get a physical extinction power, and the imaginary part will not contribute. Consequently, in the integrals in Eq. C.43, rather than having to consider three contributions to $\mathbf{E}_i$, we need only consider the contributions from the transmitted and reflected plane waves. We need not consider contributions to $\mathbf{E}_i$ from the incoming wave.

C.5.2 The key integral

To evaluate the integral in Eq. C.43, we consider each medium separately. We consider only the first term, since the second term has equal magnitude, as argued above. For convenience, we change the coordinate system from that shown in Fig. C.4.1. We will separately consider the contributions to $\mathbf{E}_i$ from the transmitted and reflected plane waves, and for each of these plane waves choose the z axis to be parallel to the direction of propagation. This makes it easy to express the plane waves as $e^{ink_\circ r\cos\theta}$, but complicates the limits of integration. The outgoing fields remain in the form $(\boldsymbol{\xi}(\theta,\varphi)/k_\circ r)\exp ink_\circ r$.

Referring to Eq. C.43, we thus have to compute integrals of the form:

$$\int_{\text{medium}} \mathbf{E}_i \cdot \mathbf{E}_s^*\, r^2\, d\Omega = \int_\varphi \int_{\text{interface}}^{\cos\theta=1} \frac{1}{k_\circ r}\boldsymbol{\xi}^*(\theta,\varphi)\cdot\mathbf{E}_\circ e^{-ink_\circ r(1-\cos\theta)} r^2\, d\cos\theta\, d\varphi \quad \text{(C.46)}$$

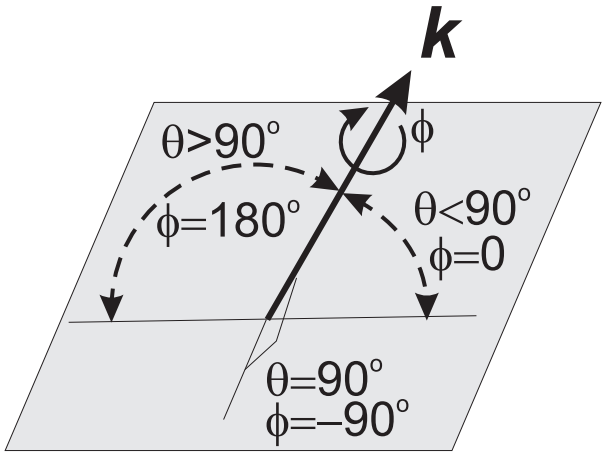

Figure C.5.2: The polar angle θ (measured with respect to the $\mathbf{k}$ vector) at the interface depends on the azimuthal angle φ.

where $\mathbf{E}_o$ is the amplitude of the appropriate plane wave. The lower limit on θ depends on the value of φ, as shown in Fig. C.5.2.

We first do the integral over $\cos\theta$, integrating by parts:

$$\int_{\text{medium}} \mathbf{E}_i \cdot \mathbf{E}_s^* \, r^2 \, d\Omega = \int_\varphi \boldsymbol{\xi}^*(\theta,\varphi) \cdot \mathbf{E}_o \frac{e^{-ink_o r(1-\cos\theta)}}{ink_o^2}\bigg|_{\text{interface}}^{\cos\theta=1} d\varphi$$
$$- \int_\varphi \int_{\text{interface}}^{\cos\theta=1} \frac{1}{ink_o^2} \frac{\partial \boldsymbol{\xi}^*(\theta,\varphi)}{\partial \cos\theta} \cdot \mathbf{E}_o e^{-ink_o r(1-\cos\theta)} \, d\cos\theta \, d\varphi \qquad \text{(C.47)}$$

Only the first term in Eq. C.47, the boundary term from integrating by parts, survives in the far field. In the boundary term, a factor of $1/r$ from the asymptotic dependence of the fields and an additional factor of $1/r$ from integrating the exponential together cancel the factor of r^2 from integrating over area. The second term of Eq. C.47 vanishes in the far field: further integration by parts would result in two more terms each with an additional factor of $1/r$.

The boundary term in Eq. C.47 is straightforward to evaluate at the upper bound. Subsequently, integration over φ – around the pole in spherical coordinates – gives a factor of

2π, since $\boldsymbol{\xi}$ is independent of φ at $\theta = 0$. We therefore obtain

$$\int_{\text{medium}} \mathbf{E}_i \cdot \mathbf{E}_s^* \, r^2 \, d\Omega = 2\pi \frac{\boldsymbol{\xi}^*(\theta, \varphi) \cdot \mathbf{E}_0}{ink_0^2} + \text{interface term.} \tag{C.48}$$

The first term on the right comes from the upper bound, and there is an additional contribution from evaluating the boundary term in Eq. C.47 at the lower bound, which occurs at the interface.

Evaluating the interface term results in a serious problem. Components of the "incident" and scattered fields parallel to the interface must be continuous across the interface. The Fresnel coefficients enforce this condition for the "incident" plane waves, and we require $\boldsymbol{\xi}$ to be continuous across the interface. However, $\exp ink_0 r(1 - \cos\theta)$ is not continuous across the interface. Consequently, the terms in each medium arising from evaluating Eq. C.47 at the interface do not cancel each other unless the media have the same refractive index. We thus have a result for the extinction power that depends on r, which is clearly unphysical.

It is tempting to assume that these terms at the interface vanish upon integration over φ, since the integrand contains a rapidly-oscillating exponential. But for incident beams that are normal or nearly normal to the interface, θ is approximately 90° at the interface, and the $1 - \cos\theta$ factor in the exponent (approximately 1) depends only weakly on φ when integrating around the interface. Integrating over φ only gives a vanishing result if $\exp nk_0 r(1 - \cos\theta)$ oscillates more rapidly than $\boldsymbol{\xi}(\boldsymbol{\theta}, \boldsymbol{\varphi})$ as a function of φ. For an off-normal incoming wave and $r \to \infty$ this condition is satisfied, but not for a normal incoming wave. Likewise, for an incoming wave that is close to normal incidence, the extinction power could oscillate as a function of r at distances out to $\lambda/\Delta\theta$ (where $\Delta\theta$ is the deviation from normal incidence). For small $\Delta\theta$ this oscillation of the extinction power could thus persist at distances typically associated with the far-field. Consequently, we have the potential for unphysical oscillatory dependence of the extinction power on r in the far-field.

The only resolution of this problem is to require that $\boldsymbol{\xi}$ be zero at the interface. With this condition in hand, we conclude that the value of the key integral, Eq. C.46, is given (in the

limit of large r) by Eq. C.48:

$$\int_{\text{medium}} \mathbf{E}_i \cdot \mathbf{E}_s^* \, r^2 \, d\Omega = \frac{2\pi}{ink_o^2} \boldsymbol{\xi}^*(\theta, \varphi) \cdot \mathbf{E}_o. \tag{C.49}$$

C.5.3 The generalized Optical Theorem

To go from the key integral, Eq. C.49, to the generalized Optical Theorem, we apply the following steps. We already showed in C.5.1 that we only need to consider the reflected and transmitted contributions to the "incident" wave $\mathbf{E}_i$. From Eq. C.43 and the results of C.5.1, for these two contributions, we add the complex conjugate of the result in Eq. C.49, yielding twice the real part. This factor of 2 cancels a factor of $1/2$ from computing a time average. Moreover, we have a prefactor of n/μ in front of the integrand in the key integral. We thus obtain

$$\begin{aligned} W_{ext} &= -\frac{2\pi}{k_o^2} \text{Re} \left(\frac{1}{i\mu_2} \boldsymbol{\xi}^*(\mathbf{k}_t) \cdot \mathbf{E}_{2,t} + \frac{1}{i\mu_1} \boldsymbol{\xi}^*(\mathbf{k}_r) \cdot \mathbf{E}_{1,r} \right) \\ &= -\frac{2\pi}{k_o^2} \text{Im} \left(\frac{1}{\mu_2} \boldsymbol{\xi}^*(\mathbf{k}_t) \cdot \mathbf{E}_{2,t} + \frac{1}{\mu_1} \boldsymbol{\xi}^*(\mathbf{k}_r) \cdot \mathbf{E}_{1,r} \right). \end{aligned} \tag{C.50}$$

Here, $\mathbf{E}_{1,r}$ is the reflected plane wave in medium 1 and $\mathbf{E}_{2,t}$ is the transmitted plane wave in medium 2. Since the Fresnel coefficients are real, the "incident" fields have real amplitudes, and we can re-express this in terms of $\boldsymbol{\xi}$ at the expense of a minus sign:

$$W_{ext} = \frac{2\pi}{k_o^2} \text{Im} \left(\frac{1}{\mu_2} \boldsymbol{\xi}(\mathbf{k}_t) \cdot \mathbf{E}_{2,t} + \frac{1}{\mu_1} \boldsymbol{\xi}(\mathbf{k}_r) \cdot \mathbf{E}_{1,r} \right). \tag{C.51}$$

To go from power to cross-section we divide by the intensity of the incident beam, which is $\mu_1/2n_1$, according to Eq. C.39. We find that the extinction cross-section is:

$$\sigma_e = \frac{4\pi n_1}{\mu_1 k_o^2} \text{Im} \left(\frac{1}{\mu_2} \boldsymbol{\xi}(\mathbf{k}_t) \cdot \mathbf{E}_{2,t} + \frac{1}{\mu_1} \boldsymbol{\xi}(\mathbf{k}_r) \cdot \mathbf{E}_{1,r} \right). \tag{C.52}$$

This result, our generalized Optical Theorem, is equivalent to that of Torrungrueng *et al.* [159] and reduces to the traditional Optical Theorem in the absence of an interface, when

there is no reflected plane wave. The incoming polarization and the Fresnel coefficients determine $\mathbf{E}_{1,r}$ and $\mathbf{E}_{2,t}$. Other conventions for the assumed forms of the "incident" plane waves and scattered wave could lead to slightly different factors of n, 2, and π, and possibly the replacement of the real part with the imaginary part, depending on the definition of $\boldsymbol{\xi}$. The key point remains that the extinction cross-section is determined by the scattering amplitude in the directions of the transmitted and reflected plane waves.

D

Studying Inertial Focusing with Holography: Modeling Motion Blur

We discuss in this chapter aspects of a side project that the author has worked on in collaboration with Anna Wang and with Joseph Martel, a student in Mehmet Toner's laboratory at the Massachusetts General Hospital. We do not go into details of the complex but fascinating fluid dynamics underlying the inertial focusing phenomena that motivated this work. We do, however, discuss the modeling of holograms of rapidly moving particles. We discuss some aspects of this problem that have not been published elsewhere, and in particular address a blurring technique based on Fourier transforms that has not previously been applied to holograms. These techniques enable the measurement of the 3D position as well as velocity of a rapidly moving colloidal particle.

D.1 Introduction to Inertial Focusing

Imagine flowing a colloidal suspension down a microfluidic channel – for instance, a cylindrical glass capillary with a radius R of say 50 μm. In a dilute colloidal suspension, the particles are not structured in any way. So, if the suspension initially starts flowing through the capillary with the particle positions randomly dispersed through a cross section of the capillary, one would expect to obtain a random distribution further down the capillary. This intuition is correct for sufficiently slow flows, but it turns out to be wrong for fast fluidic flows. For in such cases, inertial focusing can occur: the particles will eventually all be found to lie within an annulus located at a radial distance of $\sim 0.6R$ from the centerline of the channel [160–162]. Such phenomena were first observed in the early 1960's by Segre and Silberberg [160, 161], although the first good theoretical explanations did not come until the 1980's [163]. It turns out that in addition to the drag forces from the fluid on the particles, the presence of the capillary walls results in lift forces on the particles, which result in the inertial focusing. Similar focusing effects happen in rectangular channels, where the particles focus to four symmetric points in the channel cross section [164].

These phenomena are difficult to study quantitatively because in modeling them, the standard simplifying assumptions of fluid dynamics are invalid. The viscosity η of the fluid cannot be neglected, but the fluid inertia cannot be neglected either. It is thus necessary to solve the full Navier-Stokes equations in some manner, generally perturbatively. We refer the interested reader to the review by Di Carlo for further details and references [162].

Additional phenomena can occur in curved channels, as the curvature induces a secondary Dean circulating flow. The Dean flow results in drag forces perpendicular to the direction of the principal flow down the channel and can change the positions to which particles focus [165]. The positions to which particles focus depend on parameters that include the particle size; it is therefore hoped that such physical effects could be the basis for marker-free cell sorting technologies. The detailed physical mechanisms of these effects remain under active investigation.

One problem that has arisen in the course of such investigations is illustrated in Figure D.1.1, from [165]. The figure shows a fluorescence streak micrograph that contains many particles; the particle velocity is high enough relative to the shutter time that the particles

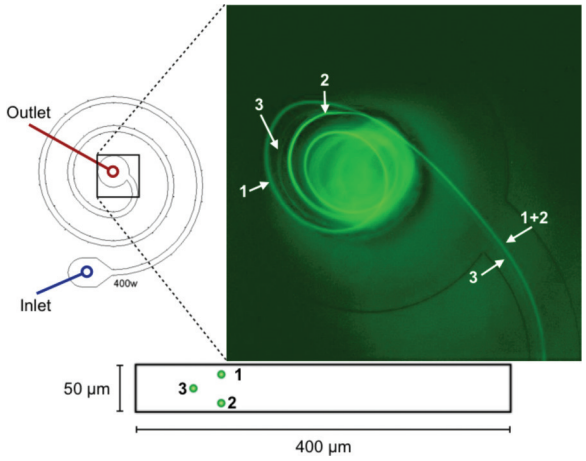

Figure D.1.1: Schematic diagram and fluorescence streak micrograph of particle separation during flow in a curved channel. A dilute suspension of fluorescent particles flows through a spiral channel. At sufficiently high flow rates, the particles localize to one of the three indicated positions in the channel cross-section. Positions 1 and 2 mirror each other vertically; this is not visible within the channel and is only qualitatively observed at the outlet. Reprinted with permission from [165]. Copyright 2012, American Institute of Physics.

appear as continuous streaks. Under the flow conditions in the figure, the particles appear to focus to three positions in the channel, where two of the positions are vertically on top of each other. It is not possible to quantitatively determine the height of these positions (labeled 1 and 2) just with fluorescence microscopy. We therefore investigated holographic microscopy as a potential solution.

Preliminary experiments using a Phantom V9 high speed camera with a minimum shutter time of 1μs soon revealed that at typical flow rates, the particle holograms did not qualitatively resemble holograms of stationary particles. This was due to the particles, moving at speeds of $\sim$ 1 m/s in the channel, travelling appreciably over the shutter time of the camera. A typical experimentally recorded blurred hologram is shown in Figure D.1.2. Effects of moving particles in holography were first investigated by Dixon *et al.* [166], who used a phenomenological model based on a decrease in contrast of the hologram fringes to model the blurring. Here we describe two methods we have developed to model blurred

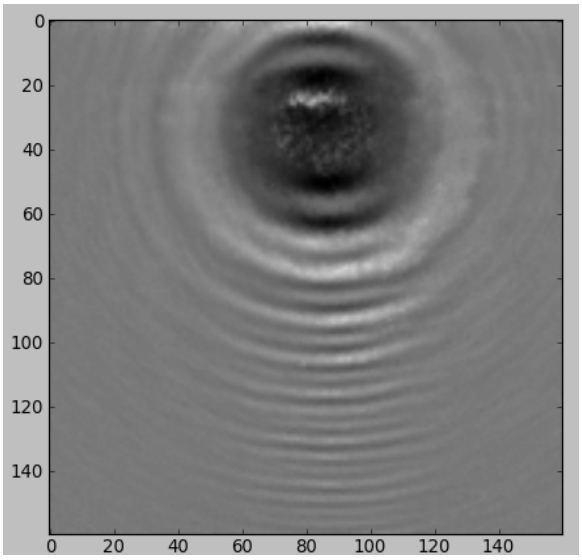

Figure D.1.2: Experimentally recorded hologram of a polystyrene particle moving from left to right. The motion causes the hologram fringes in the direction of motion to be blurred.

holograms and present some initial results obtained therein.

D.2 Simple Blurring Algorithm

The main thing to note about motion blurring in holograms is that it results from a superposition of *intensities* and not of fields, as in the case of the Mie superposition approximation. Blurring, in this picture, merely amounts to the adding up of holograms calculated for a particle at different positions.

Consider a particle that at $t = 0$ is at $\mathbf{r} = \mathbf{r}_0$. If the particle moves with velocity $\mathbf{v}$, its position at an instant Δt later is just $\mathbf{r}_0 + \mathbf{v}\Delta t$. If the camera has an exposure time of T, we may compute n holograms at evenly spaced time intervals between 0 and T. We use a dimensionless number β to determine the number of holograms to be summed:

$$n = \frac{\beta |\mathbf{v}| T}{\lambda_{med}} \tag{D.1}$$

where λ_{med} is the incident wavelength in the medium. We typically find $\beta = 4$ adequate (4

holograms per wavelength traveled by the particle). We compute the n holograms and then divide their sum by n to model the blurring. This approach is rigorous, involving no phenomenological models, and works well, but has the diadvantage of being computationally intensive, particularly for the $\sim$ 10 μm particles typically used in experiments. Many scattering quantities are redundantly computed. We therefore describe an alternate method for modeling blurring that is computationally much more efficient.

D.3 Fourier Transform Blurring Algorithm

The simple blurring model is inefficient because it involves making many redundant computations of scattering. A much more efficient approach, without these redundancies, is given by Potmesil and Chakravorty [167]. This approach is less general than the simple blurring algorithm, in that it can only be applied to lateral particle motions (in x and y), but that is not a limitation for the intertial focusing experiments.

The Potmesil & Chakravorty algorithm applies to any image of moving objects, not just holograms, so our discussion here will not assume we are dealing with holograms[1]. In the algorithm, motion blur is regarded as a convolution. Adopting their notation, let $f(x', y')$ be an image of a stationary object that is to be blurred, and let $g(x'', y'')$ denote the blurred image. Any pixel in the blurred image will be an integral over portions of the unblurred image:

$$g(x'', y'') = \frac{1}{T} \int_0^T f(x(t), y(t))\, dt. \tag{D.2}$$

Here $x(t)$ and $y(t)$ denote the positions in the unblurred image that are mapped to (x'', y'') in the blurred image at time t. In particular, for a velocity $\mathbf{v} = v_x\hat{\mathbf{x}} + v_y\hat{\mathbf{y}}$,

$$x(t) = x'' - v_x t;\ \ y(t) = y'' - v_y t. \tag{D.3}$$

In this way, Equation D.2 can be written as a convolution integral:

$$g(x'', y'') = \frac{1}{T} \int_0^T \iint f(x', y')\delta(x' - x(t), y' - y(t))\, dx'dy'\, dt \tag{D.4}$$

[1] The original paper [167] applies the algorithm to images, including a picture of a house.

where the spatial integrals run over the image f. It follows that we can Fourier transform into the reciprocal space (u, v) where the convolution becomes a product. We use Equation D.3 to evaluate the trivial integrals over x' and y', and do Fourier transform integrals over x'' and y'':

$$\begin{aligned} G(u,v) &= \iint g(x'',y'') \exp[-2\pi i(ux'', vy'')]\, dx''dy'' \\ &= \frac{1}{T}\iint \int_0^T f(x''-v_x t, y''-v_y t) \exp[-2\pi i(ux'', vy'')]\, dx''dy''\, dt. \end{aligned} \tag{D.5}$$

If we define constants a and b via $v_x = a/T$ and $v_y = b/T$, we can apply the translation property of Fourier transforms:

$$G(u,v) = \frac{1}{T}F(u,v)\int_0^T \exp\left[-2\pi i(ua+vb)\frac{t}{T}\right]\, dt \tag{D.6}$$

where $F(u, v)$ is the Fourier transform of f. This is clearly a product between $F(u, v)$ and a transfer function $H(u, v)$:

$$H(u,v) = \frac{1}{T}\int_0^T \exp\left[-2\pi i(ua+vb)\frac{t}{T}\right]\, dt. \tag{D.7}$$

This integral may be evaluated to give

$$H(u,v) = \frac{\sin\left(\pi(ua+vb)\right)}{\pi(ua+vb)}\exp[-i\pi(ua+vb)]. \tag{D.8}$$

Blurred holograms h_{blur} may thus be calculated in the following way:

1. Calculate a hologram h of a particle located at $\mathbf{r} = \mathbf{r}_0$.
2. Compute the fast Fourier transform of h.
3. Multiply by the transfer function in Equation D.8.
4. Compute the inverse fast Fourier transform to obtain h_{blur}.

D.4 Preliminary Results

A series of preliminary experiments have been conducted using microfluidic devices fabricated by Joseph Martel and samples of polystyrene spheres in an aqueous solution density-matched with iodixanol. Data has been taken with particles with diameters of 5, 10 and 15 μm. We collect data by continuously recording high-speed movies of flow through a channel using a Phantom V9 camera with typical exposure times of 1 μs and frame rates of 6600 frames per second. The samples are sufficiently dilute that most of the recorded frames contain no particles; we select the frames that do. Furthermore, the particles move rapidly enough that each particle typically appears in only a single frame. We first show, in Figure D.4.1, that using the simple blurring model, we can successfully fit holograms of rapidly moving particles. The fits depend on the particle 3D position as well as the particle velocity (assumed to be in one horizontal direction). While the 3D position information is what we need to study inertial focusing, getting particle velocities is a useful by-product.

By looking at many particles in the channel, we can successfully measure distributions of particle heights. Figure D.4.2 shows a bimodal height distribution; this is readily observed using DHM and an appropriate scattering model, but almost impossible to obtain quantitatively using streak microscopy.

Finally, we show that the rapid blurring algorithm based on Fourier transforms gives results that are the same as the simple blurring model. Preliminary tests indicate that the transform method is more than an order of magnitude computationally faster, particularly with large particles that move several wavelengths during the exposure time. Figure D.4.3 compares two holograms computed using the simple and Fourier transform techniques; the images agree with each other to 0.1%.

Further experiments and analysis are in progress; in particular, the tremendous computational speed enhancement gained through the Potmesil-Chakravorty method should make further fits much less tedious.

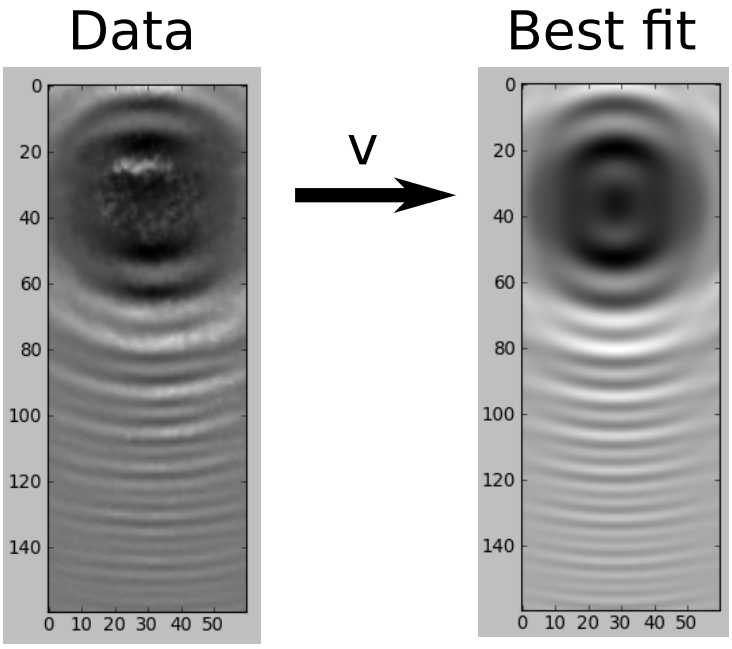

Figure D.4.1: Hologram of a 10 μm diameter particle flowing in a channel. Image has been cropped to remove fringes from non-index matched microfluidic channel walls. The particle moves to the right at 3.3 m/s, where the speed has been determined from fitting a moving sphere model to the hologram.

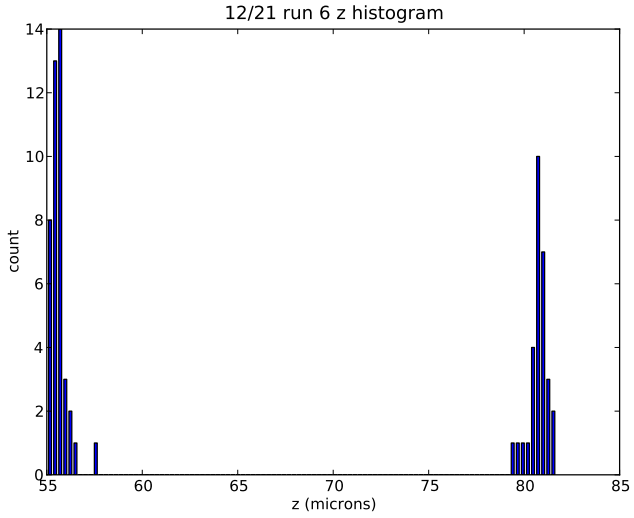

Figure D.4.2: Bimodal distribution of particle heights in a channel; heights determined using DHM.

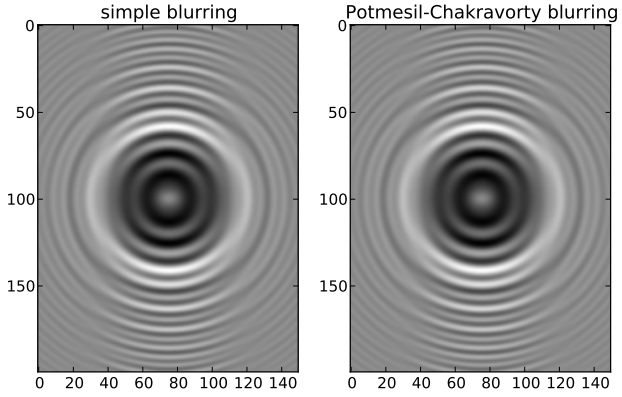

Figure D.4.3: Simulated holograms of a 10 μm diameter polystyrene sphere moving to the right at $v_y = 2$ m/s. Left: computation using simple blurring algorithm. Right: computation using Potmesil-Chakravorty Fourier transform algorithm.

References

[1] P. N. Pusey and W. van Megen. Phase behaviour of concentrated suspensions of nearly hard colloidal spheres. *Nature*, 320(6060):340–342, March 1986.

[2] Ki-Chang Lee and Han-Ah Wi. Highly crosslinked micron-sized, monodispersed polystyrene particles by batch dispersion polymerization, part 1: Batch, delayed addition, and seeded batch processes. *Journal of Applied Polymer Science*, 115(1):297–307, 2010.

[3] Nicholas Metropolis, Arianna W. Rosenbluth, Marshall N. Rosenbluth, Augusta H. Teller, and Edward Teller. Equation of state calculations by fast computing machines. *The Journal of Chemical Physics*, 21(6):1087, June 1953.

[4] Eric R. Weeks, J. C. Crocker, Andrew C. Levitt, Andrew Schofield, and D. A. Weitz. Three-dimensional direct imaging of structural relaxation near the colloidal glass transition. *Science*, 287(5453):627–631, January 2000.

[5] A. M. Alsayed, M. F. Islam, J. Zhang, P. J. Collings, and A. G. Yodh. Premelting at defects within bulk colloidal crystals. *Science*, 309(5738):1207–1210, August 2005.

[6] Vinothan N. Manoharan, Mark T. Elsesser, and David J. Pine. Dense packing and symmetry in small clusters of microspheres. *Science*, 301(5632):483–487, July 2003.

[7] Eric Lauga and Michael P. Brenner. Evaporation-driven assembly of colloidal particles. *Physical Review Letters*, 93(23):238301, December 2004.

[8] Guangnan Meng, Natalie Arkus, Michael P. Brenner, and Vinothan N. Manoharan. The free-energy landscape of clusters of attractive hard spheres. *Science*, 327(5965):560–563, January 2010.

[9] Rebecca W. Perry, Guangnan Meng, Thomas G. Dimiduk, Jerome Fung, and Vinothan N. Manoharan. Real-space studies of the structure and dynamics of self-assembled colloidal clusters. *Faraday Discuss.*, 159(1):211–234, March 2012.

[10] Sharon C. Glotzer and Michael J. Solomon. Anisotropy of building blocks and their assembly into complex structures. *Nature Materials*, 6(8):557–562, August 2007.

[11] Yaroslav A. Urzhumov, Gennady Shvets, Jonathan A. Fan, Federico Capasso, Daniel Brandl, and Peter Nordlander. Plasmonic nanoclusters: a path towards negative-index metafluids. *Optics Express*, 15(21):14129–14145, October 2007.

[12] J. C Crocker and D. G Grier. Methods of digital video microscopy for colloidal studies. *Journal of Colloid and Interface Science*, 179(1):298–310, 1996.

[13] Piotr Habdas and Eric R. Weeks. Video microscopy of colloidal suspensions and colloidal crystals. *Current Opinion in Colloid & Interface Science*, 7(3–4):196–203, August 2002.

[14] V. Prasad, D. Semwogerere, and Eric R. Weeks. Confocal microscopy of colloids. *Journal of Physics: Condensed Matter*, 19(11):113102, March 2007.

[15] Akira Kose, Masataka Ozaki, Kaoru Takano, Yoko Kobayashi, and Sei Hachisu. Direct observation of ordered latex suspension by metallurgical microscope. *Journal of Colloid and Interface Science*, 44(2):330–338, August 1973.

[16] Pawel Pieranski. Two-dimensional interfacial colloidal crystals. *Physical Review Letters*, 45(7):569—572, 1980.

[17] Pawel Pieranski, L. Strzelecki, and B. Pansu. Thin colloidal crystals. *Physical Review Letters*, 50(12):900–903, March 1983.

[18] David H. Van Winkle and C. A. Murray. Layering transitions in colloidal crystals as observed by diffraction and direct-lattice imaging. *Physical Review A*, 34(1):562–573, July 1986.

[19] C. A. Murray, W. O. Sprenger, and R. A. Wenk. Comparison of melting in three and two dimensions: Microscopy of colloidal spheres. *Physical Review B*, 42(1):688–703, July 1990.

[20] David G. Grier and Cherry A. Murray. The microscopic dynamics of freezing in supercooled colloidal fluids. *The Journal of Chemical Physics*, 100(12):9088–9095, June 1994.

[21] Alexandros Pertsinidis and X. S. Ling. Diffusion of point defects in two-dimensional colloidal crystals. *Nature*, 413(6852):147–150, September 2001.

[22] Jean Perrin. Mouvement brownien et réalité moléculaire. *Annales de Chimie et de Physique*, 18:1–114, 1909.

[23] Bruce J. Berne and Robert Pecora. *Dynamic Light Scattering: With Applications to Chemistry, Biology, and Physics*. Wiley, 1976.

[24] T. G. Mason and D. A. Weitz. Optical measurements of frequency-dependent linear viscoelastic moduli of complex fluids. *Physical Review Letters*, 74(7):1250–1253, February 1995.

[25] T. G. Mason, K. Ganesan, J. H. van Zanten, D. Wirtz, and S. C. Kuo. Particle tracking microrheology of complex fluids. *Physical Review Letters*, 79(17):3282–3285, October 1997.

[26] Joshua Apgar, Yiider Tseng, Elena Fedorov, Matthew B. Herwig, Steve C. Almo, and Denis Wirtz. Multiple-particle tracking measurements of heterogeneities in solutions of actin filaments and actin bundles. *Biophysical Journal*, 79(2):1095–1106, August 2000.

[27] M. T. Valentine, P. D. Kaplan, D. Thota, J. C. Crocker, T. Gisler, R. K. Prud'homme, M. Beck, and D. A. Weitz. Investigating the microenvironments of inhomogeneous soft materials with multiple particle tracking. *Physical Review E*, 64(6):061506, November 2001.

[28] Yiider Tseng, Thomas P. Kole, and Denis Wirtz. Micromechanical mapping of live cells by multiple-particle-tracking microrheology. *Biophysical Journal*, 83(6):3162, December 2002.

[29] Y. Han, A. M. Alsayed, M. Nobili, J. Zhang, T. C. Lubensky, and A. G. Yodh. Brownian motion of an ellipsoid. *Science*, 314(5799):626–630, October 2006.

[30] David Chandler. *Introduction To Modern Statistical Mechanics*. Oxford University Press, Incorporated, 1987.

[31] Grace Martinelli Kepler and Seth Fraden. Attractive potential between confined colloids at low ionic strength. *Physical Review Letters*, 73(2):356–359, July 1994.

[32] M. G. Nikolaides, A. R. Bausch, M. F. Hsu, A. D. Dinsmore, M. P. Brenner, C. Gay, and D. A. Weitz. Electric-field-induced capillary attraction between like-charged particles at liquid interfaces. *Nature*, 420(6913):299–301, November 2002.

[33] A. Ashkin, J. M. Dziedzic, J. E. Bjorkholm, and Steven Chu. Observation of a single-beam gradient force optical trap for dielectric particles. *Optics Letters*, 11(5):288–290, May 1986.

[34] J. C. Crocker, J. A. Matteo, A. D. Dinsmore, and A. G. Yodh. Entropic attraction and repulsion in binary colloids probed with a line optical tweezer. *Physical Review Letters*, 82(21):4352, May 1999.

[35] W. Benjamin Rogers and John C. Crocker. Direct measurements of DNA-mediated colloidal interactions and their quantitative modeling. *Proceedings of the National Academy of Sciences*, September 2011.

[36] John C. Crocker and David G. Grier. Microscopic measurement of the pair interaction potential of charge-stabilized colloid. *Physical Review Letters*, 73(2):352, July 1994.

[37] John C. Crocker and David G. Grier. When like charges attract: The effects of geometrical confinement on long-range colloidal interactions. *Physical Review Letters*, 77(9):1897–1900, August 1996.

[38] Sunil K. Sainis, Vincent Germain, and Eric R. Dufresne. Statistics of particle trajectories at short time intervals reveal fN-Scale colloidal forces. *Physical Review Letters*, 99(1):018303, July 2007.

[39] Jason W. Merrill, Sunil K. Sainis, and Eric R. Dufresne. Many-body electrostatic forces between colloidal particles at vanishing ionic strength. *Physical Review Letters*, 103(13):138301, September 2009.

[40] Michael Speidel, Alexandr Jonás, and Ernst-Ludwig Florin. Three-dimensional tracking of fluorescent nanoparticles with subnanometer precision by use of off-focus imaging. *Opt. Lett.*, 28(2):69–71, January 2003.

[41] Zhipeng Zhang and Chia-Hsiang Menq. Three-dimensional particle tracking with subnanometer resolution using off-focus images. *Appl. Opt.*, 47(13):2361, April 2008.

[42] R. Colin, M. Yan, L. Chevry, J.-F. Berret, and B. Abou. 3D rotational diffusion of micrometric wires using 2D video microscopy. *Europhys. Lett.*, 97(3):30008, February 2012.

[43] Dennis C. Prieve and Nasser A. Frej. Total internal reflection microscopy: a quantitative tool for the measurement of colloidal forces. *Langmuir*, 6(2):396–403, February 1990.

[44] Herman Chew, Dau-Sing Wang, and Milton Kerker. Elastic scattering of evanescent electromagnetic waves. *Applied Optics*, 18(15):2679–2687, August 1979.

[45] Dennis C. Prieve and John Y. Walz. Scattering of an evanescent surface wave by a microscopic dielectric sphere. *Applied Optics*, 32(9):1629–1641, March 1993.

[46] Dennis C. Prieve. Measurement of colloidal forces with TIRM. *Advances in Colloid and Interface Science*, 82(1-3):93–125, October 1999.

[47] D. L. Sober and J. Y. Walz. Measurement of long range depletion energies between a colloidal particle and a flat surface in micellar solutions. *Langmuir*, 11(7):2352–2356, July 1995.

[48] A. D. Dinsmore, Eric R. Weeks, Vikram Prasad, Andrew C. Levitt, and D. A. Weitz. Three-dimensional confocal microscopy of colloids. *Applied Optics*, 40(24):4152–4159, August 2001.

[49] Thomas G. Dimiduk, Ekaterina A. Kosheleva, David Kaz, Ryan McGorty, Emily J. Gardel, and Vinothan N. Manoharan. A simple, inexpensive holographic microscope. In *Biomedical Optics and 3-D Imaging*, OSA Technical Digest (CD), page JMA38. Optical Society of America, April 2010.

[50] Dennis Gabor. A new microscopic principle. *Nature*, 161(4098):777–778, 1948.

[51] Dennis Gabor. Microscopy by reconstructed wave-fronts. *Proceedings of the Royal Society of London. Series A, Mathematical and Physical Sciences*, 197(1051):454–487, July 1949.

[52] Thomas Kreis. *Handbook of Holographic Interferometry: Optical and Digital Methods*. Wiley-VCH, Weinheim, 2005.

[53] U. Schnars and W. Jüptner. Direct recording of holograms by a CCD target and numerical reconstruction. *Applied Optics*, 33(2):179–181, January 1994.

[54] Etienne Cuche, Patrick Poscio, and Christian D. Depeursinge. Optical tomography at the microscopic scale by means of a numerical low-coherence holographic technique. *Proceedings of the SPIE*, 2927:61–66, December 1996.

[55] Tong Zhang and Ichirou Yamaguchi. Three-dimensional microscopy with phase-shifting digital holography. *Optics Letters*, 23(15):1221–1223, August 1998.

[56] Etienne Cuche, Pierre Marquet, and Christian Depeursinge. Simultaneous amplitude-contrast and quantitative phase-contrast microscopy by numerical reconstruction of fresnel off-axis holograms. *Applied Optics*, 38(34):6994–7001, December 1999.

[57] Hans J. Kreuzer, N. Pomerleau, K. Blagrave, and Manfred H. Jericho. Digital in-line holography with numerical reconstruction. pages 65–74, August 1999.

[58] W. Xu, M. H. Jericho, I. A. Meinertzhagen, and H. J. Kreuzer. Digital in-line holography of microspheres. *Applied Optics*, 41(25):5367–5375, September 2002.

[59] Sang-Hyuk Lee, Yohai Roichman, Gi-Ra Yi, Shin-Hyun Kim, Seung-Man Yang, Alfons van Blaaderen, Peter van Oostrum, and David G. Grier. Characterizing and tracking single colloidal particles with video holographic microscopy. *Opt. Express*, 15(26):18275–18282, December 2007.

[60] Jian Sheng, Edwin Malkiel, and Joseph Katz. Digital holographic microscope for measuring three-dimensional particle distributions and motions. *Applied Optics*, 45(16):3893–3901, June 2006.

[61] Thomas M. Kreis. Frequency analysis of digital holography with reconstruction by convolution. *Opt. Eng.*, 41(8):1829, 2002.

[62] Ye Pu and Hui Meng. Intrinsic aberrations due to mie scattering in particle holography. *Journal of the Optical Society of America A*, 20(10):1920–1932, October 2003.

[63] Ben Ovryn and Steven H. Izen. Imaging of transparent spheres through a planar interface using a high-numerical-aperture optical microscope. *Journal of the Optical Society of America A*, 17(7):1202–1213, July 2000.

[64] Fook Chiong Cheong, Bhaskar Jyoti Krishnatreya, and David G. Grier. Strategies for three-dimensional particle tracking with holographic video microscopy. *Optics Express*, 18(13):13563–13573, June 2010.

[65] Lisa Dixon, Fook Chiong Cheong, and David G. Grier. Holographic deconvolution microscopy for high-resolution particle tracking. *Optics Express*, 19(17):16410, August 2011.

[66] F.C. Cheong, K. Xiao, and D.G. Grier. Technical note: Characterizing individual milk fat globules with holographic video microscopy. *Journal of Dairy Science*, 92(1):95–99, January 2009.

[67] Fook Chiong Cheong, Bo Sun, Rémi Dreyfus, Jesse Amato-Grill, Ke Xiao, Lisa Dixon, and David G. Grier. Flow visualization and flow cytometry with holographic video microscopy. *Optics Express*, 17(15):13071, July 2009.

[68] Ke Xiao and David G. Grier. Multidimensional optical fractionation of colloidal particles with holographic verification. *Physical Review Letters*, 104(2):028302, January 2010.

[69] Milton Kerker. *The scattering of light, and other electromagnetic radiation*. Academic Press, 1969.

[70] James A. Lock and Gérard Gouesbet. Generalized Lorenz–Mie theory and applications. *Journal of Quantitative Spectroscopy and Radiative Transfer*, 110(11):800–807, July 2009.

[71] Craig F. Bohren and Donald R Huffman. *Absorption and Scattering of Light by Small Particles*. Wiley-Interscience, 1998.

[72] W. J. Wiscombe. Improved mie scattering algorithms. *Applied Optics*, 19(9):1505–1509, May 1980.

[73] Hendrik Christoffel van de Hulst. *Light scattering: by small particles*. Courier Dover Publications, 1957.

[74] Michael I. Mishchenko, Joachim W. Hovenier, and Larry D. Travis. *Light Scattering by Nonspherical Particles: Theory, Measurements, and Applications*. Academic Press, September 1999.

[75] Frank W. J. Olver. *NIST Handbook of Mathematical Functions*. Cambridge University Press, May 2010.

[76] Ramesh Bhandari. Scattering coefficients for a multilayered sphere: analytic expressions and algorithms. *Applied Optics*, 24(13):1960–1967, July 1985.

[77] D. W. Mackowski, R. A. Altenkirch, and M. P. Menguc. Internal absorption cross sections in a stratified sphere. *Applied Optics*, 29(10):1551–1559, April 1990.

[78] Li Kai and Patrizio Massoli. Scattering of electromagnetic-plane waves by radially inhomogeneous spheres: a finely stratified sphere model. *Applied Optics*, 33(3):501–511, January 1994.

[79] Wen Yang. Improved recursive algorithm for light scattering by a multilayered sphere. *Applied Optics*, 42(9):1710–1720, March 2003.

[80] Adeline Perro, Guangnan Meng, Jerome Fung, and Vinothan N. Manoharan. Design and synthesis of model transparent aqueous colloids with optimal scattering properties. *Langmuir*, 25(19):11295–11298, October 2009.

[81] O. Peña and U. Pal. Scattering of electromagnetic radiation by a multilayered sphere. *Computer Physics Communications*, 180(11):2348–2354, November 2009.

[82] Daniel W. Mackowski and Michael I. Mishchenko. Calculation of the t matrix and the scattering matrix for ensembles of spheres. *J. Opt. Soc. Amer. A*, 13(11):2266–2278, November 1996.

[83] Daniel W. Mackowski. Analysis of radiative scattering for multiple sphere configurations. *Proceedings: Mathematical and Physical Sciences*, 433(1889):599–614, June 1991.

[84] Daniel W. Mackowski. Calculation of total cross sections of multiple-sphere clusters. *Journal of the Optical Society of America A*, 11(11):2851–2861, November 1994.

[85] Jerome Fung, K. Eric Martin, Rebecca W. Perry, David M. Kaz, Ryan McGorty, and Vinothan N. Manoharan. Measuring translational, rotational, and vibrational dynamics in colloids with digital holographic microscopy. *Opt. Express*, 19(9):8051–8065, April 2011.

[86] Michael I. Mishchenko, Larry D. Travis, and Daniel W. Mackowski. T-matrix computations of light scattering by nonspherical particles: A review. *Journal of Quantitative Spectroscopy and Radiative Transfer*, 55(5):535–575, May 1996.

[87] Michael I. Mishchenko. Calculation of the amplitude matrix for a nonspherical particle in a fixed orientation. *Applied Optics*, 39(6):1026–1031, February 2000.

[88] Bruce T. Draine and Piotr J. Flatau. Discrete-dipole approximation for scattering calculations. *Journal of the Optical Society of America A*, 11(4):1491–1499, April 1994.

[89] M.A. Yurkin and A.G. Hoekstra. The discrete dipole approximation: An overview and recent developments. *Journal of Quantitative Spectroscopy and Radiative Transfer*, 106(1–3):558–589, July 2007.

[90] Maxim A. Yurkin and Alfons G. Hoekstra. The discrete-dipole-approximation code ADDA: capabilities and known limitations. *Journal of Quantitative Spectroscopy and Radiative Transfer*, 112(13):2234–2247, September 2011.

[91] Peter W. Milonni and Robert W. Boyd. Momentum of light in a dielectric medium. *Advances in Optics and Photonics*, 2(4):519–553, December 2010.

[92] C. B. Markwardt. Non-linear least-squares fitting in IDL with MPFIT. volume 411, page 251, September 2009.

[93] W. Mendenhall and T. Sincich. *Statistics for engineering and the sciences*. Dellen Pub. Co., San Francisco, 3rd edition, 1991.

[94] Sho Asakura and Fumio Oosawa. Interaction between particles suspended in solutions of macromolecules. *Journal of Polymer Science*, 33(126):183–192, 1958.

[95] A. Vrij. Polymers at interfaces and the interactions in colloidal dispersions. *Pure Appl. Chem*, 48(4):471, 1976.

[96] R. Roth, R. Evans, and S. Dietrich. Depletion potential in hard-sphere mixtures:⊠⊠theory and applications. *Physical Review E*, 62(4):5360–5377, October 2000.

[97] M. Andersson and S. L. Maunu. Structural studies of poly(n-isopropylacrylamide) microgels: Effect of sds surfactant concentration in the microgel synthesis. *Journal of Polymer Science Part B-Polymer Physics*, 44(23):3305–3314, 2006.

[98] Karol J Mysels and Pasupati Mukerjee. *Critical micelle concentrations of aqueous surfactant systems*. NSRDS-NBS, 36. U.S. National Bureau of Standards, Washington,, 1971.

[99] Allison M. Yake, Rocco A. Panella, Charles E. Snyder, and Darrell Velegol. Fabrication of colloidal doublets by a salting Out–Quenching–Fusing technique. *Langmuir*, 22(22):9135–9141, October 2006.

[100] A. D. Dinsmore, Ming F. Hsu, M. G. Nikolaides, Manuel Marquez, A. R. Bausch, and D. A. Weitz. Colloidosomes: Selectively permeable capsules composed of colloidal particles. *Science*, 298(5595):1006–1009, November 2002.

[101] Spencer Umfreville Pickering. Emulsions. *Journal of the Chemical Society, Transactions*, 91(0):2001–2021, January 1907.

[102] Bernard P. Binks and Tommy S. Horozov. *Colloidal particles at liquid interfaces*. Cambridge University Press, Cambridge ;New York, 2006.

[103] David M. Kaz, Ryan McGorty, Madhav Mani, Michael P. Brenner, and Vinothan N. Manoharan. Physical ageing of the contact line on colloidal particles at liquid interfaces. *Nature Materials*, 11(2):138–142, February 2012.

[104] Dominic Vella and L. Mahadevan. The "Cheerios effect". *American Journal of Physics*, 73(9):817, 2005.

[105] Krassimir D. Danov, Peter A. Kralchevsky, Boris N. Naydenov, and Günter Brenn. Interactions between particles with an undulated contact line at a fluid interface: Capillary multipoles of arbitrary order. *Journal of Colloid and Interface Science*, 287(1):121–134, July 2005.

[106] Robert Aveyard, John H. Clint, Dieter Nees, and Vesselin N. Paunov. Compression and structure of monolayers of charged latex particles at Air/Water and Octane/Water interfaces. *Langmuir*, 16(4):1969–1979, February 2000.

[107] Alois Würger. Curvature-induced capillary interaction of spherical particles at a liquid interface. *Physical Review E*, 74(4):041402, October 2006.

[108] Chuan Zeng, Fabian Brau, Benny Davidovitch, and Anthony D. Dinsmore. Capillary interactions among spherical particles at curved liquid interfaces. *Soft Matter*, 8(33):8582–8594, August 2012.

[109] A. R. Bausch, M. J. Bowick, A. Cacciuto, A. D. Dinsmore, M. F. Hsu, D. R. Nelson, M. G. Nikolaides, A. Travesset, and D. A. Weitz. Grain boundary scars and spherical crystallography. *Science*, 299(5613):1716–1718, March 2003.

[110] E. M. Herzig, K. A. White, A. B. Schofield, W. C. K. Poon, and P. S. Clegg. Bicontinuous emulsions stabilized solely by colloidal particles. *Nat Mater*, 6(12):966–971, December 2007.

[111] L. Antl, J.W. Goodwin, R.D. Hill, R.H. Ottewill, S.M. Owens, S. Papworth, and J.A. Waters. The preparation of poly(methyl methacrylate) latices in non-aqueous media. *Colloids and Surfaces*, 17(1):67–78, January 1986.

[112] Ronald Pethig. Dielectrophoresis: Status of the theory, technology, and applications. *Biomicrofluidics*, 4(2):022811, 2010.

[113] Hywel Morgan, Alberto García Izquierdo, David Bakewell, Nicolas G Green, and Antonio Ramos. The dielectrophoretic and travelling wave forces generated by interdigitated electrode arrays: analytical solution using fourier series. *Journal of Physics D: Applied Physics*, 34(10):1553–1561, May 2001.

[114] Miranda Holmes-Cerfon, Steven J. Gortler, and Michael P. Brenner. A geometrical approach to computing free-energy landscapes from short-ranged potentials. *Proc. Nat. Acad. Sci. USA*, 110(1):E5–E14, January 2013.

[115] Francis Perrin. Mouvement brownien d'un ellipsoide-i. dispersion diélectrique pour des molécules ellipsoidales. *J. Phys. Radium*, 5:497–511, 1934.

[116] Avinoam Nir and Andreas Acrivos. On the creeping motion of two arbitrary-sized touching spheres in a linear shear field. *J. Fluid Mech.*, 59(02):209–223, 1973.

[117] Martin Hoffmann, Claudia S. Wagner, Ludger Harnau, and Alexander Wittemann. 3D brownian diffusion of submicron-sized particle clusters. *ACS Nano*, 3(10):3326–3334, October 2009.

[118] Yilong Han, Ahmed Alsayed, Maurizio Nobili, and Arjun G. Yodh. Quasi-two-dimensional diffusion of single ellipsoids: Aspect ratio and confinement effects. *Phys. Rev. E*, 80(1):011403, July 2009.

[119] Stephen M. Anthony, Minsu Kim, and Steve Granick. Translation-rotation decoupling of colloidal clusters of various symmetries. *J. Chem. Phys.*, 129(24):244701–6, December 2008.

[120] Deshpremy Mukhija and Michael J. Solomon. Translational and rotational dynamics of colloidal rods by direct visualization with confocal microscopy. *J. Colloid Interface Sci.*, 314(1):98–106, October 2007.

[121] Gary L. Hunter, Kazem V. Edmond, Mark T. Elsesser, and Eric R. Weeks. Tracking rotational diffusion of colloidal clusters. *Opt. Express*, 19(18):17189–17202, August 2011.

[122] Fook C. Cheong and David G. Grier. Rotational and translational diffusion of copper oxide nanorods measured with holographic video microscopy. *Opt. Express*, 18(7):6555–6562, March 2010.

[123] Daniela J. Kraft, Raphael Wittkowski, Borge ten Hagen, Kazem V. Edmond, David J. Pine, and Hartmut Löwen. Brownian motion and the hydrodynamic friction tensor for colloidal particles of arbitrary shape. *arXiv:1305.1253*, May 2013.

[124] Howard Brenner. Coupling between the translational and rotational brownian motions of rigid particles of arbitrary shape: II. general theory. *J. Colloid Interface Sci.*, 23(3):407–436, March 1967.

[125] John R. Happel and Howard Brenner. *Low Reynolds Number Hydrodynamics*. Kluwer, Dordrecht, 1991.

[126] Steven Harvey and Jose García de la Torre. Coordinate systems for modeling the hydrodynamic resistance and diffusion coefficients of irregularly shaped rigid macromolecules. *Macromolecules*, 13(4):960–964, July 1980.

[127] Stephen C. Harvey. Transport properties of particles with segmental flexibility. i. hydrodynamic resistance and diffusion coefficients of a freely hinged particle. *Biopolymers*, 18(5):1081–1104, 1979.

[128] Howard Brenner. Coupling between the translational and rotational brownian motions of rigid particles of arbitrary shape i. helicoidally isotropic particles. *Journal of Colloid Science*, 20(2):104–122, February 1965.

[129] Herbert Goldstein. *Classical mechanics*. Addison-Wesley Pub. Co., 1980.

[130] R. K. Pathria. *Statistical Mechanics*. Butterworth-Heinemann, September 1996.

[131] Peyman Pakdel and Sangtae Kim. Mobility and stresslet functions of particles with rough surfaces in viscous fluids: A numerical study. *J. Rheol.*, 35(5):797–823, 1991.

[132] Stuart A. Allison. Low reynolds number transport properties of axisymmetric particles employing stick and slip boundary conditions. *Macromolecules*, 32(16):5304–5312, August 1999.

[133] Sergio Aragon and David K. Hahn. Precise boundary element computation of protein transport properties: Diffusion tensors, specific volume, and hydration. *Biophys. J.*, 91(5):1591–1603, September 2006.

[134] J. García de la Torre and B. Carrasco. Hydrodynamic properties of rigid macromolecules composed of ellipsoidal and cylindrical subunits. *Biopolymers*, 63(3):163–167, 2002.

[135] J. K. G. Dhont. *An Introduction to Dynamics of Colloids*. Elsevier, May 1996.

[136] Jens Rotne and Stephen Prager. Variational treatment of hydrodynamic interaction in polymers. *The Journal of Chemical Physics*, 50(11):4831–4837, June 1969.

[137] Beatriz Carrasco and José García de la Torre. Hydrodynamic properties of rigid particles: Comparison of different modeling and computational procedures. *Biophys. J.*, 76(6):3044–3057, June 1999.

[138] J. García de la Torre, G. del Rio Echenique, and A. Ortega. Improved calculation of rotational diffusion and intrinsic viscosity of bead models for macromolecules and nanoparticles. *J. Phys. Chem. B*, 111(5):955–961, February 2007.

[139] L. Dale Favro. Theory of the rotational brownian motion of a free rigid body. *Phys. Rev.*, 119(1):53–62, July 1960.

[140] Jill E. Seebergh and John C. Berg. Evidence of a hairy layer at the surface of polystyrene latex particles. *Colloids Surf., A*, 100:139–153, July 1995.

[141] M. R Gittings and D. A Saville. The determination of hydrodynamic size and zeta potential from electrophoretic mobility and light scattering measurements. *Colloids Surf., A*, 141(1):111–117, October 1998.

[142] Jerome Fung, Rebecca W. Perry, Thomas G. Dimiduk, and Vinothan N. Manoharan. Imaging multiple colloidal particles by fitting electromagnetic scattering solutions to digital holograms. *J. Quant. Spectrosc. Radiat. Transfer*, 113(18):2482–2489, December 2012.

[143] Brian Moths and T. A. Witten. Full alignment of colloidal objects by programed forcing. *Physical Review Letters*, 110(2):028301, January 2013.

[144] D.W. Mackowski and M.I. Mishchenko. A multiple sphere t-matrix fortran code for use on parallel computer clusters. *Journal of Quantitative Spectroscopy and Radiative Transfer*, 112(13):2182–2192, September 2011.

[145] Sangtae Ahn and Jeffrey A. Fessler. Standard errors of mean, variance, and standard deviation estimators. *University of Michigan: EECS Department*, 2003.

[146] E. L. Lehmann and George Casella. *Theory of Point Estimation*. Springer, August 1998.

[147] H. Flyvbjerg and H. G. Petersen. Error estimates on averages of correlated data. *J. Chem. Phys.*, 91(1):461–466, July 1989.

[148] Thierry Savin and Patrick S. Doyle. Statistical and sampling issues when using multiple particle tracking. *Physical Review E*, 76(2):021501, August 2007.

[149] J. D. Jackson. Examples of the zeroth theorem of the history of science. *American Journal of Physics*, 76(8):704, 2008.

[150] Daniel A. Beard and Tamar Schlick. Unbiased rotational moves for rigid-body dynamics. *Biophysical Journal*, 85(5):2973–2976, November 2003.

[151] Miguel X. Fernandes and JosÃ© GarcÃ-a de la Torre. Brownian dynamics simulation of rigid particles of arbitrary shape in external fields. *Biophysical Journal*, 83(6):3039–3048, December 2002.

[152] B. B. Guzina and M. Bonnet. Topological derivative for the inverse scattering of elastic waves. *The Quarterly Journal of Mechanics and Applied Mathematics*, 57(2):161–179, May 2004.

[153] Owen B. Toon and T. P. Ackerman. Algorithms for the calculation of scattering by stratified spheres. *Applied Optics*, 20(20):3657–3660, October 1981.

[154] Marek. Sitarski. Internal heating of multilayered aerosol particles by electromagnetic radiation. *Langmuir*, 3(1):85–93, January 1987.

[155] Gorden Videen. Light scattering from a sphere on or near a surface. *Journal of the Optical Society of America A*, 8(3):483–489, March 1991.

[156] Gorden Videen. Light scattering from a sphere on or near a surface: errata. *Journal of the Optical Society of America A*, 9(5):844–845, May 1992.

[157] John David Jackson. *Classical Electrodynamics*. Wiley, January 1999.

[158] Marcus J. Grote and Joseph B. Keller. Exact nonreflecting boundary conditions for the time dependent wave equation. *SIAM Journal on Applied Mathematics*, 55(2):280–297, April 1995.

[159] D. Torrungrueng, B. Ungan, and J.T. Johnson. Optical theorem for electromagnetic scattering by a three-dimensional scatterer in the presence of a lossless half space. *IEEE Geoscience and Remote Sensing Letters*, 1(2):131–135, 2004.

[160] G. Segré and A. Silberberg. Radial particle displacements in poiseuille flow of suspensions. *Nature*, 189(4760):209–210, January 1961.

[161] G. Segré and A. Silberberg. Behaviour of macroscopic rigid spheres in poiseuille flow part 2. experimental results and interpretation. *Journal of Fluid Mechanics*, 14(01):136–157, 1962.

[162] Dino Di Carlo. Inertial microfluidics. *Lab on a Chip*, 9(21):3038–3046, November 2009.

[163] Jeffrey A. Schonberg and E. J. Hinch. Inertial migration of a sphere in poiseuille flow. *Journal of Fluid Mechanics*, 203:517–524, 1989.

[164] Dino Di Carlo, Daniel Irimia, Ronald G. Tompkins, and Mehmet Toner. Continuous inertial focusing, ordering, and separation of particles in microchannels. *Proceedings of the National Academy of Sciences*, 104(48):18892–18897, November 2007.

[165] Joseph M. Martel and Mehmet Toner. Inertial focusing dynamics in spiral microchannels. *Physics of Fluids*, 24(3):032001–032001–13, March 2012.

[166] Lisa Dixon, Fook C. Cheong, and David G. Grier. Holographic particle-streak velocimetry. *Optics Express*, 19(5):4393, February 2011.

[167] Michael Potmesil and Indranil Chakravarty. Modeling motion blur in computer-generated images. *SIGGRAPH Comput. Graph.*, 17(3):389–399, July 1983.